# Matériaux Nanohybrides à Large Bande Interdite: Études de Synthèses, Propriétés et Applications

Aurore Said

## ▶ To cite this version:

Aurore Said. Matériaux Nanohybrides à Large Bande Interdite: Études de Synthèses, Propriétés et Applications. Physique [physics]. Université de la Méditerranée - Aix-Marseille II, 2007. Français. NNT : . tel-00266833

HAL Id: tel-00266833
https://theses.hal.science/tel-00266833

Submitted on 25 Mar 2008

***UNIVERSITÉ DE LA MÉDITERRANÉE AIX-MARSEILLE II***
***FACULTÉ DES SCIENCES DE LUMINY***
***ÉCOLE DOCTORALE « PHYSIQUE ET SCIENCES DE LA MATIÈRE »***

*N° attribué par la bibliothèque*

# THÈSE

Présentée en vue de l'obtention du grade de

## *DOCTEUR DE L'UNIVERSITÉ DE LA MÉDITERRANÉE*

Spécialité : ***Sciences des matériaux, Physique, Chimie et Nanosciences***

Par ***Aurore SAID***

**Titre :**

# *Matériaux Nanohybrides à Large Bande Interdite: Études de Synthèses, Propriétés et Applications*

Soutenue le 21 décembre 2007 devant la commission d'examen composée de :

| | | |
|---|---|---|
| Dr. GACOIN Thierry | LPMC – Paris | Rapporteur |
| Dr. SNOECK Etienne | CEMES – Toulouse | Rapporteur |
| Prof. LEROUX Christine | L2MP – Toulon | Membre du jury |
| Prof. SAFAROV Viatcheslav | CRMCN – Marseille | Président du jury |
| Dr. ACKERMANN Jörg | GCOMM – Marseille | Membre invité |
| Prof. GIORGIO Suzanne | CRMCN – Marseille | Co-directrice de thèse |
| Dr. MARINE Wladimir | CRMCN – Marseille | Directeur de thèse |

# Acknowledgments

*This work was done at the "Centre de Recherche en Matière Condensée et Nanosciences" successively headed by Prof. Viatcheslav Safarov and Dr. Claude Henry. I would like to thank them both for greeting me during these three years of thesis.*

*I would also like to convey thanks to the CNRS for providing me the financial means via a BDI scholarship.*

*While being an individual work, my PHD thesis benefited from the insights and aid of several people. I want to thank all of them, including those not mentioned here by name.*

*First of all I wish to express my sincere gratitude to my thesis supervisor, Wladimir MARINE who was abundantly helpful and offered by his wide knowledge invaluable assistance, and guidance throughout these three years. Deepest gratitude is also due to Suzanne GIORGIO, my co-supervisor, for her constant assist, support and kindness. I want to thank them both for their availability and their patience even in the most difficult moments. I would like to thank them for their advice as much on the technical aspects and on the interpretation of the results.*

*Next I am deeply thankful for the reporters and the other members of my thesis committee, Dr. Thierry GACOIN (research director at the "Laboratoire de Physique de la Matière Condensée, Ecole Polytechnique, Paris"), Dr. Etienne SNOECK (research director at the "Centre d'Elaboration de Matériaux et d'Etudes Structurales, Toulouse") and Prof. Christine LEROUX (Professor at the "Université du Sud Toulon-Var"). I greatly appreciate Prof. Viatcheslav SAFAROV for his willing to preside my jury committee. I'm really honoured and thankful to all of them for the time they spent reviewing my thesis. Indeed, each individual provided comments and suggestions that guided and challenged my thinking, substantially improving the completed product.*

*A major part of my thesis project was performed in collaboration with the chemists group at the GCOM2 laboratory headed by Prof. Frederic FAGES whom I like to truthfully thank. Special thanks go to the CNRS researcher Jörg ACKERMANN, with whom I directly worked, for the many discussions that we have had and for the valuable suggestions that he provided me. I must also acknowledge Prof. Olivier SIRI and the PHD students that I worked with, namely Cyril MARTINI and Guillaume POIZE.*

*I express my profound and affectionate appreciation to the Research Engineer Daniel PAILHAREY who offered me the possibility to work on his AFM apparatus. I thank also the CNRS researcher Daniel FERRY for giving me the opportunity to use his FTIR equipment. I also extend my appreciation to the CNRS researcher Xavier MORIN from the IBDML lab who lent to me the optical microscope.*

*I would like to express my gratefulness to the engineers who participated in the smooth functioning of this work: Frederic BEDU of the MEB service, Franck JANDARD of the electronic service and Bruno GELY of the informatics service, and very particularly to*

*Serges NITSCHE and Damien CHAUDANSON of the TEM service. My thanks are also dedicated to the technician Marcel FERNANDEZ of the mechanical workshop.*

*I thank the entire laboratory for allowing me to work in a friendly environment. Best regards to my colleagues at the PIALA platform: Laszlo SAJTI with whom I worked out the laser ablation process in the part of the thesis concerning the ZnO nanoparticles' elaboration via laser ablation route, and Artak KARAPETYAN.*

*I owe special and warm gratitude to the persons with whom I found continuous support and sincere friendship. Thank u Prof. Yves MATHEY and thank u dear friend Carole SCOMPARIN.*

*I'm forever grateful to Dr. Malek TABBAL at the American University of Beirut, my dearest and precious friend, whom I regard with high esteem for his sincere and non-stop moral support.*

*Above all, I'm greatly indebted to my beloved family: my father Joseph, my mother Najah, my sister Ramona and my two brothers Romeo and Georges for their continuous and unconditional support, encouragement and love.*

# Contents

**<u>Appendix</u>**

# INTRODUCTION

Nanoscience and nanotechnology are the two research topics that bring into play the study and the manufacture of matter on the scale of 1 to 100 nanometers, a scale at which novel physical, chemical and biological properties enable novel applications. Engineering of functional systems at the molecular scale is essentially at the base of "the nearest industrial revolution" and the most significant technological development of the 21st century. These nanotechnologies could have a considerable impact on almost all the aspects of our existence. They regroup many disciplines and industries. Thus, placing interests at the forefront of the nanoscience revolution identifies current challenges and development paths due to influence fields ranging from materials, physics, chemistry and biomedicine to technology development critical to research at atomic scales. The early stage of development of the majority of the nanotechnologies prohibited however to give a detailed scale of time. Moreover, the products and the potential applications will be born only under at least two conditions: on the one hand if they answer at the request of a market and on the other hand if inexpensive manufacturing methods, able to be extrapolated with great volumes and preserving the properties on a nanometric scale of the final product can be developed.

Nanotechnology refers to the expected ability to construct items “*from the bottom-up”*, atom by atom or molecule by molecule, or “*from the top-down”,* nanoscale devices by using larger ones, by the means of techniques and tools being developed today to make complete, highly advanced products. These products have particular properties because of their small size. On the one hand, the nanomaterials possess a surface area to mass ratio much more important than their parent materials at a larger scale; this can induce a higher chemical surface reactivity. On the other hand, quantum effects strongly influence the physico-chemical properties of nanoscale materials thus modify their optical, electric, mechanical and magnetic properties.

Elaborating nanostructured *“Hybrid”* materials with new physical properties experiences nowadays a colossal growth and appeared as one of the most stimulating research fields. Composed of inorganic matrix hosting organic dye molecules, these nanohybrids present a very promising approach for innovative nanomaterials by combining the properties of organic and inorganic materials in one nanoparticle to be incorporated in nanodevices having novel tailor-made multifunctionalities.

Associated to an important class of transparent high mobility semiconducting nanomaterials and having particular optical and electrical properties, the II-VI semiconductor Zinc oxide (ZnO), of large band gap energy of 3.37 eV [1], is the inorganic biocompatible semiconductor used in the form of nanoparticles representing the inorganic part of the hybrid systems that we are trying to develop all along this research theme. We prepared ZnO nanoparticles through two different methods; by *femtosecond laser ablation in liquid medium* and by *chemical processes*.

Femtosecond laser ablation in liquid medium incarnates the very cleanest and powerful method to fabricate several nanocrystalline materials [2-4]. In our case, defectless nanospherical shaped ZnO, prepared by femtosecond laser ablation in divers liquids, are grafted with selected dye molecules whose Lowest Unoccupied Molecular Orbital (LUMO) is positioned at a lower energy than the ZnO Conduction Band (CB). This parameter is required to assure electron transfer from ZnO, upon two-photon excitation of ZnO, to the dye whose luminescence is monitored. The nanohybrid emanating from this ablation process can be applied as nanoprobes in high resolution imaging at the single cell level, in medical diagnostics and therapeutics [5]. It can as well be pertinent in the bi-photonic imagery in biology concerning the comprehension of the neuronal structures and the dynamics of living cell [6,7]. The main task of ZnO is to be excited through two-photon excitation instead of the UV single-photon excitation which is destructive to cells and tissues.

Nevertheless and despite its elite outcome properties, laser ablation in liquids produces “small” quantities of “uniquely” nanospherical shaped-ZnO. However, we need “greater” quantities of ZnO nanoparticles to be used in our other application field of photovoltaic cells that require abundance of spherical- and rod-shaped ZnO. For this reason we switched on to manufacture large amount of ZnO nanospheres and nanorods through simple chemical solution-based processes [8].

As the evidence of global warming persists to build-up, it is becoming crucial to find ways to produce electricity without the release of greenhouse gases as the carbon dioxide that will increase by 70% by the year 2030 [9]. The capital of fossil fuels, supplying 80% of all energy consumed [10], will fall over the long term that is roughly 40 years for oil, 60 years for natural gas and 200 years for coal [11]. Nowadays energy fuel- and nuclear-based networks will not be adequate to grant the increment energy demand in a sustainable way, besides of their harmful side effects. Hence, it is mandatory to find alternative clean power sources. Sufficient supplies of clean energy are intimately allied with worldwide stability, economic prosperity, and quality of human life. Fortunately, we have the sun as the very clean inexhaustible abundant natural power source. Sunlight provides the Earth with $4.3 \times 10^{20}$ J in one hour, which is more than the total world-widely energy consumed in one year [12]!!! Currently, this solar resource is exploited through solar electricity using solar cells. So far, in 2001, solar electricity supplies less than 0.1% of the world's electricity. Hence, the colossal gap that exists between our exploitation of solar energy through photovoltaic technology and its huge unripe prospective defines the large title in the upcoming energy exploration.

At the moment, commercially available photovoltaic modules are primarily based on expensive all-inorganic solar cells, and to a small extent on inorganic/organic hybrid systems. One route to harvesting the energy of the sun involves learning to imitate natural photosynthesis. Here, sunlight falls on an organic dye which plays a central role in capturing light. This opens the way widely to the hybrid solar cell perception that consists on blending of organic and inorganic materials thus, combines the unique properties of inorganic semiconductors with organic dyes and polymers. Conceptual and practical breakthroughs were achieved in the late 1980s by the work of Grätzel and co-workers, who introduced the application of nanostructured semiconductors for dye-sensitized solar cells [13]. In the following years, the Grätzel cell has become the eminent prototype of research in photovoltaics.

To date, several studies were carried out on the wide gap $TiO_2$ oxide while very few studies were performed on the solution processed Zinc oxide (ZnO) [14,15], which embodied our field of interest. ZnO nanoparticles by themselves show limited photoactivity under UV-visible irradiation. However the ZnO material can be made sensitive to visible light by means of the principle referred to “dye-sensitization”. The choice of the dye type should respond to several constraints as for example its electron affinity with respect to the other solar cell active components. Hence, the dye’s Lowest Unoccupied Molecular Orbital (LUMO) is positioned at higher energy level than the ZnO Conduction Band (CB). This mechanism operates contrary to that of ZnO-based hybrid systems produced through laser ablation as mentioned above. Here, the dye transfers its electron to ZnO upon illumination. Our present study is thus based on grafting in solution of organic dye molecules on inorganic ZnO colloidal nanoparticles so as to greatly increase the contact surface of both materials hence, enlarging their photoactive interface being the heart of the carriers exchange. This hybrid blend is next mixed with the organic conducting polymer P3HT. Two types of dye molecules were chosen; namely, “Porphyrin” and “Ruthenium-containing” sensitizing dyes. The very few reported studies on ZnO-based Dye-Synthesized Solar Cells incorporating the above mentioned dye families [16-18] boost our present main interests and studies.

This thesis, emerged from the nanometric world, consists on the synthesis and the study of a new family of nanohybrids by grafting of organic molecules on the surface of the inorganic nanoparticules. It is designed in five chapters that are each structured to give an introduction to the subject matter, including a briefed literature review to place the work into context, pursued by experimental details, results, discussions and conclusions. The first chapter gives an overview of some of the known basic properties of ZnO. The second chapter is dedicated to the synthesis of nanohybrid based-ZnO nanoparticles by femtosecond laser ablation in liquid medium, where we show the experimental setup, mechanisms of laser ablation. We describe the characterization of the ablated ZnO nanoparticles in different liquids, and then the optical (Photoluminescence and Absorbance) and morphological (Atomic Force Microscopy (AFM) and High Resolution Transmission Electron Microscopy (HRTEM)) properties when grafting of several organic dye molecules onto the ZnO nanospheres, to be used in the bio-imaging. The third chapter explores the elaboration of ZnO nanorods through chemical processes whose morphological growth is monitored through High Resolution Tansmission Electron Microscopy (HRTEM). The fourth chapter deals with the optical analyses of the colloidal hybrid samples, when grafting of dye molecules onto the chemically fabricated ZnO nanospheres and nanorods, which are done by Photoluminescence and absorbance measurements. The photovoltaic properties of solar cells based on dye/rodlike-ZnO chemically made are presented in the fifth chapter. Finally, in the conclusion, some general concluding perceptions are drawn along with projected open-ways for possible future study guidelines.

# Bibliography

[1] I. Ozerov, M. Arab, V. I. Safarov, W. Marine, S. Giorgio, M. Sentis, and L. Nanai, Appl. Surf. Sci. 226 (2004) 242

[2] T. Tsuji, T. Kakita, and M. Tsuji, Appl. Surf. Sci. 206 (2003) 314

[3] A. V. Kabashin, M. Meunier, C. Kingston, and J. H. T. Luong, J. Phys. Chem. B 107 (2003) 4527

[4] J. P. Sylvestre, A. V. Kabashin, E. Sacher, and M. Meunier, Appl. Phys. A 80 (2005) 753

[5] Vo-Dinh Tuan. Nanotechnology in Biology and Medicine: Methods, Devices, and Applications. Editor: Duke University, North Carolina, USA.

[6] N. J. Emptage, C. A. Reid, A. Fine, and T. V. Bliss, Neuron 38 (2003) 797

[7] L. Forti, M. Bossi, A. Bergamaschi, A. Villa, and A. Malgaroli, Nature 388 (1997) 874

[8] B. Sun, and H. Sirringhaus, Nano Letters 5 (2005) 2408

[9] International Energy Agency World Energy Outlook (2002)

[10] International Energy Agency Renewables in Global Energy Supply An IEA Fact Sheet (2002)

[11] British Petroleum Statistical Review of World Energy (2003)

[12] BASIC RESEARCH NEEDS FOR SOLAR ENERGY UTILIZATION, Report on the Basic Energy Sciences Workshop on Solar Energy Utilization, April (2005)

[13] B. O'Regan, and M. Grätzel, Nature 353 (1991) 737

[14] W. J. E. Beek, M. M. Wienk, and R. A. J. Janssen, Adv. Mater. 16 (2004) 1009

[15] W. Beek, M. Wienk, M. Kemerink, X. Yang, and R. J. Janssen, Phys. Chem. B, 109 (2005) 9505

[16] M. Law, L. E. Greene, J. C. Johnson, R. Saykally, and P. Yang, Nat. Mater. 4 (2005) 455

[17] E. Galoppini, J. Rochford, H. Chen, G. Saraf, Y. Lu, A. Hagfeldt, and G. Boschloo, J. Phys. Chem. B 110 (2006) 16159

[18] P. Ravirajan, A. Peiro, M. Nazeeruddin, M. Graetzel, D. Bradley, J. Durrant, and J. Nelson, J. Phys. Chem. B 110 (2006) 7635

# Chapter 1

# Properties of the zinc oxide semiconductor (ZnO)

In this chapter, we outline the basic properties of ZnO, including the crystal structure and energy band gap structure along with its modifications due to size reduction, as well as a short overview of the electronic and optical properties of ZnO.

## 1.1 Crystal structure and lattice parameters

Under ambient pressure and temperature conditions, ZnO crystallizes in the wurtzite structure, as shown in figure 1, which is classified as a hexagonal lattice (a = b = 0.32497 nm and c = 0.52042 nm [1]) belonging to the space group $P6_3mc$.

The ZnO crystals are generally elongated along the c-axis, limited at the lateral edges by six faces parallel to (100), (010) and (1-10), and at the top and the bottom by two (001) faces. Sometimes, at the end of the rod, the shape is a sharp pyramid with 6 faces parallel to (101), (011) and (1-11).

The ZnO crystal structure can be described as two close hexagonal packing HCP-lattices which are inserted into each other. The O-lattice is shifted by a 0.382 fraction of the unit cell height in the longitudinal c-direction with respect to the Zn-lattice, see figure 1. These two interconnecting sublattices composed of alternate layers of $Zn^{2+}$ and $O^{2-}$ are arranged so that each Zn ion is surrounded by four nearest neighbors of O ions, and vice-versa.

This tetrahedral coordination of packed planes of Zn and O piled along the c-axis leads to a crystal of polar symmetry along the hexagonal longitudinal c-axis. This polarity is accountable for a number of ZnO properties, and is also a key factor in its crystal growth mechanism.

The common planes of ZnO crystal are the Zn and O faces perpendicular to the *c*-axis [001], (100) and (1-10) faces parallel to the lateral edges of the prisms, (101) faces parallel to the edges of the pyramids at the top of the crystal. The atomic structure of each face is characterized by an elementary layer repeated in the crystal structure, which, according to Hartmann [2,3], consists of the minimum structural atomic planes unit of thickness Δ. To determine the thicknesses Δ(hkl) of the elementary layers, we need to build the schemes of the atomic structure [3,4,5].

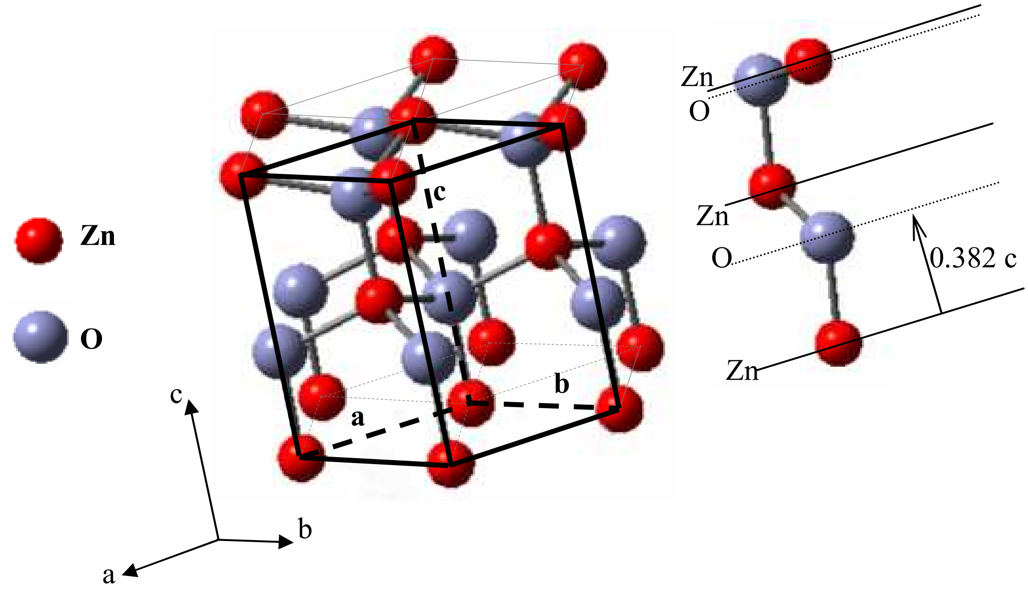

Figure 1. ZnO “wurtzite structure”. One unit cell is sketch out in intense black lines for accuracy. The O-lattice shifted by a 0.382 fraction of the unit cell height “c” from the Zn-lattice.

Let us simplify the task by considering the basal hexagonal plane (001) containing Zn atoms as the reference plan. So we can find the placements of Zn at (0, 0, 0) and $(\frac{2}{3}, \frac{1}{3}, \frac{1}{2})$ and those of O at (0, 0, 0.382) and $(\frac{2}{3}, \frac{1}{3}, \frac{1}{2}+0.382)$.

The different ZnO planes and the corresponding elementary layer thicknesses are shown in figures 2, 3 and 4. We can obviously see the atomic composition and the spacing between the planar atomic nets of each plane family [6]. The atomic charts displayed in figures 1, 2, 3 and 4 representing the ZnO crystal structure seen in different angles are drawn from the graphical program simulation GaussView (version3). GaussView is a complete graphic interface for Gaussian, which can build molecular systems in 3D structure and display molecular orbitals by using the function of construction of the molecules. In figures 2, 3 and 4, the heavy black lines designate the projections of a unit cell onto the plane specific for each figure. Zn and O planes are sketched with black solid and dotted lines, respectively (see figures 2 and 3). Combination of (Zn, O) planes are outlined by dash-dot lines, while the (Zn, O, Zn, O) planes by dash-dot-dot lines (see figure 4). Structure, composition and thickness of each elementary layer are illustrated, where numbers to the right of the atomic planes represent their position, i. e. height, in fractions of the corresponding interplanar spacing indicated to the left [5].

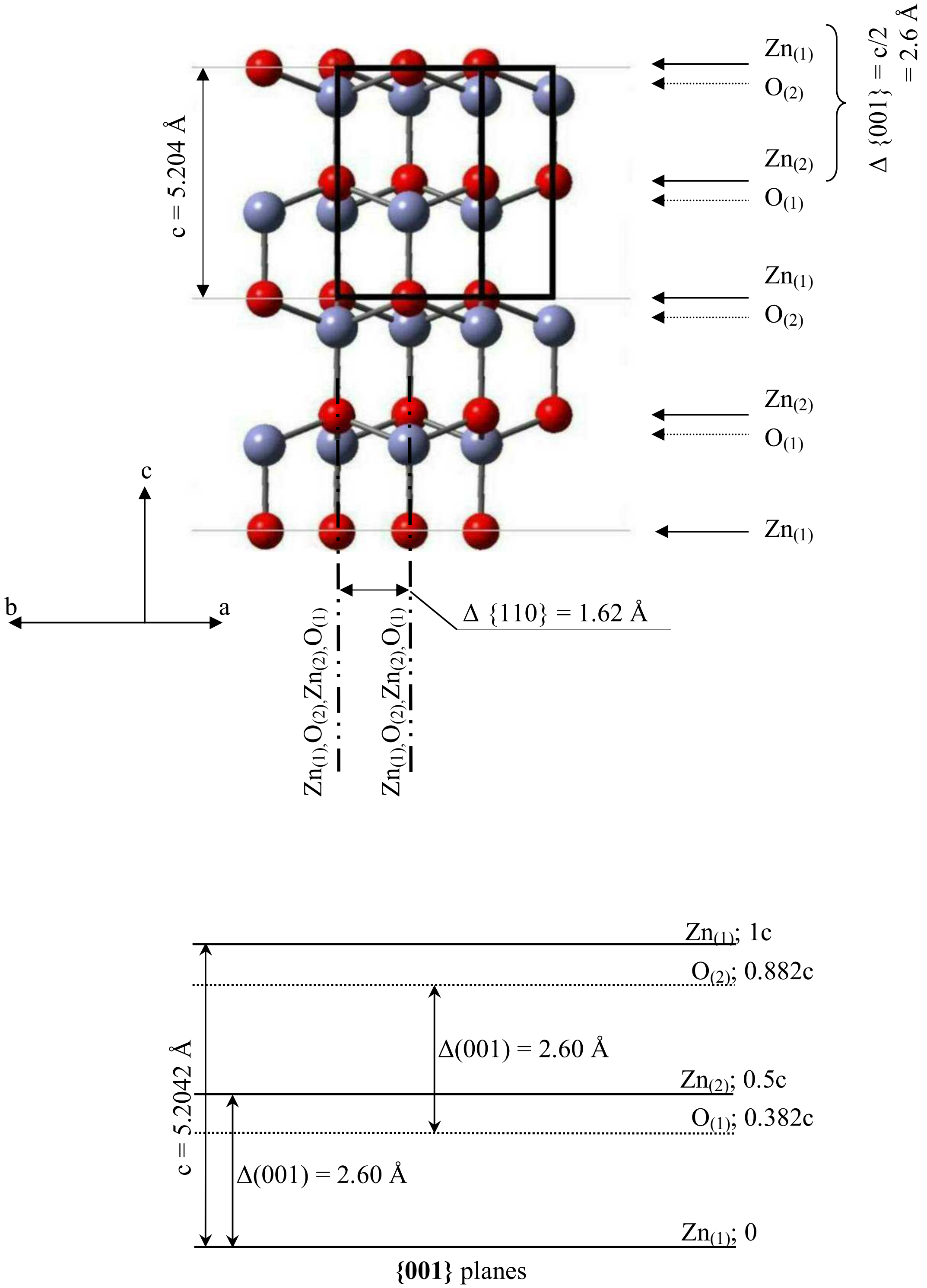

Figure 2. ZnO structure projected onto the (100) plane along with structure, composition and thickness of elementary layers parallel to {001} planes.

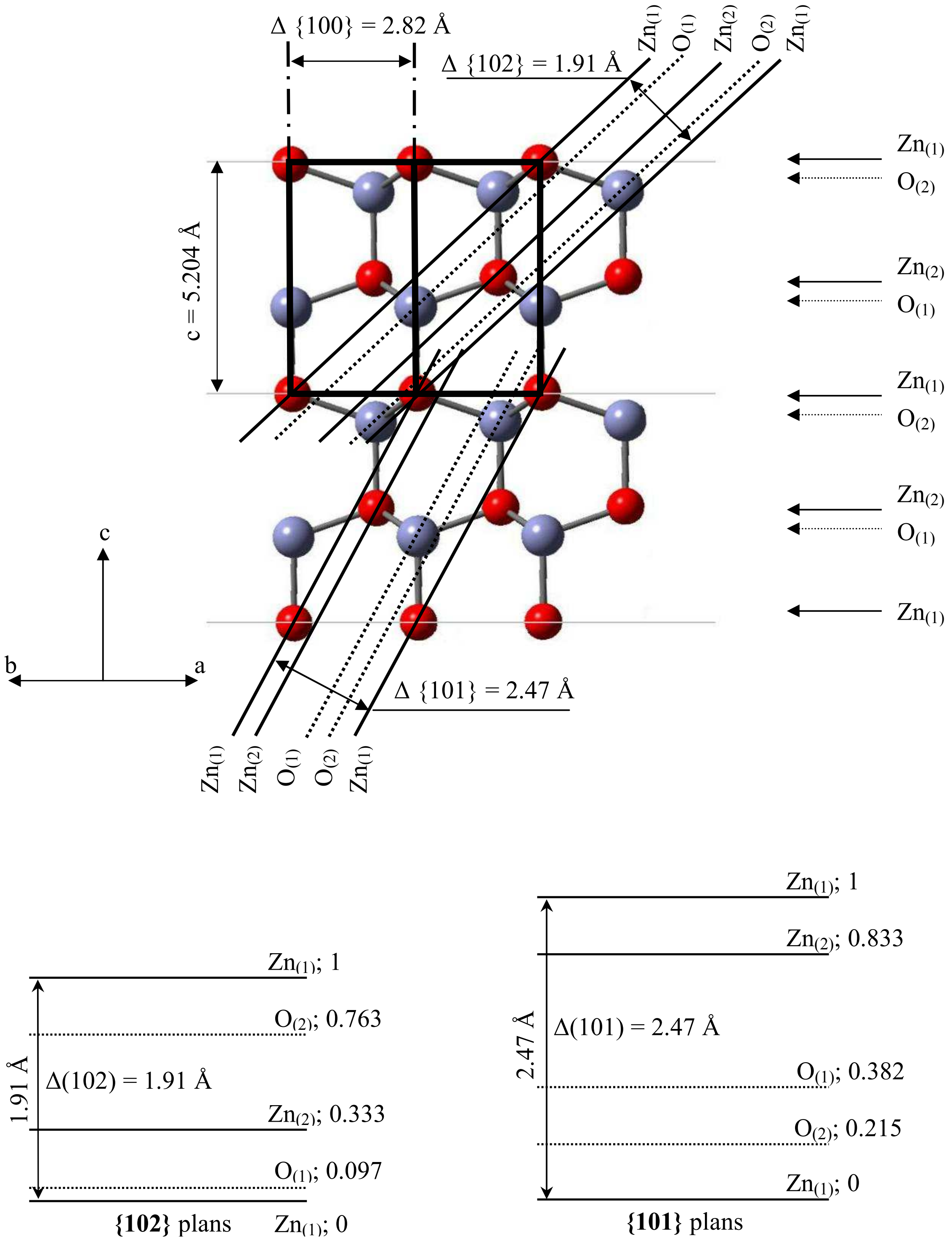

Figure 3. ZnO structure projected onto the (110) plane along with structure, composition and thickness of elementary layers parallel to (102) and (101).

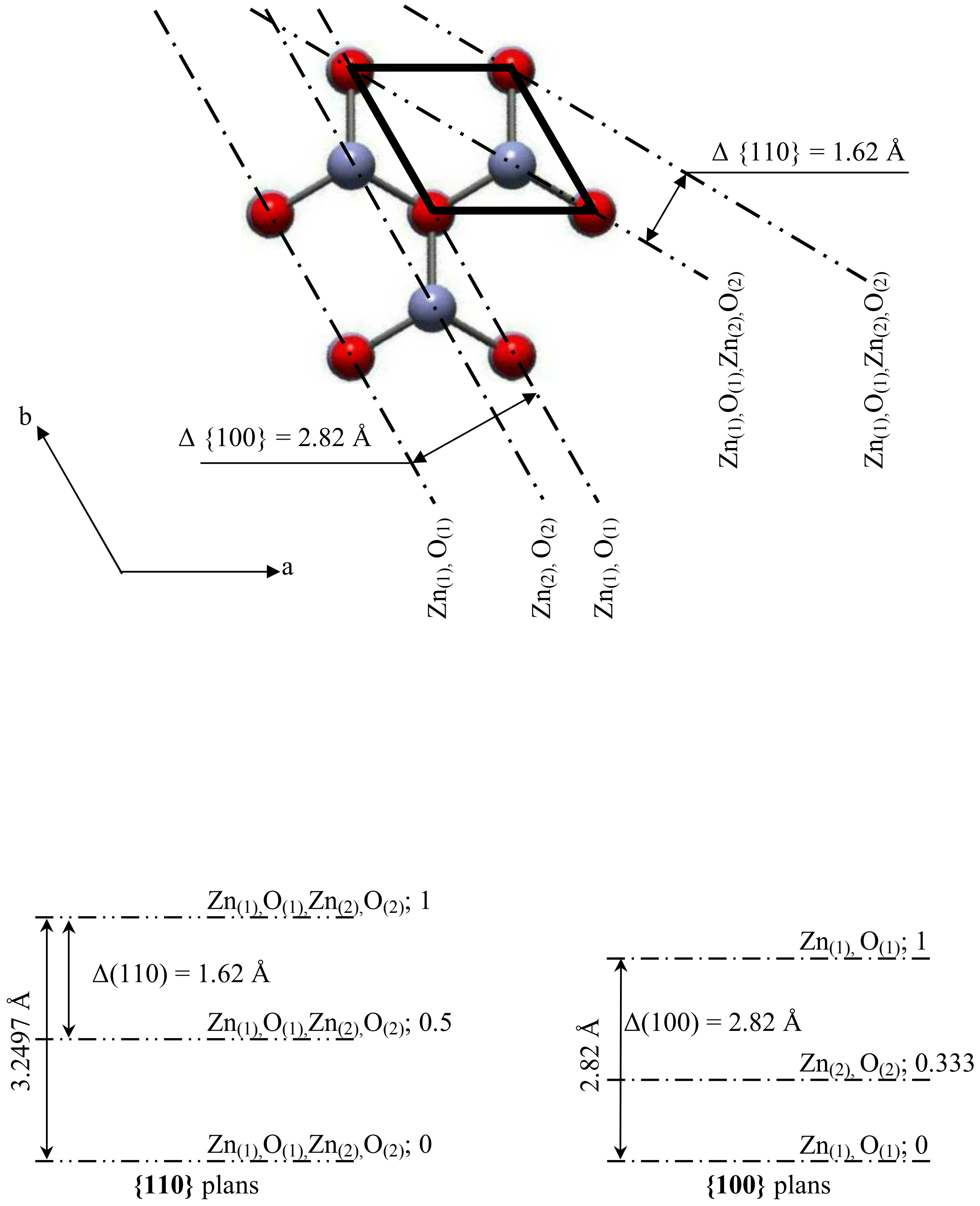

Figure 4. ZnO structure projected onto the (001) plane with structure, composition and thickness of elementary layers parallel to (110) and (100).

Figure 2 shows the projection of the ZnO crystal structure onto the (100) plane where we can see the elementary layers parallel to (001) and the (110) faces. The elementary layer parallel to (001) is constructed by three repetitive sequential planes: Zn plan at zero height, O plan at height 0.382c, and Zn plan at height 1/2c. This leads to visible lattice planes (002) with an elementary distance equal to the half of c namely Δ(002) = 2.6 Å and (110) with a distance Δ(110)=1,62 Å. On the other hand, the O elementary layers have the same thickness of that of the Zn, but with different electric charges. The Zn atoms of (001) have a positive charge close to 2, while the O atoms have a negative charge of -2 [7].

Figure 3 is the projection on (110) plane where we can see the (100), (101) and (102) planes. The distance between the (102) planes is 1.91 Å. The shortest distance between the neighboring distinguished Zn and O pyramidal planes is in the order of 0.2 Å, and the distance between the (101) planes is 2.47 Å. They are constructed by the alternation of two by two plans of the same atomic kind.

The non-polar (110) layers consist of alternating planes, each one composed of a double combination of Zn and O, that is to say (Zn, O, Zn, O). The thickness Δ(110) of its corresponding elementary layer, as shown in figure 4, is 1.62 Å. The other non-polar (100) layer is constructed via alternating planes composed of a combination of both Zn and O on the same plan. The sequence of these planes are repeated every 2.82 Å, which represents the thickness Δ(100) of its corresponding elementary layer, as shown in figure 4.

So far, we offered a detailed study of the ZnO crystallographic structure. Other typical ZnO bulk properties are listed in table 1 [8,9].

| | |
|---|---|
| Phase Stable at 300K | Wurzite [10] |
| Ionic radius | $Zn^{2+}$: 0.74 A, $O^{2-}$: 1.32 A [6] |
| Molecular weight | 81,38 g/mole |
| Density | 5.605 g/cm$^3$ [11] |
| Energy Gap $E_g$ at 300 K | 3.37 eV, Direct |
| Exciton binding Energy | 60 meV |
| Intrinsic carrier concentration | < 106 cm-3 |
| Thermal Conductivity | 0.6 W.cm$^{-1}$.$^{o}$C$^{-1}$ |
| Melting Point | 1975 $^{o}$C [12] |
| Electron effective mass | 0.24 |
| Electron mobility (T = 300 K) | 200 cm$^2$/V s |
| Hole effective mass | 0.59 |
| Hole mobility (T = 300 K) | 5-50 cm$^2$/V s |

Table 1. Physical properties of bulk wurtzite ZnO.

In this tetrahedral coordination of the ZnO crystal, we find the sp3 covalent bonding. However, the Zn - O bond possesses very strong ionic nature, which gives ZnO a mixed ionic-covalent character. So according to the Phillips ionicity scale [13], ZnO resides at the intermediate between an ionic crystal and a covalent crystal, with an ionicity of $f_i = 0.616$. Most probably, this mixed ionic-covalent character implies difficulties in determining the electronic structure of ZnO.

## 1.2 Electronic band structure

ZnO has been considered as an archetype material for probing the precision in calculating through different methods the electronic structure and the band gap energy. A number of authors have consequently investigated ZnO by theoretical and experimental methods [14-26].

Figure 5 shows a schematic energy diagram of the ZnO semiconductor where valence bands (VB) and conduction bands (CB) are separated by the band gap (Eg). Electron affinity and work function are exposed as well. Electron affinity is a measure of the energy change when an electron is added to the conduction band of a neutral atom to form a negative ion, and work function is the energy necessary to remove an electron from the valence band of a the neutral atom to vacuum level. Lots of calculated values for the ZnO affinity and the work function are given in literature; electron affinity is in the range 4.1-4.5 eV, and work function is in the range 7.3-7.7 eV.

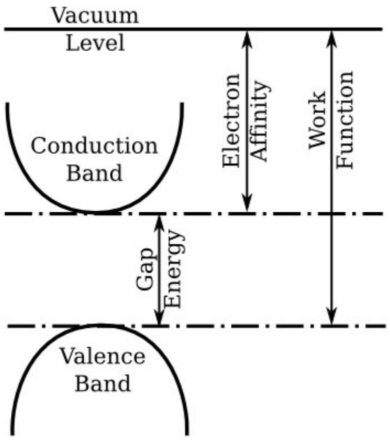

Figure 5. ZnO Band diagram.

Since we are dealing, in this thesis, with ZnO nanometric systems, the laws of traditional physics are no more appropriate. To explain the properties of such systems, it is necessary to call upon the quantum mechanics which predicts particular unusual behaviors known as the “quantum confinement effects”. Accordingly, we are interested in studying the electronic properties of the ZnO nanocrystals. These nanocrystals are usually made up of tens to thousands of atoms. This fact promotes a very high surface-to-volume ratio, compared to the bulk version of the same nanocrystal. In this nanoscale regime, the electrons are confined in a space delimited by the particle dimensions. Thus, their confined behavior typically adopts the particle-in-a-box model [27-30].

### 1.2.1 Modifications in the band gap properties due to size reduction: Quantum confinement.

An object namely an electron, having a mass m, confined within a box of length *L* with infinitely high potential walls is described in the one-dimensional case by solving the Schrödinger wave equation:

$$\frac{d^2\Psi}{dx^2}+\frac{2m}{\hbar^2}(E-U)\Psi=0 \qquad (1\text{-}1)$$

with $\Psi$ (wave function), E (mechanical energy) and U (potential energy). $\hbar$ is the Dirac constant ($\hbar=\frac{h}{2\pi}=1{,}054.10^{-34}\,J.s$ with $h$ being the Planck's constant).

This equation can be used in the particular case of a semiconductor particle of nanometric size. Indeed, it is helpful to compare this situation with that of a particle in a box whose potential energy is null inside and infinite on the walls situated at x=0 and x=L (see figure 6).

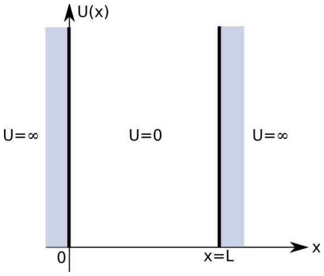

Figure 6. Sketch of a confining box with potential energy: zero inside and infinite on the walls.

Inside the box, the Schrodinger equation becomes:

$$-\frac{\hbar^2}{2m}\frac{d^2\Psi}{dx^2}=E\Psi \qquad (1\text{-}2)$$

The wave function $\Psi_k(x)$ and the energy $E_k$ emanating from this equation are as follows:

$$\Psi_k(x)=A.e^{ikx}+B.e^{-ikx}=(A+B)\cos kx+i\,(A-B)\sin kx \qquad (1\text{-}3)$$

$$E_k=\frac{k^2\hbar^2}{2m} \qquad (1\text{-}4)$$

Such states satisfy the boundary conditions that require the wave functions to vanish at the box edges. This implies that at:

$$x=0\Rightarrow\Psi(0)=0\Leftrightarrow A+B=0 \qquad (1\text{-}5)$$

and at:

$$x=L\Rightarrow\Psi(L)=0\Leftrightarrow i\,(A-B)\sin kL=0 \qquad (1\text{-}6)$$

Thus:

$$\sin kL=0\Rightarrow kL=n\pi\Leftrightarrow k=\frac{n\pi}{L} \quad \text{with} \quad n=1,2,3\ldots \qquad (1\text{-}7)$$

So the energy levels for the particle-in-a-box are quantified and are given by:

$$E_n = \frac{n^2h^2}{8mL^2} \quad \text{with} \quad n=1,2,3\ldots \tag{1-8}$$

The quantified energy of an authorized state n increases with the degree of confinement (L decreases). It is a well-known result of quantum mechanics [31].

This approach is not only applied for freely moving electrons or holes, it is used to consider confinement of excitons. An exciton is an electron-hole pair created when, under photoexcitation with energy equal to the band gap, an electron leaves the valence band and enters the conduction band. A hole is left behind in the position where the electron once resides. There is a non-negligible amount of negative Coulombic attraction between the electron and its associated vacancy. Excitons have a natural physical separation between the electron and the hole that varies from material to material; this average distance is called the Exciton Bohr Radius. In a large semiconductor crystal, the Exciton Bohr Radius is small when compared to the crystal, thus the exciton is free to wander throughout the crystal, and possess continuous energy levels. But when the Exciton Bohr Radius is of the order or smaller than the physical dimension of the crystal, the exciton is confined with discrete energy levels.

Acting as a cousin to the hydrogen atom, the Exciton Bohr Radius can be easily estimated. In the hydrogen atom model, Bohr postulates that the electron moves around the core (the proton) in circular orbit and that the centripetal force $\frac{mv^2}{R}$ which maintains it on this orbit is compensated exactly by a Coulomb electrostatic attraction force $\frac{1}{4\pi\varepsilon_0}\frac{e^2}{R^2}$. So:

$$\frac{mv^2}{R} = \frac{1}{4\pi\varepsilon_0}\frac{e^2}{R^2} \tag{1-9}$$

The wavelength of the light can be connected to the mass of the corresponding particle through:

$$\lambda = \frac{h}{mv} \tag{1-10}$$

To obtain a standing wave in the case of the electron on its orbit, it is necessary that the length of the orbit is equal to an integer number n of the electron wavelengths $\lambda$.

$$2\pi R = n\lambda = n\frac{h}{mv} \Leftrightarrow mvR = \frac{nh}{2\pi} \tag{1-11}$$

Accounting between equations (1-9) and (1-11), we can find that:

$$R = \frac{4\pi\varepsilon_0\hbar^2}{me^2} \tag{1-12}$$

In analogy to the hydrogen atom model, the separation of electron and hole can be introduced as exciton Bohr radius. So the Bohr Radius of any material can be written as:

$$R = \frac{4\pi\varepsilon\,\hbar^2}{\mu e^2} \quad \text{where} \quad \frac{1}{\mu} = \frac{1}{m_e^*} + \frac{1}{m_h^*} \tag{1-13}$$

with $\mu$ is the reduced mass of the electron and the hole whose effective masses are $m_e^* = 0.24m_e$ and $m_h^* = 0.59m_e$, respectively, and $\varepsilon = \varepsilon_r\varepsilon_0$ is the dielectric permittivity of the semiconductor material.

The **Bohr radius of the ZnO** is about 2.34 nm [32].

For nanocrystal of dimension R which is below its corresponding excitonic Bohr radius, quantum confinement results in a blue shift in the position of the density of states. This energy shift is proportional to $1/R^2$ as $E_n = \frac{n^2h^2}{8\mu R^2}$ with n=1,2,3,… as derived in equation (1-8). If we apply the result given by this relation to an electron of effective mass $m_e^*$ in the conduction band of a spherical-shaped solid crystalline of size R, thus the energy of first state is expressed by:

$$E_{e,1} = E_c + \frac{h^2}{8m_e^*R^2} \quad (1\text{-}14)$$

where $E_c$ is the energy of the bottom of the conduction band.
If the size of the solid is very big (bulk material), we can find that $E_{e,1} = E_c$. In the case of small sized crystallites of dimension R, the energy of the initial state $E_c$ is increased by the energy of confinement $\frac{h^2}{8m_e^*R^2}$.
Energy levels of the conduction band are then quantified s according to relation:

$$E_{e,n} = E_c + \frac{n^2h^2}{8m_e^*R^2} \quad (1\text{-}15)$$

Identically, the holes of effective mass $m_h^*$ in the valence band acquire as well additional energy due to confinement of about $\frac{h^2}{8m_h^*R^2}$ with quantified energy levels as:

$$E_{h,n} = E_v - \frac{n^2h^2}{8m_h^*R^2} \quad (1\text{-}16)$$

where $E_v$ is the energy from the top of the valence band.
Thus, the confinement of the carriers in a crystallite of size R is therefore translated by an increase of the gap given by the subtraction of equations (1-15) and (1-16):

$$E_g^{'} = E_g + \frac{h^2}{8R^2}\left(\frac{1}{m_e^*} + \frac{1}{m_h^*}\right) \quad (1\text{-}17)$$

where $E_g = E_c - E_v$ the bulk gap energy.
Energy levels quantization shown in figure 7 is as follows:

$$E_{g,n}^{'} = E_g + \frac{n^2h^2}{8R^2}\left(\frac{1}{m_e^*} + \frac{1}{m_h^*}\right) \qquad \text{with} \quad n=1,2,3,\ldots.. \quad (1\text{-}18)$$

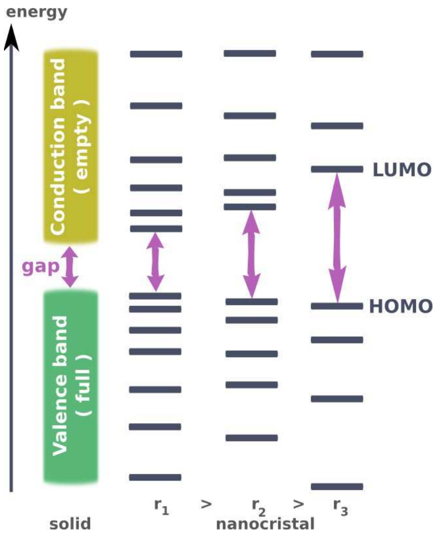

Figure 7. Electronic band structure evolution from bulk material to nanocrystals with decreasing sizes.

Nevertheless, other important factors require the addition of extra terms to fully describe the relationship of the gap energy level variation as function of nanocrystal dimension. We need to add the exciton's electron-hole coulombic attraction potential that is proportional to 1/R. This attractive potential, between the electron and hole of opposite charges, leads to further reduction in their confinement energy. Hence, the band gap energy $E_g^{'}$ (eV) of nanosized ZnO is [33]:

$$E_g^{'} = E_g + \frac{h^2}{8R^2}\left(\frac{1}{m_e^*} + \frac{1}{m_h^*}\right) - \frac{1.8e^2}{4\pi\varepsilon R} \tag{1-19}$$

## 1.3 Optical properties of nano-sized ZnO

Nanocrystals thus have the ability to have their gap energy manipulated in a controlled manner, correlated with particle size. Lin et al. [34] showed that ZnO size-dependent blue shifts of photoluminescence and absorption spectra revealed the quantum confinement effect as shown in figure 8 where the band gap enlargement is in agreement with the theoretical calculation based on the effective mass model (given by equation (1-19)). Calculated variations of the band gap following equation (1-9) are also studied by Chandezon et al. [35].

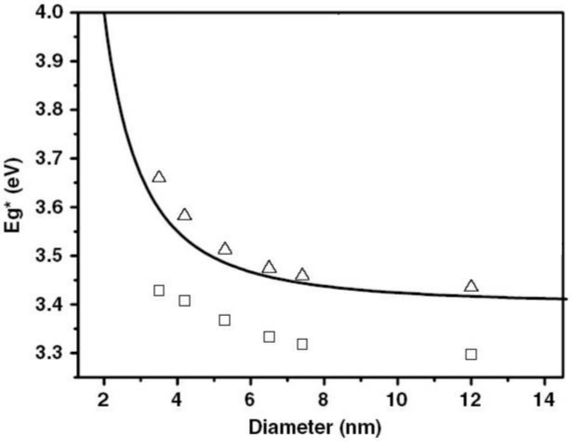

Figure 8. Dependence of the band gap enlargement versus the ZnO Quantum Dots diameter as calculated from the effective mass model (equation (1-9)) and the corresponding experimental data of Photoluminescence exciton peak maximum (□) and the Absorption onset (Δ) (taken from [34]).

Investigations by Li at al. [36] on the evolution of the band gap energy with the size of ZnO particles are illustrated in figure 9. A significant blue shift of the absorption edge compared to that of bulk ZnO in the absorption spectra is observed when the particles' size decreases. This blue shift confirms the theory of quantum confinement effect.

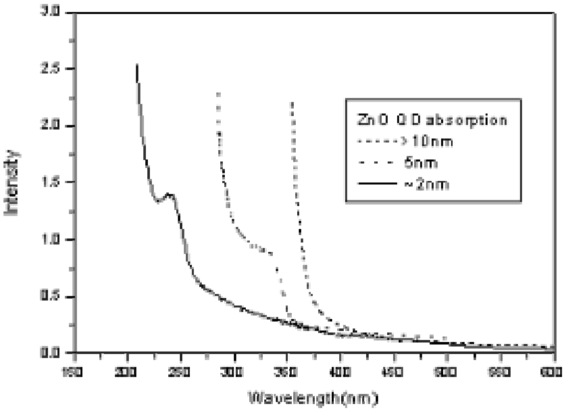

Figure 9. Absorption spectra that ZnO quantum dots of respective sizes (~2nm, 5nm, >10nm) band blue-shifting increases when decreasing the particles size (taken from [36]).

## 1.4 Summary

Detailed investigations on the essential properties of ZnO were performed concerning its crystal structure and energy band gap structure. The latter possesses the possibility to be modulated due to quantum confinement correlated with particle size once comparable to ZnO Bohr radius of 2,34 nm [32] . Hereafter, we can proceed to explore syntheses and applications outcomes of the ZnO.

# Bibliography

[1] H. Karzel,W. Potzel, M. Koerlein,W. Schiessl, M. Steiner, U. Hiller, G. M. Kalvius, D. W. Mitchell, T. P. Das, P. Blaha, K. Schwarz, and M. P. Pasternak, Phys. Rev. B 53 (1996) 11425

[2] R. A. Laudise, in Crystal growth: an introduction, Ed. By Hartmann (North-Holland, Amesterdam, (1973), Vol. 1, p. 162

[3] P. Hartmann, Z. Kristallogr. 119 (1963) 65

[4] N. Z. Evsikova, Zap. Vses. Mineral. O-va 94 (1965) 129

[5] L. N. Dem'yanets, D. V. Kostomarov, and I. P. Kuz'mina, Inorg. Mater. 38 (2002) 171

[6] L. N. Demianets, D. V. Kostomarov, I. P. Kuz'mina, and S. V. Pushko, Crystallography Reports. 47 (2002) S86

[7] G. Heiland and P. Kunstmann, Surf. Sci. 13 (1969) 72

[8] S. J. Pearton, D. P. Norton, K. Ip, Y. W. Heo, and T. Steiner, Prog. Mater. Sci. 50, 293 (2005).

[9] Fan, Zhiyong, and Lu, Jia G., Journal of Nanoscience and Nanotechnology, Vol 5, Number 10 (2005) 1561

[10] L. Smart, and E. Moore, "Solid State Chemistry", (Chapman & Hall: 2nd Edition) (1995) 208

[11] D. R. Lide (editor), CRC Handbook of Chemistry and Physics, CRC Press, New York, 73rd edition (1992).

[12] Handbook of Chemistry & Physics, Edition 53 (CRC Press, 1972-1973)

[13] P. Hohenberg, and W. Kohn W., Phys. Rev. B 136 (1964) 864

[14] J. R. Chelikowsky, Solid State Comm. 22 (1977) 351

[15] I. Ivanov, and J. Pollmann, Phys. Rev. B 24 (1981) 7275

[16] P. Schroer, P. Kruger and J. Pollmann, Phys. Rev. B. 47 (1993) 6971

[17] C. K. Yang, and K. S. Dy, Solid State Comm. 88 (1993) 491

[18] V. A. Ermoshin, and V. A. Veryazov, Phys. Stat. Sol. B 189 (1995) K49

[19] S. Massidda, R. Resta, M. Posternak, and A. Baldereschi, Phys. Rev. B 52 (1995) R16977

[20] M. Oshikiri, and F. Aryasetiawan, Phys. Rev. B 60 (1999) 10754

[21] J. P. Perdew, and A. Zunger, Phys. Rev. B 23 (1981) 5048

[22] D. Vogel, P. Kruger, and J. Pollmann, Phys. Rev. B 52 (1995) R14316

[23] D. Vogel, P. Kruger and J. Pollmann, Phys. Rev. B, 54 (1996) 5495

[24] U. Ozgur, Ya. I. Alivov, C. Liu, A. Teke, M. A. Reshchikov, S. Dogan, V. Avrutin, S. J. Cho, and H. Morkoc, J. Appl. Phys. Rev., 98, (2005) 041301

[25] G. Zwicker, and K. Jacobi, Solid State Comm. 54, (1986) 701

[26] R. T. Girard, O. Tjernberg, G. Chiaia, S. Soderholm, U. O. Karlsson, C. Wigren, H. Nylen, and I. Lindau, Surf. Sci. 373, (1997) 409

[27] P. Yu, M. Cardona, Fundamentals of Semiconductors, Chapter 2, Springer, Berlin, (1996)

[28] L.E. Brus, J. Chem. Phys, 80 (1984) 4403

[29] G.W. Bryant, Phys. Rev. B 37 (1988) 8763

[30] Y. Kayanuma, Phys. Rev. B 38 (1988) 9797

[31] C. Cohen Tannoudji, B. Diu, F. Laloë, “Mécanique Quantique” Tome 1 pp 76-79, Coll. Enseignement des Sciences, Ed. Hermann (1973), 293, r. Lecourbe, 75015 Paris.
[32] R. T. Senger, and K. K. Bajaj, Phys. Rev. B 68 (2003) 045313
[33] L. Brus, J. Phys. Chem., 90 (1986) 2555
[34] K. F.Lin, H. M.Cheng, H. C. Hsu, L. J. Lin, and W. F. Hsieh, Chem. Phys. Lett. 409 (2005) 208
[35] F. Chandezon, and C. Reynaud, Clefs CEA, 52 (2005) 55
[36] C. Li, S. Xiyu, W. Zhenyu, Z. Bingsuo, D. Jiahua, and X. Sishen, Chem. Ma., Vol.4 No.9 (2002) 45

# Chapter 2

# Synthesis of nanohybrid based-ZnO nanoparticles by Femtosecond laser ablation in liquid medium

## 2.1 Introduction

Metal and semiconductor nanoparticles prepared in liquid medium are now thoroughly studied for their potential use in material synthesis and optical detection. Thus, the control of particle size is the key factor in the synthesis of colloids, which were initially prepared by nanosecond laser ablation. For instance, Mafuné et al. reported efficient production, in an aqueous solution of surfactant, of size-controlled silver [1] and gold [2] nanoparticles. Shafeev et al. have synthezised Ti, Si, Ag and Au under ablation of corresponding metal targets in different liquid medium (water, ethanol and dichloroethane) [3,4], they realized as well the formation of nanoparticles of ZnSe and CdS by ablation of their bulk semiconductors in several liquids [5]. Furthermore, Liang et al. demonstrated the possibility of producing oxide nanocrystals [6] and nanostructured magnesium hydroxide [7], as well as the preparation of zinc hydroxide [8], by laser ablation in pure water or in surfactant solutions. Moreover, the zinc oxide nanoparticles, representing our field of interest, of average diameters ranging from 12 to 40 nm, were reported, for the first time, to be effectively prepared in several surfactant solutions by Usui et al. [9]. But unfortunately, nanosecond laser ablation had led to the formation of ZnO nanoparticles with strong size dispersion. In order to get nanoparticles with less dispersion, pulsed femtosecond laser emerge as a pioneer process to ablate several kinds of metals in solution. Indeed, it was shown that the size of silver colloids prepared by femtosecond pulses were less dispersed than that of colloids prepared by nanosecond pulses [10]. Formation of gold nanoparticles with 2 nm mean size in aqueous biocompatible cyclodextrins solution was achieved by Kabashin et al. [11-13]. Even though the physical aspects of the femtosecond laser ablation in liquids are still ambiguous, it is quite evident that nanoparticles can outcome from this technique.

The work that I present in this section was a work that I have done, on a common thesis subject with Laszlo SAJTI, during my first year of thesis before I switched to the chemically synthesized ZnO. Within this work, we produced defectless and highly crystalline nanoparticles of ZnO by pulsed femtosecond laser ablation in different liquids. We propose using the hybrids composed of these inorganic ZnO nanoparticles and of organic fluorophore dye molecules as sensors for biological labeling. This mechanism should be accomplished through two-photon pumping of the ZnO pursued by monitoring the fluorescence detection of the dye after receiving the transferred electrons or emitted energy from the ZnO, as shown in figure 1.

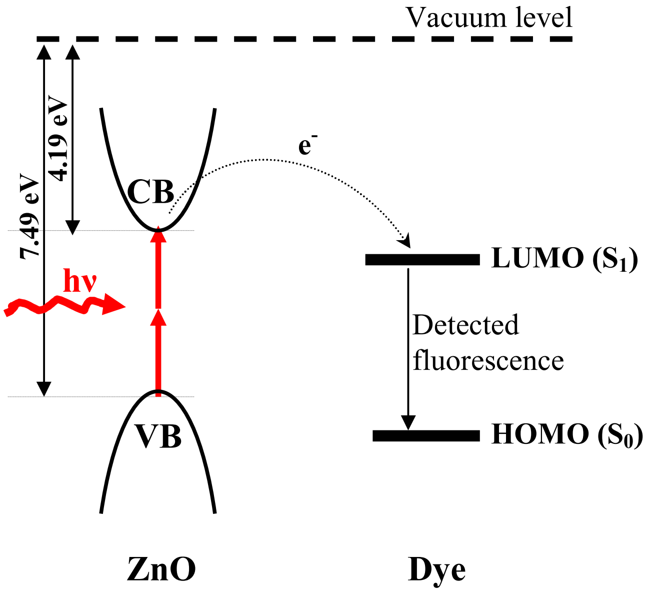

Figure 1. Two-photon pumping of ZnO pursued by monitoring the dye fluorescence after receiving the transferred electrons or energy from the ZnO.

Talking about exchange transfers, it is worth referring to some theoretical aspects in the energy and electron transfer. In a binary system consisting of two different materials or molecules with different electronic levels, energy and electron transfer processes are usually observed in addition to the intrinsic photophysical decay mechanisms.

- In an energy transfer reaction, the excitation energy of one component (the donor) is transferred to the other component (the acceptor), which has an energetically lower excited state. Consequently, the donor returns to the ground state and the acceptor is obtained in the excited state. Herein, emission and absorption spectra of acceptor and donor, respectively, must overlap relatively. Förster model involves a resonant coupling of transition dipole moments at the donor and acceptor, resulting in the return of the photoexcited donor to the ground state and excitation of the acceptor, as shown in the figure 2.

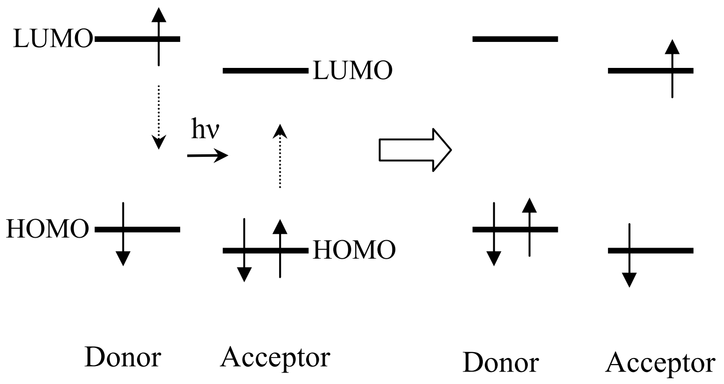

Figure 2. Schematic representation of the mechanisms of Förster energy transfer occurring via the exchange of a virtual photon (hν). This requires a Coulombic interaction between the transition dipole moments of the donor and the acceptor.

The Förster transfer efficiency depends on many parameters that can be grouped as follows:

- the distance between the donor and the acceptor
- the spectral overlap of the donor emission spectrum and the acceptor absorption spectrum
- the relative orientation of the donor emission dipole moment and the acceptor absorption dipole moment

Hence, the energy transfer efficiency, E, depends on the inverse sixth power of the distance, R, separating the donor and acceptor due to the dipole-dipole coupling mechanism [14]:

$$E = \frac{1}{1 + \left(\frac{R}{R_0}\right)^6} \qquad (2\text{-}1)$$

with $R_0$ being the Förster distance of the pair donor/acceptor at which the Förster efficiency is 50%. The Förster distance depends on the overlap integral of the donor emission spectrum with the acceptor absorption spectrum and their mutual dipole orientation as:

$$R_0^6 = 8{,}8.10^{-28}\kappa^2 n^{-4} Q_0 J \qquad (2\text{-}2)$$

where $\kappa^2$ is a factor that takes into account the relative orientation of the two transitions dipoles, n is the refractive index of the medium, $Q_0$ is the fluorescence quantum yield of the donor in the absence of the acceptor, and J is the spectral overlap integral given by:

$$J = \int f_D(\lambda)\varepsilon_A(\lambda)\lambda^4 d\lambda \qquad (2\text{-}3)$$

where $f_D$ is the normalized donor emission spectrum, and $\varepsilon_A$ is the acceptor molar excitation coefficient.

● In electron transfer reactions, the additional energy of an absorbed photon is used to form a charged-separated state, where the donor is positively and the acceptor is negatively charged. When the excitation involves the donor, an electron is promoted by absorption of a photon from its highest occupied molecular orbital (HOMO) to its lowest unoccupied molecular orbital (LUMO). This electron can be transferred from the donor to the acceptor molecule, when the LUMO of the donor is higher in energy than the LUMO of the acceptor.

Alternatively, the acceptor may be excited, followed by electron transfer from the HOMO of the donor to the vacant position in the HOMO of the acceptor.

In the following subsections, we will give the basic mechanisms in the laser ablation along with its experimental setup. We will present our studies concerning the influence of the liquid medium and laser parameters in order to stage-manage the nanoparticles size as well as their morphology. We grafted two types of dyes having different kinds of anchoring groups, namely S (sulfur) and COOH, onto the ZnO nanospheres. Morphology and optical studies of the manufactured systems were carried out in grand details.

## 2.2 General description

### 2.2.1 Experimental setup

A commercial Ti:Sapphire oscillator with a regenerative amplifier operating at a wavelength of 800 nm was used. This system (Mai-Tai coupled with TSA, Spectra Physics) delivers 90 femtoseconds FWHM pulses at a repetition rate of 10 Hz. The radiation was guided through apertures followed by a lens of 10 cm focal length to impinge vertically on the surface of a 1cm-diameter sintered ZnO target settled on the bottom of a glass container filled with 15 or 20 ml of fluid, which corresponds to a thickness of about 3.5 cm of liquid layer above the target. The target was manufactured by compressing the ZnO powder (99,999 % purity Aldrich Chemical Inc.) and sintering at 600 °C for 2 days. Through the ablation procedure, the target was continuously moved across the beam to assure uniform target consumption. All ablation runs were carried out at room temperature and at atmospheric pressure. In fact, the ablated species were produced in diverse solutions under several laser conditions which are manifested by using different fluences along with diverse number of pulses. The operating experimental setup of the femtosecond laser is shown in figure 3.

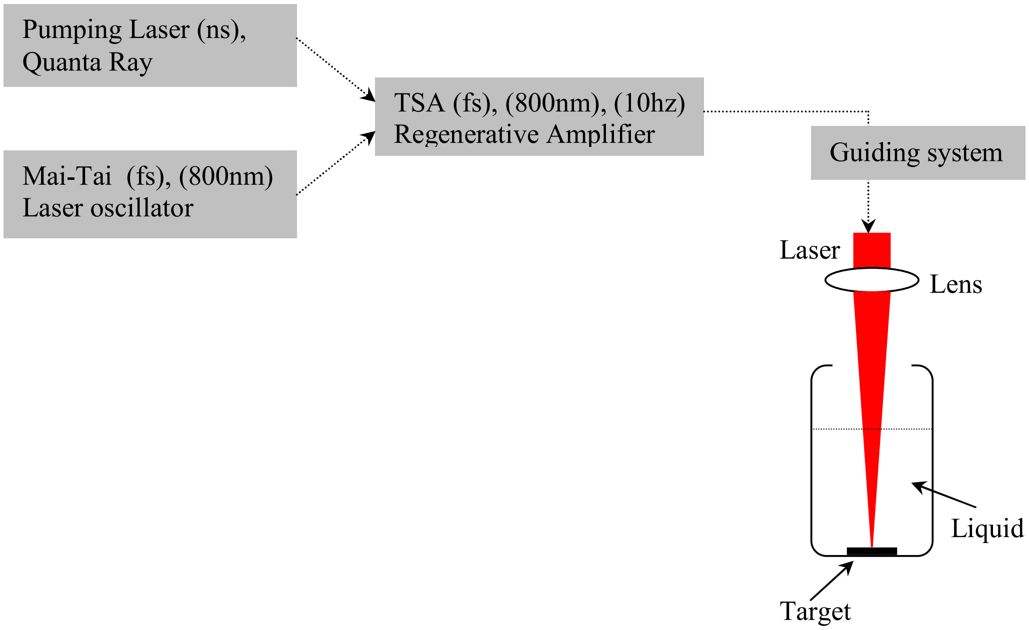

Figure 3. Briefed representation of the experimental setup of the femtosecond laser.

The hybrids were manufactured, in ethanol solutions, either ex-situ by blending the dye to the already-ablated ZnO, or in-situ by ablating ZnO directly in a containing-dye solution. Hence, the dye tetramethylrhodamine B isothiocyanate (TRITC) (Aldrich Chemical Inc.) with concentrations varying from $5\times10^{-9}$ to $2\times10^{-6}$ mol/L was used. On the other hand another dye of the porphyrin family named the protoporphyrin IX (Aldrich Chemical Inc.) was also used to test its grafting status through its two anchoring COOH groups.

A MultiMode SPM (NanoScopeIII) was used to execute the Atomic Force Microscopy (AFM) analyses in order to find the average grain size and to image the surface topography at atomic scale of the samples (see Appendix I). These samples were prepared by drying, on mica substrates and at room temperature, droplets of ablated cluster solution. In addition, the size and morphology of the so-ablated nanoclusters as well as the nanohybrids (after 2 hours of dye addition) were studied by the High Resolution Transmission Electron Microscopy HRTEM (JEOL, 300 kV) (see Appendix II). Owing 1.6 Ǻ as resolution, this HRTEM operates on samples obtained after dehydration at room temperature of a specimen solution drop on an amorphous carbon film coating a copper mesh. Furthermore, the optical properties of the ZnO colloidal suspensions and the emanating hybrids, in a quartz vessel of 1cm width, were assessed by photoluminescence measurements done by the one-photon excitation of a 325 nm He-Cd laser and a mercury lamp operating at 254 nm (see Appendix III). Spectra were collected by a Peltier cooled photomultiplier (Hamamatsu) tied to a grating monochromator. Photoluminescence measurements induced by multiphoton excitation were carried out using a large band IR femtosecond laser (Coherent, Cameleon). The laser power was fixed at 700mW with a repetition rate of 80MHz. Here, photoluminescence spectra were recorded by a gated intensified CCD camera (PI-MAX, Princeton Instruments) linked to a grating monochromator (Acton 500i). The optical transmission measurements of the samples were obtained by a two-path UV-Vis optical spectrophotometer (Cary VARIAN 50), (see Appendix III).

### 2.2.2 Basics and mechanisms of laser ablation

Laser ablation is a complex process that is relatively hard to approximate theoretically because of the extreme conditions that are involved. This process is mainly based on thermodynamic and gas dynamic concepts and can be divided into the following three stages: (i) removal of a target material through light-material interaction, (ii) plasma formation in the vapor plume and (iii) particle growth.

When laser radiation is absorbed by a solid material, the electromagnetic energy is converted first into electronic excitation, which then can turn into thermal and mechanical energy of translational and vibrational motion of the atoms in the system and thus increases their temperature, depending on the properties of the material and the wavelength, intensity and duration of the irradiation. The material must be irradiated with fluences exceeding the ablation threshold that results from free evaporation enthalpy of surface needed to break chemical bonds and initiate atom vibrations. Hence, the chemical bonds of majority of excited atoms in the lattice are weakened or broken. The temperature rises faster than mechanical relaxation in the system, consequently a nearly constant volume heating occurs and the pressure increases. When the pressure gradient in the direction normal to the surface exceeds the mechanical strength of the material, it causes break-down followed by a forwarded ejection of a significant part of the irradiated region.

Two regimes can be distinguished for the interaction of a pulse of laser light with a solid material, depending on the pulse duration. Laser-solid interactions with nanosecond or longer laser pulses are of sufficient duration to couple not only into the electronic, but also the vibrational wavefunction of the material, whereas in the case of picosecond or femtosecond pulses the duration of the excitation is too short to couple directly into the vibrational wavefunction. And since we are dealing through this part of the thesis with the femtosecond laser ablation of ZnO semiconductor systems in liquids, we will try to give a briefing view of the thus-ablating regime.

The photon absorption of incident beam inside the material is expressed in the nonlinear equation (2-4) by Beer-Lambert law [15]:

$$I(z) = I_0(1 - R(\lambda))e^{-\alpha(\lambda)z} \tag{2-4}$$

where z is the direction of laser beam axis inside material (z = 0 corresponds to the upper-edge of target), $I_0$ is the laser incident energy; $R(\lambda)$ and $\alpha(\lambda)$ are the reflection and absorption coefficients, respectively.

In femtosecond laser regime, the laser light specifically heats up the electron distribution. At short time-scales, only the electrons equilibrate through electron-electron coupling, giving an immediate rise in the electron temperature, while the lattice remains at a low (ambient) temperature. The hot electrons start to diffuse within the target material because of the electron temperature gradient. The temperature of the lattice rises over a longer time-scale, which depends on the electron-phonon coupling strength. After this time the electron and the lattice temperatures equilibrate. The difference in the time scale of the heat diffusion among electrons and through the lattice is well explained via the two-temperature model developed by Anisimov et al. [16], treating separately the temperature conduction dynamics for the lattice on one hand and the electrons on the other hand in short laser pulse interaction with materials.

Under optimal experimental conditions, the pulsed and ultrashort nature of the process limits the dissipation of the excitation energy to the volume that is ablated during the pulse. This would occur if the thickness of the layer ablated per pulse is of the order of the greater one of the two following characteristic depths: the heat penetration depth $l_T = 2(D\tau)^{1/2}$ and the optical penetration depth $l_\alpha = \alpha^{-1}$ with D being the thermal diffusion coefficient, $\tau$ the pulse duration, $\alpha$ the optical absorption coefficient [17]. In our ultrashort laser pulses regime, we can assume that the excited electrons transfer their energy to the lattice within few picoseconds and heating begins within the optical absorption depth of the material $l_\alpha = \alpha^{-1}$.

The second most important aspect of ablation by a laser beam seems to be the interaction of the evolving hot vapor with the beam itself. Thereafter, a dense plasma forms in the vapor plume from both species emission from the hot surface and from photon absorption by the vapor itself.

Because of strong gradients of concentration and pressure, this vapor/plasma of ablated particles expands into the liquid environment. Numerous chemical reactions take place within this plasma and at the leading edge of the plume because of collisions of ablated particles between themselves and with the surrounding liquid molecules. Hence, the nanoclusters are synthesized during the expansion and cooling of the ablated species. These ablated species can be (i) directly ejected from the target and (ii) condensed in gas phase during the plume expansion and cooling. The liquid medium should favor the condensation of nanoclusters and their stabilization by collisions with the liquid molecules. The smaller clusters and molecules directly ejected from the target play a role of nucleation centers for condensation of the nanometric particles. Bigger particles can be formed by further particle growth and coalescence.

Hence, the femtosecond laser ablation seems to be a powerful technique to synthesize semiconductor (ZnO) nanoparticles leaving clean craters in the target thanks to its powerful ultrashort pulse duration. Despite a long history of laser ablation processes, much still remains to be learned about the fundamental mechanisms that governs the interaction between powerful femtosecond laser pulses and transparent semiconductor materials.

## 2.3 Caracterization and analysis of the ablated nanoparticles in different liquids

### 2.3.1 Ablation in deionized water

Figure 4-a shows the image taken by AFM of the ZnO clusters synthesized in 15 mL deionised water at a fluence of 3 J/cm$^2$ and 2000 laser shots where ZnO particles of about 1 nanometer were detected (figure 4-b). Whereas, figures 5-a and -b stand respectively for AFM image and size distribution of ZnO nanoparticles prepared in deionized water at 5 J/cm$^2$ and 2000 shots.

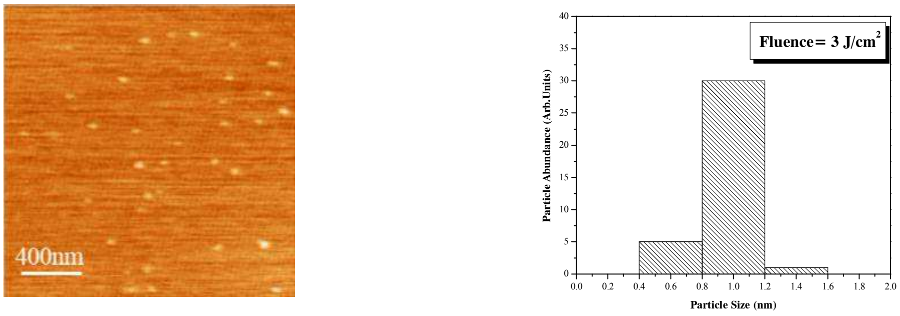

(a) (b)

Figure 4. (a) AFM image of ZnO nanoparticles prepared in deionized water at 3 J/cm$^2$ and 2000 shots along with (b) its size distribution.

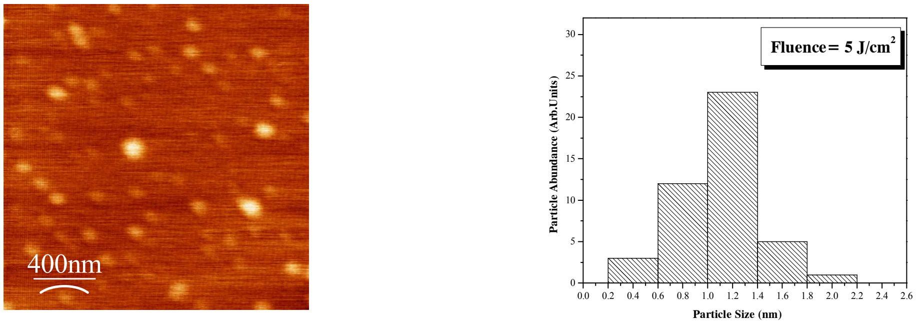

(a) (b)

Figure 5. (a) AFM image of ZnO nanoparticles prepared in deionized water at 5 J/cm$^2$ and 2000 shots along with (b) its size distribution.

Additional increase in the laser fluence led to the growing in the size of the ZnO nanoparticles as depicted in figure 6-b, as quantified by the size distribution histograms of figures 4-b, 5-b and 6-a. We can see through the particle size histograms that when increasing the laser fluence the distributions move to higher particle sizes accompanied by further broadening of the corresponding distribution width. We can also notice the presence of relatively bigger particles of about 40 nm in the case of 11 J/cm$^2$ fluence. Hence, the mean particle size increased from 1 nm to 11 nm when the laser fluence was varied from 3 J/cm$^2$ to 11 J/cm$^2$.

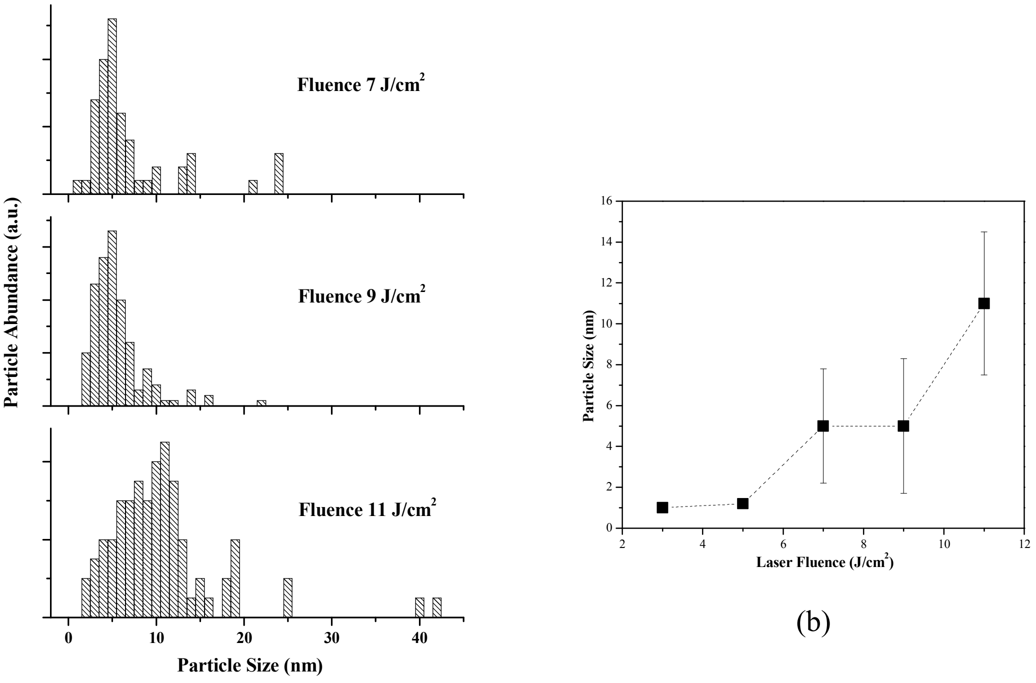

(b)

(a)

Figure 6. (a) AFM Cluster size distribution of ZnO nanoparticles prepared in water at 2000 shots at several laser fluences, and (b) mean particle size as a function of laser fluence.

On the other hand, the very small ZnO particles at low laser fluence, namely 3 J/cm$^2$, were barely seen by the HRTEM because of the low contrast between the amorphous carbon film and the very thin ZnO nanospheres, as seen in figure 7.

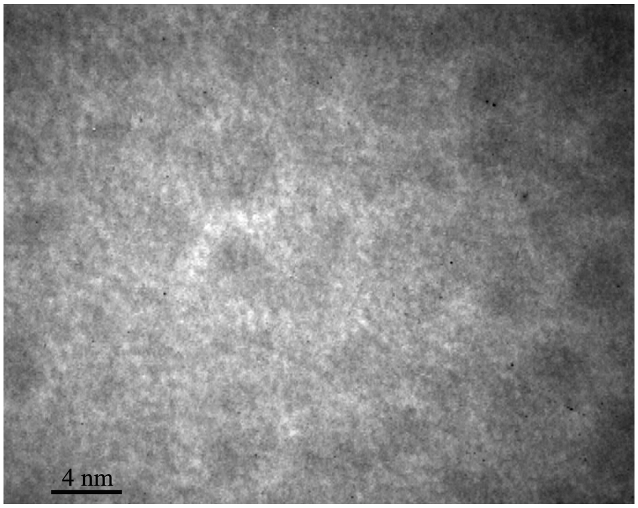

Figure 7. HRTEM image of ZnO nanoparticles elaborated at 3 J/cm$^2$ and 2000 shots in deionized water.

Indeed, the presence of these small-sized ZnO nanoparticles was validated by the photoluminescence measurements that show the effect of the quantum confinement demonstrated by the increasing of the band gap energy [18,19]. Figure 8-a illustrates the existence of additional photoluminescence peaks, for an excitation by a 254 nm radiation, which are located by fitting the original plot, in the photoluminescence spectrum of ZnO produced at laser fluence of 3 J/cm$^2$. Basically, these peaks correspond to several particle sizes, which depend on the actual value of the band gap energy ($E_g^*$). The relationship between the band gap energy and the size of the particles considered as spherical particles can be given by the following equation as already settled in Chapter 1 equation (1-19):

$$E_g^* = E_g + \frac{h^2}{8\mu R^2} - \frac{1.8e^2}{4\pi\varepsilon_0\varepsilon_\infty R} \tag{2-5}$$

where, $E_g$ is the ZnO bulk band gap, $\mu$ the effective mass of the exciton, $R$ the diameter size of the particle, $\varepsilon_0$ is the vacuum permittivity and $\varepsilon_\infty$ the relative permittivity. The corrections to be done on the bulk band gap energy are given by two terms. The first one is the confinement term that is proportional to $R^{-2}$ and the second one stands for the Coulomb interaction term that is usually negligible [21].

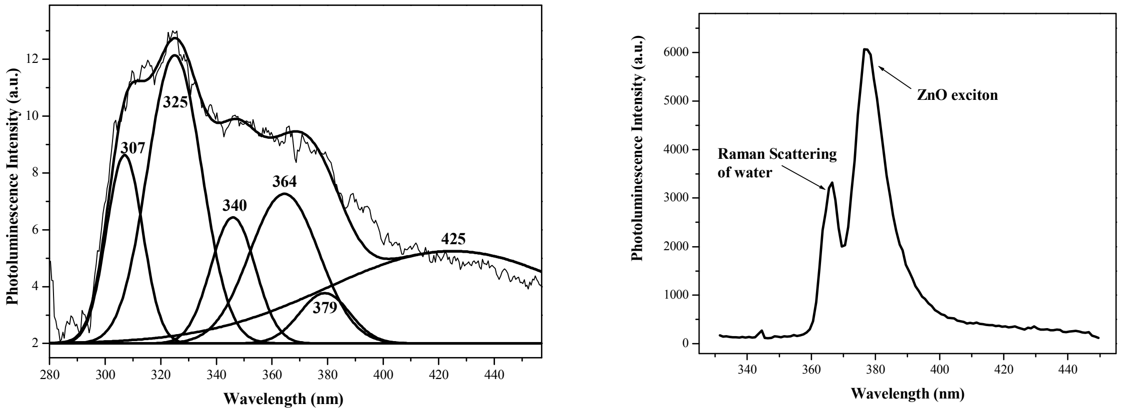

(a) (b)

Figure 8. (a) Photoluminescence spectrum (excitation by a 254 nm radiation) of ZnO colloidal suspensions produced through ablation in water for a 3 J/cm$^2$ laser fluence.
(b) Photoluminescence spectrum (excitation by a 325 nm radiation) of ZnO colloidal suspensions produced through ablation in water for a 11 J/cm$^2$ laser fluence.

The peak that appears, in figure 8-a, at the wavelength 307 nm indicates the increasing of the band gap energy and it is basically coming from ZnO particles having 1.83 nm as radius, according to calculation done through the band gap equation (2-5). This particle radius is effectively less than the Bohr radius being 2.34 nm [22]. This exciting information appears to be consistent with the results reached through AFM as already mentioned. Furthermore, the second peak positioned at 325 nm corresponds to particle radius of 2.24 nm, which is roughly equal to the radius of the previous particle plus the ZnO characteristic monolayer dimension of 0.3 nm. The same reasoning can be applied to the 2.83 nm particle-radius whose peak appears at 340 nm. And as expected, the bulk ZnO free and bounded exciton peaks appear at a wavelength of 364 and 379 nm, respectively, while the broad peak that appears at the violet 425 nm corresponds to ZnO emission in solution with $OH^-$ excess ions [23].

Then again, the effect of the laser fluence on the ZnO nanoparticle size exposed by AFM analyses was confirmed by photoluminescence plots. These data revealed a considerable particle size growth when the laser fluence was increased from 3 J/cm$^2$ to 11 J/cm$^2$, as shown in figure 8-b. Accordingly, there is no increase in the band gap energy, which signifies that we are dealing here with large particles with radius much bigger than the Bohr radius. Figure 8-b presents only two peaks, the ZnO exciton emission at 379 nm and the Raman scattering of water at 364 nm with 3298 cm$^{-1}$ as energy difference from that of the excitation radiation, which matches the stated value of 3300 cm$^{-1}$ as being the Raman peak of water [24].

In fact, increasing the fluence means delivering more energy that implies ablating larger amount of material. And this fact was also observed while monitoring the ablation process. Actually, we can clearly see a plasma plume directly on the surface of the target and a cloud of ZnO colloids formed in the liquid. As we increase the laser energy and by consequence the fluence, the plasma plume becomes more intense and the ZnO colloidal particles cloud becomes denser. Most likely, this means that bigger particles will be present and probability of cluster aggregation increases. In other words, atoms and nanoscale clusters ablated under laser radiation tend to aggregate during and after the laser pulse [13]. This fact leads to creation of larger particles [2] that becomes more prominent when the density of the ZnO clusters increases further with increasing the fluence, as clearly suggested by figure 6-b.

### 2.3.2 AbLation in Ethanol

Laser ablation was also carried out in 15 mL pure ethanol. Figure 9-a shows an AFM depiction of ZnO particles of about 4 nanometers manufactured at 3 J/cm$^2$ after 5000 shots, while figure 9-b states their size distribution.

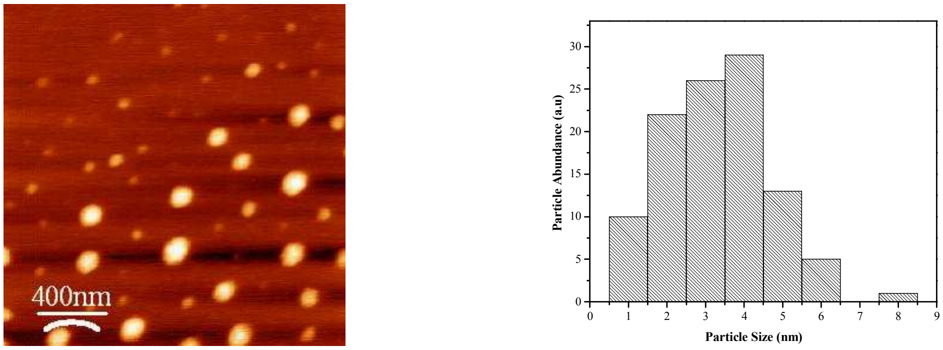

(a) (b)

Figure 9. (a) AFM image and (b) size distribution of ZnO nanoparticles prepared in ethanol $C_2H_5OH$ at 3 J/cm$^2$ and 5000 shots.

Figure 10-a represents a spherical monocrystalline nanocluster of ZnO, showing atomic planes perpendicular to the [001] direction (i.e. c-axis). This image is done by the high resolution transmission electron microscope on the same sample prepared in ethanol and at the same conditions, which are 3 J/cm$^2$ as fluence and 5000 as number of pulses. The plot of the corresponding particle size (diameter) distribution, exposed in figure 10-b, certifies the occurrence of ZnO particles of about 4 nanometers in diameter. Thus, we can assume that performing TEM measurements outcomes with results that show fair correlation with measurements performed with AFM in what concerns the average particle size. However, if we compare the two size distribution plots belonging to AFM analyses (see figure 9-b) and TEM analyses (see figure 10-b), we notice that for analysis with TEM the size dispersion is relatively narrower than that given by AFM. Probably, this difference can be explained by partial convolution of the tip and particles of smaller size when operating in contact mode. Therefore, analyses done by the transmission electron microscopy (TEM) are much more reliable.

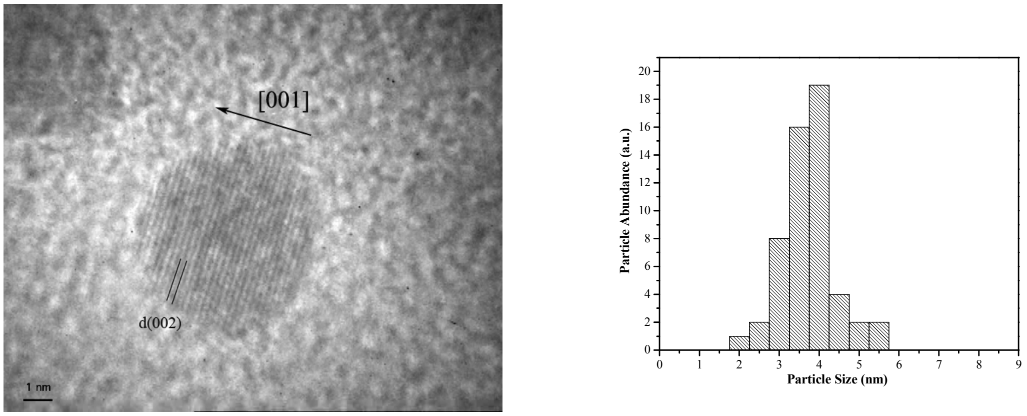

(a) (b)

Figure 10. (a) HRTEM image and (b) size distribution of ZnO nanoparticles prepared in ethanol $C_2H_5OH$ after 5000 shots at 3 J/cm$^2$.

However, if we increase slightly the laser fluence to 4 J/cm$^2$ keeping the same number of laser shots, two populations of nanoparticles appear, as realized by TEM and shown in figure 11. These distributions are fairly described by two Gaussian functions with two maxima centered at 4.25 and 10 nm with dispersion of 2.45 and 7.2 nm, respectively. So, we found a distribution at 4.25 nm that equals the one found with a fluence of 3 J/cm$^2$. In addition, another distribution at 10 nm appears suggesting that the growth mechanism depends on the fluence. So a slight increase in fluence leads to increase in the size of ZnO nanoclusters, as already shown when ablating in water. In fact, the presence of the first less dispersed population can be qualified as the consequence of pure radiation of the femtosecond laser ablation followed by the coalescence mechanism in the liquid medium. Whereas, the target heating by the plasma as well as its erosion by the collapse of formed bubbles were suggested to be responsible of the formation of the second highly dispersed population with larger nanoparticles [12-13]. We can notice as well that the second particles population is peaked at the mean average size of 10 nm, which is approximately the double of the ZnO size value at 4.25 nm given by the first population (figure 11). This fact might be attributed to the coalescence between several particles to constitute a larger particle of double size. This coalescence by oriented attachment will be much detailed in the subsequent chapter where we are to find this same process among ZnO nanoparticles synthesized via chemical routes.

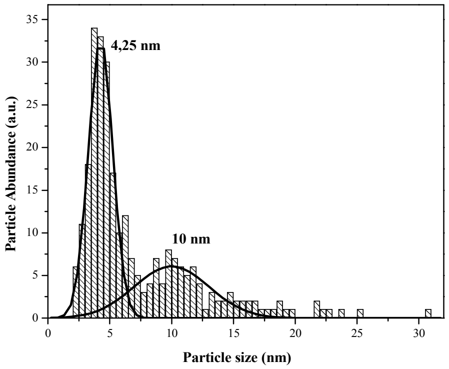

Figure 11. HRTEM size distribution of ZnO nanoparticles prepared in ethanol $C_2H_5OH$ at 4 J/cm$^2$ and 5000 shots.

Ablation, in 20 mL ethanol, at constant laser fluence but with different amount of laser shots is to be exploited in the following paragraph. Herein, the laser fluence was set at 5 J/cm$^2$ whereas we varied its shots as 2000, 5000, 10 000, 20 000 and 50 000 shots' number. Figure 12-a demonstrates a TEM image of perfectly spherical-shaped ZnO nanoparticles prepared in ethanol at the highest number of laser shots (50 000). The resultant fluorescence emission of these ZnO nanospheres is depicted in figure 12-b, showing a sharp ZnO exciton emission at 379 nm with no presence of defect band, and a little Raman emission at 359 nm recognized as that of the ethanol. On the other hand, the lifetime of the femtosecond laser generated ZnO plasma, for the sample at 50 000 shots and 5 J/cm$^2$, was proved to last for 10 ns. This fact is the interpretation of the extremely fast cooling process done by the surrounding liquid particles. This physical approach leads directly to a great advantage of the liquid phase ablation, that small particles with narrow size distribution can be achieved since the condensation and the crystallisation process are drastically shortened [13,25].

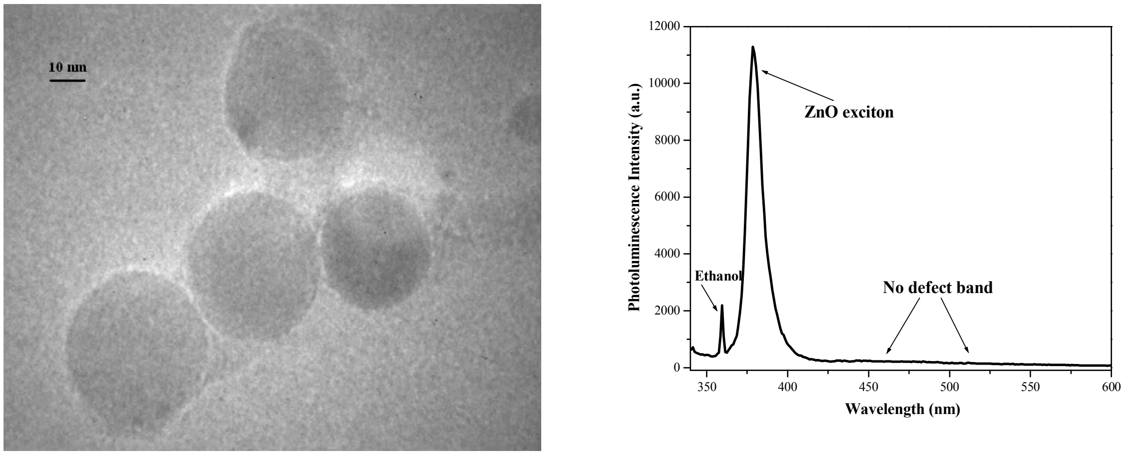

(a)

(b)

Figure 12. (a) TEM image and (b) emission intensity of ZnO nanoparticles prepared in ethanol after 50 000 shots at 5 J/cm$^2$.

HRTEM size distribution of the various ZnO nanoparticles prepared under different number laser shots are exposed in figure 13 where the insets show ZnO size histograms for 2000, 20 000 and 50 000 shots. Fitting of these distribution histograms was done trough Normal-Logarithmic curves. ZnO size is affected by the change in the laser shots; it increases with increasing the number of shots from 2000 to 10 000, while it decreases for 20 000 shots, to increase once more for the highest shots' number 50 000.

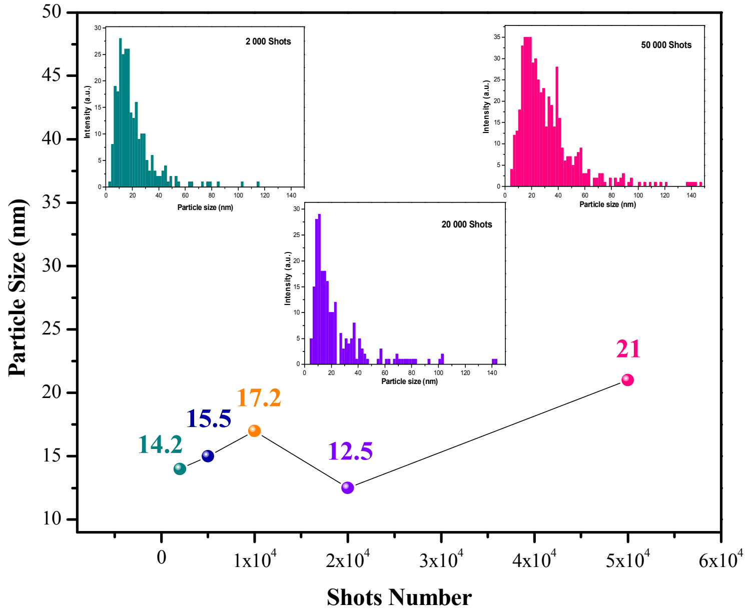

Figure 13. HRTEM size distribution of ZnO nanoparticles prepared in ethanol $C_2H_5OH$ at 5 J/cm$^2$ and 2000, 5000, 10 000, 20 000 and 50 000 shots, along with their average size (nm). The insets showing the ZnO size histograms for 2000, 20 000 and 50 000 shots.

Typically, the mechanism of the production of ZnO colloids starts with the formation of a dense cloud (plume) of zinc and oxygen atoms and of ZnO clusters directly etched from the target due to the instantaneous high femtosecond impinging energy, immediately after the laser ablation. This cloud is built over the laser spot of the ZnO target plate. After the plume formation, embryonic ZnO particles grow rapidly by condensation of (Zn,O) atoms and ZnO clusters as fast as they are supplied until they are run out in close vicinity of the as-formed ZnO aggregate. However, supply of atoms through diffusion causes the particle to grow further but slower than in the first rapid growth phase [2]. Eventual coalescence among ZnO particles is likely to happen with time.

Following this reasoning, we will try to explain the behavior of the ZnO size by varying the amount of laser shots. We can assume that up to 10 000 pulses with relatively constant Full Width Half Maximum of size distribution, the previously stated mechanism of colloidal growth is happening but with an increase in the ZnO particles' size through coalescence as increasing the ablation time. However, the drop in the ZnO size after 20 000 laser shots could be attributed to the decrease in the etching rate, probably due to the accumulation of high suspensions density, reducing the transparency of the liquid thus reducing the ablation. These eye-visible highly present suspensions could also be fragmentized by the incoming laser pulses hence the reduction in the ZnO particles' size. Operating at 50 000 laser pulses increases the time of experimental proceeding. Therefore, higher degree of aggregation among ZnO particles is likely to take place as well as the relative presence of fragmented smaller particles, as demonstrated by the increase in the ZnO average size and the broadening of its related histogram.

However, ablation in ethanol must differ from that in water (performed in the previous subsection). This difference resides in the solvent's polarity. Certainly the water ($H_2O$) with its higher polarity will lead to more reaction between its molecules and the freshly ablated species in the plasma plume, thus leading to formation ZnO nanoparticles with small sizes if compared to those ablated in ethanol of much weaker polarity.

### 2.3.3 Ablation in solutions of do-decanethiol

Analyses done by AFM of ZnO nanoparticles ablated in dodecanethiol ($C_{12}H_{26}S$) show that the average particle size is 1.4 nm. Whereas when analyses were performed by HRTEM for the same sample, the particles were estimated to be higher than 10 nanometers. The remarkable difference in size evaluation may outcome from the fact that the AFM is unable to locate the zero level, above which the scanning can be achieved, as sketched in figure 14. This can be possibly explained by the presence of large dodecanthiol molecules surrounding the ZnO particles. Thus, it seems mandatory to rely on HRTEM results owing to its precision when dealing with thiol solutions.

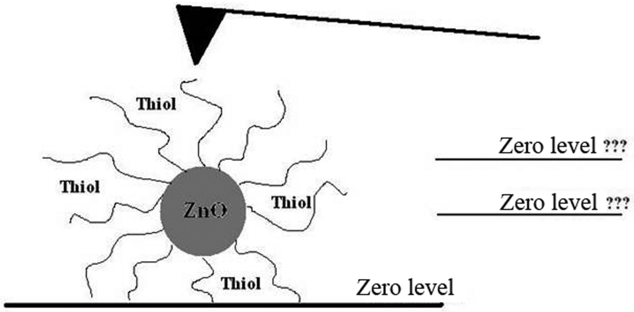

Figure 14. AFM cantilever tip failure to locate the scanning zero level.

Figure 15 shows selected HRTEM image of ZnO nanocolloids prepared, in the solution of dodecanethiol (2,8.$10^{-4}$ moles/$cm^3$), at the same laser fluence as that for the nanoparticles of the figures 9 and 10 that was prepared in pure ethanol. From the figure 15, we can clearly see increase in the nanoparticle size. Close examination of the morphology of these particles reveals a formation of the well developed facets for the particles with dimension more than 15 to 20 nm. Facets are indicated by straight lines on the figure 15 [18]. This kind of morphology shows obvious change of the growth condition comparing with pure ethanol, which is probably related to the decrease of the growth rate due to partial decoration of the nanocrystals by thiol molecules that leads to slow diffusion of the metal and oxygen atoms from the thiol solution. Here, the increase in the particle size could be due to the growth via Ostwald repining mechanism (that will be detailed in the next chapter). The developed presence of the Ostwald repining growth might be explained as follows: the presence of the thiol molecules slows the particle growth, thus leading to the further formation of clusters with sizes smaller than the minimum critical size of stable clusters. These unstable clusters will certainly dissociate and the thus-emanating species will diffuse to the nearest stable particles, which are enlarged by further reception of these diffused species. This might be the reason why we found larger nanoparticles ablated in the presence of the thiols with respect to those ablated in pure ethanol solution.

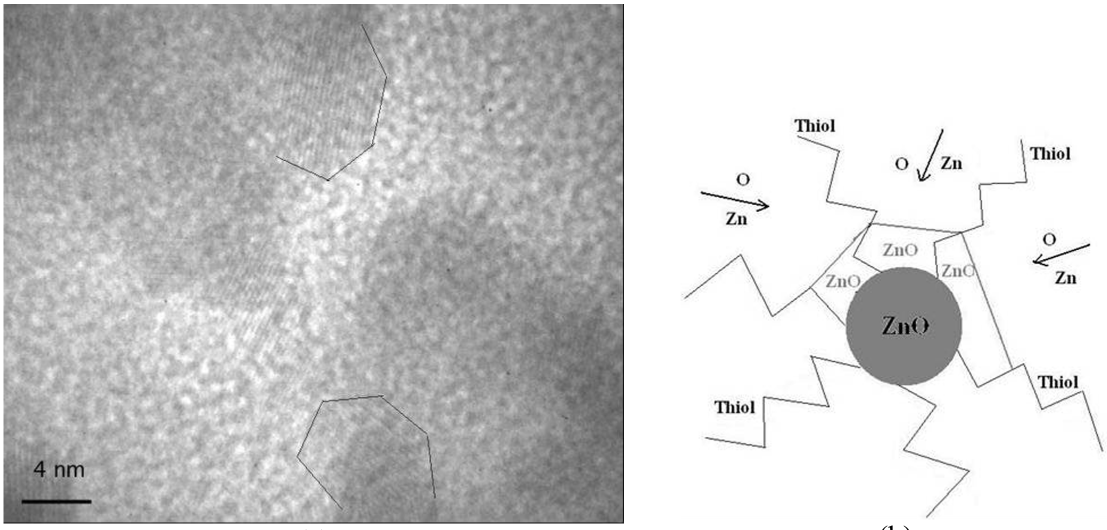

(a) (b)

Figure 15. (a) HRTEM image of ZnO nanoclusters synthesized at 3 J/cm$^2$ at 5000 shots in solution of dodecanthiol in ethanol. (b) A sketch of a ZnO nanoparticle decorated by thiol molecules.

## 2.4 Grafting of organic dye molecules onto the ZnO laser-processed nanospheres

### 2.4.1 Grafting the tetramethylrhodamine B isothiocyanate (TRITC)

Tetramethylrhodamine B isothiocyanate (TRITC) is the organic chromophore that was chosen to be grafted to the surface of the ZnO nanoparticles. Molecular structure of this dye is depicted in figure 16-a. The choice of this dye relies on its electronical properties in receiving electrons from the photoexcited ZnO thanks to its energy diagram structure as demonstrated in figure 16-b. The TRITC LUMO level of (-6.1 eV) is positioned lower than that of the ZnO conduction band (-4.19 eV) enabling charge transfers assisted by the electron affinity difference of both hybrid components' energy levels; ZnO nanospheres and TRITC molecules.

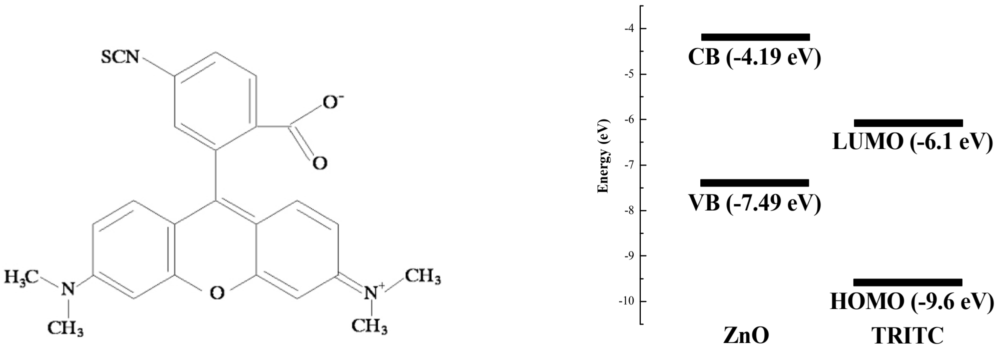

(a) (b)

Figure 16. (a) Molecular structure and (b) energy diagram structure of the TRITC dye.

#### 2.4.1.1 Two-step built-up Nanohybrid

This concept relies first on the production of pristine ZnO nanospheres by femtosecond laser ablation in 20 mL ethanol at a fluence of 5 J/cm$^2$ and 50 000 shots, and second by grafting the TRITC onto the as-synthesized ZnO. Dye solutions with concentrations ranging from 5.10$^{-9}$ mol/L to 2.10$^{-6}$ mol/L were used.

The morphology of pristine ZnO nanoparticles was found to be perfectly spherical as already mentioned (figure 12-a), with an average size of 21 nm. Addition of the TRITC dye solution, at a 2.10$^{-6}$ mol/L concentration, directly after ablation gave rise to nanoparticles with the mean size of about 17 nm confirming indirectly that dyes did absorb on the ZnO surface hence prevented further aggregation of the nanoparticles. We noticed as well an important morphology difference between ZnO nanoparticles and nanohybrids-based ZnO when the organic dye concentration was $2.32\times10^{-7}$ mol/L, moreover this difference became more pronounced at higher dye concentrations. Formation of well developed facets, as pictured in figure 17, is a clear indication of the change in the growth condition owing to the presence of the dye molecules grafted onto the surface of the ZnO particles.

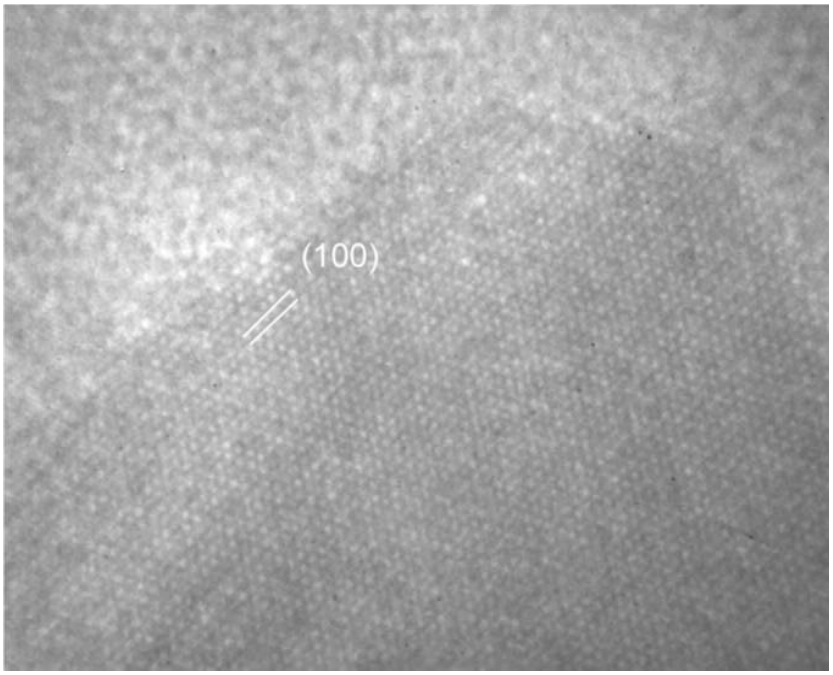

Figure 17. HRTEM image of facetted edges of a ZnO nanoparticle, observed along the [001] direction, after grafting TRITC molecules of 2.10$^{-6}$ mol/L concentration.

The optical properties of the nanohybrids were investigated by conventional optical transmission, and photoluminescence spectroscopy. The absorption band of TRITC in ethanol had a maximum at 536 nm (figure 18-a) and the photoluminescence maximum was observed at 565 nm (figure 19-a).

Figure 18 presents some typical transmission spectra of pure-, and grafted-dye solutions. After adding the ZnO to the dye solutions, transmission spectra were considerably modified through optical scattering that is related to the particle size (Figure 18-b). We can clearly notice that with high concentration of dye the scattering of hybrid solutions decreases, implying that the size of the grafted nanoparticles is reduced.

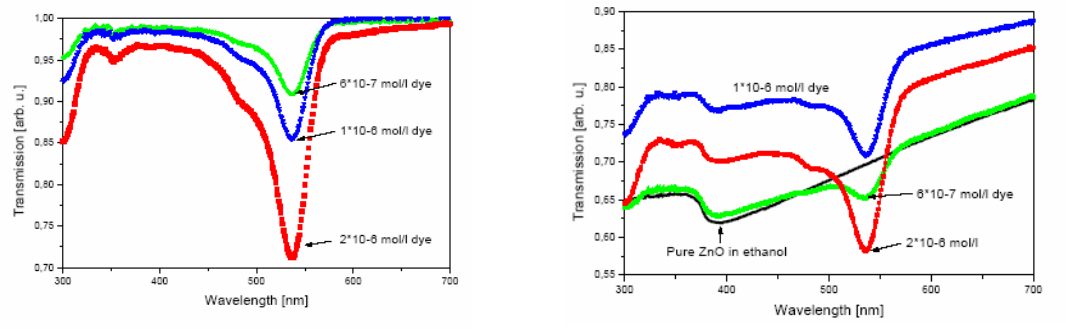

(a) (b)

Figure 18. Some typical transmission spectra of (a) pure-, and (b) grafted-dye solutions [25].

On the other hand, photoluminescence spectra of pure ZnO solution and hybrid solutions reveal the ZnO exciton and the dye emission peaks (figure19-a). Adding the ZnO nanoparticles to the dye solutions induces some significant changes. The intensity of the exciton peak of ZnO at 379 nm decreased nearly exponentially, whereas the intensity of the dye emission band increased linearly with the dye concentration, as seen in figure 19-b. This implies that one-photon excitation of the nanohybrid at 325 nm results in energy and electron transfer from the ZnO core toward the dye molecules.

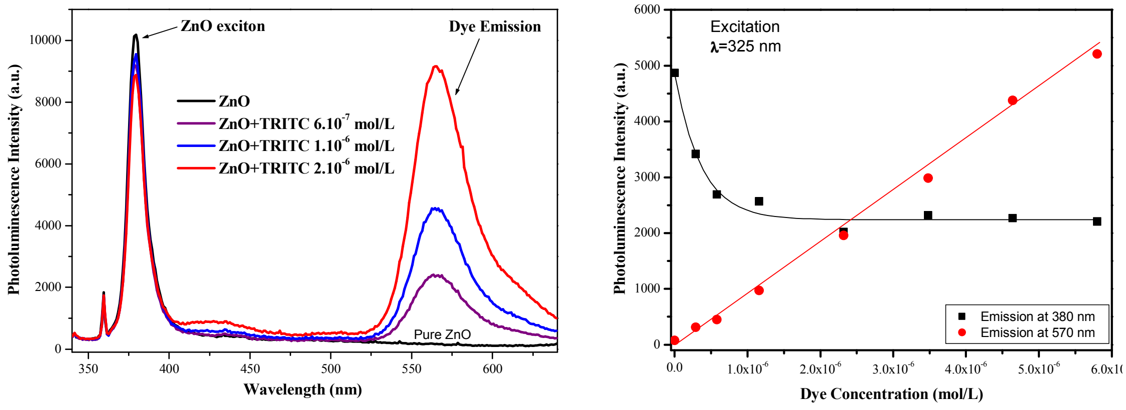

(a) (b)

Figure 19. (a) Photoluminescence spectra of ZnO nanohybrids after addition of different amounts of TRITC (excitation at 325 nm). (b) Emanating intensities of both ZnO and dye emissions in hybrid systems upon excitation.

Figure 20 gives the photoluminescence intensities detected at 565 nm (excitation at 325 nm) for different TRITC concentrations without ZnO (open triangles) and with ZnO (filled triangles). At TRITC dye concentration higher than $6.10^{-7}$ mol/L, dye emissions from the nanohybrid samples are equivalent to dye emissions in free pure solutions. It means that at this dye concentration, the number of the grafted molecules attends its limits of ZnO total surface coverage, concentration quenching also increases at the higher dye concentrations. The energy and electron transfer are evidently marked when the dye concentration is lower than the 6.10$^{-7}$ mol/L dye concentration as shown in figure 20. This exchange transfer is manifested by the increase in the grafted-dye emission with respect to that of its corresponding pure dye [25]. And since we find an increase in the radiative recombination intensities of the dye, we can assume that the energy is transferred from the ZnO to the dye via the Förster energy transfer model.

Furthermore, it is worth mentioning that high resolution optical measurements performed on these hybrid samples confirm that both dye photoluminescence and absorption maxima undergo a blue shift if compared to those of the pure dye itself. Hence, this observed blue shift is an additional evidence of binding of the dye molecules to the ZnO nanospheres surface. For instance the 3.10$^{-8}$ mol/L solution of TRITC demonstrates blue shifts of 3.6 and 3.0 nm for the photoluminescence and absorption bands, respectively.

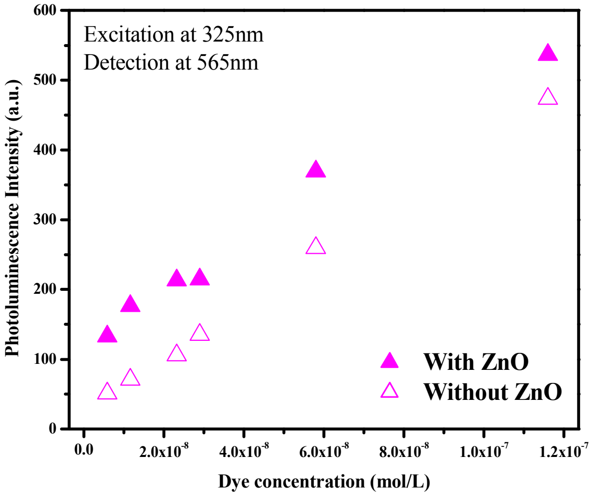

Figure 20. Photoluminescence intensities at 565 nm for different TRITC concentration without ZnO (*empty triangles*) and with ZnO (*filled triangles*).

For additional confirmation of the exchange transfer, two-photon excitation was carried out on pure ZnO, pure dye (10$^{-7}$ mol/L) and hybrid matrix [26]. Figure 21-a exposes the excitation spectrum of the pure ZnO nanoparticles in ethanol detected at 379 nm. This excitation spectrum represents the wavelengths that contribute to the present species emission; here the ZnO nanoparticles can be easily excited in the range of 690-720 nm with a maximum at 705 nm, which matches to the two-photon absorption gap of ZnO. Excitation spectra of the pure dye TRITC and the nanohybrids are shown in figure 21-b. TRITC ethanol solution exhibits strong two-photon absorption band at about 825 nm and a weaker one at 715 nm. Moreover, the nanohybrids exhibit the same absorption maximum at 825 nm related to absorption of the dye, but they strongly absorb as well at 700 nm that is accredited to the two-photon absorption of the modified ZnO inorganic core. This reality confirms the phenomenon of electron transfer from ZnO to the attached TRITC dye molecules via two-photon absorption [26].

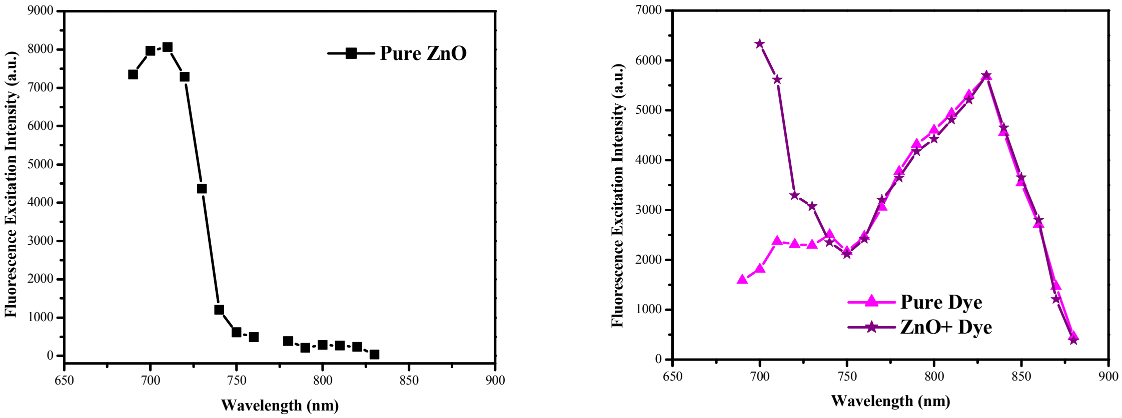

(a) (b)

Figure 21. (a) Infrared excitation spectra of the ablated ZnO nanoparticles in ethanol detected at 379 nm. (b) Infrared excitation spectra of $10^{-7}$ mol/L TRITC solution (*triangles*) and ZnO nanohybrids (*stars*) detected at 565 nm.

### 2.4.1.2 One-step built-up Nanohybrid

Herein, the synthesis of the hybrid based-ZnO was performed directly through a single step procedure. Same laser parameters were applied for the femtosecond ablation that was carried out on the ZnO target in an ethanol solution blended with TRITC molecules. Via this route, we can predict that in-situ binding of the dye molecules by the freshly produced nanoparticle surface will be stronger as the particles are hot and electronically excited. These in-situ prepared ZnO-dye nanohybrid particles were studied and compared with the previous results of ex-situ grafting.

Two HRTEM photos revealing the morphology of the hybrid sample prepared in the $3.10^{-7}$ mol/L TRITC solution are present in figures 22-a and -b. No faceted-like morphology as in the case of the ex-situ samples was observed. The nanohybrids were found to be spherical as the pristine ZnO nanoparticles prepared in ethanol. Yet, the average size of the particles prepared in the presence of TRITC shrinks down to 12 nm and the size distribution become narrower, as demonstrated in figure 22-c. Similar effects on the particle size was observed previously for metals ablation in the presence of surfactants [2]. During the in-situ ablation, the grafting of the dye molecules is likely to be instant with the fresh ablated ZnO clusters and particles. This immediate reaction amongst the ZnO nanoparticles and the dye molecules slows down the growth of the nanoparticles during the condensation phase, while dye addition via ex-situ process leads to reaction with the already-grown ZnO. Without doubt, the dye molecules absorbed on the surface relatively stop the ZnO growth process and prevent further aggregation among ZnO nanoparticles.

Photoluminescence measurements showed that emission of the dye element in the in-situ prepared nanohybrids is more intense than that of the ex-situ prepared samples. The observed enhancement was about 20% when the $3.10^{-7}$ mol/L TRITC solution was used throughout ablation. For that reason, we can assume that the in-situ ablation procedure provides a higher degree of efficient grafting if compared to the ex-situ process.

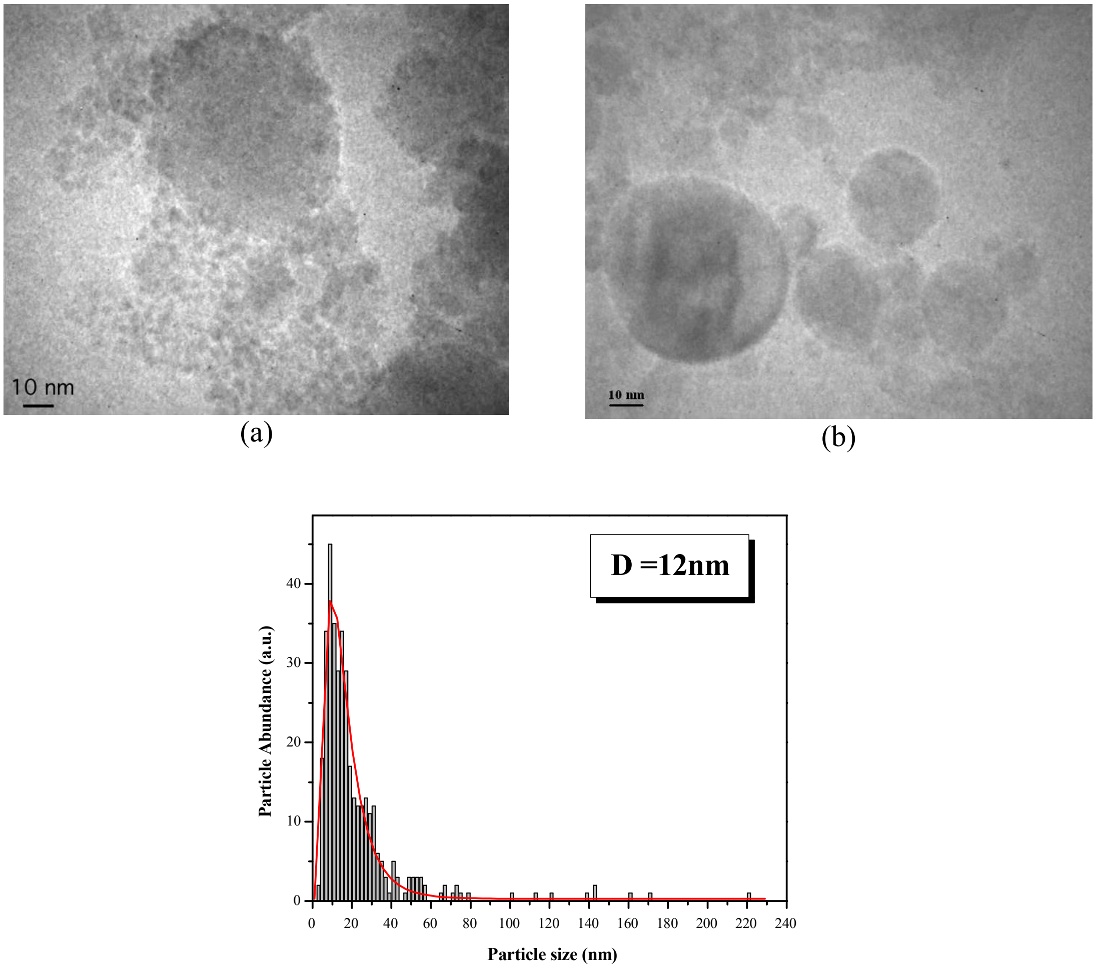

(a) (b)

(c)

Figure 22. (a), (b) Two HRTEM photos of the hybrid sample prepared in-situ at $3.10^{-7}$ mol/L TRITC solution, along with (c) its size distribution histogram.

Summing up, TRITC dye molecules were grafted ex-situ and in-situ onto the ZnO nanoparticles synthesized in ethanol solution. Ex-situ nanohybrids present facetted structures with average particle size smaller than the size of pure ZnO. Absorption measurements reached the equilibrium when the concentration of the dyes is as low as $6.10^{-7}$ mol/L. Energy and electron transfers from the inorganic ZnO core towards the grafted organic dye molecules take place by means of one-photon and two-photon excitations.

## 2.4.2 Grafting the protoporphyrin IX (PP9)

This dye presents another type of dye molecules totally different from the TRITC of the previous case. The PP9 possesses two COOH anchoring groups, as illustrated in figure 23. Although the LUMO level of this dye is higher than the conduction band of the ZnO, we used this dye to test its grafting behavior once grafted onto the surface of the defectless ZnO nanoparticles elaborated via femtosecond laser ablation.

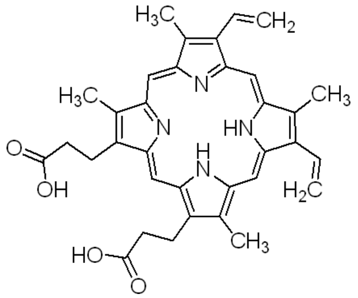

Figure 23. Molecular structure of the protoporphyrin IX (PP9).

### 2.4.2.1 Steady state fluorescence measurements

Grafting of the PP9 onto the ZnO was done ex-situ with two different dye concentrations, namely $10^{-6}$ and $10^{-4}$ mol/L. Photoluminescence spectra at 325 nm excitation of these hybrids along with their parallel pure dyes are plotted in figure 24-a and -b, which corresponds to the hybrid sample before and after filtering. The filtering was done through membranes of 20 nm pore diameter, and where the hybrids were recuperated by ultra-sonicating the membranes in THF (tetrahydrofuran) solutions. Figure 24-a shows a decrease in the ZnO exciton when increasing the density of PP9 molecules that exhibit intense emissions. After filtering, figure 24-b shows a decreasing in the ZnO exciton, and an increasing in the dye emission with mounting the dye concentration. It is worth recalling that the ZnO presents no defect bands in the visible region. The change in the relative ratio among the dye emission peaks in the hybrid regime for the dye at $10^{-6}$ mol/L is clearly visible in figure 24-b, where we can see a great increase in the emission at 672 nm at the expense of the emission at 635 and 705 nm. This later observation proves that the dye emission behavior has changed once it was grafted onto the surface of the ZnO.

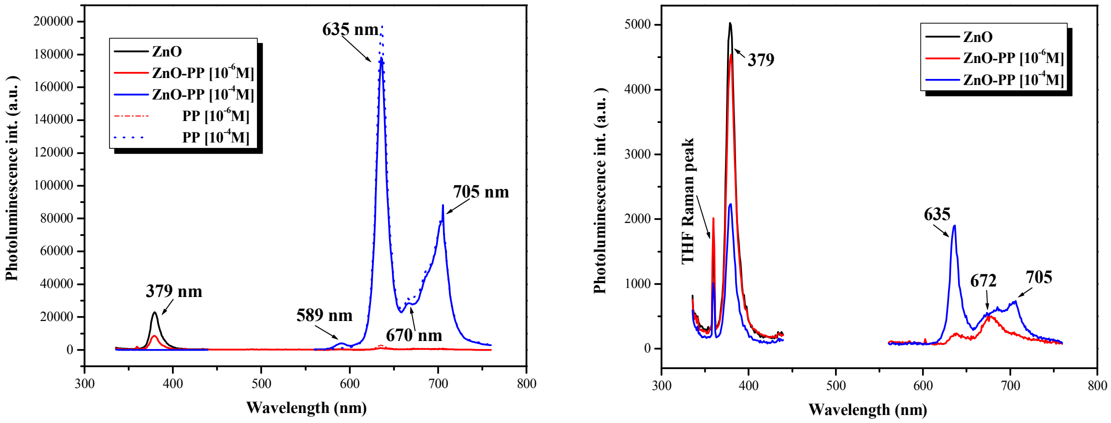

(a) (b)

Figure 24. Photoluminescence spectra at 325 nm excitation of hybrids with $10^{-6}$ and $10^{-4}$ mol/L dye concentrations (solid lines) along with their pure dyes (dotted lines) (a) before and (b) after filtering.

On the other hand, we subjected the a hybrid solution of the ZnO grafted with the PP9 and its corresponding pure dye solution to the fluorescence time resolved spectroscopy in order to inspect the changes in the dye fluorescence dynamics before and after grafting. Let us state the theoretical background of this measurement process.

### 2.4.2.2 Fluorescence time-resolved measurements

#### 2.4.2.2.A Theoretical background

Fluorescence is used spectroscopically as a method of probing the dynamics (time-dependent behavior) of the electronically excited state after light excitation. When a molecule absorbs a photon it moves from its energy ground state to an excited state. Upon releasing the photon the molecule relaxes and returns to its ground state. Hence, Fluorescence lifetime refers to the average time that the molecule spends in its excited state before returning to its ground state. Accordingly, fluorescence lifetime, in a hybrid system for example, can be used to measure the time it takes for certain molecular interaction to take place following the changes in its fluorescence lifetime.

The intensity of fluorescence $I_f$ is proportional to the number of molecules in the excited state, N, which changes as molecules relax to the ground state:

$$I_f(t)\ \alpha\ N(t) \tag{2-6}$$

Thus, monitoring the intensity of fluorescence emitted by the sample as a function of time (typically a few nanoseconds) permits the relaxation rate to be measured directly. For example, a first order rate equation for the relaxation of the excited state population is as follows:

$$\frac{dN}{dt} = -k_r N \tag{2-7}$$

with $k_r$ being the fluorescence decay radiative rate.

This implies that the intensity of fluorescence will damp exponentially as:

$$I(t) = I_0 e^{-k_r t} \tag{2-8}$$

Therefore for a decay equal to $\left(\frac{1}{e}\right) I_0$, the fluorescence lifetime is $\tau_f = \frac{1}{k_r}$. Experimentally, we are up to measure the thus-defined term $\tau_f$. Nevertheless, several relaxation processes as the intersystem crossing, the internal conversion and the interfacial electron transfer could occur. This induces an additional term in the fluorescence lifetime, defined as the nonradiative rate $k_{nr}$:

$$\tau_f = \frac{1}{k_r + k_{nr}} \tag{2-9}$$

Fluorescence Time decay profiles can be fitted through several exponential by following relation:

$$I(t) = \sum_i A_i e^{-\frac{t}{\tau_i}} \tag{2-10}$$

$A_i$ being the individual intensity amplitude.

### 2.4.2.2-B Fluorescence decay time of free PP9 and PP9/ZnO hybrids

To measure the fluorescence decay time, we used a gated CCD camera where the gate time was fixed at 3ns, and whose experimental setup along with its operational functioning is given in the Appendix IV. Fluorescence decay time measurements studied for the different emission peaks in free-PP9 and grafted-PP9 on ablated ZnO nanoparticles are depicted in figures 25-a and -b, respectively; here each point represents the dye emission intensity at a certain period of time.

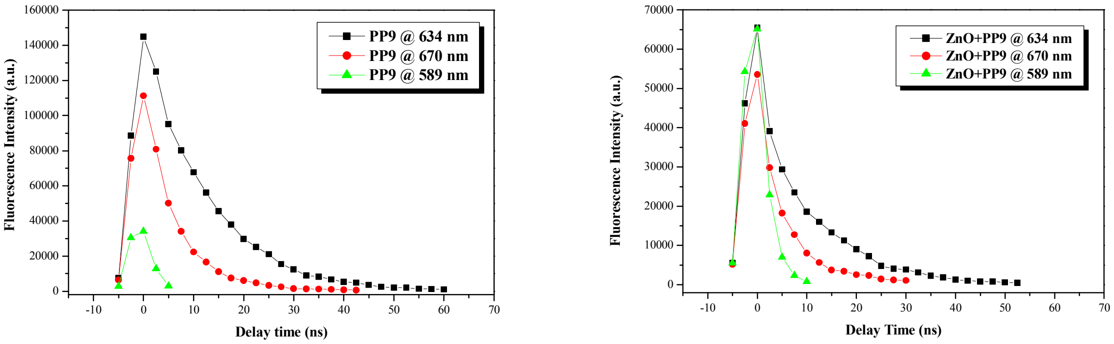

(a) (b)

Figure 25. Fluorescence decay time measurements studied for the different emission peaks in (a) free-PP9 and (b) grafted-PP9 on ZnO nanoparticles in THF solution. (Excitation wavelength was 400 nm).

We can clearly see that the intensities of both emissions at 634 and 670 nm decrease after dye grafting, while the emission intensity at 589 nm increases after grafting. This fact indicated that the grafted-dye optical behavior differs a lot from that of the pure dye, confirming the certainty of grafting inducing the opening of several carrier exchange channels between the ZnO and the grafted PP9 dye molecules. This certainty is supported as well by the duration of the radiative recombination decay of the dye at the 652 nm emission (*black square plot*):

In pure PP9, the time profile fits a first-order decay as:

$$I(t) = i_0 + A_1 e^{-\frac{t}{\tau_1}} \tag{2-11}$$

where $i_0$ is the offset position and $\tau_1 = 12{,}61$ ns

While in hybrid systems (see figure 25-b), the time profile fits a second-order decay as:

$$I(t) = i_0 + A_1 e^{-\frac{t}{\tau_1}} + A_2 e^{-\frac{t}{\tau_2}} \tag{2-12}$$

showing two decay time: a fast time and a slower fall time of $\tau_1 = 1{,}54$ ns and $\tau_2 = 13{,}11$ ns. This difference in lifetime duration and conduct indicates the presence of charges exchange channels in the hybrid matrix. Yet further experiments should be done to establish a more precise comprehension of the photophysical and exchange processes among these hybrids.

Indeed, we succeeded to graft this porphyrin with COOH anchoring groups onto the defectless ablated ZnO nanospheres, and confirmed the existence of exchange mechanisms in the hybrid system.

## 2.5 Conclusion

For the first time, in our knowledge, we proved the ability of femtosecond laser in ablating ZnO pressed pellets (targets) in liquid medium to create particles of a few nanometers [18]. For samples prepared in deionized water at low laser fluence, photoluminescence measurements explicitly reveal the effect of quantum confinement which is directly linked to the presence of small particles whose radius is less than Bohr radius. Indeed, particles of about 1 to 2 nm were identified by AFM and TEM observations, which also unveil the increase in ablated particle size when raising the fluence. Ablating in the dodecanethiol solution leads to slow cluster-growth manifested by the development of facetted particles, providing evidence of the graft of the thiol molecules onto ZnO nanoparticles. This result opens the way to further investigation concerning diverse molecule-grafting onto ZnO nanoparticles in order to produce inorganic-organic nanohybrids.

Two types of dye molecules namely the Tetramethylrhodamine B isothiocyante with a sulfur (S) anchoring groups and the protoporphyrin IX with COOH anchoring groups were successfully grafted onto the defectless laser ablated ZnO nanospheres.

Using ethanol as a solvent for nanohybrid preparation enables handling organic components that are not restricted to those of water soluble derivatives. Tetramethylrhodamine B isothiocyante (TRITC) dye molecules were grafted ex-situ and in-situ onto the ZnO nanoparticles. Ex-situ nanohybrids crystallize as strongly facetted structures with average particle size smaller than the size of pristine ZnO. And, the absorption process supported by spectroscopy reached the equilibrium when the concentration of the dyes is as low as $6.10^{-7}$ mol/L. Energy transfer from the inorganic ZnO core towards the grafted organic dye molecules occurs via two excitation processes; (i) one-photon and (ii) two-photon excitations. These outcomes show that femtosecond laser ablation is a compelling tool for manufacturing complex nanohybrid materials to be applied in bio-sensing technology.

# Bibliography

[1] F. Mafuné, J. Kohno, Y. Takeda, T. Kondow, and H. Sawabe, J. Phys. Chem. B 104 (2000) 9111

[2] F. Mafuné, J. Kohno, Y. Takeda, T. Kondow, and H. Sawabe, J. Phys. Chem. B 105 (2001) 5114

[3] A. V. Simakin, V. V. Voronov, G. A. Shafeev, R. Brayner, and F. Bozon-Verduraz, Chem. Phys. Lett. 348 (2001) 182

[4] S. I. Dolgaev, A. V. Simakin, V. V. Voronov, G. A. Shafeev and F. Bozon-Verduraz, Appl. Surf. sci. 186 (2002) 546

[5] K. V. Anikin, N. N. Melnik, A. V. Simakin, G. A. Shafeev, V. V. Voronov, and A. G. Vitukhnovsky, Chem. Phys. Lett. 366 (2002) 357

[6] C. Liang, Y. Shimizu, T. Sasaki, and N. Koshizaki, J. Phys. Chem. B 107 (2003) 9220

[7] C. Liang, T. Sasaki, Y. Shimizu, and N. Koshizaki, Chem. Phys. Lett. 389 (2004) 58

[8] C. Liang, Y. Shimizu, M. Masuda, T Sasaki, and N. Koshizaki, Chem. Mater. 16 (2004) 963

[9] H. Usui, Y. Shimizu, T. Sasaki, and N. Koshizaki, J. Phys. Chem. B 109 (2005) 120

[10] T. Tsuji, T. Kakita, and M. Tsuji, Appl. Surf. sci. 206 (2003) 314

[11] A. V. Kabashin, M. Meunier, C. Kingston, and J. H. T. Luong, J. Phys. Chem. B 107 (2003) 4527

[12] A. V. Kabashin, and M. Meunier, J. Appl. Phys. 94 (2003) 7941

[13] J. P. Sylvestre, A. V. Kabashin, E. Sacher, and M. Meunier, Appl. Phys. A 80 (2005) 753

[14] Clegg, Robert. The Vital Contributions of Perrin and Förster. Biophotonics International, September (2004)

[15] D. B. Chrisey, G. K. Hubler, Eds. "Pulsed Laser Deposition of Thin Films", Wiley Interscience, New York (1994)

[16] S. I. Anisimov, M. I. Tribel'ski, and G.Ya. Epel'baum, Sov. Phys. JETP 51 (1980) 802

[17] D. Bäuerle, Laser Processing and Chemistry. Springer, 3rd Edition (2000)

[18] A. Said, L. Sajti, S. Giorgio, and W. Marine, J. Phys.: Conf. Ser. 59 (2007) 259

[19] K. F. Lin, H. M. Cheng, H. C. Hsu, L. J. Lin, and W. F. Hsieh, Chem. Phys. Lett. 409 (2005) 208

[20] L. Brus, J. Phys. Chem. 90 (1986) 2555

[21] A. van Dijken, E. A. Meulenkamp, D. Vanmaekelbergh, and A. Meijerink, J. Luminescence 90 (2000) 123

[22] R. T. Senger, and K. K. Bajaj, Phys. Rev. B 68 (2003) 045313

[23] S. Monticone, R. Tufeu, and A. V. Kanaev, J. Phys. Chem. B 102 (1998) 2854

[24] P. Vallee, J. Lafait, M. Ghomi, M. Jouanna, and J. Morthange, J. Mol. Struct. 651 (2003) 371

[25] L. Sajti, A. Said, S. Giorgio and W. Marine, Proc. of SPIE 6191 (2006) 242

[26] L. Sajti, S. Giorgio, V. Khodorkovsky, W. Marine, New nanohybrid materials for biophotonics, Applied Physics A. 89 (2007) 315

# Chapter 3

# Elaboration of ZnO nanospheres and nanorods via Chemical processes to be dye-functionalized and applied in photovoltaic cells

## 3.1 Introduction

Our ultimate goal through this part of the thesis is to generate dye functionalized-ZnO hybrid solar cells with relatively improved photon-to-current conversion efficiencies. In this approach, ZnO nano-spheres and -rods are fabricated through chemical procedures based on solution processes. A technique realized by material growth in simple solution and without use of surfactant. Associated to an important class of transparent high mobility semiconducting nanomaterials, ZnO nanopatricles emanating from this low cost fabrication technique, have been successfully applied to solution processed solar cells [1] and transistors [2].

In this chapter, we report on the synthesis and especially the detailed investigations on morphological and optical properties of the ZnO elaborated via chemical ways.

## 3.2 Full descriptions of the chemically synthesized ZnO

### 3.2.1 Experimental requirements

ZnO nanorods were successfully reproduced in the "***GCOM2 Laboratory***" according to the procedure developed by Pacholski [3] and modified to some extent by Sirringhaus and co-workers [4]. Typically, under argon atmosphere, to a solution of 0,8182 g of zinc acetate (Aldrich Chemicals 99.99%) in 42 mL of purified distilled methanol (Acros 99,99%) and 0.25 mL of water was added dropwise a solution of 0.4859g of potassium hydroxide (Aldrich Chemicals 99.99%) in 23 mL of methanol at 60 $^0$C under magnetic stirring.

Other alkalies were used as well, namely; sodium hydroxide (99,998%) and cesium hydroxide monohydrate (99,95%) purchased from Aldrich and lithium hydroxide (anhydrous, 99,995%) purchased from Alfa Aesar. All glass equipments were cleaned before use; first with sodium hydroxide (at concentrated solution), second with deionised water. And before mixing the synthesis reactants, all solutions were first sonicated until complete dissolution of the used materials, namely the alkalies in the form of small pallets and the Zinc acetate in powder type. For each one of the alkalies, alkali and water quantities were calculated in order to apply same conditions for all experiments.

In a first stage, nanoparticules of ZnO of an average size of few nanometers in diameter were obtained after 2 h 15 minutes. In order to acquire nanorods with controllable size, the solution mother was concentrated by a rotary pump under reduced pressure at 55 °C to 10 mL and then heated at 60°C for several hours as time reaction. Right after we stopped the synthesis reaction, the solution was left at rest to decant. The white solid precipitate was washed 3 times with 50 mL of methanol; that is by adding each time the methanol, waiting until decantation of ZnO and then throwing the superfluous of methanol. The schematic reaction is briefed for simplicity as follows:

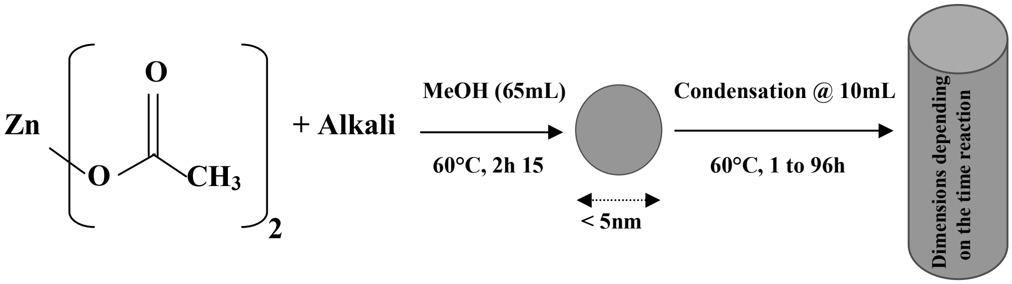

Characterisations of the so-synthesised ZnO nanoparticles and nanorods obtained via different synthesis conditions were performed through several techniques. For optical investigations, UV-Vis absorption spectra were taken using a Varian CARY 50 spectrophotometer, while fluorescence spectra were recorded with a CARY Eclipse spectrometer. These measurements are done on samples diluted in THF at $5.10^{-2}$ mg/mL. In both cases we used a 1 cm path length UV-quartz cell. For morphological analysis, High Resolution Transmission Electron Microscopy (HRTEM) studies were done with a JEOL 3010 operating at an acceleration voltage of 300 kV with a LaB6 emission filament and a pole piece (objectif) (Cs = 1.4 mm), corresponding to the point resolution of 0.21 nm. The HRTEM samples were prepared by drop casting from distinct solutions on an amorphous carbon film coating a copper mesh followed by drying at room temperature.

## 3.2.2 ZnO morphological study

### 3.2.2.1 Comparison of ZnO nanorods after modification of the alkali component in synthesis reaction

Large group of researchers have studied the crystal growth of single-crystalline ZnO nanostructures that are synthesized in alkaline systems [5-7]; studies that included the influence of solvent polarity, temperature, water content and reactant concentrations. LiOH, KOH and NaOH at different concentrations represented the alkalies that were used to construct ZnO nanorods whose facets growth mechanism was monitored [8,9]. Altering NaOH concentration and reaction time lead to ZnO nanodots and nanorods with different size and shape [10]. In addition, Uekawa et al. [11] studied the effect of alkali hydroxide (XOH: where X is Li, Na, K, Cs) on formation processes of ZnO crystallites from aqueous solutions containing $Zn(OH)_4^{2-}$ ions.

More recently the synthesis of ZnO nanorods has attracted much interest due to their unique electronic and optical properties. So far, intense research effort has been dedicated to ZnO nanorod synthesis with focus on shape and aspect ratio control of ZnO nanorods, but only small attention has been paid to the control of size distribution in length and width. It is well known that these factors depend on the nanoparticle formation process. As a consequence, one important step in the direction of controlling the dispersity of nanorods is to get a deeper understanding of the growth mechanism and to identify the role of each component used in the synthesis.

In the ***GCOM2*** laboratory, the work of the PHD student Cyril Martini is dedicated to investigate the role of the alkali metal oxide in the growth mechanism of ZnO nanorods in order to control size dispersity and crystalline quality. The present morphological studies of ZnO nanorods have been performed by me using the equipment of the ***CRMCN,*** especially the JEOL microscope 3010 operating at an acceleration voltage of 300 kV. The conclusions on the influence of the alkali metal hydroxide as a base on the nanorod shape, size and length distribution, and on the growth mechanism itself, were established according to common discussions with chemists at ***GCOM2***.

In attempt to study the influence in altering the alkalies, a comparison of ZnO nanorods fabricated with these different alkali solutions after 48 hours of time reaction is given below. These alkali solutions are as follows in the order of ascendant diameter value of the conterions: LiOH, NaOH, KOH and CsOH. HRTEM images of ZnO nanorods prepared with these different alkali solutions in a growth process of 48h (after condensation) at 60 °C under identical conditions are shown respectively in figures 1, 2, 3 and 4. Actually, for the solutions of various alkalies, the ZnO nanorods are well structured with a high degree of crystallinity.

We can notice that in the case when we used bases containing a small alkali Li and Na, the ZnO nanorods are pretty well formed with smooth regular lateral surfaces (figures 1 and 2), one pointed edge is of triangular shape while the other edge presents a plan perpendicular to the c axis. Figure 1-b shows a HRTEM image of a ZnO nanorod with LiOH with approximately ≈ 9 nm in diameter, seen in the [010] orientation, and where the c axis is parallel to the rod axis.

ZnO nanorods obtained with KOH solution of bigger alkali, reveal bumpy surfaces which diameters are often variable with one shapely pointed triangular edge, see figure 3. HRTEM image of a nanorod with KOH in figure 3-b, exposes a ZnO rod of 5 to 6 nm in diameter, observed along a [010] direction with the c axis parallel to the rod axis lying on the carbon film. With CsOH, which is the biggest alkali, the defects found in the earlier case of KOH become much more pronounced, (figure 4). Hence, nanorods with CsOH present uneven forms that differ from rodlike shape and irregular surfaces with strong variation in both length and diameter values. Indeed, the HRTEM image of the end of a nanorod with CsOH, (figure 4-b), demonstrates visibly the marked presence of defects where we can observe an irregular diameter and a rounded extremity.

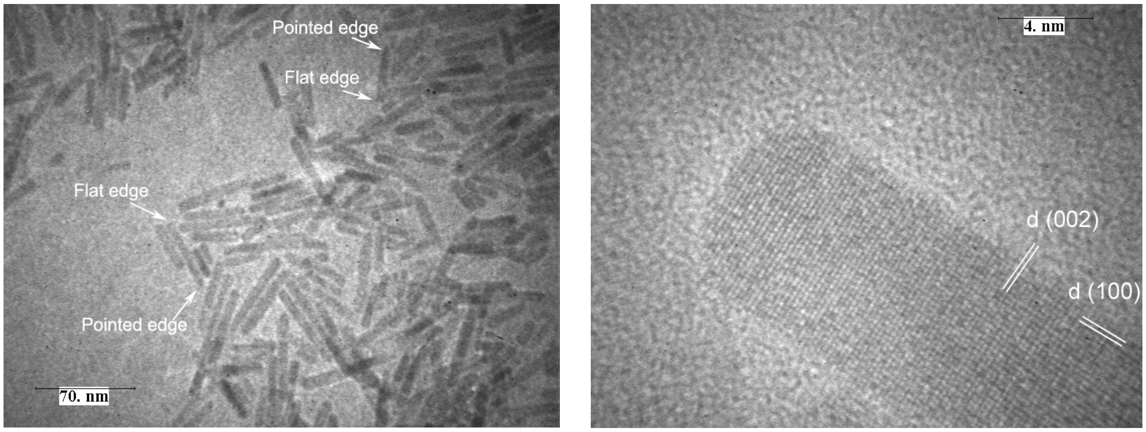

(a) (b)

Figure 1. a- Overview of ZnO nanorods synthesized with LiOH after 48 h at 60 °C
b- HRTEM of a ZnO nanorod with LiOH (≈ 9 nm in diameter), seen in the [010] orientation. The c axis is parallel to the rod axis.

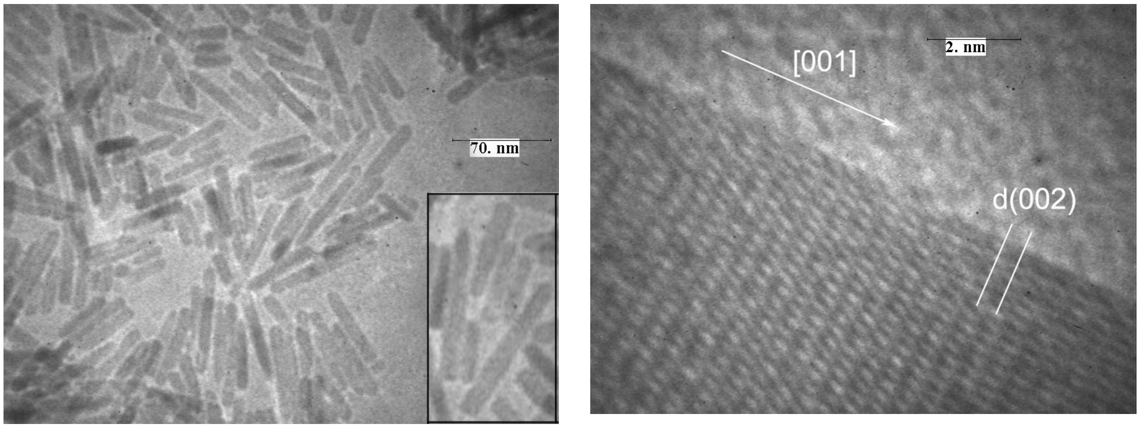

(a) (b)

Figure 2. a- Overview of ZnO nanorods synthesized with NaOH after 48 h at 60 °C. In the inset magnification of some nanorods with pointed and flat edges.
b- HRTEM magnification of a flat lateral face of a nanorod with NaOH

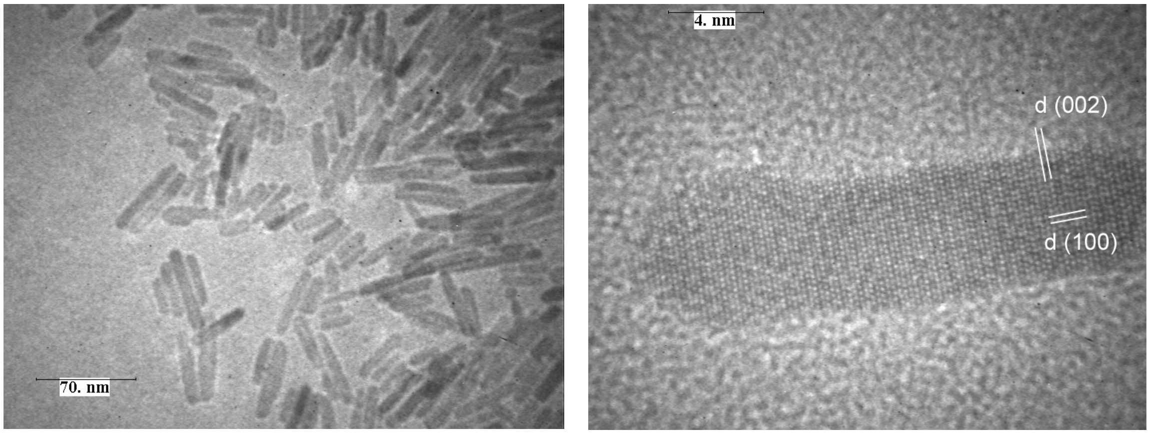

(a) (b)

Figure 3. a- Overview of ZnO nanorods synthesized with KOH after 48 h at 60 °C
b- HRTEM image of a nanorod with KOH, (5- 6 nm in diameter), observed along a [010] direction with the c axis parallel to the rod axis. One end of a nanorod is nearly sharp.

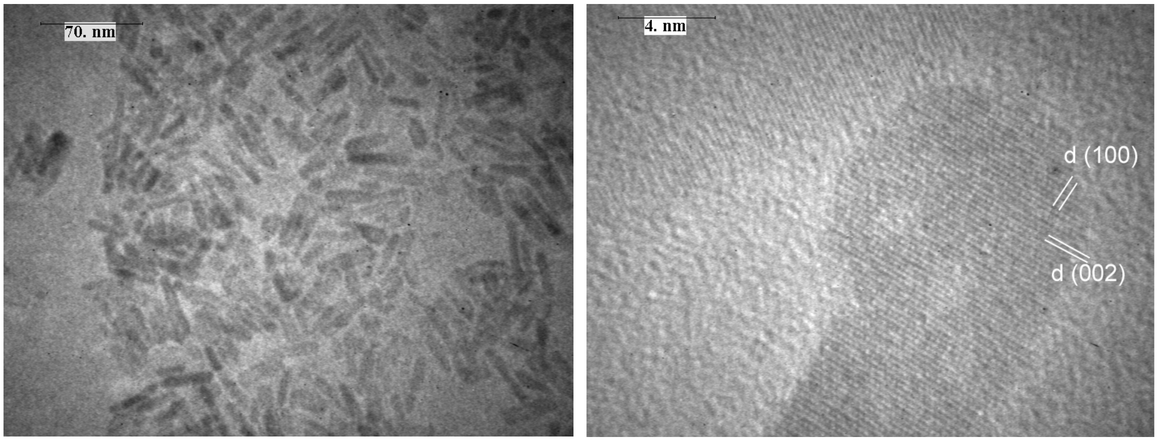

(a) (b)

Figure 4. a- Overview of ZnO nanorods synthesized in CsOH after 48 h at 60 °C
b- HRTEM image of the end of a nanorod (with CsOH), with an irregular diameter and a rounded extremity.

Statistical analyses for each one of the alkaline systems were executed, where we have seen that both length and diameter show strong differences according to the base used. We noticed that the diameter distributions of LiOH and NaOH are visibly narrower than those with KOH and CsOH, implying regular diameter values attend during the growth process of ZnO with LiOH and NaOH. We also found that the largest and widest ZnO rods are those prepared with NaOH while we see the thinnest rods with LiOH. ZnO lengths and diameters decrease for KOH and decrease much further with CsOH.

In attempt to explain and justify the final product after 48 hours of ZnO nanorods according to different alkali solutions, we need to consider the alkali size and to monitor the solubility of these alkalies in methanol. The ionic radius of the cations $Li^+$, $Na^+$, $K^+$, $Cs^+$ are

0.76, 1.02, 1.38 and 1.67 Å, respectively [11], while the ionic radius of $Zn^{2+}$ is about 0.74 Å [8]. Nevertheless, and after observation, we can clearly class the alkalies solubility in the following ascendant order: LiOH < NaOH < KOH < CsOH.

For the CsOH with the biggest ionic radius, we can postulate that due to its high solubility the CsOH is giving his -OH much easier and thus creating much more nucleation sites during the reaction with the zinc acetate [11]. This fact may explain the formation of smaller ZnO rods. On the other hand and through the TEM photos (see figure 4), the rods have very rough and irregular surfaces, and this gives the impression of the presence of the fusion mechanism among smaller particles emanating from different nucleation sites. Therefore, we have ZnO of large Full Width Half Maximum diameter distribution due to fusion occurrence probability.

When using KOH in the ZnO fabrication process, the arguments given for CsOH can be applied but with less impact due to the fact that the KOH is less soluble than CsOH. This leads to less nucleation sites and longer nanorods probably due to fusion between particles.

In the case of NaOH, and due to its low solubility, the $Na^+$ is probably interacting with $O^-$ present on the surface of the ZnO nanorods thus preventing the fusion between particles.

The LiOH with its low degree of solubility cannot initiate a lot of nucleation sites as it was in the previous cases, namely for KOH and CsOH. Strong interaction of $Li^+$ with the $O^-$ of the ZnO surfaces leads to slower growth mechanism, as compared with the case of NaOH. On the other hand, the ionic radius of $Li^+$ and $Zn^+$ are nearly the same, which allows Li ions to replace Zn ions on the cation site. The replacement of Zn ions by Li ions with lower positive charge reduces the growth rate of hexagonal faces as well as prism faces [9]. These $Li^+$ adsorbed on the monohedron layers reduce their both free energy and effective positive charge on the (001), which slows down the attachement of $ZnO_2^{2-}$ anions (whose presence is explained in the next paragraph) [8]. So we obtain ZnO nanorods with smaller lengths and widths than those obtained for NaOH. No evidence of fusion mechanism is detected in the TEM photos. Indeed, this induced slow nucleation process inhibited the formation of aggregated morphology.

Now, all we need is to study and understand the ZnO crystal growth mechanism versus synthesis “time” reaction when using a specific alkali solution. Hence, detailed investigations of the growth as function of time of ZnO nanorods synthesized with NaOH and KOH were established.

But, let us first try to elucidate the chemical processes that occur in the first 2 hours and 15 minutes when mixing the Zinc acetate solution where a small amount of water was added (in methanol) and the alkali solution (in methanol). Two species emanate from this combination: the $Zn^{2+}$ precursors and the $OH^-$ ions, whose reaction has been thoroughly studied [12,13]. For all the alkali systems, at the beginning of the synthesis process, that is when adding the base dropwisely, the solution turns progressively to white. This white tint predicts the formation of $Zn(OH)_2$ solid species that are insoluble in methanol. After a short while, the solution becomes colourless. Here the $Zn(OH)_2$ precipitate could be progressively converted into soluble $ZnO_2^{2-}$. This clear solution exists for a certain time, and then it becomes white again indicating the formation of ZnO nanoparticles. Indeed, the preliminary steps of the nucleation and growth are resumed in the following chemical reaction equations [10], which match exactly our experimental observations:

$$\mathrm{Zn^{2+}(solution) + 2OH^- \leftrightarrow Zn(OH)_2(solid)} \qquad (1)$$

$$\mathrm{Zn(OH)_2(solid) + 2OH^- \leftrightarrow ZnO_2^{2-}(solution) + 2H_2O} \qquad (2)$$

$$\mathrm{ZnO_2^{2-}(solution) + H_2O \leftrightarrow ZnO(solid) + 2OH^-} \qquad (3)$$

The next step is the condensation of the solution after the first 2h 15m under reduced pressure, and then put the solution back under stirring at 60°C for a certain period. This period is defined as the "synthesis time reaction".

Generally, the growth process of the ZnO particle has been drawn in three distinct steps: nucleation, growth (sphere-like shaped ZnO) and further growth (transition to rod-like shaped ZnO. The final morphologies of nanocrystals are settled on according to many internal and external factors that interfere during the nucleation and growth process. ZnO crystallographic characteristics are among these factors.

Recalling back from the first chapter, the ZnO "wurtzite structure" and the composition and properties of its crystallographic faces: in a ZnO nanorod, the two limiting faces parallel to the (001) plane are composed of $Zn^{2+}$ ions on one side and $O^{2-}$ ions on the opposite side. Thus, this different face charges induce the polar fact along the c direction. For the neutral prism faces (100) and (110) (lateral faces parallel to the rod axis), the elementary planes are constructed by a network with mixed composition of Zn and O. The polar (101) and (102) pyramid faces, which are limiting the edges of the pyramids at the end of the rod, are composed of alternating planes of Zn and O. As a consequence, through simple analysis of the ZnO structure forms, several statements can be postulated [14]:

i. Polar growth have to be prominent in usual crystal growth mechanism
ii. Growth velocity of Zn layers is higher than that of opposite O layers, (due to surface charge difference)
iii. Growth velocity of (100) layers equals that of (110), (due to similar layers composition)
iv. Growth velocities of (101) and (102) faces are defined by growth conditions as for example environment chemical composition

The fact that the basal faces are polar and the lateral ones are neutral implies essentially a difference of growth velocity amongst different crystallographic directions. Consequently, the growth rate along the [001] directions (perpendicular to (001) faces) is much faster than along other directions. Hence, length evolution along [001] directions of the ZnO nanocrystals, i. e. along the c-axis, is fully expected, which guarantees the development of one-dimensional ZnO rod-like structures. This anisotropy in the rod growth having hexagonal crystal structure has been confirmed via many researches [15-17]. A direct consequence derives from this: the formation of ZnO with rod silhouette is principally due to its hexagonal wurtzite crystal structure. Moreover, the growth rate of the polar (001) faces, along the c-axis, may as well be affected by the solvent polarity. For example, in weaker polar ethanol solvent, the growth rate of the (001) faces is faster than in methanol solvent [18]. The role of water in the synthesis of ZnO from alcohol solution is complex and not wholly understood although it is known to facilitate the dissolution and ionization of the zinc salts [7,19].

After nucleation, the particles grow by diffusion of reactant components to the surface of the so-grown particles. The reactants include the $ZnO_2^{2-}$ ions, which are obtained following the chemical reaction equation (2). These $ZnO_2^{2-}$ ions are proposed to be responsible for the polar growth of ZnO. It will lead to fast anisotropic growth of ZnO along the c-axis. They add on the (001) polar faces. Then, the reactions that occur on the outmost positive and negative surfaces parallel to (001) plane are as follows, [8]:

$$\mathrm{Zn^{2+}(surface) + ZnO_2^{2-}(solution) \leftrightarrow 2ZnO(crystal)} \quad (4)$$

$$\mathrm{O^{2-}(surface) + ZnO_2^{2-}(solution) + 2H_2O \leftrightarrow ZnO(crystal) + 4OH^-} \quad (5)$$

We can notice the addition of two units of ZnO on the Zn face while only one ZnO unit is added to the O face, implying higher growth velocity at the Zn faces.

Now we can proceed by studying the detailed features of the ZnO crystal growth versus time when using two distinct alkaline systems, namely KOH and NaOH. In this contest, we are trying through optical and morphological observations to understand and then settle on the mechanism held responsible of the ZnO growth. So we will expose first the entire studies as a function of time in the case of ZnO with KOH, and afterwards those of ZnO with NaOH.

### 3.2.2.2 Detailed study of KOH-based synthesized ZnO

After 2 h 15 minutes of mixing the synthesis reaction ingredients, that is just before the condensation step, nanoparticules of ZnO with KOH of an average size of few nanometers in diameter were obtained. Figure 5-a depicts a general overview of the nearly spherical shaped ZnO particles. We can barely distinguish these nanoparticles because of their very small dimensions. HRTEM magnification of some of these ZnO nanoparticles is shown in figure 5-b, barely showing crystallized dispersed species due to their small size and thus their relatively low contrast.

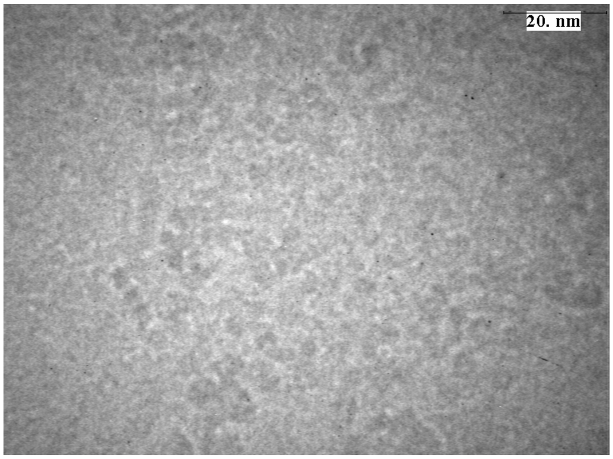

(a)

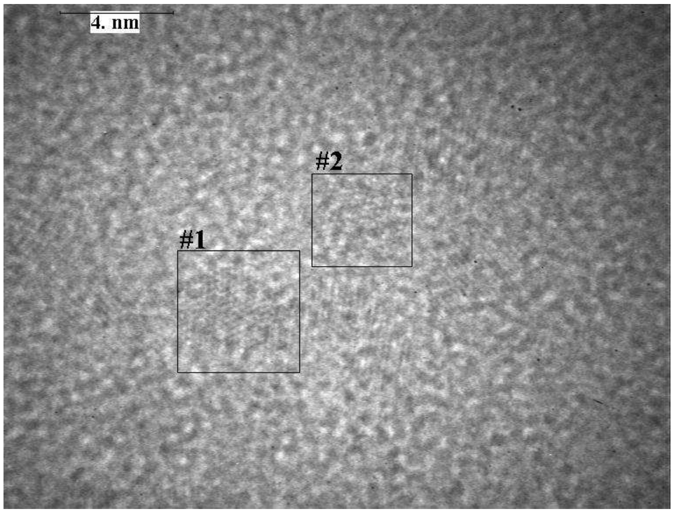

(b)

Figure 5. a- Overview of nearly spherical shaped ZnO nanoparticles with KOH right after the first 2h 15m and just before condensation
b- HRTEM image of a number of very small ZnO particles showing highly crystallized species

The planes orientation of the two highlighted particles (#1 and #2) in figure 5-b are studies through Fourier Transform of the selected windows in the numerical images. Figure 6-a exposes the FFT (Fast Fourier Transform) by Scion image program of the ZnO particle #1, which matches the electron diffraction patterns simulated by EMS program on a ZnO seen in the [001] direction. As a result, the particle labelled #1 is seen in the [001] direction, i. e. the c-axis. Same reasoning could be applied on the particle #2, which is seen in the [100] direction, see figure 7-a and -b.

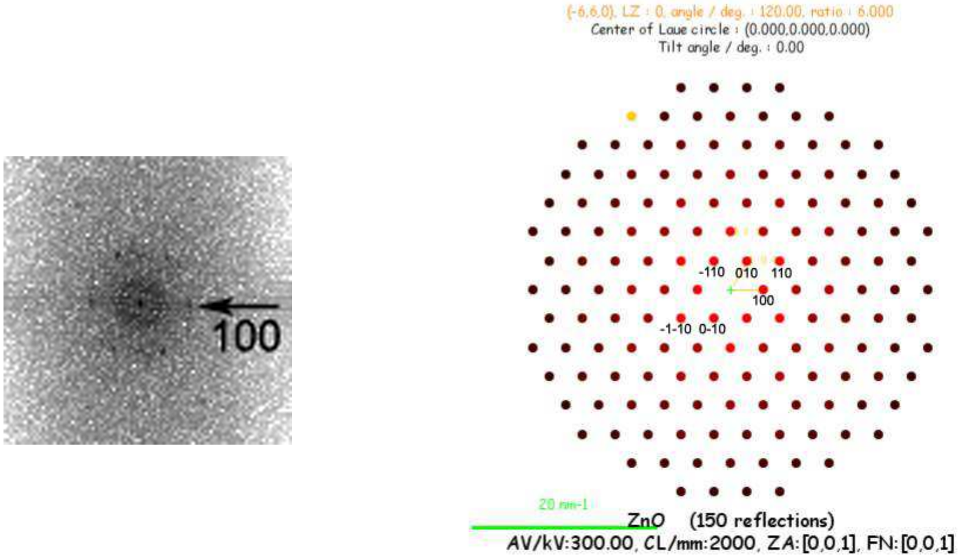

(a) (b)

Figure 6. (a) Fact Fourier Transform FFT (calculated by Scion image) applied on the ZnO particle labeled #1 in a 128×128 window in figure 7-b, which corresponds to (b) ZnO diffraction in the [001] direction (simulated by EMS program)

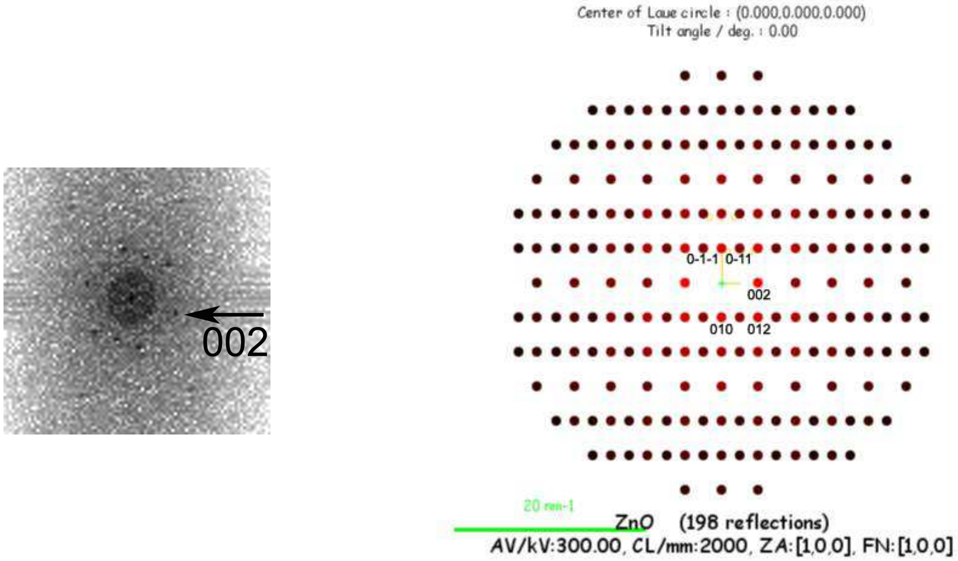

(a)

(b)

Figure 7. (a) Fourier Transform FFT (simulated by Scion image) applied on the ZnO particle labeled #2 in a 128×128 window in figure 7-b, which corresponds to (b) ZnO diffraction in the [100] direction (simulated by EMS program)

During the second step, which is the concentration by solvent removal by rotary evaporation of the synthesis mother solution, bigger ZnO particles are formed, as seen in the TEM image in figure 8-a. The forced ZnO primary cluster colloid concentration induces supersaturation conditions among the quasi-spherical ZnO colloids leading to formation of bigger nanoparticles without changing their shapes. The growth mechanism might be interpreted by Ostwald ripening mechanism [3,6]. The Ostwald ripening is defined as the growth of larger crystals from those of smaller size which have a higher solubility than the larger ones. In this process, many small crystals formed initially slowly disappear, except for a few that grow larger, at the expense of the small crystals. Actually, this is a spontaneous proccess that occurs because bigger crystals are more energetically favored than smaller ones. As a result of their ability of easy nucleation, the formation of many small particles is kinetically favored, that is small particles have a larger surface area to volume ratio thus much easier to be produced. However, larger particles are thermodynamically favored thanks to their greater volume to surface area ratio, which implies a lower energy state. That's why many small crystals will reach a lower energy state, i. e. the stability, once transformed into larger crystals. Indeed, figure 8-b shows a highly crystalline ZnO nanoparticle formed through Oswald growth mechanism when increasing the particle concentration: it is seen in its [001] direction, where we can clearly see the hexagonal structure.

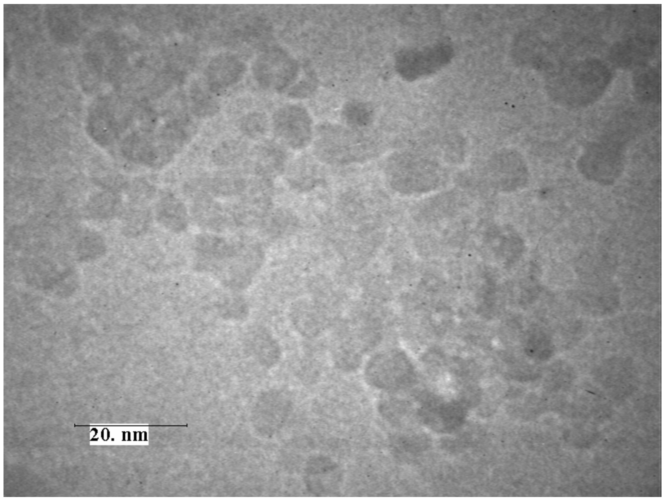

(a)

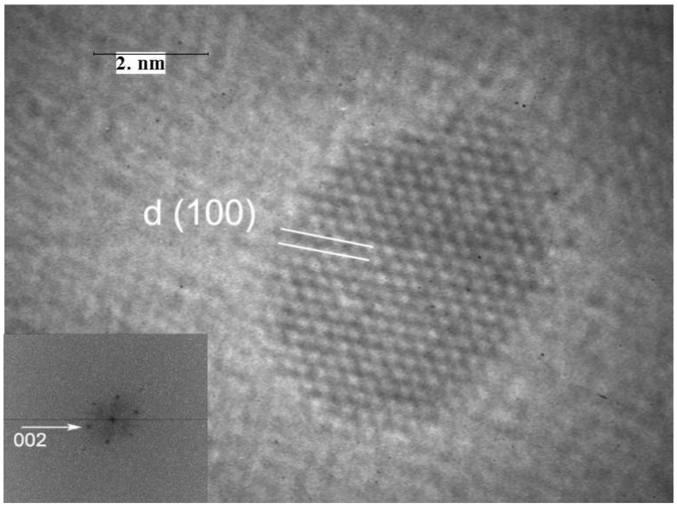

(b)

Figure 8. a- Overview of ZnO nanoparticles with KOH right after the condensation
b- HRTEM image of a ZnO particle showing highly crystallized structure, the inset figure is the FFT showing its crystal orientation seen in the [001] direction

After the concentration step, the colloid solution was subjected to the final step, that is heating under continuous stirring and 60 C, for different lengths of synthesis time.

One hour of time reaction leads to the formation of drop-like quasi-elongated ZnO nanoparticles, see figure 9-a, where the ZnO shapes differ from those reached during the concentration step. Figure 9-b shows a crystallized ZnO nanoparticle of irregular shape, mainly limited by (100) and (002) planes. We can clearly see epitaxial fusion among several particles along the c axis and laterally parallel to c axis. This epitaxial fusion amongst particles refers to the “oriented attachment” growth mechanism [3].

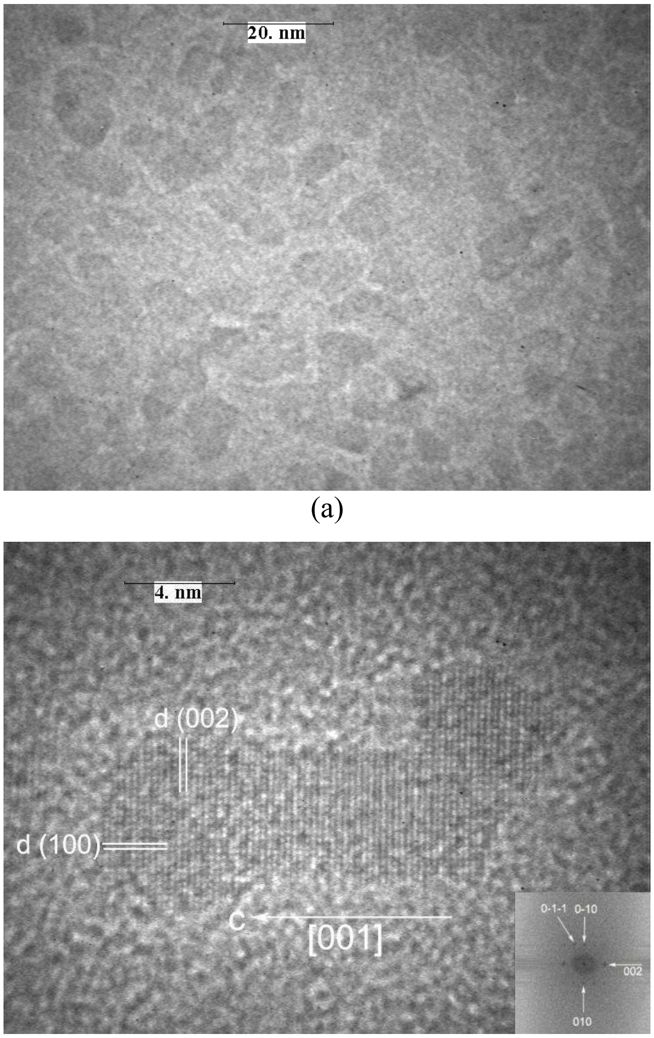

(a)

(b)

Figure 9. a- Overview of ZnO nanoparticles with KOH at 1 hour of time reaction
b- HRTEM image of a highly crystallized ZnO particle: evidence of perfect fusion of several small particles throught oriented attachment. The inset figure is the FFT showing the crystal orientation.

The increase of heating time, namely after 5 hours, generally leads to the increase in the elongation of the particle along the c axis, see figure 10-a. Bumpy surfaces are quite visible in figure 10-a. Oriented attachment of small nanoparticles along the c axis is likely to happen, that’s why there is lack in material (figure 10-b) at the bottlenecks between the adjacent particles, (indicates by arrows) (See figure 10-a). The observed lattice planes in figure 10-b are the (002) or the (100), which are perpendicular or parallel to the c axis, respectively.

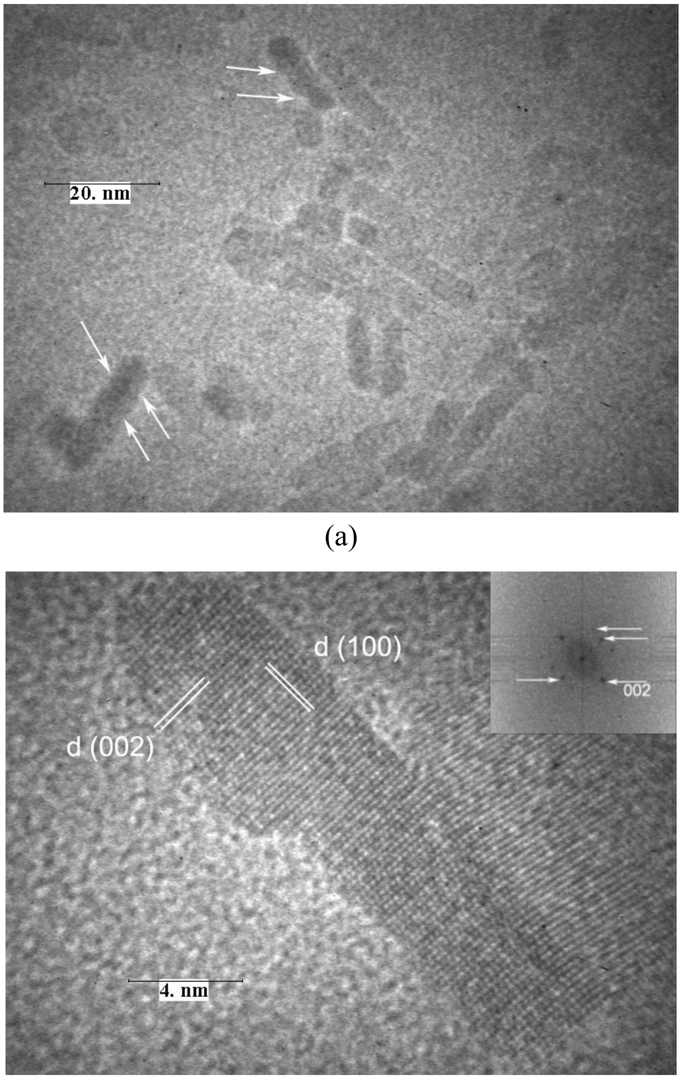

(a)

(b)

Figure 10. a- Overview of ZnO nanoparticles with KOH at 5 hours of time reaction
b- HRTEM of a highly crystallized ZnO particle with rough surfaces. The inset figure is the FFT showing its crystal orientation

Further increase in the time reaction to 17 hours implies further increment in the ZnO growth along the c axis, see figures 11-a and -b. The preferential growth along the c axis arises from the nature of the ZnO wurtzite structure itself, as previously fully explained. Bumpy surfaces remains indicating the occurrence of the “oriented attachment” growth mechanism. Besides we can clearly find some ZnO nanorods with well formed surfaces (no presence of bottlenecks). This fact implies that the “oriented attachment” growth mechanism is assisted by the “Ostwald ripening” growth, which participates in increasing the rod length and in filling the surface gaps by the nutrients provided by the slow decomposition of small crystals at the expense of the bigger ones. This is revealed by the high resolution TEM images, depicted in figures 11-c and -d, where the formation of nearly homogeneous straight surfaces begins to take place.

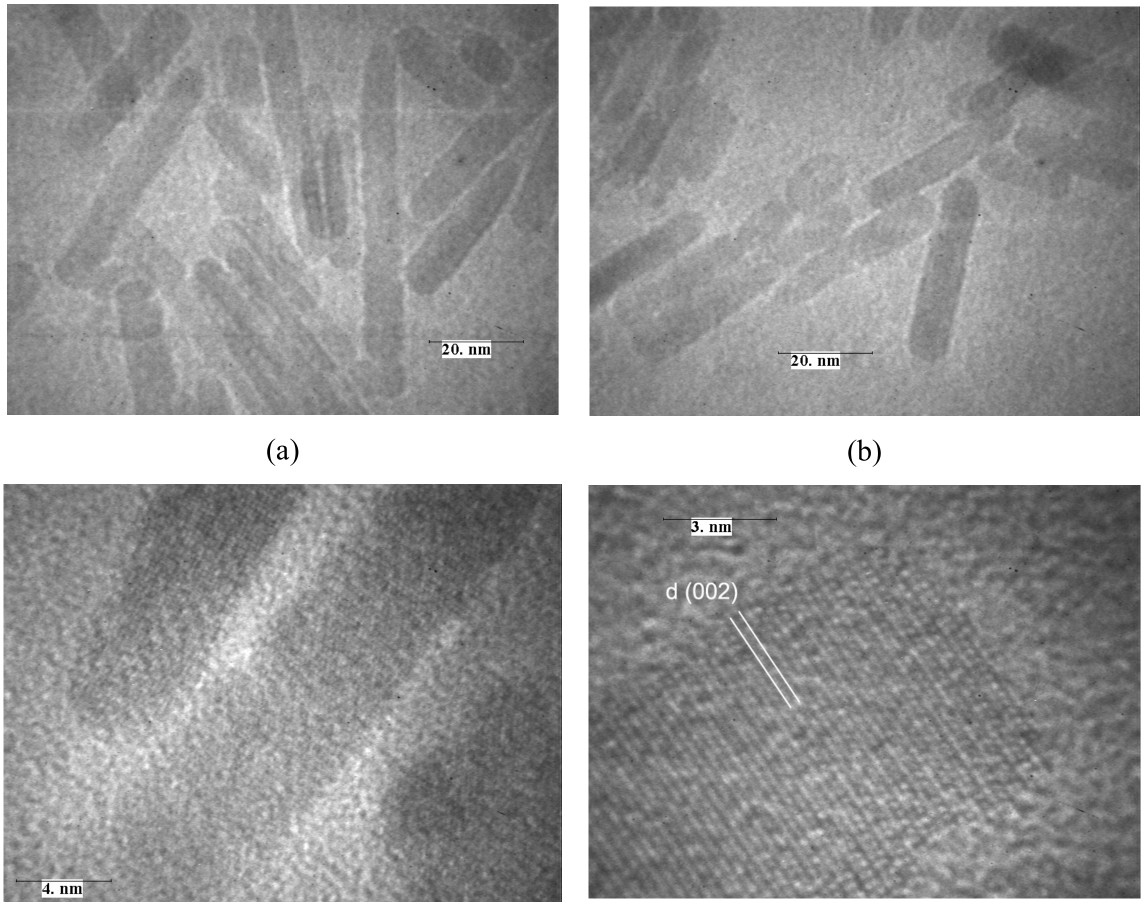

(a) (b)

(c) (d)

Figure 11. a-b- Overview of ZnO nanoparticles with KOH at 17 hours of time reaction
c-d HRTEM of well formed ZnO particles showing highly crystallized structure

The “oriented attachment” and the “Ostwald ripening” growth mechanisms are very present in the ensemble of figures 12, which represents the ZnO nanorods after 48 hours of time reaction. Most of the nanorods present extremities of two different types: one is sharply pointed while the other one is flat. This predicts different growth rate on each extremity. We still can see rough and uneven surfaces due to further oriented attachment that is happening at slower rate. The reason is that the mechanism of Oswald ripening becomes more pronounced as small particles are present in the solution. These small particles are most probably emanating from bigger particles that shrink due to Oswald ripening version. And the species emanating from their dissolution will promote the growth of larger nanorods. Selected area diffraction taken from an assembly of nanorods is seen in figure 13. The diffraction pattern corresponds to the hexagonal wurtzite structure. The first circle is diffraction from the ZnO (100), the second circle by the ZnO (002), the third circle by the ZnO (101), the fourth by the ZnO (102), and the fifth by ZnO (110) planes of the wurtzite structure.

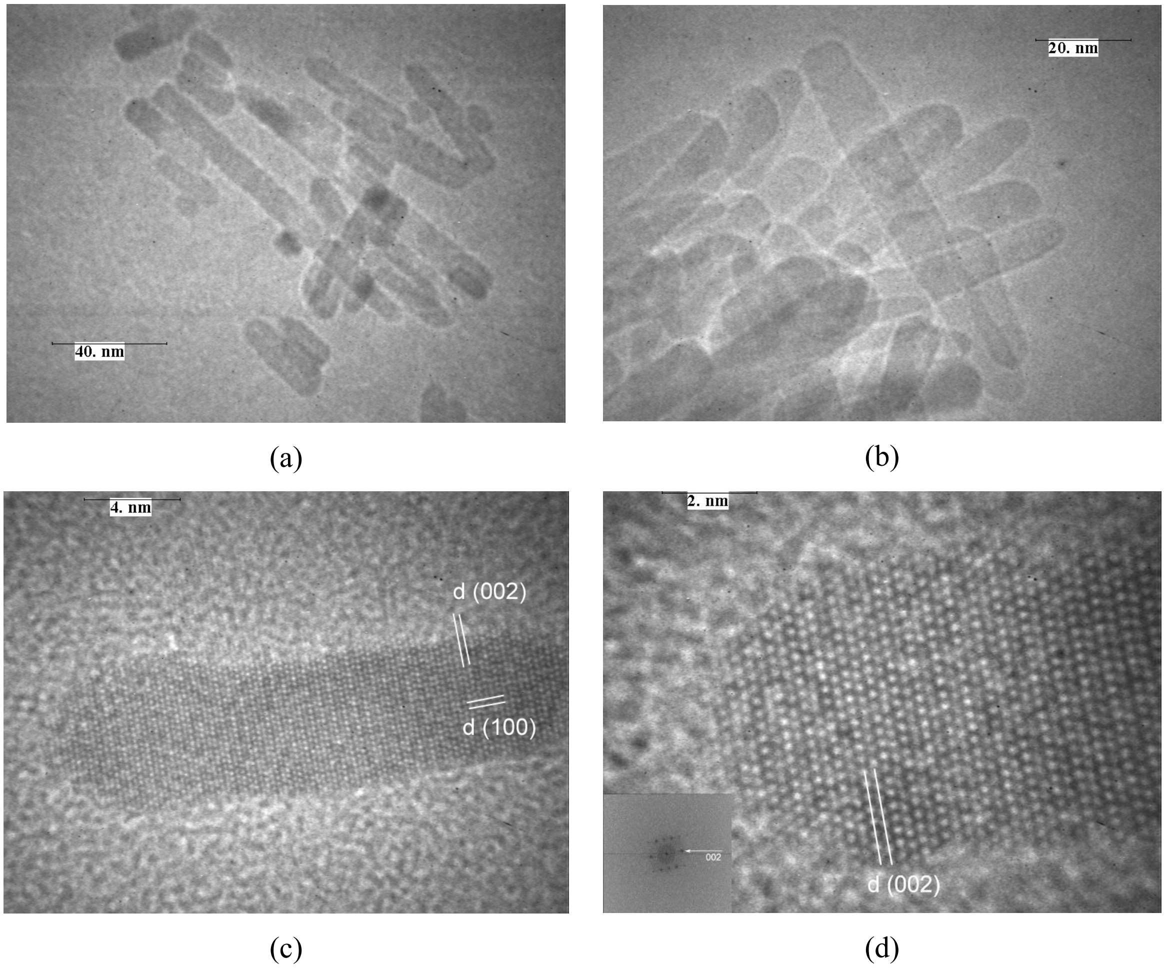

(a) (b)

(c) (d)

Figure 12. a-b- Overview of ZnO nanoparticles with KOH at 48 hours of time reaction
c-d HRTEM of ZnO particles with highly crystallized structure, the inset in figure d is the FFT showing its crystal orientation

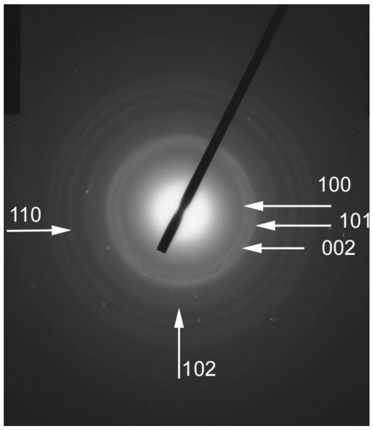

Figure 13. Polycrystalline diffraction pattern result of a ZnO nanorod corresponding to the hexagonal wurtzite structure

The contrast in the image of the single ZnO nanorod illustrated in figure 12-c varies along the [001] direction. The difference in the observational aspect along the c axis is actually due to the variation in lateral thickness of the ZnO nanorod. This is demonstrated in figure 14. The figure 14-a is the series of simulated images by the multislice technique (EMS program from Stadelmann) of ZnO observed in the [010] orientation, for increasing thichnesses from 1.6 nm to 6.4 nm. This simulated image shows the effect of the variation in the ZnO lateral thicknesses along the c axis by EMS simulation seen in the [010] direction. We took this specific direction because in figure 12-c, the ZnO nanorod is seen in the [010] direction. The EMS simulation was performed first on a ZnO virtual crystal of a thickness 1.6 nm which is equivalent to 10 elementary layers of (110) planes. Increasing the sample thickness to 20, 30 and 40 elementary (110) layers, means increasing the contrast thus better HRTEM images. The similarity in the planes visualization between the two simulated and real images guides us to deduce that the ZnO nanorod in figure 14-b is not of homogeneous lateral thickness, leading to consider that we have the fusion of at least 3 ZnO particles of different sizes. This fact strengthens the evident occurrence of the oriented attachment along the crystal c axis.

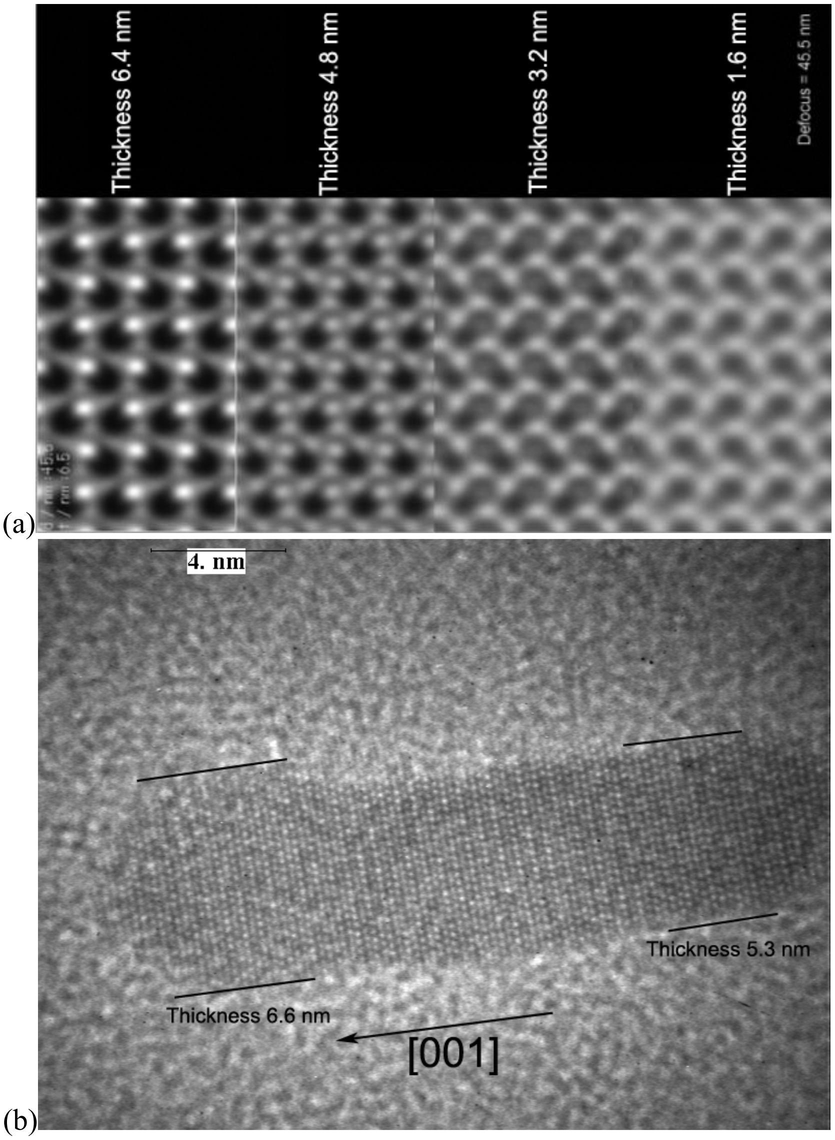

Figure 14. a- EMS slices simulation seen in [010] direction showing different ZnO thicknesses

b- Replica of figure 14-c, which is the HRTEM magnification of a ZnO particle: showing the effect of the difference in the ZnO thickness along the c axis.

No remaining small particles are found among the ZnO nanorods synthesized after 96 hours. Only well formed ZnO nanorods with smooth surfaces are present, see figures 15-a and -b. Here, we can postulate that the only responsible growth mechanism is that of Ostwald ripening.

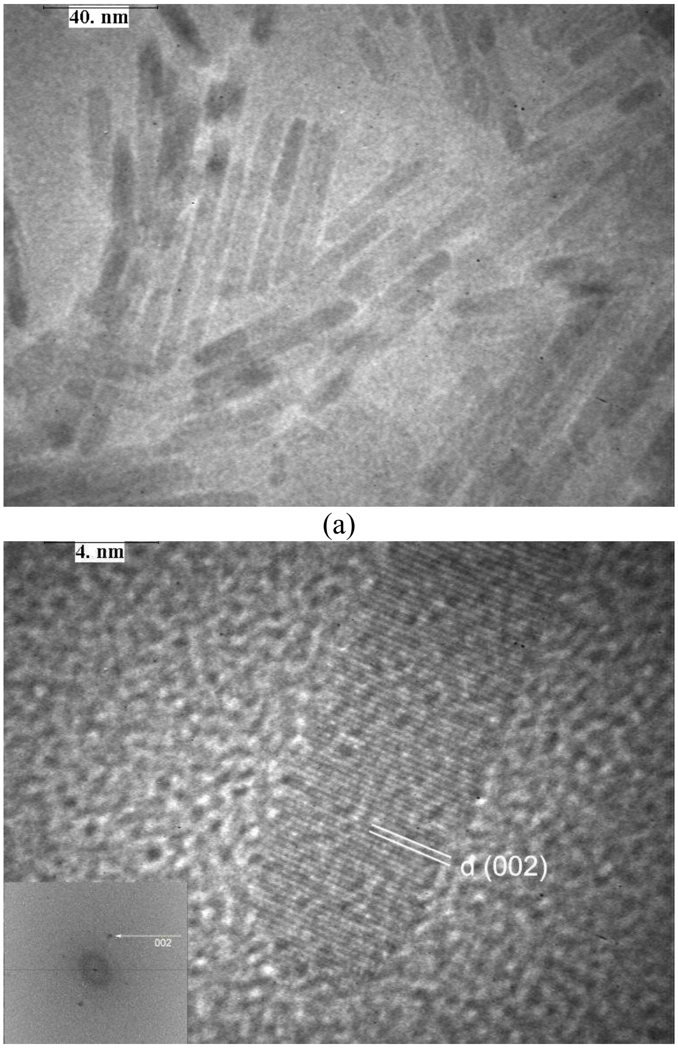

(a)

(b)

Figure 15. a- Overview of ZnO nanoparticles with KOH at 96 hours of time reaction
b- HRTEM magnification of a ZnO particle, the inset figure is the FFT showing its crystal orientation seen in the [100] direction: the 2 intense points refer to (002) planes

Meticulous inspections are executed on the TEM images in order to measure length and width of the ZnO rods prepared by employing the KOH base solution at the already mentioned stages of the reaction synthesis. Hence, statistical estimations of over 500 ZnO nanorods size distributions are exposed at similar scales in figure 16, where we can find the length histograms and their corresponding widths in the insets. Figures 16-a, -b, -c, and -d refer to the ZnO prepared after 5, 17, 48 and 96 hours, respectively. ZnO length and diameter mean values are depicted in figure 17. We clearly observe that the length increases, and its distribution further widens when raising the ZnO synthesis time reaction. This broadening is expected due to the presence of two growth mechanisms; oriented attachment overlapped with Ostwald ripening. This overlap induces non-homogeneity in the growth, which yields, for each elaboration stage, ZnO nanorods of different sizes, so the coexistence of small and large particles. This is also visible in the width distributions (in the insets), where the rods continue to grow laterally by addition of smaller particles through oriented attachment, or atoms and ions through Ostwald process on the ZnO lateral sides. However, the width histogram for ZnO at 48 hours is broader than that at 96 hours. This is quite reasonable due to the fact that at the late phases of the 96 hours the only acting growth mechanism seems to be the Ostwald ripening; well formed ZnO nanorods with smooth surfaces are present, as stated earlier according to the TEM measurements.

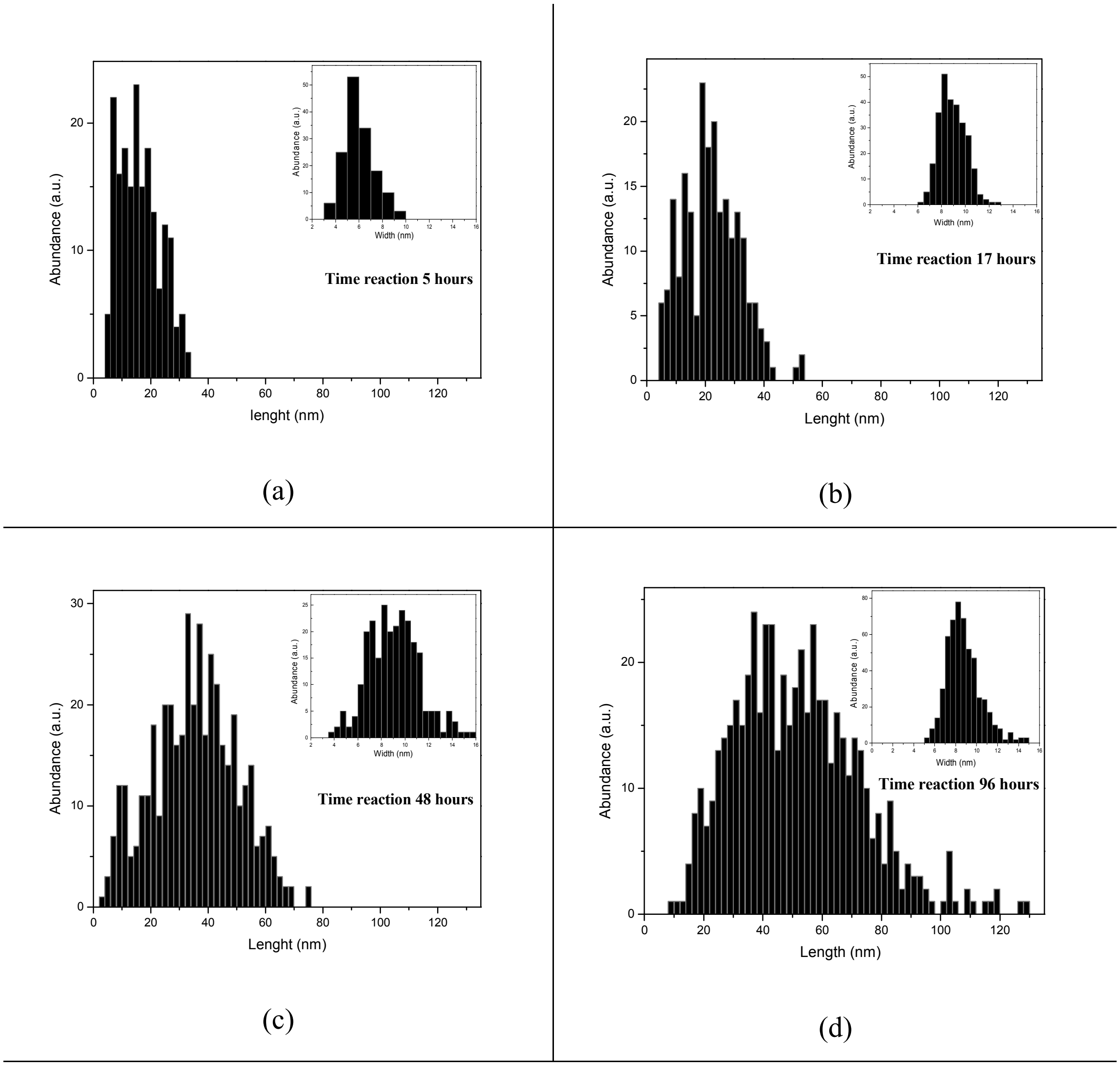

(a)

(b)

(c)

(d)

Figure 16. Size distribution of ZnO nanorods with KOH versus time reaction; Lengths versus time: (a) 5h, (b) 17h, (c) 48h and (d) 96h. Widths or diameters are presented in the insets.

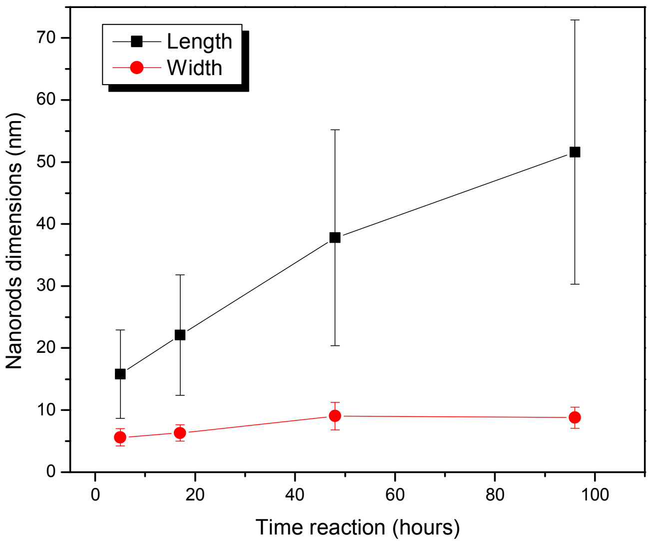

Figure 17. Length and diameter mean values of ZnO nanorods synthesized with KOH.

To summarize, we presented a detailed study of growth mechanisms of ZnO nanorods elaborated with KOH. The manufacturing process of these nanorods synthesized with KOH was initially described in its first stage by “Oswald ripening” growth, followed by a growth model based on a directed fusion and assembly coil-assembled “oriented attachment" in combination with the process of “Oswald ripening” growth mechanism being the maturation stage.

We were interested as well in the mechanism of formation of the nano-sticks of ZnO when using the NaOH base solution with an aim of obtaining them in a more homogeneous structure. Hence, a detailed study of the elaboration of ZnO by employing the NaOH at different time stages is exposed subsequently.

### 3.2.2.3 Detailed study of NaOH-based synthesized ZnO

Nanoparticules of ZnO with NaOH of an average size of few nanometers were obtained after 2 h 15 minutes after injection of the synthesis reactants. Figure 18-a gives a general picture of nearly spherical shaped ZnO nanoparticles. As a result of their small size, these nanoparticles are barely distinguishable due to their relatively insufficient contrast with the carbon film. HRTEM enlargement of one of these ZnO nanoparticles is shown in figure 18-b, showing highly crystallized structure seen in the [010] direction as revealed by the FFT images (see the inset).

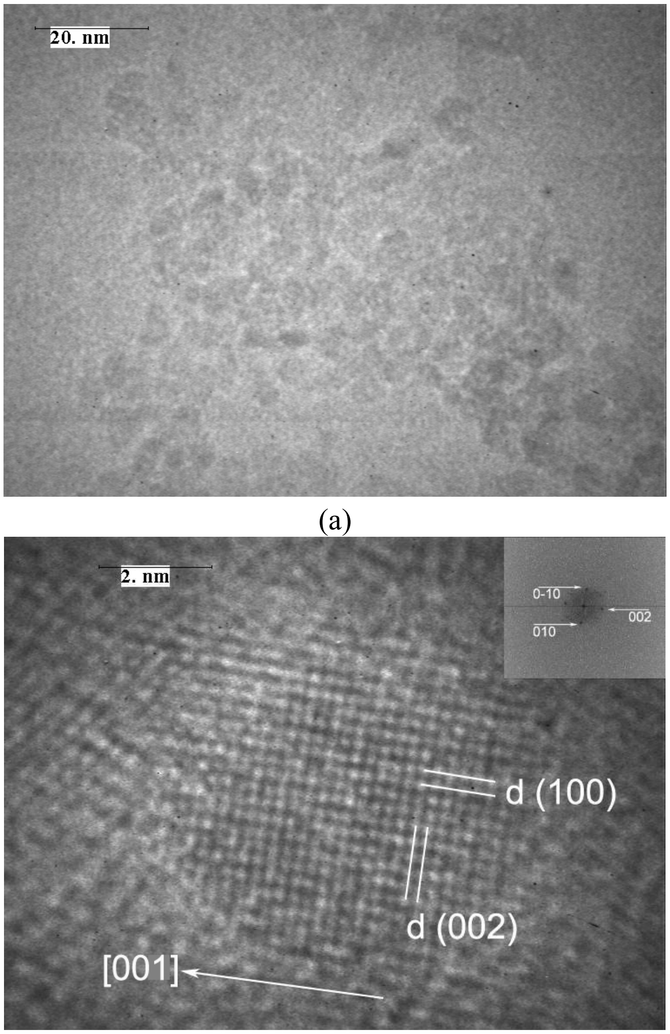

(a)

(b)

Figure 18. a- Overview of nearly spherical shaped ZnO nanoparticles with NaOH right after the first 2h 15m and just before condensation
b- HRTEM magnification of a very small ZnO particle showing highly crystallized species

Relatively bigger ZnO particles, observed in the TEM image in figure 19-a, are formed during the second step, that is the concentration step. Bigger ZnO nanoparticles are formed from the primary clusters when reaching the supersaturation state during forced concentration. So as to understand the growth mechanisms that stand behind the formation of these nanoparticles, we need to inspect the High Resolution TEM images, shown in figures 19-b and -c. the HRTEM images show highly crystalline ZnO nanoparticles seen in their [010] direction, and where the sketched c axes are parallel to the observational plan. The high crytallinity might be interpreted by the growth through Ostwald ripening mechanism [10]. Though it is clearly visible that epitaxial attachment ("oriented attachment) starts to occur along the c axis and at the lateral sides as seen in figure 19-b and figure 19-c, respectively. Epitaxial coarsening among these secondary particles may likely to take place at the final stages of the concentration step.

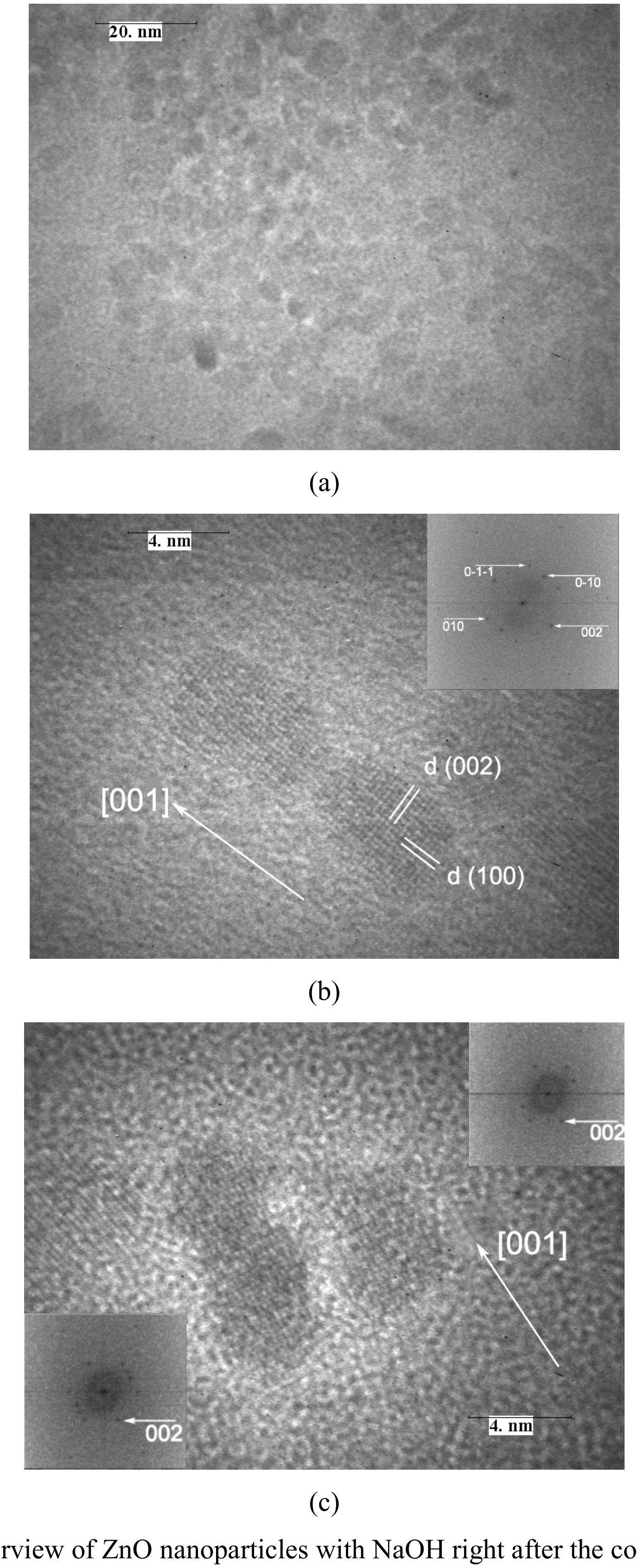

Figure 19. a- Overview of ZnO nanoparticles with NaOH right after the condensation
b-c- HRTEM of highly crystallized ZnO particles showing fusion mechanism, the inset figure is the FFT showing its crystal orientation seen in the [010] direction

Right after the condensation step, comes the final step where the colloid solution was heated under continuous stirring and 60 °C, for different lengths of synthesis time. One hour of time reaction leads to the formation of ZnO nanoparticles of different shapes (droplike, rodlike, pyramidlike), however the dominate shapes are the triangular or pyramid ones, see figure 20-a. Figure 20-b shows a perfectly crystallized ZnO nanoparticle of triangular shape in projection and whose lattice planes are exposed. The planes that shaped the very pointed edge are the (011) and (01-1) planes limiting the pyramidal shape at the end, whereas the planar base is the (002) face whose width measures statistically around 15 nm. This perfect compact single-crystalline pyramid is likely to be constructed through Ostwald ripening growth means.

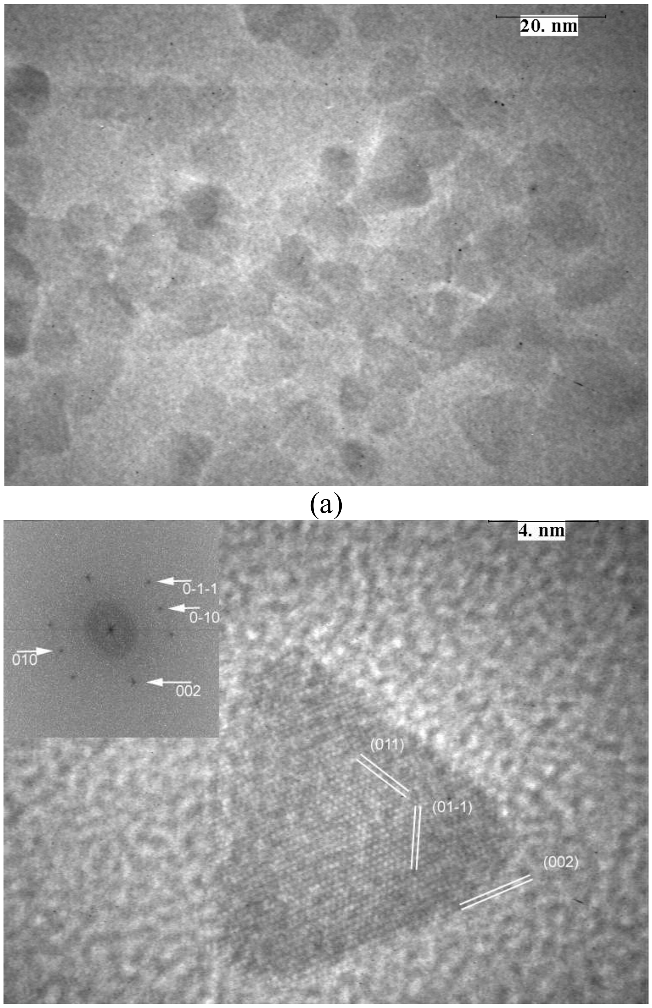

(a)

(b)

Figure 20. a- Overview of ZnO nanoparticles with NaOH at 1 hour of time reaction
b- HRTEM image of a highly crystallized triangular shaped ZnO particle, the inset figure is the FFT showing its crystal electron diffraction seen in the [010] direction.

Five hours after condensation, the ZnO particles growth mainly along the c axis results in the formation of 1-dimentional rods, see figure 21-a. The observed lattice planes in figure 21-b are the (002), the (100) and the (011) whose FFT diffraction is portrayed in the inset. Little imperfections are found at the lateral surfaces, with one pointed edge and other flat edge. So we can assume that the nanorods developed from the pyramidal shapes by growth along the longitudinal c axis. However, the primary nanopyramids observed after one hour had the basal side of about 15 nm, but after 5 hours the nanorods are found to have 8 nm as average diameter. For that reason, dissolution of some laterally parts of a nanopyramids is almost certainly happening, thus creating nutrients in the intention to assist the Ostwald ripening growth process.

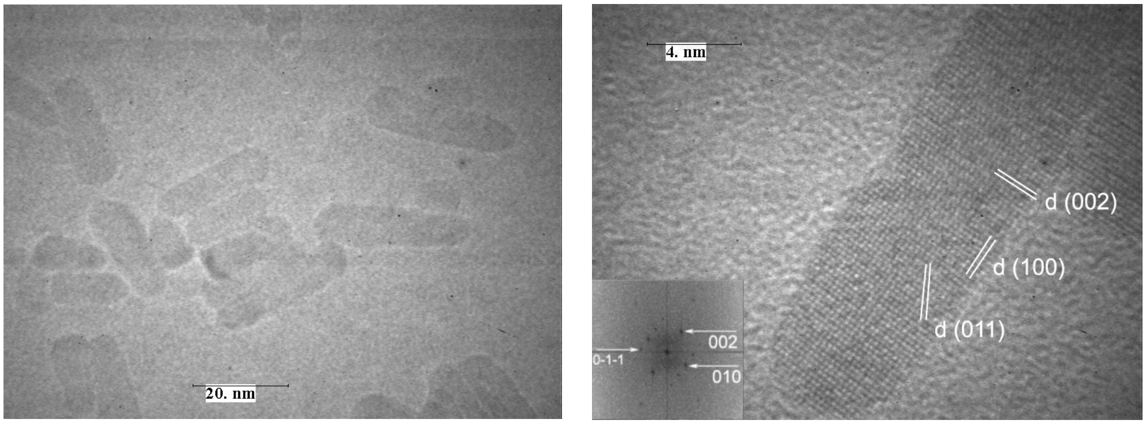

(a) (b)

Figure 21. a- Overview of ZnO nanoparticles with NaOH at 5 hours of time reaction
b- HRTEM of a highly crystallized ZnO particle with smooth surface. The inset figure is the FFT showing its crystal orientation

Increase in the time reaction to 17 hours implies further increment in the ZnO growth along its longitudinal c axis, see figures 22-a and -b. ZnO nanorods with well formed surfaces are fairly present. This homogeneous growth implies that the “Ostwald ripening” is the only responsible growth mechanism [6,12]. HRTEM image, depicted in figure 22-b, shows that homogeneous straight surfaces are practically well established.

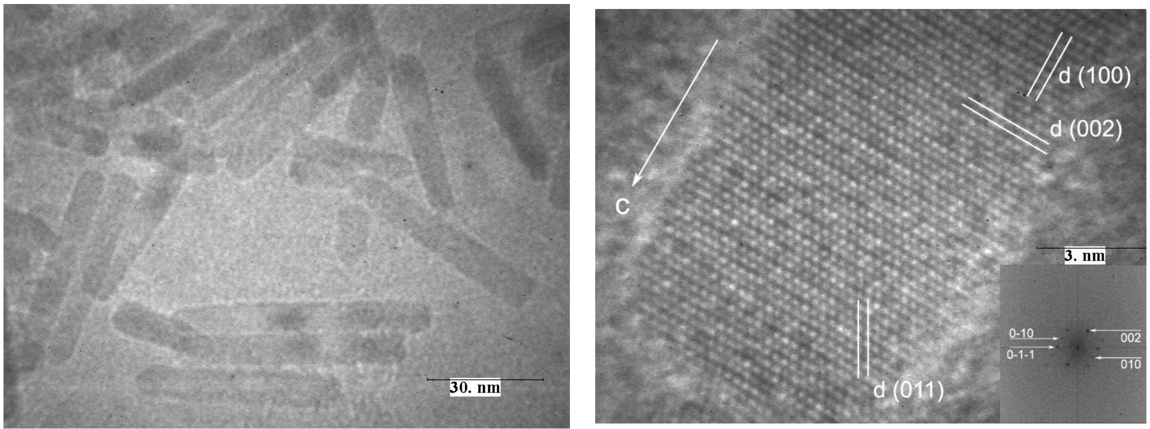

(a) (b)

Figure 22. a- Overview of ZnO nanoparticles with NaOH at 17 hours of time reaction
b- HRTEM of a well formed ZnO particle showing highly crystallized structure

Figures 23 refer to the ZnO nanorods formed after 48 hours of time reaction. Nicely homogeneous ZnO nanorods with very smooth lateral and edge surfaces are quite noticeable, see figures 23-a and -b. HRTEM magnification of a lateral side of a highly crystallized ZnO particle basically shows no defects, and demonstrates the high surface quality thanks to homogeneous "Ostwald ripening" growth.

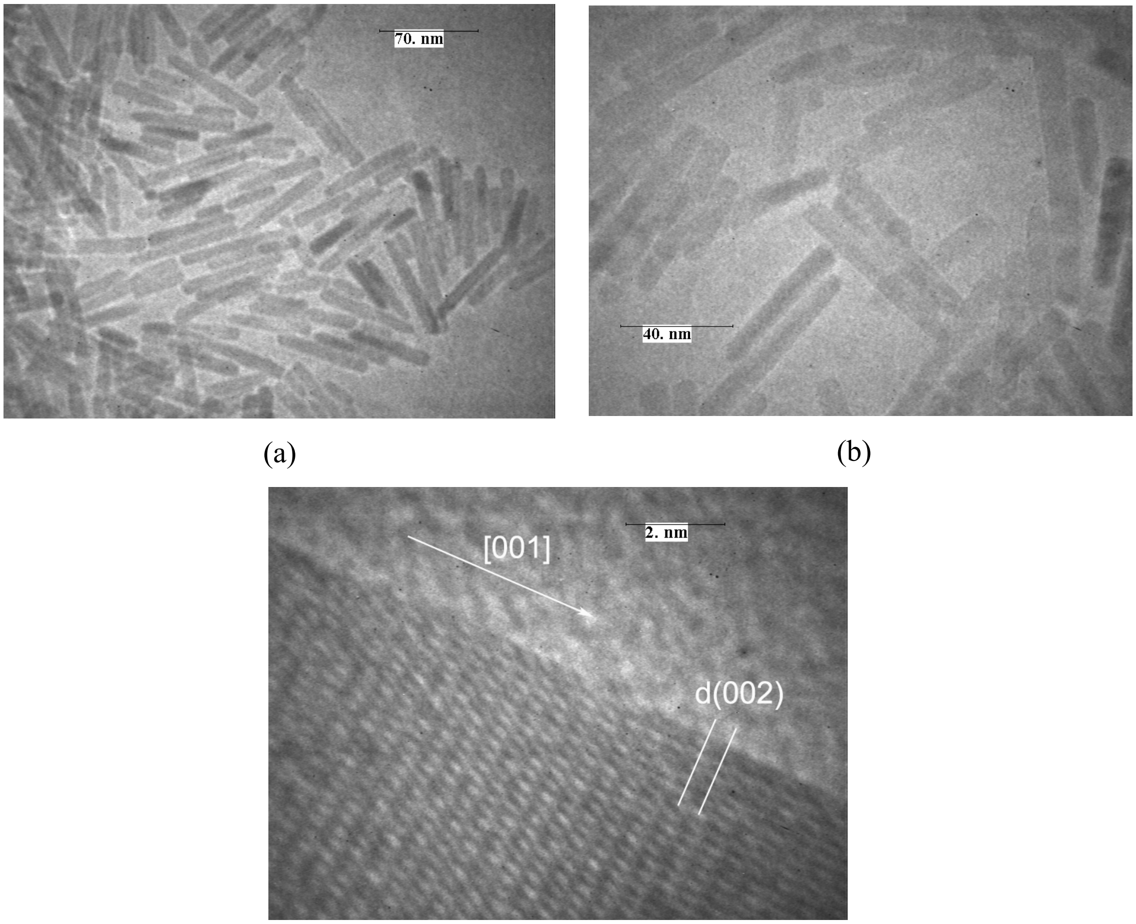

(a) (b)

(c)

Figure 23. a-b- Overview of ZnO nanoparticles with NaOH at 48 hours of time reaction
c- HRTEM magnification of ZnO particle with highly crystallized structure and very smooth surface.

Highly uniform and homogeneous ZnO nanorods synthesized after 96 hours are exposed in general outlook in the figures 24-a and -b. High Resolution TEM image in figure 24-c represents a sharply pointed edge of a ZnO nanorod terminated by pyramidal shaped end limited by the planes (011) and (01-1), as revealed by its FFT crystal electron diffraction seen in the [010] direction (refer to the inset).

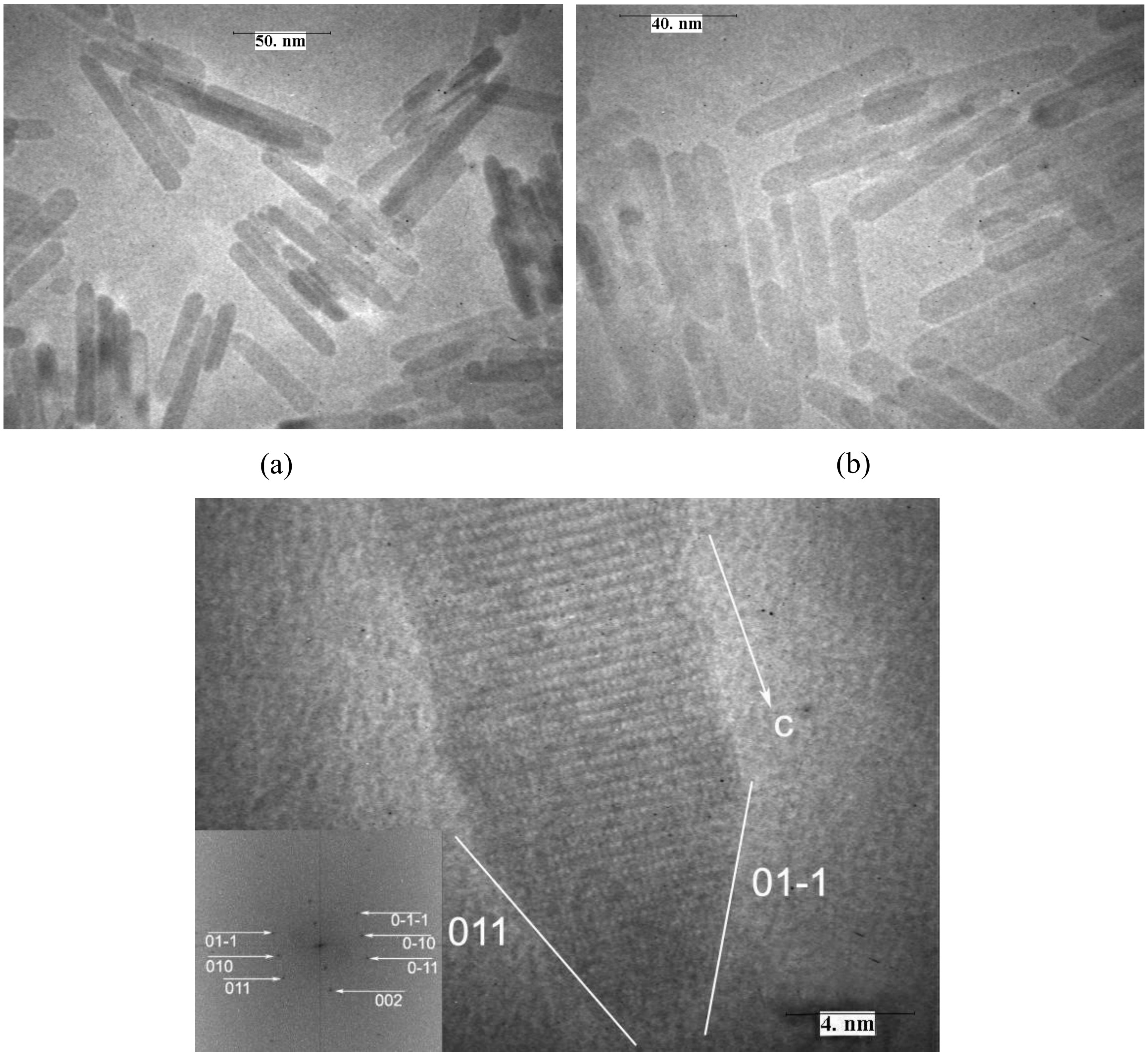

(a) (b)

(c)

Figure 24. a-b- Overview of ZnO nanoparticles with NaOH at 96 hours of time reaction
c- HRTEM magnification of a ZnO particle, the inset figure is the FFT showing its crystal orientation seen in the [010] direction: the nanorod's pointed edge is terminated by 6 planes, two of them (011) and (01-1)are parallel to the microscope electron beam.

We have seen that the ZnO (NaOH based) particle sizes, obtained by means of size distribution statistically driven from TEM images, present "symmetric" (increasing) length distributions that further widen when raising the ZnO synthesis time reaction. The mean widths increase as a function of time but with rather slim distribution histograms. This means that here laterally growth is not taking place as in the case of ZnO with KOH alkali solution, where additional smaller particles are epitaxially attached inducing broad width or diameter distributions. Indeed, we found that their width distributions are slighter than those of ZnO with KOH-base solution that remained asymmetric toward large widths as previously observed (insets of figure 16). On the other hand length and diameter increase uniformly faster for ZnO nanorods NaOH based synthesis (figure 25) than those with KOH based synthesis (figure 17). This supports the previously detailed idea, which states that in the case of NaOH the $Na^+$ is most likely interacting with $O^-$ present on the surface of the ZnO nanorods. These interactions will prevent the fusion between particles and consequently the formation of aggregated morphology and thus support the Ostwald ripening process. So the homogeneity in ZnO nanorods with NaOH-base synthesis is well established.

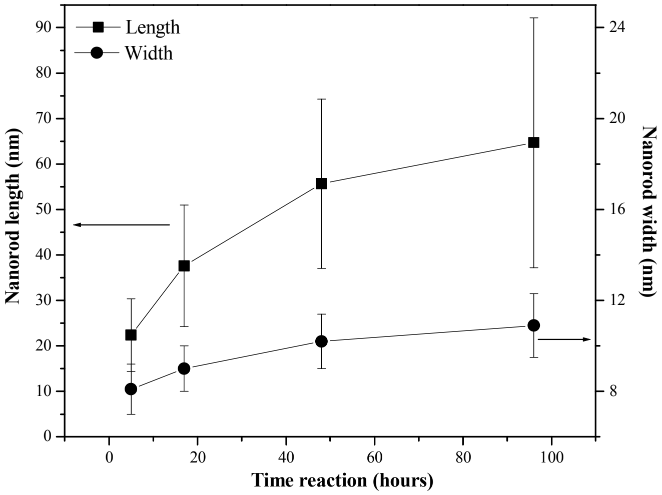

Figure 25. ZnO nanorods length and diameter mean values.

Detailed study of growth mechanism of ZnO nanorods elaborated with NaOH was hypothesized. The manufacturing process of these nanorods was basically described with the process of “Oswald ripening” growth mechanism, however small evidence of “oriented attachment" is present at the very primary stage of growth.

Summing up, we proposed a fundamental understanding of the nucleation and growth process, where the Oswald ripening mechanism is the main driving factor in the growth ZnO prepared with different alkaline systems. Additionally, epitaxial cluster aggregation known as oriented attachment is also present in some cases and under some conditions and can lead to complex-shaped larger single crystals.

On the other hand, the optical characterizations of the as-grown ZnO nanoparticles are accomplished with transmission and photoluminescence studies and presented in the subsequent section.

### 3.2.3 Optical properties of elaborated ZnO

These measurements are done on samples diluted in THF at $5.10^{-2}$ mg/mL. The reason that stands behind the choice of this colloidal concentration is to prevent, on one hand the quenching and diffusion of the excitation light source in higher concentrated solution, and on the other hand the insufficiency of material in lower concentrated solution. To validate this perspective, we relied on transmission and emission observations of KOH-based ZnO colloidal nanorods prepared after 48 hours, which are diluted into 9 different solutions.

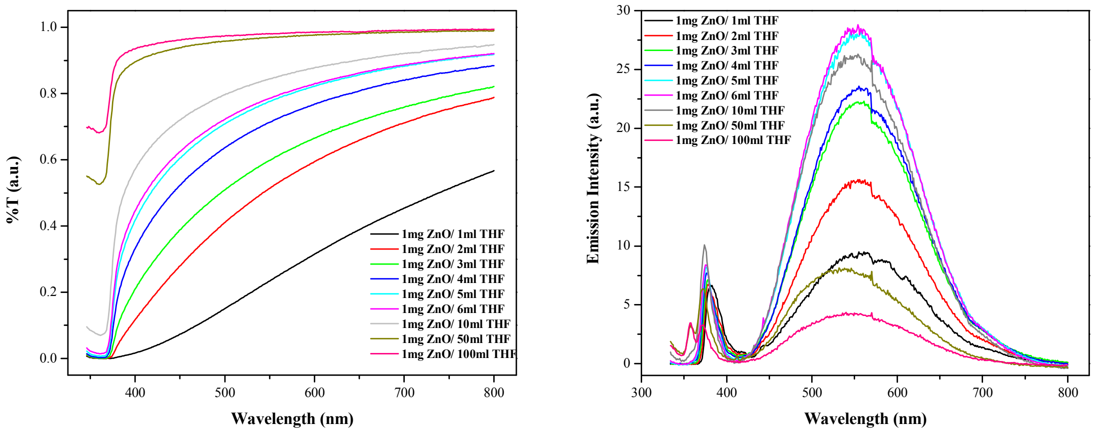

(a) (b)

Figure 26. (a) Transmission and (b) photoluminescence spectra of several KOH-based ZnO (synthesized after 48h) diluted solutions

| Sample's # | ZnO (mg) | THF (ml) | Coord. Exciton (E) | | Coord. Defects (D) | | Ratio (D)/(E) |
|---|---|---|---|---|---|---|---|
| | | | X (nm) | Y (int.) | X (nm) | Y (int.) | |
| 1 | 1 | 1 | 381 | 6.67 | 558 | 9.36 | 1.4 |
| 2 | 1 | 2 | 378 | 6.7 | 556 | 15.6 | 2.3 |
| 3 | 1 | 3 | 378 | 7.1 | 556 | 22 | 3.1 |
| 4 | 1 | 4 | 377 | 7.7 | 556 | 23 | 2.98 |
| 5 | 1 | 5 | 376 | 8.2 | 556 | 28 | 3.4 |
| 6 | 1 | 6 | 376 | 8.4 | 556 | 28 | 3.3 |
| 7 | 1 | 10 | 374 | 10.1 | 552 | 26.2 | 2.6 |
| 8 | 1 | 50 | 372 | 6.4 | 535 | 8 | 1.25 |
| 9 | 1 | 100 | 372 | 3.3 | 543 | 4.1 | 1.24 |

Table 1. ZnO dilution conditions and different aspect ratios of their defect to exciton emission intensities.

Transmission and photoluminescence spectra of the several ZnO (synthesized after 48h) diluted solutions, presented in figures 26-a and -b, reveal severe differences in their absorption and emission responses to the light source. Figure 26-a demonstrates that the absorption peak of the ZnO (at ~ 360 nm) of the sample "1" with the highest concentration is not discernable and very wide, in other word the absorption and scattering are huge, due to the highly concentrated species. This lowers the transmission at higher wavelengths and engenders the scattering among the highly packed colloidal particles. The ZnO absorption peak starts to properly appear and the effect of scattering decreases as soon as we dilute the samples. However, very dilute solution (sample "9") induces weak detection signals.

The photoluminescence spectra from the THF solution of ZnO nanorods (see figure 26-b), and whose data are depicted in table 1, consist of two emission bands at room temperature: a near-band-edge (UV) exciton emission at 372-381 nm, and a broad deep-level (visible) emission at 543-558 nm [20,21]. The overall shape of the visible emission is usually attributed to various intrinsic defects produced during preparation and post-treatment of ZnO [22,23]. This luminescence located around 550 nm originates likely from deep-level oxygen vacancies [24,25]. Aggregation among ZnO particles implies the occurrence of quasi-bulk optical response properties. Indeed, this aggregation provoked the emission at 381 nm (bulk emission) in the sample “1”. Actually, two effects can contribute to the observed decrease in intensity and red-shift in the exciton emission at higher concentrations: (1) interaction of charged defects at the surface of the aggregates leading to the formation of surface trapped exciton, and (2) the superposition of the photoluminescence emission of the dense colloidal solution with their transmission spectra which act as a filter. Therefore, to really get the correct measurements we need to dilute this sample, thus preventing the aggregation and promoting the presence of well dispersed single nanoparticles. This interpretation is confirmed through samples “8” and “9” having 372 nm as excition emission caused by the unique presence of well diffused ZnO nano-colloids. Emission intensities of both exciton and defects peaks are relatively quenched in the highly concentrated samples, “1” and “2”. This quenching, considered as the underestimation of the real emission, is attributed to the scattering and diffusion of the excitation light source along with the thus-emitted light among the highly crowded colloidal particles. Exciton and defects emission intensities increase by increasing the dilution, to decrease later at higher diluted solutions due to material deficiency, as in the case of sample “9”.

So we must find a compromise in the intention to avoid unreal effects contribution. That is why we chose a colloidal solution whose dilution 5.10$^{-2}$ mg/mL (1mg/20mL) is situated between the samples “7” and “8”.

Adopting this optimal concentration, we can now proceed by comparing the optical properties of ZnO nanospheres before concentration with respect to ZnO nanorods at 48h of time reaction. Both transmission and emission spectra from the THF solutions of the two different ZnO specimens reveal a Bleu shift of ZnO peak, see figures 27-a and -b. The spectra of the nanospheres are bleu shifted from those of the nanorods.

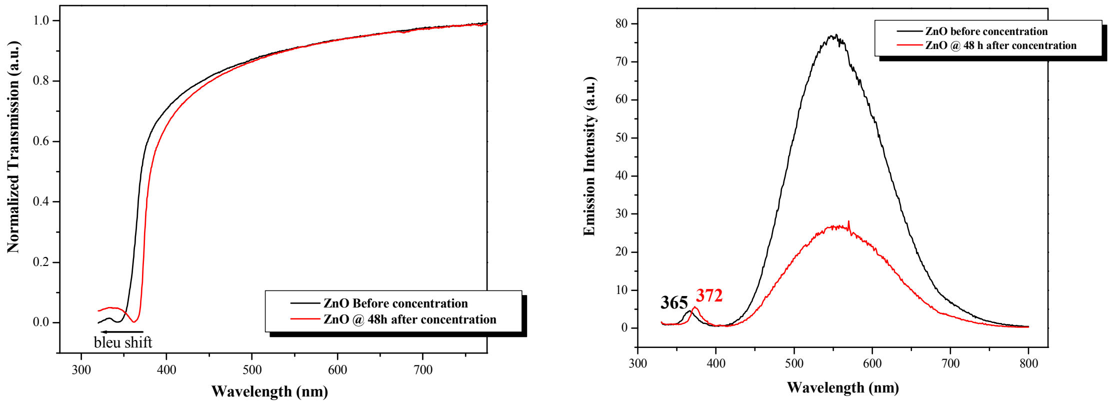

(a) (b)

Figure 27. Bleu shift of ZnO peak in (a) Transmission and (b) Emission spectra of ZnO before concentration with respect to ZnO at 48h of time reaction after concentration

For a direct band gap semiconductor, the construction of a *Tauc Plot* $(Ah\nu)^2$ versus $h\nu$ allows the estimation of the band gap. Tauc plot are given by the following equation [26]:

$$\alpha = \frac{C\left(h\nu - E_g\right)^{1/2}}{h\nu} \tag{3-1}$$

where $\alpha$ is the absorption coefficient, C is a constant, $h\nu$ is the photon energy, and $E_g$ is the bulk band gap. Figure 28 shows the Absorbance spectrum of the ZnO nanoparticles (just before condensation). The inset of figure 28 depicts the corresponding plot of $(Ah\nu)^2$, "A" being the Absorbance proportional to $\alpha$ (see Appendix III), versus the photon energy $h\nu$. Extrapolation of the linear region to the photon energy axis yields the band gap of 3.44 eV. And since a size dependent blue shift is present, as already mentioned, this implies that these ZnO nanospheres, obtained just before condensation, are subjected to quantum size effects. The relationship between the band gap energy and the size of the particles, as derived in the equation (1-19) of the Chapter 1, is given by:

$$E_g^* = E_g + \frac{h^2}{8\mu R^2} - \frac{1.8e^2}{4\pi\varepsilon_0\varepsilon_\infty R} \tag{3-2}$$

where, $E_g$ is the bulk band gap of the semiconductor material, $\mu$ the effective mass, $R$ the size of the particle, $\varepsilon_0$ is the vacuum permittivity and $\varepsilon_\infty$ the relative permittivity. So for a band gap of 3.44 eV, the average size of the ZnO particles is about 5.6 nm.

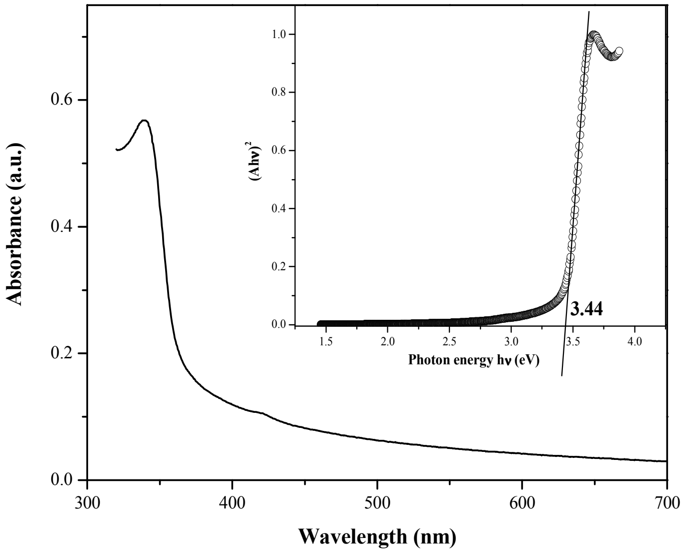

Figure 28. Absorption spectrum of the KOH-based ZnO nanoparticles (just before condensation). The inset depicts the corresponding plot of $(Ah\nu)^2$ versus the photon energy.

To describe changes in the electronic properties all along the growth process stages, a qualitative Molecular Orbital model can be suggested [5], which is expressed as well via band gap variations determined by the quantum confinement size effect as drown in figure 29, and as already explained in chapter I. Primary clusters, which are produced during the first 2 hours 15 minutes preceding condensation, have the largest band gap "$E_{g1}$" ($a_0 \rightarrow a_1$ transition) and a low density of electronic states. As they start to combine after condensation at the early growth stages, bond formations occur due to molecular orbital overlap generating a new smaller band gap "$E_{g2}$"; designed as $b_0 \rightarrow b_1$ transition. Consequently, the density of electronic states of the newly produced levels increases if compared to their composite clusters; this screens the $a_0 \rightarrow a_1$ transition in the primary cluster. During the final crystal growth stages, development of strong chemical bonds is likely to happen in the well developed lattices of the ZnO nanorods, producing an energy band gap "$E_{g3}$" ($c_0 \rightarrow c_1$ transition), which will hide the transition at higher energies of smaller particles.

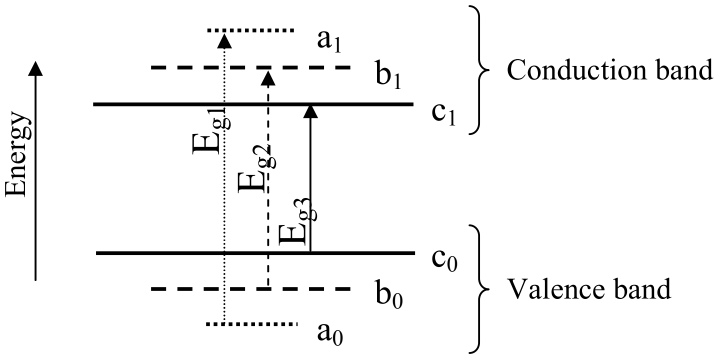

Figure 29. Molecular orbital band diagram model for the ZnO growth at different stages.

Another feature caused by size effect appears in the photoluminescence spectra in figure 27-b. The intensity of defects in the large visible band decreases when going from ZnO nanospheres prepared just before condensation to ZnO nanorods after 48 hours. In bigger particles, smaller amount of defects can be found because of the high lattice order in the ZnO crystals. Thus, leading to think that these defects originate from the particle surface; small particles with larger surfaces incorporate higher amount of defects.

Optical measurements performed on NaOH-based ZnO resemble to some extent to those of KOH-based ZnO if we are to compare between nanospheres and nanorods obtained at different stages of time reaction. We can find in both cases the effect of the quantum confinement at small sized particles that is just being explained for the KOH-based ZnO. But with a difference in the oxygen vacancy defects emission that is found in NaOH-based ZnO to be less than that of KOH-based ZnO as it was already seen by TEM images through the nearly defectless surfaces in the NaOH-based ZnO.

## 3.3 Conclusion

We reported, through this chapter, the synthesis and especially the detailed investigations on morphological and optical properties of the ZnO synthesized via chemical ways. We studied in great details the growth mechanisms of ZnO nanorods elaborated with KOH and NaOH base solutions, at different time stages of the synthesis reaction.

● We found that the growth of nanorods synthesized with KOH is described in its first stage by “Oswald ripening” growth, followed by a growth model based on a directed fusion and assembly “oriented attachment" in combination with the process of “Oswald ripening” growth mechanism being the maturation stage. This explains the formation of ZnO nanorods with bumpy surfaces.

● Nanorods synthesized with NaOH were basically formed by means of the process of “Oswald ripening” growth mechanism, however small evidence of “oriented attachment" is present at the very primary stage of growth. This fact clarifies the formation of nanorods with smooth surfaces.

● Through Optical measurements of both KOH and NaOH-based ZnO nanparticles, we found the effect of the quantum confinement at small sized spherical-shaped ZnO particles. Yet, all of the NaOH-based ZnO particles showed small degree of oxygen vacancy defects incorporation with respect to the KOH-based ZnO, as it was already confirmed by TEM images through the nearly defectless surfaces in the NaOH-based ZnO.

Done with the studies of the as-prepared ZnO nanorods, we can now proceed to the next chapter where we subjected the ZnO to grafting different kinds of dye molecules, thus enabling them to be introduced in different applications, namely in designing the solar cells.

# Bibliography

[1] W. J. E. Beek, M. M. Wienk, and R. A. J. Janssen, Adv. Mater. 16 (2004) 1009

[2] B. Sun, and H. Sirringhaus, Nano Letters 5, (2005) 2408

[3] C. Pacholski, A. Kornowski, H. Weller, Angew. Chem. Int. Ed., 41 (2002) 1188

[4] B. Sun, and H. Sirringhaus, Nano Lett., 5 (2005) 2408

[5] L. Spanhel, And M. A. Anderson,. J. Am. Chem. Soc., vol 113 (1991) 2826

[6] E. A. Meulenkamp. J.Phys. Chem. B., vol 102 (1998) 5566

[7] Z. Hu, J. F. Herrera Santos, G. Oskam, and P. Searson, Journal of colloid and Interface Science., vol 288 (2005) 313

[8] L. N. Dem'yanets, D. V. Kostomarov, I. P. Kuz'mina, Inorg. Mater., 38 (2002) 124

[9] L. N. Demianets, D. V. Kostomarov, I. P. Kuz'mina, and S. V. Pushko, Crystallography Reports, vol 4738 (2002) S86

[10] H. L. Cao, X. F. Qian, Q. Gong, W. M. Du, X. D. Ma, Z. K. Zhu, Nanotechnology, 17 (2006) 3632

[11] Naofumi Uekawa, Ryo Yamashita, Yong Jun Wu and Kazayuki Kakegawa. Phys. Chem. Chem. Phys., vol 6 (2004) 442

[12] B. Liu, and H. C. Zeng, Langmuir, 20 (2004) 4196

[13] W. J. Li, E. W. Shi, W. Z. Zhong, and Z. W. Yin, J. Cryst. Growth , vol 203 (1999) 186

[14] L. N. Dem'yanets, L. E. Li, and T. G. Uvarova, J. Mater Sci, 41 (2006) 1439

[15] B. Gates, Y. D. Yin, and Y. N. Xia, J. Am. Chem. Soc., 122 (2000) 12582

[16] B. Mayers, B. Gates, Y. D. Yin, and Y. N. Xia, Adv. Mater., 13 (2001) 1380

[17] Y. N. Xia, P. D. Yang, Y. G. Sun, Y. Y. Wu, B. Mayers, B. Gates, Y. D. Yin, F. Kim, and H. Q. Yan, Adv. Mater., 15 (2003) 353

[18] B. Cheng, and E. T. Samulski, Chem. Commun. (2004) 986

[19] M. S. Tokumoto, S. H. Pulcinelli, C. V. Santilli, and V. Briois, J.Phys. Chem. B., vol 107 (2003) 568

[20] V. A. Fonoberov, and A. A. Balandin, Appl. Phys. Lett., vol 85 (2004) 5971

[21] J. M. Lim, K. C. Shin, H. W. Kim, and C. M. Lee, J. Lumi., vol 109 (2004) 181

[22] N. E. Hsu, W. K. Hung, and Y. F. Chen, Appl. Phys., vol 96 (2004) 4671

[23] D. Li, Y. H. Leung, A. B. Djurisic, Z. T. Liu, M. H. Xie, S. L. Shi, S.J. Xu, and W. K. Chan, Appl. Phys. Lett., vol 85 (2004) 1601

[24] M. Liu, A. H. Kitai, and P. J. Mascher, Lumi., vol 54 (1992) 35

[25] L. E. Greene, M. Law, J. Goldberger, F. Kim, J. Johnson, Y. Zhang, R. J. Saykally, and P. Yang, Angew. Chem. Int. Ed., vol 42 (2003) 3031

[26] M. Dare-Edwards, J. B. Goodenough, A. Hamnett, and P. Trevellick, Chem. Soc., Faraday Trans, vol 79 (1979) 2027

# Chapter 4

# Optical and morphological properties of nanohybrids based on dye functionalized-ZnO nanoparticles fabricated by Chemical processes

## 4.1 Introduction

The ZnO nanopatricles, emanating from the low cost fabrication chemical technique presented in the previous chapter, show limited photoactivity under UV-visible irradiation. Thus binding of photoactive chromophores onto ZnO nanoparticles' surface endows the organic-inorganic hybrid nanoassemblies with light-harvesting and flexible optoelectronic properties as demonstrated for functionalized gold nanoparticles [1,2]. This strategy could also lead to photosensitization effects resulting in a strong improvement in solar cell performance. The choice of the dye type should respond to several constraints as for example its electron affinity with respect to the other solar cell active components. Two types of dye molecules were selected; namely, "Porphyrin" and "Ruthenium-containing" sensitizing dyes. Porphyrin dyes with carboxylic acid anchoring groups constituted the core of several researches in building novel solar cells [3-20] as well as the "Ruthenium-containing" dyes that are now successfully applied in nanocrystalline TiO2 semiconductor (SC)-based Dye-Synthesized Solar Cells [21,22]. Though, very few studies on ZnO-based Dye-Synthesized Solar Cells incorporating the above mentioned dye families are reported [23-26], that is why working to boost the studies in this field is our present main interest.

In this chapter, we report on a new type of hybrid nanoparticles based on a semiconducting ZnO nanoparticles grafted with different types of dye molecules that are functionalized by carboxylic acid functions. Hence, two different porphyrin molecules were selected, namely the H2TCPP and the PP9. These abbreviate nominations are adopted for simplicity to designate the 4,4',4'',4'''-(Porphine-5,10,15,20-tetrayl) tetrakis (benzoicacid) and the protopophyrin IX, respectively. On the other hand, new Ruthenium-containing sensitizing dyes with enhanced optical absorption in the visible The Z907 is the third dye molecule to be tested. Z907 is the briefing of Ruthenium 520-DN with the chemical name: *cis*-bisisothiocyanato)(2,2'-bipyridyl-4,4'-dicarboxylato)(2,2'-bipyridyl-4,4'-di-nonyl) uthenium(II). Figure 1 exhibits the molecular structure of our three chosen dyes; H2TCPP, PP9 and Z907.

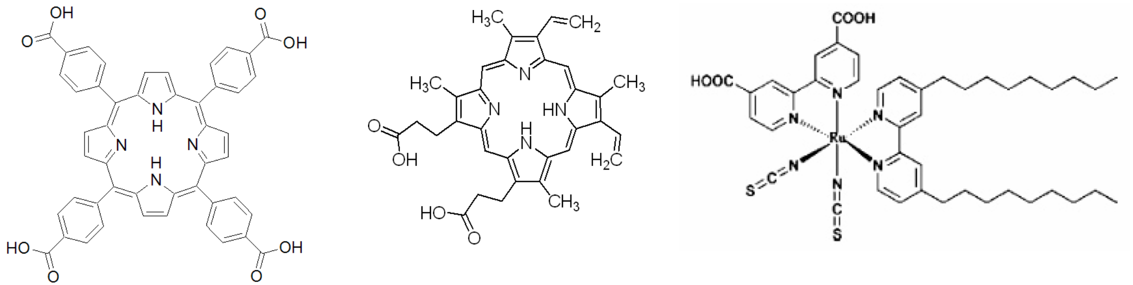
H2TCPP PP9 Z907

Figure 1. Molecular structure of H2TCPP, PP9 and Z907 dyes.

Selection of these sensitizer dyes responds to several conditions, some of which are:

1. Dye's absorption spectrum should show overlap with the solar spectrum as much as possible.
2. It must carry attachment groups such as carboxylate to firmly graft it to the semiconductor oxide surface.
3. The energy level of the dye's excited state should be at higher level with respect to the lower band edge of the conduction band of the oxide.
4. Upon excitation it should inject electrons into the conduction band of the oxide.

Figure 2 illustrates the energy diagram of each one of the dyes in comparison to that of ZnO. Conduction band (CB) and valence band (VB) of ZnO are shown, as well as the Lowest Unoccupied Molecular Orbital (LUMO) and Highest Occupied Molecular Orbital (HOMO) of the H2TCPP and the Z907. The energy levels of the PP9 are missing because we found "no" reliable values of its LUMO and HOMO levels in the literature data-base.

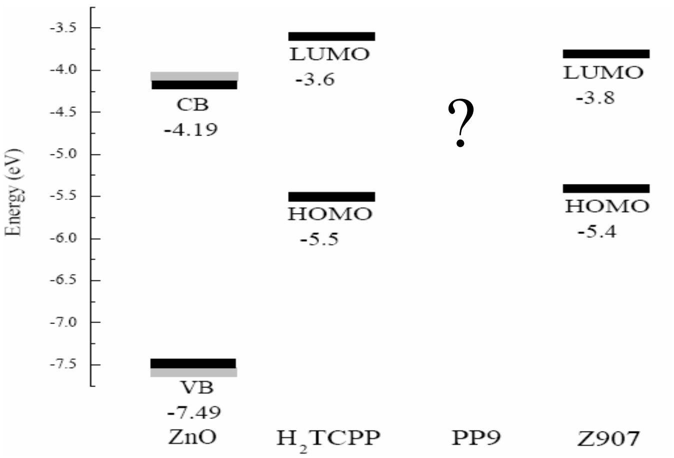

Figure 2. Energy levels of (a) ZnO, (b) H2TCPP, (c) PP9 and (d) Z907.

However, the choice of the two porphyrins relies on another important parameter that will influence the charge exchange with the ZnO nanoparticles. This parameter designates the degree of overlapping among the absorption spectral band of the porphyrin and the exciton emission band of the ZnO. The degree of this overlap will define the amount and the efficiency of energy transfer from the ZnO to the dye via the Förster mechanism, as explained earlier in the introduction of Chapter 2. For instance, we can see, through the figures 3-a and -b, the amount of overlapping between the exciton emission of the ZnO [nanospheres (*Black plot*) and nanorods (*Red plot*)] with the Soret band absorbance (*Blue plot*) of the H2TCPP and the PP9, respectively. Intensities of both emissions and absorbance are normalized for better comparison. For both dyes, we can notice that their overlaps with the exciton emission of the ZnO nanorods are bigger than those with the ZnO nanospheres. We assure this reality because of the exciton being blue-shifted for the ZnO nanospheres with respect to the nanorods, due to confinement effects related to the small-sized ZnO nanospheres. Hence, with both dyes, we suppose that the energy transfer in the nanorod-based hybrids is slightly more favored than in the nanospheres-based hybrids.

Moreover, we can clearly see, in figure 3-a and -b, that the overlap of the ZnO exciton emission with the PP9 Soret band absorbance is much larger than that with the H2TCPP case. This statement will guarantee that the energy transfer via Förster model is much more developed in the hybrids based on the PP9 dye-grafting. Yet, in the case of H2TCPP, this energy transfer exists but with modest efficiencies.

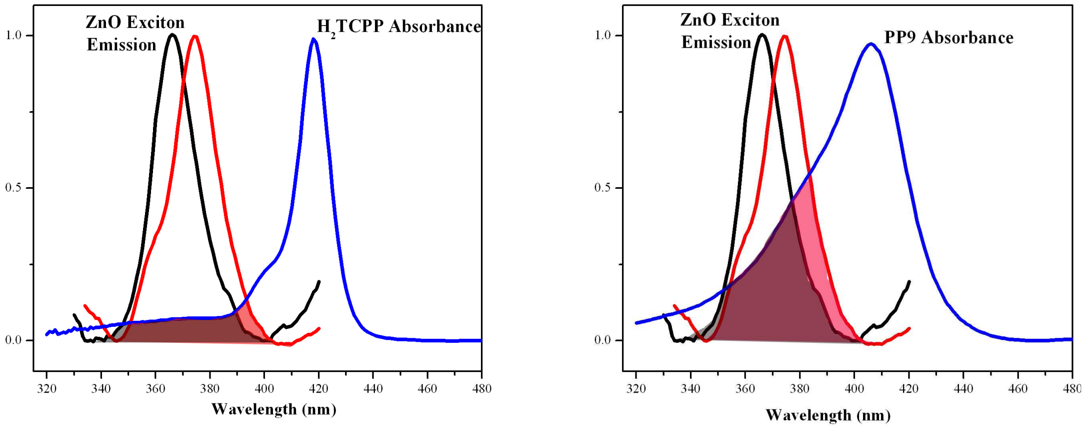

(a) (b)

Figure 3. Normalized spectra showing the degree of overlapping between the exciton emission of the ZnO [nanospheres (*Black plot*) and nanorods (*Red plot*)] with the Soret band absorbance (*Blue plot*) of (a) the H2TCPP and (b) the PP9.

Below, we start by stating the experimental grafting processes followed by detailed investigations of porphyrin dye grafting results, which are exposed by presenting the optical data outcomes to show and discuss the grafting evidence and the thus-derived properties, based on the variation of ZnO shape and size on the one hand and the dye concentrations on the other hand. It is worth noting that we studied extensively and in great details the properties of the hybrids based on the H2TCPP dyes, while only the very important briefed studies of the hybrids when grafting the PP9 are given, but the studies concerning the Z907 will be briefed in the Appendix VII. First we will look at the morphological studies done by HRTEM to give a global vision of the ZnO nano-spheres and -rods morphologies after being grafted with our famous dyes.

## 4.2 Experimental

Experimental wise, all the porphyrin-based nanohybrids that we created are produced by adsorbing overnight the above-mentioned dyes H2TCPP and PP9 on the KOH-based ZnO surface in the tetrahydrofuran solvent (THF) at different dye concentrations. Both dyes were purchased from Sigma-Aldrich and used without further purification. Molecules of both porphyrin dyes were grafted onto two series of ZnO nanoparticles: (i) the very small quasi-nanospheres of ZnO, obtained right after the 2 hours and 15 minutes that is just prior to the condensation step, and (ii) the rod-like ZnO achieved after 48 hours following the condensation step.

Each sample is a combination of a certain volume of ZnO nanoparticles (or rods) in suspension in THF at a concentration of $1.10^{-3}$ g/ml with the same volume of a dye solution at different concentrations; i.e. $2.10^{-6}$; $1.10^{-5}$; $1,5.10^{-5}$; $2.10^{-5}$; $6.10^{-5}$; $1,2.10^{-4}$; $2.10^{-4}$; $3.10^{-4}$; and $2.10^{-3}$ mol/L. The mother samples emanating from these mixing conditions are labeled as “concentrated” samples. But because of optical measurement constraints due to the high material concentration, each sample was diluted 10 times with THF, which leads to the “diluted” sample series. Nevertheless, and in order to obtain clean samples, the concentrated samples were centrifuged at 40 RPM (round per minute) twice for 5 minutes each. Indeed, clean sample is a sample containing only the dye-grafted ZnO and where the excess in non-grafted dye molecules is being eliminated through centrifugation. The centrifuged species were collected from the bottom of the centrifugation tube and then dissolved in the same THF volume as its corresponding concentrated sample; accordingly, we obtain the “centrifuged” sample series. These centrifuged samples are diluted 10 times in THF, representing the “centrifuged diluted” samples. The “diluted” and the “centrifuged diluted” nanohybrid samples are subjected to morphological and optical measurement studies to analyze grafting conditions and consequences. It is worth mentioning that the pure dyes solutions were as well diluted 10 times in order to constitute the references when comparing with their corresponding hybrids.

The samples’ treatment by centrifugation applies only in the case of porphyrin and not in the case of Z907 (purchased from Solaronix). This is attributed to the higher solubility of Z907 which renders impossible the centrifugation process. Following the same grafting process, the Z907 was grafted onto the ZnO at the concentrations: $0,5.10^{-4}$; $1,5.10^{-4}$; and $2,5.10^{-4}$ mol/L. Nevertheless, studies were performed on the emanating diluted Z907-based hybrids where the ZnO nanorods templates used were those fabricated by means of the NaOH base, after 48 hours of time synthesis.

Under these conditions, UV-Vis absorption spectra were taken by a Varian CARY 50 spectrophotometer, while photoluminescence spectra were recorded with a CARY Eclipse spectrophotometer (see Appendix III). In both cases we used a 1 cm path length quartz cell. Morphological studies were carried out by JEOL (300 kV) the High resolution transmission electron microscope (HRTEM), where samples are prepared by drop casting of “diluted” solutions on the mesh-coated carbon film.

## 4.3 Morphological studies of the hybrids

Our HRTEM observations show that, grafting the surface of the small ZnO nanoparticles (obtained 2 hours and 15 minutes just before condensation) with both H2TCPP and PP9 molecules leads to no change in the ZnO morphology. Before and after grafting, we can find quasi-spherical shaped ZnO, of about 5 nm in size, having high crystalline structures, as we can see in figure 4 (for H2TCPP) where each particle is delimited by a rectangle for clearness. Here, the small size of ZnO particles renders difficult the TEM observational statistics.

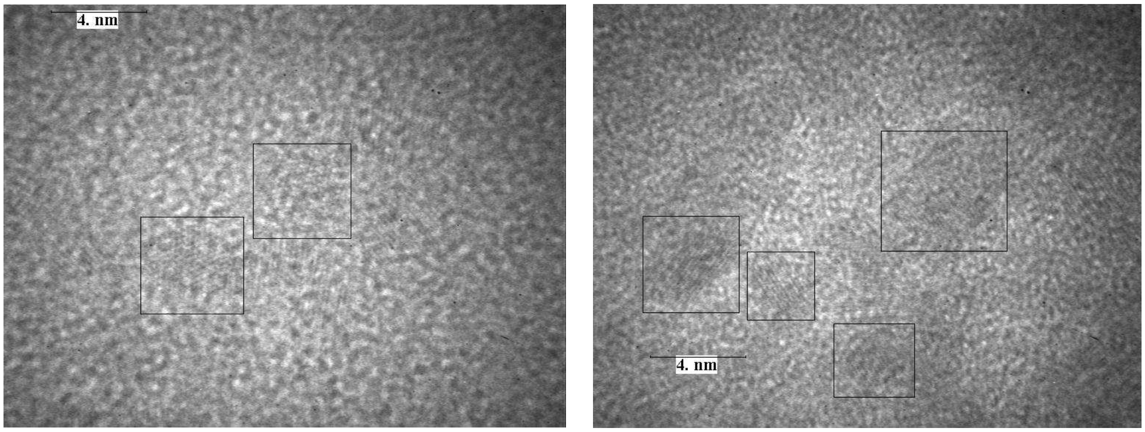

(a) (b)

Figure 4. HRTEM of the ZnO nanospheres (a) before and (b) after H2TCPP dye grafting.

On the other hand, grafting the surface of the ZnO nanorods with both H2TCPP and PP9 molecules reveals highly crystalline ZnO nanorods, as seen for example in figure 5-b (for H2TCPP). Looking at the organization of the nanorods on the graphite grid shown in figure 5-a and -c, we can find some vertical oriented clusters in the case of $H_2$TCPP-ZnO nanorods as compared to pristine ZnO nanorods. This effect is even visible even for low dye coverage. The origin of the vertical orientation is believed to stem from the presence of dye molecules that promote self-assembly via: (i) establishment of hydrogen bonded networks involving the carboxylic acid groups or (ii) strong interaction between the porphyrin rings (if the dye is flat at the surface of ZnO). While in the case of PP9 grafting, modest existence of vertical oriented ZnO nanorods clusters is detected, indicating that interactions among grafted-dyes on two adjacent ZnO rods are higher for H2TCPP than for PP9. In the case of the Z907, we found that the ZnO nanorods tend to form well aligned networks of parallel adjacent rods lying along the carbon grid.

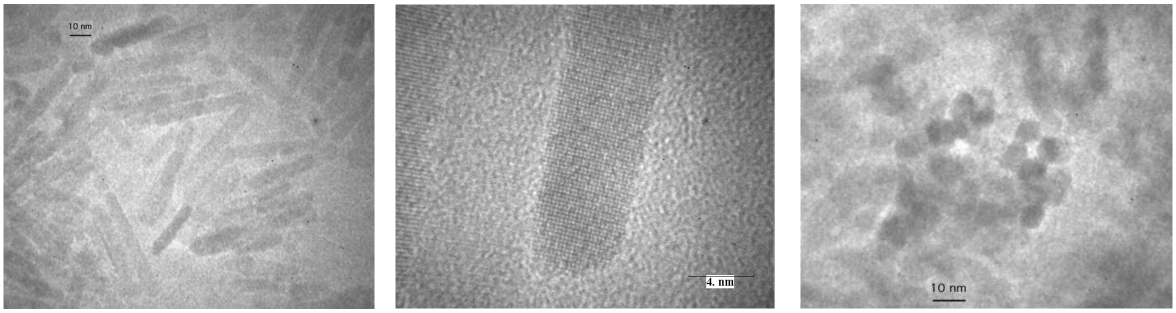

(a) (b) (c)

Figure 5. HRTEM of the ZnO nanorods (a) before and (b,c) after H2TCPP dye grafting.

Hence, we can conclude that the ZnO morphology via HRTEM observations was not affected by the adsorbed dyes. Whereas, some preferential orientations among the nanorod-hybrids could take place as a consequence of the interaction that is established between two close ZnO particles through grafted-dyes.

## 4.4 $H_2$TCPP-ZnO hybrids

### 4.4.1 Optical properties of pure $H_2$TCPP solutions along with their aggregation approach

H2TCPP molecule structure, sketched in figure 6, reveals a molecule functionalized by four carboxylic acid functions. Figure 7-a shows the first ($S_1$) and second ($S_2$) singlet excited states of H2TCPP. While figure 7-b depicts its optical, namely absorbance and fluorescence spectra. Absorbance spectrum of this porphyrin is characterized by the intense near-UV Soret-band absorption (transition $S_0 \rightarrow S_2$) in the blue end of the visible region peaked at 418 nm with a slight shoulder at higher energy 381 nm, and by four Q-bands (transition $S_0 \rightarrow S_1$) located in the visible spectral region of 500-650 nm. Two intense emission peaks emanating via S1(S0 relaxation (from photoexcited or internal conversed charges) are positioned at 651 and 716 nm for an excitation wavelength of 420 nm.

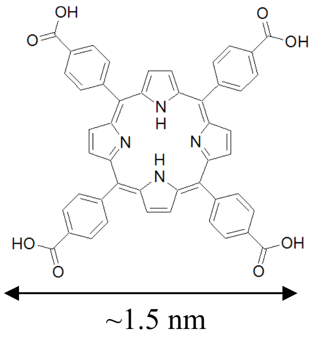

Figure 6. H2TCPP molecular structure.

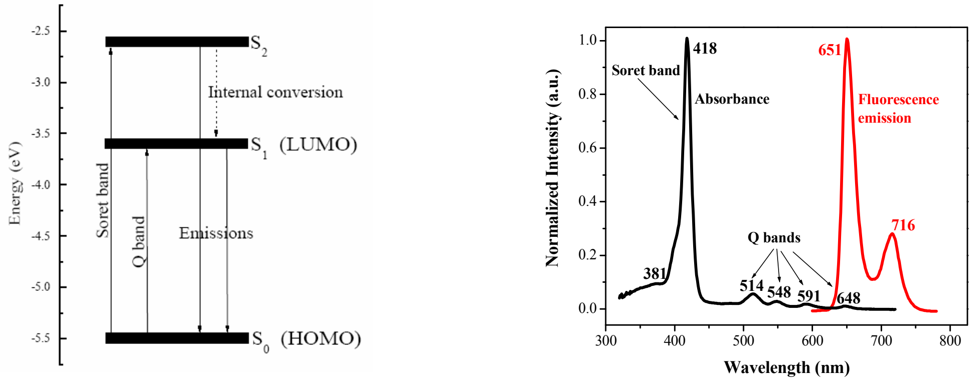

(a) (b)

Figure 7. (a) Energy-level diagram of the excited states of H2TCPP along with its (b) absorbance and emission spectra (at 420 nm excitation).

Let us, for the moment, study the H2TCPP free molecules of several concentrations in THF solutions before starting to graft them onto ZnO nanoparticles.

H2TCPP at different concentrations; i.e. 2.10-6; 1.10-5; 1,5.10-5; 2.10-5; 6.10-5; 1,2.10-4; 2.10-4; 3.10-4; and 2.10-3 mol/L, were exploited. UV-Vis absorption spectra of these samples exposed in figure 8-a, show that the dye absorption, which is mainly made via the Soret band, increases with increasing its concentration. However, these Soret peaks reveal higher bandwidths at lower concentrations, as depicted in figure 8-b.

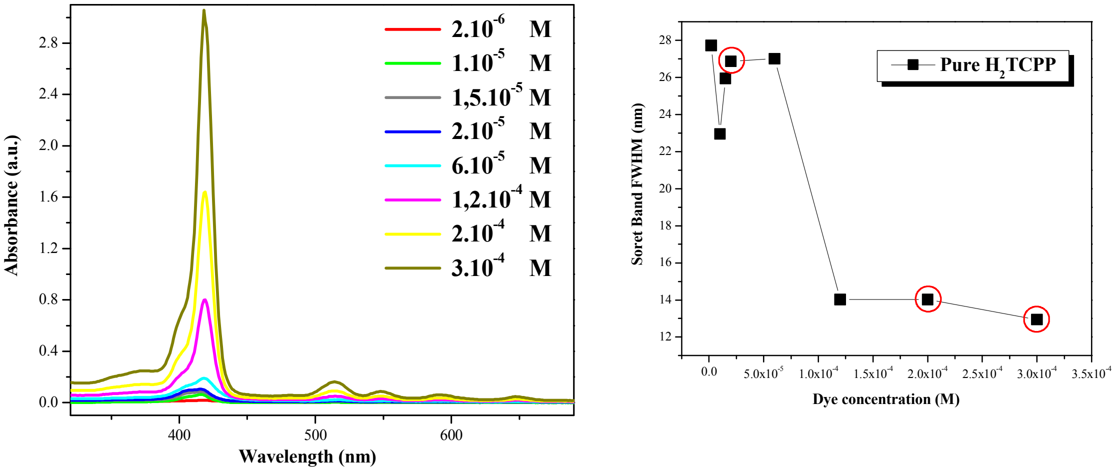

(b)

(a)

Figure 8. (a) Absorbance spectra of “diluted” free H2TCPP solutions at different dye concentrations, with (b) their corresponding Soret peak bandwidths at the Full Width Half Maximum.

In order to understand the bandwidth behavior of the free dye at the Soret band, meticulous inspections of the Soret absorption peak are performed. Three different concentrations were picked up, which are $2.10^{-5}$; $2.10^{-4}$; and $3.10^{-4}$ M, indicated by the encircled points in the bandwidth plot (figure 8-b). Simple Gaussian deconvolution of the Soret absorption peak yielded four individual bands in the three dye solutions, as seen in figure 9 showing the spectral maxima and bandwidths of these fitting components.

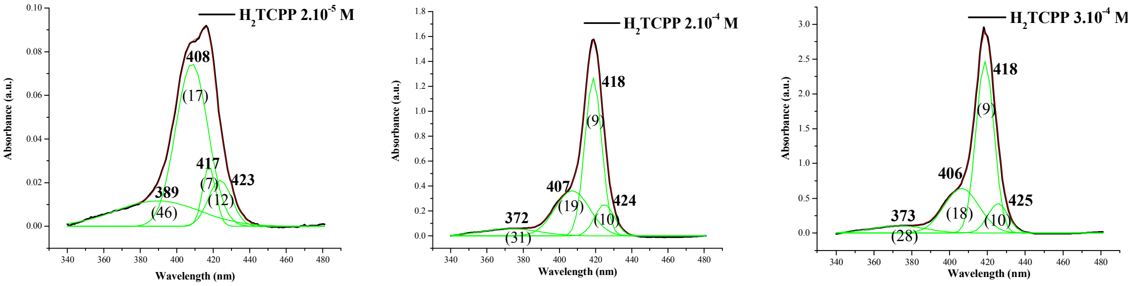

(a) (b) (c)

Figure 9. H2TCPP Absorption spectra of the Soret band of pure dye at the concentration (a) $2.10^{-5}$, (b) $2.10^{-4}$, and (c) $3.10^{-4}$ M. Green lines show the individual components; their summation in red solid line is the best fit to the experimental absorption spectra. Accuracy in the Soret maxima and bandwidths (between brackets) is about ± 1nm.

H- and J- aggregates are known to be produced on aggregation of dyes suspended in solutions [27]. In the aggregates, a strong exciton coupling will exist between two neighboring porphyrins [28,29]. Energy relaxation from excited states of molecular aggregates [30] in porphyrin stacked face-to-face in a sandwish-type H-aggregate (π-aggregation) implies a blue shift relative to the monomer excited-state level, whereas broadened red-shifted Soret band takes place in long-range tilted stacked porphyrins in the J-aggregate type. These band-shifts depend on several parameters as the degree of aggregation, the orientation of dye molecules in the aggregates and the intermolecular separation distance. Intermolecular electronic interactions among dye molecules within the aggregates lift the degeneracy in the excited states energy levels. As a result, a transition between the lowest ground state and the antibonding (π* states) excited-state levels results in blue-shifted absorption in H aggregates. In the case of J-aggregates, transitions to the lower energy excited state are allowed, resulting in a red shift of the absorption bands [27], as sketched in figure 10.

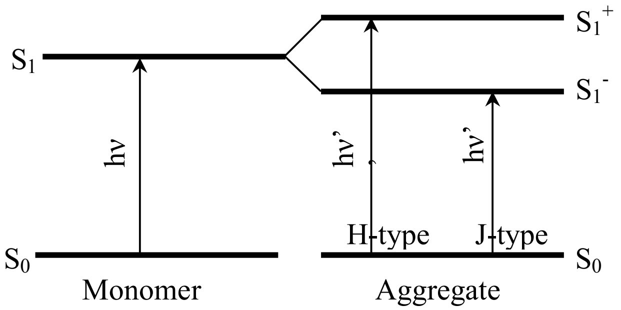

Figure 10. Representation of energy levels of the dye monomer and aggregate [31].

Pure H2TCPP molecules generate aggregates which can be classified into different structures by studying the several band components of the Soret band (in figure 9), which differ from the monomer H2TCPP molecules having only one component Soret peak [27]. Relative intensities of these several bands depend on the initial concentration of the solution. This difference points to several types of aggregation of porphyrin molecules characterized by different geometric arrangements of the dyes [32].

Absorption Soret band of H2TCPP monomer is equal to 414 nm (dissolved in water of pH 10) [27], and equal to 419 nm (dissolved in DMF) [33]. So in THF solvent the Soret band position should be around these values. In figure 9-a, the existence of four fitting peaks in the pure dye Soret band indicates the presence of both H- and J-aggregates, but the intense blue shifted peak at 408nm reveals that the dominant aggregation type is the H-aggregates. While, for the pure dye of higher concentration in figures 9-b and 9-c, the dominant aggregation type is the J-aggregates manifested by the red-shifted fitting peaks. Hence, the reason behind the decrease in bandwidths of pure dyes for concentrations less than $1\times10^{-4}$ M in figure 8-b as we increase the dye concentration, is that the H2TCPP molecules display very narrow red-shifted Soret bands that are typical of dye J-aggregates [27].

Fluorescence "excitation" spectra of pure dyes are presented at different concentrations in figure 11-a and were registered at the maximum value of λ emission at 652 nm. The excitation spectrum represents a measurement of the relative ability of different wavelengths of light to stimulate the fluorescent emission. This spectrum tells us what wavelengths of light will make a particular substance fluoresce. Excitation spectra of our dye are thus determined by monitoring fluorescence emission at the wavelength of maximum intensity (i. e. 652 nm) while the dye is being excited through a group of successive wavelengths. Only emission light at 652 nm is allowed to pass to the detector, the result is then a plot presenting the fluorescence excitation intensity produced by excitation over a spectrum of excitation wavelengths.

We can clearly notice from figures 11-a that the shape of excitation spectra (Soret and Q-bands) of pure dye at concentration less than $2\times10^{-4}$ M correlate with their corresponding absorbance spectra in figure 8-a. When the dye concentration is equal or higher than $2.10^{-4}$ M, splitting of Soret band into two Lorentzian bands is produced as seen in figure 11-a [34]. According to the decrease of concentration it can be seen that the lower energy Soret band at 435 nm, associated with J-type aggregate mode, decreases gradually while the high-energy Soret band around 418 nm, roughly associated with monomer, appears in diluted systems [34-35]. This observation is in great accordance to that observed for the TPyP which is a porphyrin derivative as plainly depicted in figure 11-b [34].

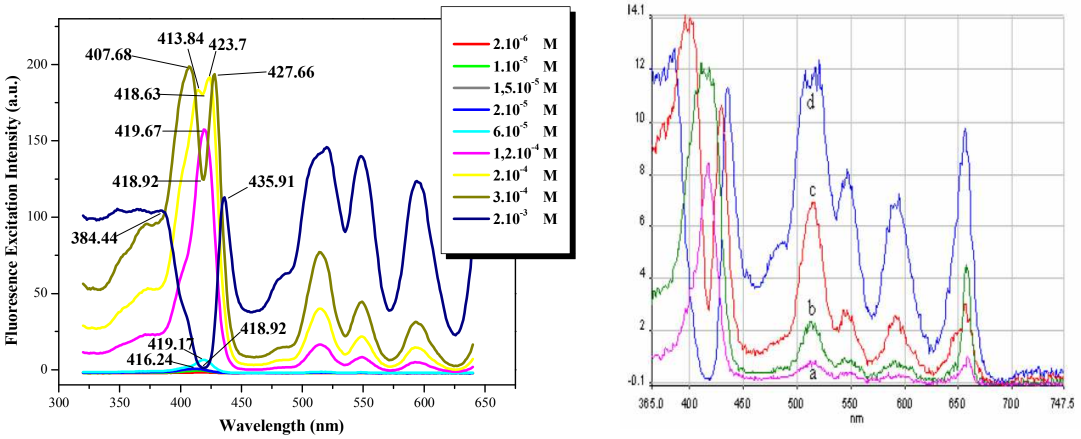

(a) (b)

Figure 11. (a) Fluorescence excitation spectra of pureH2TCPP at different dye concentrations. (b)Fluorescence spectra of 5,10,15,20-tetrakis(4-pyridyl)-21H,23H-porphine (TPyP) in THF at different concentrations: 1,11.10$^{-6}$M (a); 5,56.10$^{-6}$M (b); 2,78.10$^{-5}$M (c); 1,39.10$^{-4}$M (d), $\lambda_{em}$= 656 nm, as taken from [34].

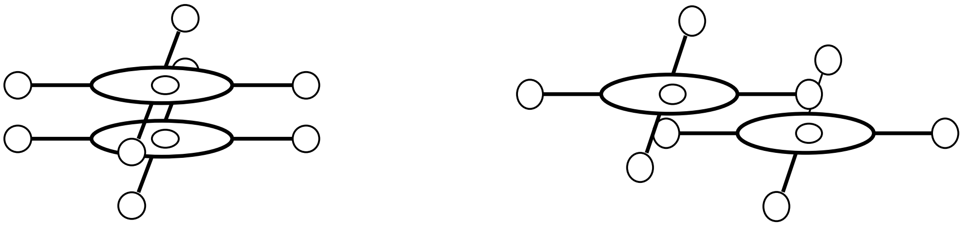

(a) (b)

Figure 12. Schematic representation of a possible arrangement of two porphyrin units of (a) H-structure and (b) J-structure.

Summing up, and following our observational interpretations we can postulate that pure dyes in THF solutions are generally H-aggregated for small dye concentrations (< 1.10$^{-4}$ M), while they softly agglomerate in the J-aggregate forms for higher concentrations, as sketched in figure 12.

H2TCPP molecules were then grafted onto two series of ZnO nanoparticles. To begin with, the very small quasi-nanospheres of ZnO, obtained right after the 2 hours and 15 minutes just prior to the condensation step, constitute the first type of the inorganic ZnO. Then, the second ZnO type is of rod-like shape achieved after 48 hours following the condensation step.

## 4.4.2 Optical studies of H2TCPP-based nanohybrids of quazi-nanospherical shaped ZnO

Here, the templates are the ZnO nanoparticles of about 5 nm in diameter obtained right after the 2 hours and 15 minutes prior to the condensation step. We determine the number of the dye molecules associated with each ZnO nanoparticle by first determining the particle concentration of ZnO colloids which is of $2.10^{15}$ particles/mL with an available surface area of 98.5 $nm^2$/ZnO particle. Table 1 below lists the samples' names along with their corresponding dye concentration values and the theoretically calculated number of dye molecules per ZnO nanoparticle.

| Sample Name | H2TCPP concentration [M] | # of dyes /one ZnO nanoparticle |
|---|---|---|
| A | zero | zero |
| B | $2.10^{-6}$ | 0.6 |
| C | $1.10^{-5}$ | 3 |
| D | $2.10^{-5}$ | 6 |
| E | $6.10^{-5}$ | 18 |
| F | $1,2.10^{-4}$ | 36 |
| G | $2.10^{-4}$ | 60 |

Table 1- Names of nanohybrid samples with their corresponding dye concentrations.

These samples are next subjected to absorbance and photoluminescence measurement studies to analyze grafting conditions and outcomes.

### 4.4.2.1 Absorbance measurements

The UV-Vis absorption spectra of the "concentrated' hybrid $H_2$TCPP-ZnO samples at different dye concentrations in THF are shown in figure 13-a. We can clearly see that the absorption signals of the ZnO are quite saturated due to the high material concentration, while the saturation in the dye Soret band begins for the sample "E", i.e. at $6.10^{-5}$M dye concentration (refer to table 1). The saturation in absorbance detection is located approximately at the value 3.5, as seen in figure 13-a. That's why we need to dilute the samples as already mentioned.

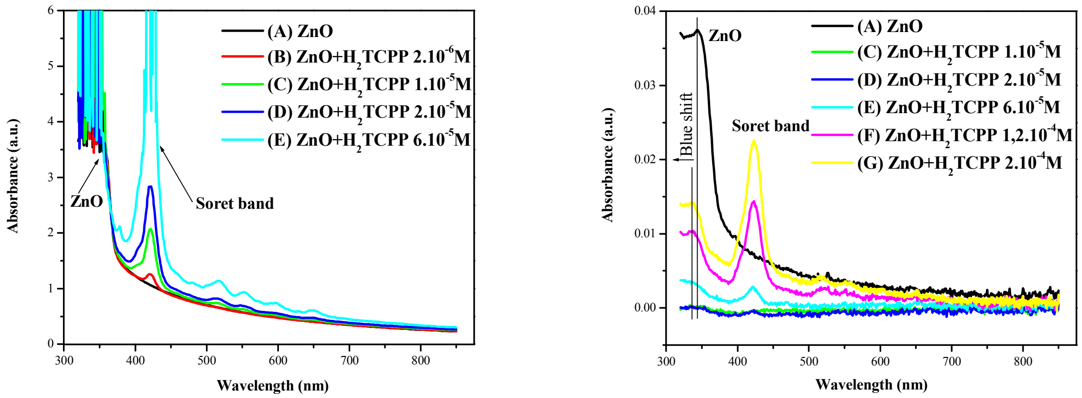

(a) (b)

Figure 13. Absorbance spectra of (a) mother-concentrated H2TCPP-ZnO hybrid solutions at different dye concentrations, and (b) upper colorless liquids of the non-agitated corresponding samples.

Actually, in the non-agitated mother-concentrated solutions, we noticed that the colored grafted species precipitate at the bottom of the small glass bottles leaving a colorless upper liquid. Absorbance spectra of the upper colorless liquid are exposed in figure 13-b. If we are to compare the pure ZnO sample “A” in both cases, we can find that the ZnO participates, on account of its weight, at the bottom leaving only 0.9% of ZnO nanoparticles in the upper liquid. This percentage vanishes for the grafted samples “C” and “D”, where we can find no more ZnO; which is a consequence of the ZnO being over-weighted by the grafted dye molecules. For these both samples “C” and “D”, no remaining traces of ZnO and dye molecules are detected signifying total dye grafting. For higher dye concentrations, one can find dye-grafted ZnO floating in the upper liquid which means that the liquid begins to be saturated caused by high species concentrations. Furthermore, and in these samples namely “F” and “G”, little blue shift in the ZnO absorption peak indicates the presence of grafted ZnO nanoparticles of smaller size. Reviewing the absorption intensities of ZnO (figure 13-b), it is obvious that the ZnO absorption intensity of the grafted samples is smaller than that of the pure ZnO. These observations prove that the dye molecules grafted onto the ZnO nanopatricles drag the ZnO down to the bottom suggesting aggregation occurrence among the hybrids, and pointing toward the certainty of grafting.

To enlighten the grafting manner, we need to study the optical effects induced through dye grafting by analyzing the Absorbance and Photoluminescence spectra of the diluted nanohybrid samples. Nevertheless, special care must be taken into account when interpreting the raw Absorbance and Photoluminescence data. Several factors influence and distort the spectra and necessitate some corrections to reach “true” spectra. Distortions can be sorted as being either instrumentally or sample related. To begin with, the intensity and the wavelength characteristics of the light source vary over time between experiments and even during each experiment. Besides, no lamp has a constant intensity at all frequencies. Moreover, the percentage of detected photons, i. e. detection efficiency, varies with wavelength and mainly with time as the detector certainly deteriorates. Correction of all of these instrumental factors meant for getting a “typical” spectrum is a very tedious procedure that is merely applied when strictly needed. The sample itself is as well an important source of distortions as already mentioned. Several sample aspects exist as the photodecomposition (that decreases the fluorescence intensity over time), the light scattered by Rayleigh scattering and the sample species-contained concentration. High concentrations of absorbing species results in the nonhomogeneity of the excitation light intensity throughout the sample solution. Another aspect to be considered is the Reabsorption that occurs when a molecule absorbs at the wavelengths at which the other molecule emits radiation.

In the present work the corrections that were done are attributed to several factors. Firstly, the problem of high species concentrations was solved by a proper sample dilution. The main difficulty is the one that arises from the lost of some ZnO nanoparticles when cleaning the hybrid samples through centrifugation. Thus in order to correctly analyze the Absorbance spectra of the centrifuged samples, they should be normalized to the same ZnO absorbance peak intensity of their corresponding non-centrifuged samples. Accordingly, photoluminescence spectra of all samples before and after centrifugation were numerically divided by their corresponding ZnO absorbance peak intensity to assure the normalization of all samples when analyzing the emission spectra of fluorescent light.

Original non-treated Absorbance spectra of the “diluted” and “centrifuged diluted” samples are presented in figures 14 and 16, respectively.

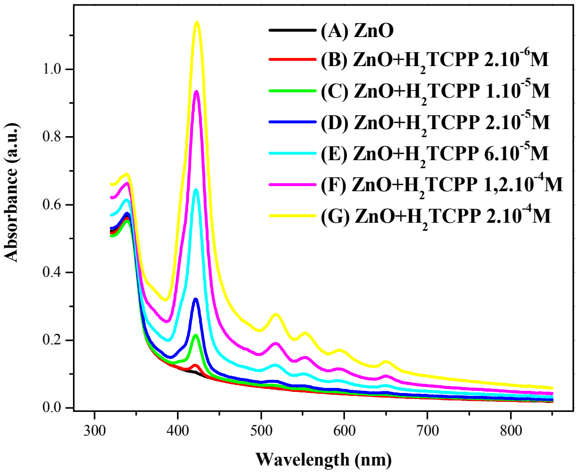

Figure 14. Absorbance spectra of “diluted” H2TCPP-ZnO hybrid solutions at different dye concentrations

In figure 14, we can see the Absorbance spectrum originating from each hybrid system at a constant ZnO quantity and a specific dye concentration, and where the mother “concentrated” sample is diluted 10 times. An increase in the concentration of the dye molecules in the hybrid systems induces an increase in the dye absorption located at the Soret and the Q-bands peaks. We can also notice a very important feature seen in the increase of the “overall” absorbance spectra when increasing the dye concentration, as if the plots are shifted “as a whole” towards higher absorption values. Normally, increase in the absorbance means decrease in the transmitted light detected at the exit of the sample. This decrease in the transmitted light is attributed to the absorbance of the light by the present species, besides the presence of another mechanism that is the scattering of incident light. This mechanism depends on several parameters; as the colloidal concentrations and sizes, and the light wavelengths. By scattering, a part of the incident light is diffracted and lost within the colloidal solution sample thus less transmitted light is detected. So what do we mean by scattering? and what concluding remarks about grafting can thus be engendered through this scattering approach?

The scattering of light might be thought of as the redirection of light that happens when an incident light beam, i.e. electromagnetic wave (EM), encounters obstacles, which are in our case the colloidal hybrid particles. The light EM wave interacts with the particle inducing dipole moments that oscillate with the same frequency as the electric field of the incident EM wave, thereby resulting in scattered light. Briefly, two theoretical frameworks are proposed to interpret the light scattering: the Rayleigh theory applied to small particles, and the Mie theory for larger particles. In the Rayleigh scattering regime, the size of the scattering particle is much less than the wavelength of the scattered light. This corresponds physically to the hypothesis that the particle is sufficiently small such that the particle meets a uniform electric field at any moment, consequently the time for infiltration of the electric field is much less than the period of oscillation of the EM wave. This approach is perfectly applicable in our case where we have ZnO spherical particles of about 5 nm diameter.

The intensity *I* of light scattered by a single small particle, as sketched in figure 15, from an unpolarized light beam of wavelength λ and intensity $I_0$ is given by [36,37]:

$$I = I_0 \frac{1+\cos^2\theta}{2R^2}\left(\frac{2\pi}{\lambda}\right)^4\left(\frac{n^2-1}{n^2+2}\right)^2\left(\frac{d}{2}\right)^6 \tag{4-1}$$

where *R* is the observation distance to the particle, θ is the scattering angle with the initial direction of the incident light beam, *n* is the refractive index of the particle, and *d* is the diameter of the particle.

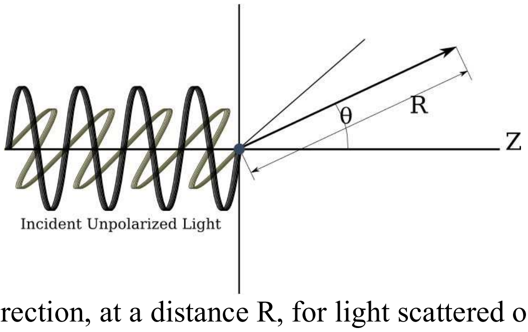

Figure 15. Observation direction, at a distance R, for light scattered off a particle located at the origin in a direction that makes an angle $\theta$ with respect to the z axis.

The Important Features of Rayleigh Scattering are the strong size and wavelength dependence. The scattered intensity is proportional to:

i- $d^6$, so it is much stronger for slightly larger particles than slightly smaller particles

ii- $\frac{1}{\lambda^4}$, so it is much stronger for shorter wavelengths (that is why the sky is blue!!!)

For that reason, to the absorption in figure 14 is added the light scattering. And hence all the effects induced by the later mechanism. We can notice the scattering effect in the overall shape of each spectrum, which is clearly visible for the hybrid E, F and G spectra; at shorter wavelengths, namely at the ZnO absorption peak, the shift in each spectrum (due to scattering) from the pure ZnO spectrum is much more pronounced than that at higher wavelengths around 800 nm. This $\lambda$ dependence reasoning is applied within each Absorbance spectrum of specific dye concentration. But if we are to compare between the Absorbance plots at different dye concentrations, we need to refer to the scattering dependence on the particle diameter d. As already mentioned, the scattering intensity becomes stronger for slightly larger particles than slightly smaller particles. This fact is translated through figure 14 where Absorbance spectra exhibit an ascendant move as a whole towards higher Absorption values as we increase the dye population, explicitly in the hybrids E, F and G. All of this point out to the fact that when adding more dye molecules, further aggregation among the dye-grafted ZnO is likely to happen, that is well proved by the scattering dependency on the particle size. For example, the hybrid particles in the G sample with the highest dye concentration are larger than the pure ZnO particles; that is attributed to the aggregation among the hybrid nanoparticles and formally recognized through scattering effects interpretation.

Original non-treated Absorbance spectra of the "centrifuged diluted" samples presented in figure 16, manifest quasi similar absorption and scattering features as those of the previously presented "diluted" samples (see figure 14). But with evident differences in the absorption peak widths and intensities; (i) of the dye caused by expelling the non-grafted excess, and (ii) of the ZnO due to some loss of ZnO particles during the clean-up centrifugation process.

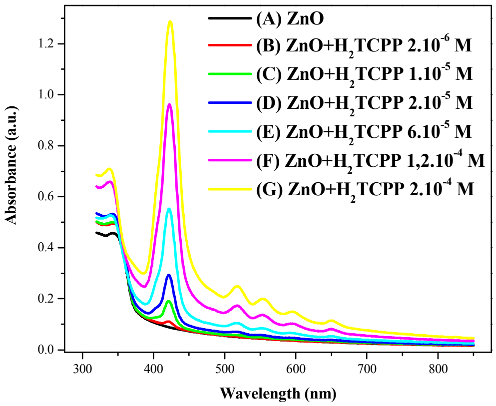

Figure 16. Absorbance spectra of "centrifuged diluted" H2TCPP-ZnO hybrid solutions at different dye concentrations.

In the intention to understand the different features and properties of grafting the H2TCPP process onto the surface of ZnO nanoparticles, we need to develop an elementary study for each hybrid sample before and after centrifugation and then comparing it with the optical properties of the corresponding pure dye. Knowing that we used the same ZnO quantity in all original diluted samples, the data of the centrifuged samples are then normalized to the same ZnO peak intensity value of each corresponding non-centrifuged sample to facilitate comparison of the spectral profiles. Figure 17 shows Absorbance spectra of the pure ZnO [(A) sample] "diluted" and "centrifuged diluted" solution where the absorbance spectrum of centrifuged ZnO is normalized so that to coincide with its corresponding non-centrifuged sample. We can notice that the ZnO absorbance peak position increases from 339,17 to 342,77 nm after centrifugation. This indicates that an important quantity of relatively very small ZnO nanoparticles (with slightly higher band gap) is lost through centrifugation.

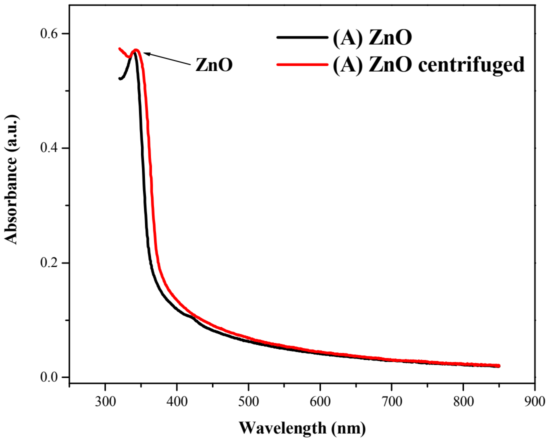

Figure 17. Absorbance spectra of the "diluted" and "centrifuged diluted" ZnO sample (A).

Absorbance spectra of the "diluted" and their corresponding treated "centrifuged diluted" spectra of dye-grafted ZnO "B", "D" and "G" samples along with the pure dye absorption are shown in figure 18-a, -b, and -c, respectively. In each hydrid sample, all dye absorption peaks in the grafted systems are red-shifted with respect to those of the pure dye, as clearly quantified by position peaks values for sample "G" in figure 18-c.

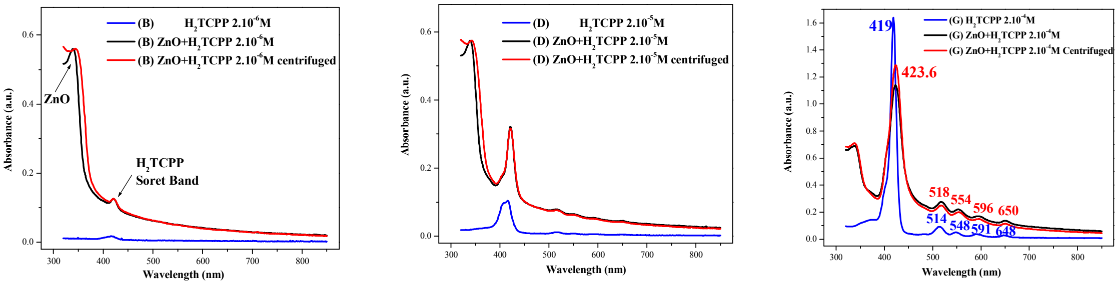

(a) (b) (c)

Figure 18. Absorbance spectra of the “diluted” and their corresponding treated “centrifuged diluted” spectra of dye-grafted ZnO solutions: (a) Sample “B”, (b) Sample “D” and (c) Sample “G”.

Absorbance plot investigations are summarized in figure 19. Positions, intensities and bandwidths of the Soret dye peak of pure dye solutions and hybrid solutions before and after centrifugation at different dye concentrations are shown in figures 19-a, -b and -c, respectively. Soret peak positions in the hybrid samples before and after centrifugation coincide approximately, while they differ from those of the pure dye with peak maxima at lower wavelengths (figure 19-a). This difference in peak position representing the red shift upon dye grafting reinforces the grafting assumption. On the other hand we can clearly notice that the wavelength of the Soret peak maximum increases when increasing the dye concentration. This event originates from the dye agglomeration, which is a typical phenomenon for porphyrins [38]. In addition, porphyrin agglomeration is well manifested by a significant broadening of the Soret band [38,39] as seen in figure 19-c, where the Soret absorption bandwidth in the hybrids increases with dye concentration providing a direct proof of the dye aggregation on the surface of the ZnO nanoparticles. A slightly less aggregation among dyes in the centrifuged hybrid “G” (with the highest dye concentration) is noticeable in a bandwidth smaller than that of its corresponding non-centrifuged sample (see figure 19-c). This is demonstrated once more in the Absorbance intensity plots, in figure 19-b; dye Soret band in the centrifuged hybrid “G” shows Soret band intensity higher than that of the non-centrifuged “G”. For the hybrids with smaller dye concentrations (< $1.10^{-4}$ M), Soret band exhibits identical absorbance intensities for both centrifuged and non-centrifuged hybrids. For that reason, we are sure that grafting of total dye quantity is taking place in the samples “B”, “C”, “D” and “E”. Beyond these dye concentrations, centrifugation is required in order to clean the hybrid sample from the surplus non-grafted dye.

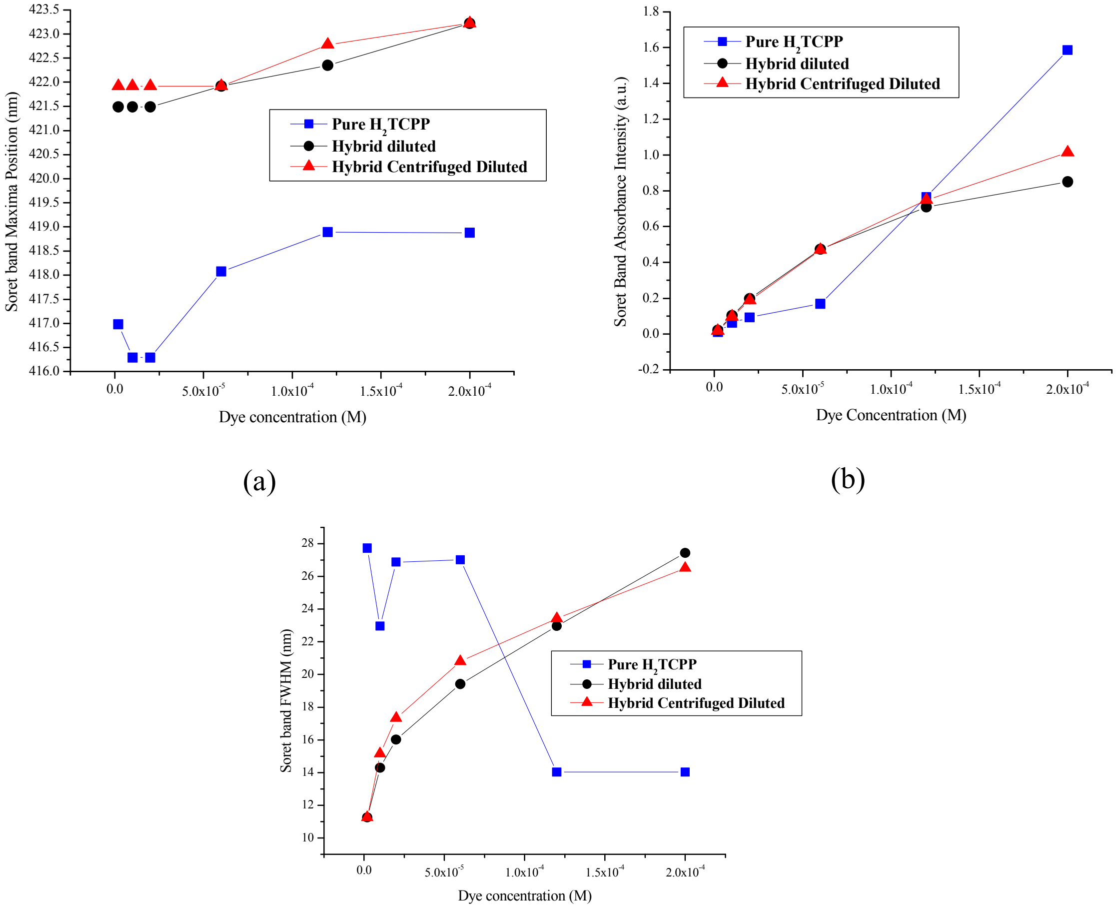

(a) (b)

(c)

Figure 19. (a) Maxima positions of Absorbance, (b) intensities and (c) Full Width Half Maximum of the Soret dye peak of pure dyes and hybrids before and after centrifugation at different dye concentrations.

The most important feature emerges from absorption analysis plots (figure 19) once we compare the intensities and bandwidths of both pure and grafted dye. At low dye concentration (< $1.10^{-4}$ M), figure 19-c shows larger Soret band absorption bandwidths of pure dye solutions than those of hybrid solutions. This fact indicates that the degree of aggregation among dye molecules suspended in pure solutions is much higher than among grafted dye molecules on the surface of ZnO nanoparticles. The aggregated pure dye molecules at small concentrations become isolated (to some extent) once grafted onto the ZnO surface. Hence, grafted dyes are expected to absorb much more than the agglomerated pure non-grafted dyes, as clearly seen in figure 19-b, for the samples “B”, “C”, “D” and “E”. For higher dye concentrations in the samples “F” and “G” (>$1.10^{-4}$ M), aggregation among grafted dyes becomes more pronounced as manifested by the lower Soret band intensities and larger bandwidths than those of the pure dyes.

Inspections of the Soret band absorption peak may enlighten the formation of different types of agglomerates at the surface of ZnO. Let us choose two dye-grafted ZnO solutions of identical concentrations to those studied for free dyes, namely $2.10^{-5}$ M (“D” sample) and

$2.10^{-4}$ M (“G” sample) as shown in figures 20-a and -b, respectively. Soret absorption peak in hybrid samples is resolved into three Gaussian individual components compared to Soret band with four individual bands for pure dye solutions in figures 9-a and 9-b. The broadening in the “G” Soret band (figure 20-b) originates from higher dye concentration arising more intermolecular interactions. Absorption peak of the grafted dyes of sample “G” showing the development of the peak at 403 nm imply that the these grafted dyes are mainly H-aggregated.

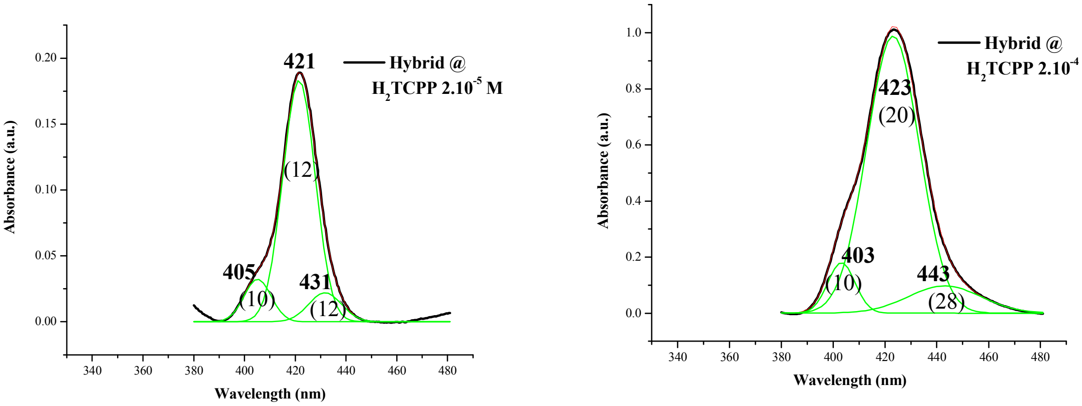

(a)

(b)

Figure 20. H2TCPP Absorption spectra of the Soret band of treated centrifuged spectra of dye-grafted ZnO solutions: (a) Sample “D” and (b) Sample “G”. Green lines show the individual components; their summation in red solid line is the best fit to the experimental absorption spectra. Accuracy in the Soret maxima and bandwidths (between brackets) is about ± 1nm.

So far, we can conclude through the absorbance data that at H2TCPP dye concentrations less than $1.10^{-4}$ M, the aggregated pure dye molecules in THF solutions become isolated to some degree when they are grafted onto the ZnO nanospheres surface. Higher dye concentrations ($>1.10^{-4}$ M) induce the H-type aggregation between the grafted dyes. This aggregation is obviously marked when increasing the dye amount by the less absorption than analogous free dyes.

### 4.4.2.2 Photoluminescence measurements

Figure 21-a exhibits the effects of varying the dye concentration on the fluorescence “excitation” spectra of grafted dyes. These spectra were registered at the maximum value of λ emission at 652 nm.

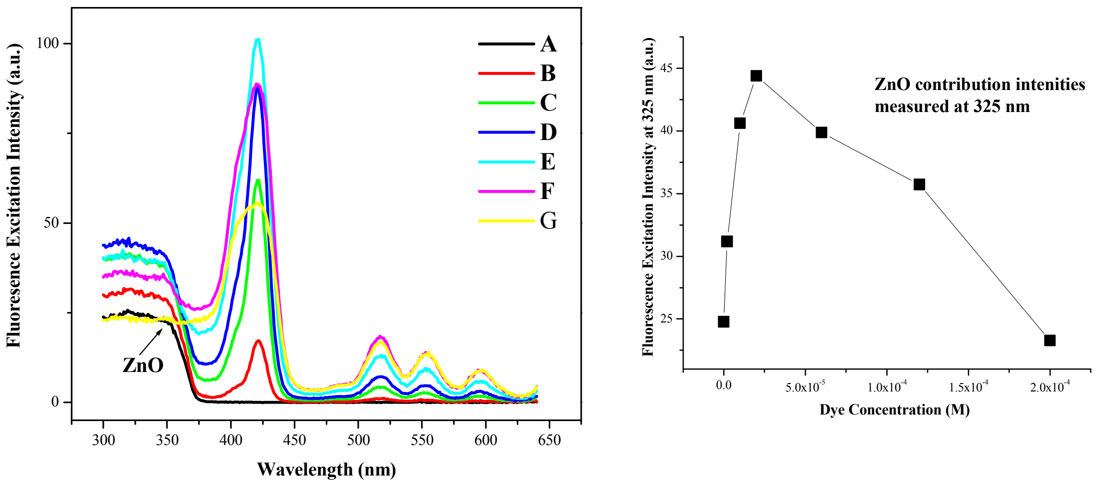

(a) (b)

Figure 21. (a) Fluorescence excitation spectra of centrifuged hybrids at different dye concentrations. (b) ZnO contribution intensities measured at 325 nm from the excitation plots in (a).

Figure 21-a shows a contribution of the ZnO absorption as well as the dye absorption bands in the emission at 652 nm. The Soret peak is red-shifted with dye addition guaranteeing once more the grafting occurrence. For low dye concentration (< $1.10^{-4}$ M), Soret band intensities in the excitation plots of hybrid systems (figure 21-a) are in agreement with their corresponding Soret band absorption (figure 18-b). That is the important observation presented by higher absorption of the grafted dyes in comparison with the non-grafted ones. While at higher dye concentrations, the grafted dye molecules exhibit lower and wider Soret band peak intensities, which are attributed to the aggregate formation among grafted dye molecules at the surface of the ZnO nanoparticles. For example, for the samples “F” and “G” with the highest dye densities, broadening of the Soret band is clearly detected as the blue-shifted band is developing thus implying the occurrence of the H-type aggregation at the surface of ZnO.

On the other hand, figure 21-a demonstrates a contribution of the ZnO absorption in the emission at 652 nm; this contribution is quantified in figure 21-b showing the ZnO input intensities as measured at the 325 nm wavelength (from plots in figure 21-a). The ZnO absorption involvement (in the dye emission) increases upon increasing the dye concentrations till reaching the $2.10^{-5}$ M concentration of the sample “D”, beyond this concentration the contributing band of ZnO decreases, as clearly seen in figures 21-a and -b. This fact might be the direct evidence of the ZnO transferring energies or electrons towards the dyes at low densities, while this transfer is blocked to some reasons at higher dye density.

Figure 22-a illustrates corrected photoluminescence spectra at 325 nm excitation wavelength of pure ZnO “A” sample before and after centrifugation. Emission spectrum is a measurement of the emitted energy as a function of wavelength for a specific excitation

wavelength. These ZnO suspensions in figure 22-a show two emission bands. One is relatively weak and quite sharp UV-band and is assigned to the radiative recombination of excitons. The second band is a more intense and broad emission band in the green region (492-577 nm) of the visible part of the spectrum. The origin of this emission band has been a subject of much debate. The deep level traps involved in the green luminescence are likely attributed to vacant oxygen sites in the ZnO lattice [40,41]. The small shift of this band (figure 22-a) from 539 to 552 nm, after centrifugation, may be explained by the relative absence of the size effects that were promoted previously by very small particles [42]. These relatively very small ZnO nanoparticles are lost through centrifugation implying a diminution of quantity of quenching centers as oxygen related defect density decreases thus the occurrence of the green band shift. This correlates well with their correspondent absorbance spectra in figure 17.

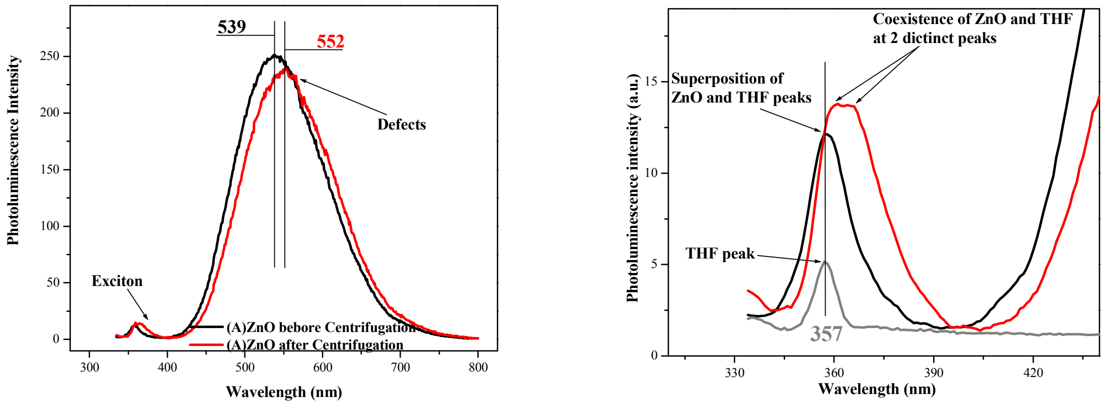

(a) (b)

Figure 22. (a) Treated photoluminescence spectra at 325 nm excitation of pure ZnO "A" before and after centrifugation. (b) magnification of the ZnO exciton peaks (of plots in (a))

For an excitation wavelength of 325 nm, that is equal to 3.8 eV excitation energy, the exciton emission of non-centrifuged ZnO located at 357 nm is a superposition of both ZnO exciton emission and THF Raman scattering peak, as shown in figure 22-b. While the exciton peak of the centrifuged ZnO is marked by the coexistence of two distinct peaks: (i) the THF emission and (ii) the real ZnO exciton that is red shifted from that of the non-centrifuged ZnO due to size effects (as already mentioned). So statically analyzing the ZnO exciton emission needs to be performed on samples excited at a different wavelength than 325 nm in order to modify the wavelength of the THF Raman scattering.

Regarding the grafting of H2TCPP, we showed earlier that the packing of dye changes the behavior of absorption. Let us examine the grafting impact on the dye's fluorescence. Photoluminescence spectra of pure dye and hybrids before and after centrifugation of samples "C" ($1\times10^{-5}$ M) and "F" ($1{,}2\times10^{-4}$ M) are shown in figures 23-a and 23-b, respectively, at 325 nm excitation wavelength assigned to excite all the sample's present species. The thus-derived statistics on fluorescence intensities and positions of the intense dye emission peak are depicted in figures 24-a and -b.

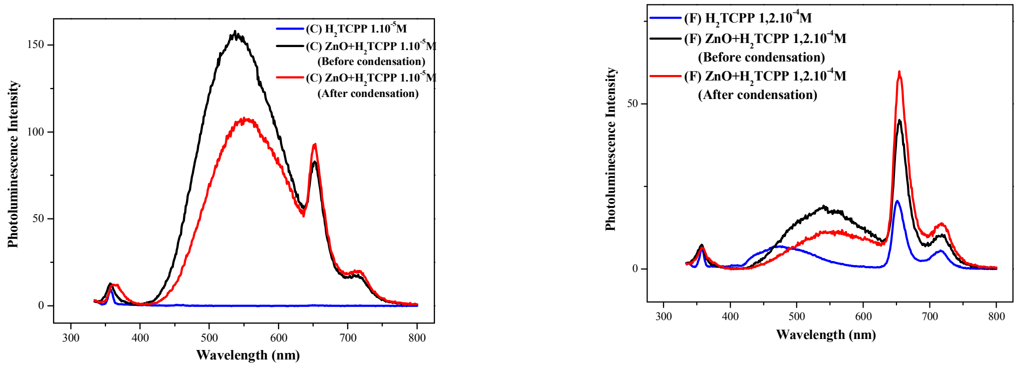

(a)

(b)

Figure 23. Fluorescence emission spectra of pure dye and hybrids before and after centrifugation of (a) sample “C” [$1\times10^{-5}$ M], and (b) sample “F” [$1{,}2\times10^{-4}$ M] at 325 nm excitation wavelength.

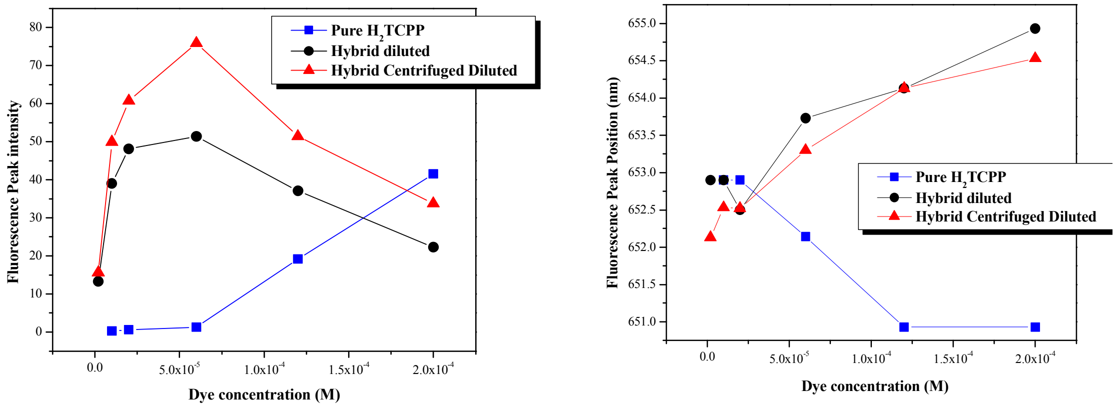

(a)

(b)

Figure 24. (a) Intensities and (b) positions of the intense emission peak (652 nm) of pure dyes and hybrids before and after centrifugation at different dye concentrations. (At 325 nm excitation wavelength).

It is clear that the intensity of fluorescence of the dye strongly depends on the concentration of this last. We have seen through absorption data (figure 19) that grafting of almost total dye quantity is taking place in the samples with dye concentrations smaller than 1.10$^{-4}$ M beyond which dye aggregation on the ZnO surface become more pronounced. This fact is precisely reflected through the fluorescence emissions (see figures 23 and 24). Strong increasing intensities of grafted dye emission being recorded with increasing dye concentration up to the sample with dye concentration of 6.10$^{-5}$ M. However with a stronger concentration (>1.10$^{-4}$ M), this emission is choked. On the other hand, the surplus non-grafted dye before centrifugation leading to more aggregation quenches further the emission intensity (figure 24-a), where the emission intensity is higher of about 30 to 40% for centrifuged diluted samples.

We can explain the behavior of the grafted dye emission, in figure 24-a (*red triangles plot*), through simple reasoning that emanates from the following relation:

$$F_d \propto N_d \cdot E_T \cdot \frac{1}{A_g} \tag{4-2}$$

Where $F_d$ is Fluorescence intensity of the dye that is: (i) proportional to the dye concentration $N_d$, (ii) proportional to the electron and (probable) energy transfer from the ZnO $E_T$, and (iii) inversely proportional to the dye aggregation factor $A_g$.

We can thus postulate that upon increasing the dye concentration $N_d$, yet remaining at very small dye concentrations, the grafted dye fluorescence intensity $F_d$ increases linearly due to its strong dependence on $N_d$. This is in addition to the second important factor $E_T$ that was previously proved to increase for low dye amount via the fluorescence excitation data (figure 21-a and -b). This $E_T$ parameter is strongly of non-linear effects as seen in the non-linear fluorescence intensities at concentrations just below $1.10^{-4}$ M. $E_T$ is dependent on the exact mechanism of electron or energy transfer. Potentially, two mechanisms can be considered: Forster energy transfer or simple electron transfer. Probably, both mechanisms are present in our case with the H2TCPP dye, yet with less impact from the Forster energy transfer because of the small overlapping among the ZnO emission band and the H2TCPP absorbance band, as detailed in the introduction of this Chapter. On the other hand, the aggregation factor $A_g$ is relatively absent at these low dye concentration. Whereas, at higher dye concentration ($>1.10^{-4}$ M), $A_g$ becomes the very dominant aspect that reduces further $F_d$ upon increasing the dye density. Aggregation between the grafted molecules of dye [43,44] is also pointed out by the emission red-shift (see figure 24-b). In this case, $E_T$ weakly interferes; that is the transfer from the ZnO to the dye molecules seems to be blocked with increasing the dye aggregation. This fact of the attenuation in $E_T$ was also confirmed at these high densities trough fluorescence excitation data in figure 21.

Another significant feature of the fluorescence emission that matches the absorption analysis plots (figure 19) is once we compare absorption and emission of both pure and grafted dye. At low dye concentration ($< 1.10^{-4}$ M), absorption indicated that the degree of aggregation among dye molecules suspended in pure solutions is much higher than among grafted dye molecules that become isolated on the surface of ZnO nanoparticles. Hence, grafted dyes are expected to absorb and emit much more than the agglomerated pure non-grafted dyes, as clearly seen in figures 19-b and 24-a. For the highest dye concentration “G”, aggregation (implying intermolecular interactions) among grafted dyes becomes more pronounced as manifested by the less absorption and quenched emission than free dyes (see figure 24-a).

Global outlook of photoluminescence spectra of centrifuged hybrids excited at 325 nm is portrayed in figure 25-a, and whose ZnO defects intensities are quantified in figure 25-b. For the time being, we can consider that the drop of the green emission of the band of defects of ZnO with the concentration of dye is allotted to the passivation of the oxygen vacancies upon surface functionalization which can be attributed to re-oxygenation of the ZnO surface by the dye acid group [45]. This indicates that the defects responsible for the green emission are located at the ZnO nanoparticle surface.

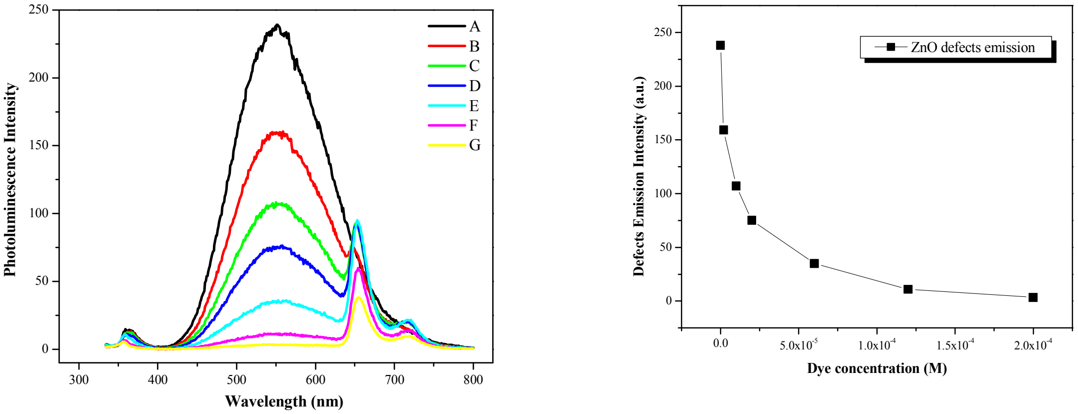

(a) (b)

Figure 25. (a) Global view of Fluorescence emission spectra of all centrifuged hybrids at 325 nm excitation wavelength. (b) ZnO defects emission intensities as a function of dye concentration.

Figure 26-b summarizes the exciton emission peak intensity and energy dependence of H2TCPP-ZnO nanospheres as a function of dye concentration, from the hybrids data for an excitation at 300 nm illustrated in figure 26-a. At 300nm excitation, the THF Raman scattering is at 326 nm, thus located out of the region of the exciton. The adsorption of $H_2$TCPP leads to a decrease of the intensity of ZnO exciton band that is additionally blue-shifted with increasing dye concentration. A similar blue-shift in the normalized ZnO absorption of the centrifuged samples is also seen in figure 26-c. This genuine phenomenon incarnated by this optical blue-shift needs to be deeply studied for its great importance in explaining the grafting consequences on the outer layers of the ZnO surfaces. This fact will be developed in the subsequent section, but let us for the moment try to elucidate the reasons standing behind the reduction in the emission of ZnO exciton and consequently its defects.

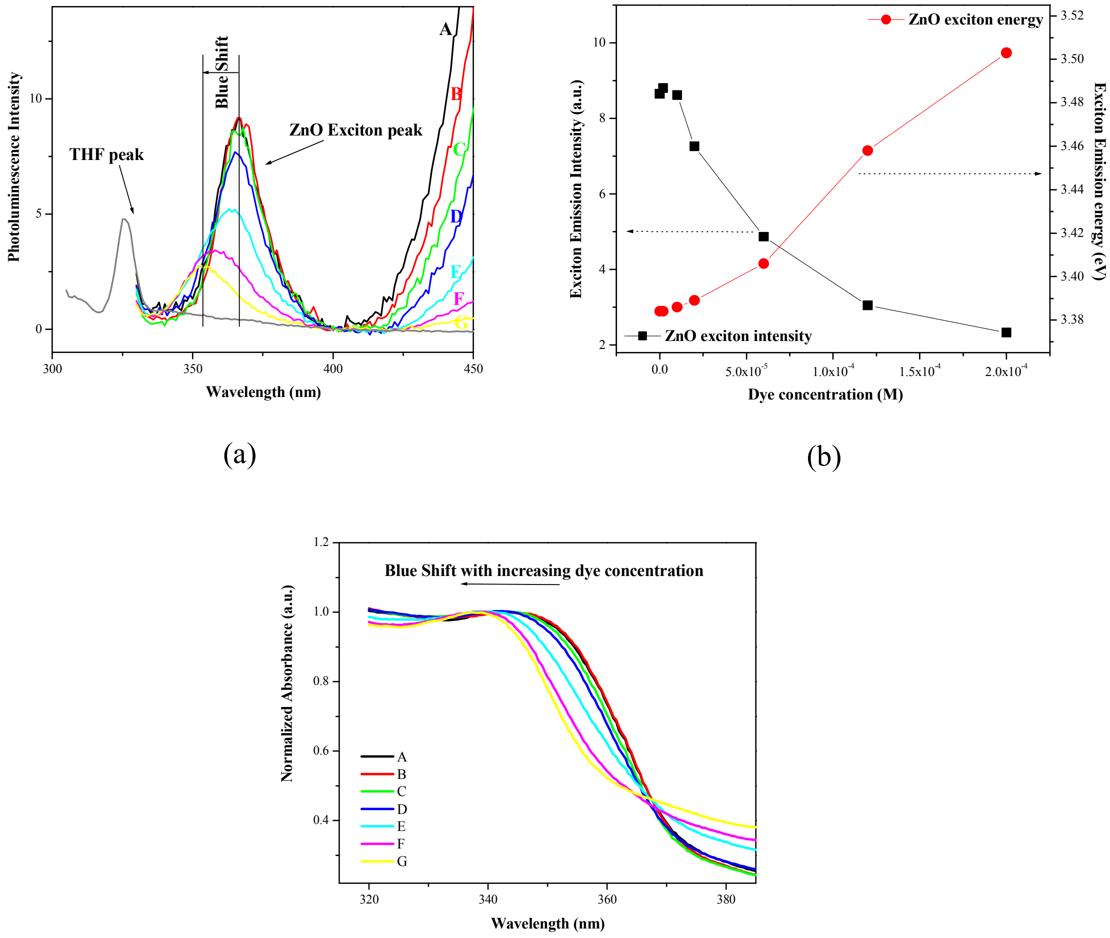

(a) (b)

(c)

Figure 26. (a) Fluorescence emission spectra for the excitation wavelength 300 nm of all centrifuged samples. (b) ZnO exciton peak intensities and energies of centrifuged samples at excitation wavelength 300 nm (illustrated in (a)) as a function of dye concentration. (c) Normalized ZnO absorption of all centrifuged samples.

Knowing that we have identical ZnO quantity in the all hybrid samples, the only changing parameter is the added dye amount. This is one of the reasons why the excitation energy is further absorbed by the mounting dye concentration at the expense of ZnO. Therefore, less excitation of ZnO nanoparticles screened by the increasing amount of dyes provokes the reduction in the intensity of UV ZnO exciton and defects emissions. Another mechanism can contribute to this exciton and defect reduction as simply demonstrated in figure 27. Excitation at the wavelength 300 nm that is equal to 4,13 eV excitation energy (greater than the ZnO band gap) excites all the sample present species mainly the ZnO. Accordingly, several photophysical processes can take place. Band gap photoexcitation (1) of ZnO can lead to two different recombinations: (3) radiative intrinsic charge recombination, (5) radiative charge defect recombination, (6) electron transfer to the LUMO and (7,8) non-radiative interfacial charge recombination to the HOMO. It is worth noting that excitation with high photon energy enhances the electron relaxation by transferring electron from ZnO to the dye's LUMO via the process (6), here the electron excess energy of about 4,13-3.3=0.83eV promotes strongly the electron transfer process along (6). For pure ZnO, all the emitted light occurs following the (3) and (5) radiative intrinsic charge recombination. When adding the dye molecules, electron transfer via path (6) is confirmed as already mentioned, followed by the molecular radiative decay (10) by recombination to the hole left in the dye's HOMO being slightly excited by the 300 nm excitation along (9). Hence, this electron transfer via (6) will decrease the recombining electrons via the defects (5), which will lead to the shrinking in their defect band emission. Furthermore, processes (7) and (8) can happen because of the electron recombination from the lower edge of ZnO conduction band (CB) and from the defect traps with the few HOMO holes, repectively; these holes being created through the slight excitation of the dye along (9) and through the interfacial electron recombination to the ZnO valence band along (11). Adding more dyes will create more recombination centers in the dye's HOMO level, thus increasing the non-radiative processes (7) and (8) at the expense of the radiative processes (3) and (5). For all of the above reasons, the attenuation of both ZnO exciton and defect emission is likely to take place.

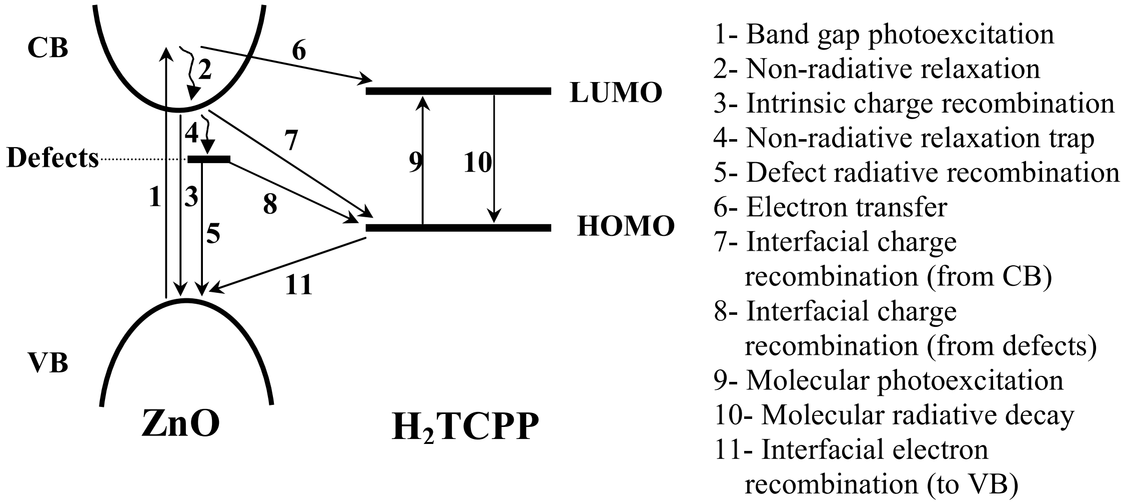

Figure 27. Schematic representations of the photophysical processes underlying interfacial charge exchange in ZnO/H2TCPP hybrids for excitation wavelength equal to 300nm.

Herein, reduction in the ZnO exciton, and consequently the ZnO defects band, is reasonably simplified, whereas its exciton blue-shift event is quite interesting and should be carefully interpreted.

#### 4.4.2.2. A H2TCPP-grafting effects on the surface of ZnO nanospheres

Our very new discovery of the blue-shifted ZnO exciton emission peaks when increasing the grafted-dye density is the most important feature that would clarify and explain the charge exchange mechanisms through the interface of the ZnO/H2TCPP hybrid. The blue shifts in the ZnO exciton emission as well as in the ZnO absorption can be seen in figure 26-a, -b and -c, respectively. Theoretically, these blue-shifts are equivalent to the increase in the band gap of the ZnO nanoparticles in the hybrid matrices. This increase in the band gap is the direct consequence of the ZnO exciton being confined more and more with increasing the amount of the grafted dye molecules. This exciton confinement might outcome from two possibilities: (i) the size reduction of the ZnO nanoparticles and (ii) the electronic modification in the outer layers of the ZnO surfaces induced by grafting. We did not detect any visible change in the ZnO dimensions via the TEM images. Hence, the most probable cause for the exciton confinement resides in the second possibility (ii) where the ZnO exciton is confined in an inner volume of the ZnO nanoparticle. This volume decreases with increasing the thickness of the surface layers that are affected by further dye grafting. So all we need in this case is to inspect the interface created between a ZnO nanoparticle and a dye molecule.

We can study the ZnO/H2TCPP interface by considering that ZnO with its oxygen vacancies is regarded as n-doped semiconductor, and the H2TCPP is considered as a donor-type material.

Theoretically, when an n-type semiconductor is placed in contact with donor-like surface states, transfer of electric charges (until electronic equilibrium is reached) produces a region on each side of the junction where the charge distribution differs from the bulk material, and this is known as the space-charge layer. In our case the dye pocesses donor states that are located at higher energies than the ZnO conduction band. Hence, these donor states $D_S$ might be partially empty (by transferring charges to the ZnO) and thus carry a positive surface charge. This charge density must be compensated by an equal amount of negative space charge in the interior of the crystal. Thus free electrons accumulate in the conduction band below the surface. This electronic space-charge of the so-called accumulation layer is related to a downward band bending to maintain the charge neutrality at the surface. This accumulation layer is due to mobile free electronic charge carriers. The illustrations in the figure 28-a and 28-b refer respectively to a single n-type semiconductor and to an n-type semiconductor together with a donor where electrons accumulate at the semiconductor side inducing the band bending at the surface, while in the bulk these bands are flat .

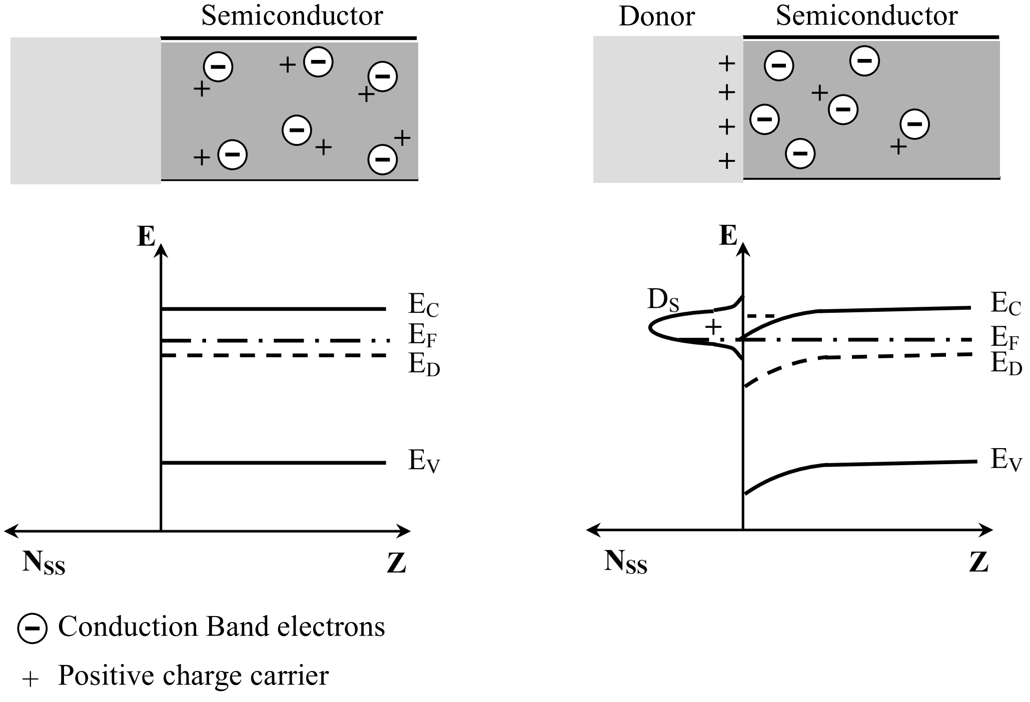

(a) (b)

Figure 28. (a) Schematic showing the electronic energy levels of an *n*-type: band energy E versus Z coordinate normal to the surface. Flat band potential, where no space-charge layer exists in the semiconductor.

(b) Schematic showing the electronic energy levels of an *n*-type in contact to a donor-type surface states (density $N_{SS}$). Accumulation layer, where excess electrons have been injected into the solid producing a downward bending of the conduction and valence band towards the interface.

$E_C$, $E_F$, $E_D$ and $E_V$ are the conduction-band edge, the Fermi energy, the energy of the bulk donor and the valence-band edge.

Adding more dye molecules leads to the increase in the electrons density at the interface in the ZnO side. Hence, these accumulating electrons will constitute a layer (at the surface of the ZnO) that will grow in thickness after further increasing the grafted-dye concentrations. A potential barrier is thus created at the surface. Figure 29 describes the formation of the growing negatively charged layer at a part of surface of the ZnO, where the exciton will be confined in a certain volume that shrinks simultaneously with the enlarged charged surface layer.

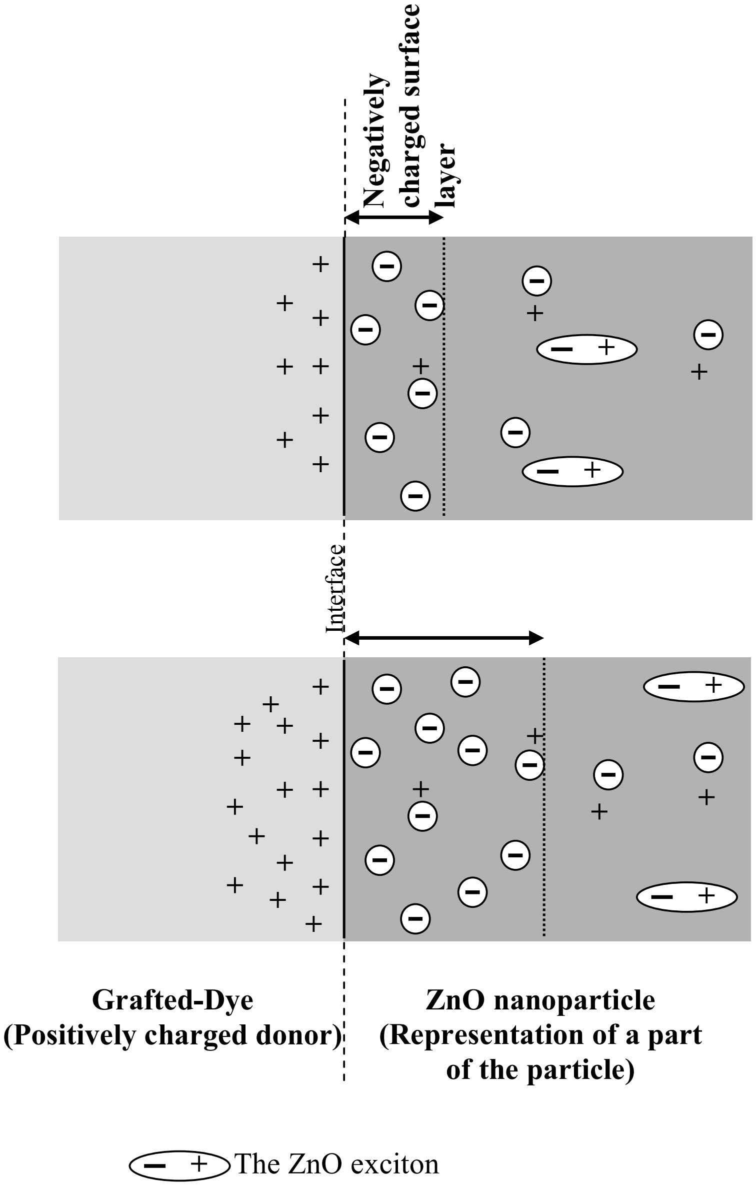

Figure 29. Formation of the growing negatively charged layer at a part of surface of the ZnO with dye increasing (more positively charged donor). Further confinement of the exciton in a shrinking volume all together with the enlarged charged surface layer.

We can see, through figure 29, that the electron in the exciton is repelled away from the negatively charged layer to be confined in a volume of decreasing dimensions. The cartoon representation in figure 29 of the interface and the exciton confinement is actually pictured at a portion of the ZnO nanoparticle surface. Nevertheless, the surface delimiting a ZnO nanoparticle is built of unequivalent facets components implying different facets polarities; in other words some parts of the surface could be constructed with Zn (001) planes, others with O (001) planes, and others with both Zn and O (110) and (100) planes. Hence, different distribution of surface charges is established inducing the nonhomogeneity in the dye grafting consequently their charges repartition. Indeed this nonhomogeneity in the charge repartition is the direct reason for an efficient confinement of the ZnO exciton.

Another mechanism could also constitute a reasonable interpretation of the behavior at the interface ZnO/dye. This mechanism relies on the aromatic characteristics of the dye molecules inducing thus delocalization of the dye's electrons. By definition, delocalized electrons are contained within an orbital that extends over several adjacent atoms. This is usually probable because electrons are free to cycle around circular arrangements of atoms, which are alternately single- and double-bonded to one another. This can apply to our porphyrin dye that presents aromatic chemical properties through the π-bonds (covalent chemical bonds) that are formed from overlap of atomic p-orbitals above and below the plane of the ring. The diagram in figure 30 shows a simple part of a porphyrin ring where we can see the positions of the p-orbitals lobes.

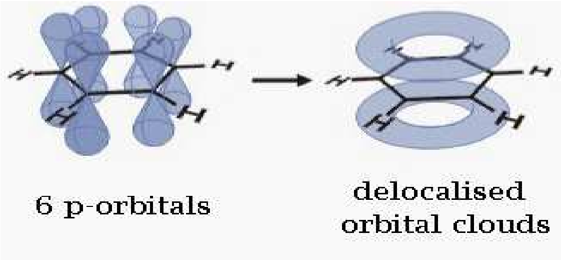

Figure 30. Representation of an aromatic ring p-orbitals inducing a π-symmetry molecular orbital via the delocalized orbital clouds.

And since these p-orbitals are out of the plane of the atoms, they can interact with each other freely, and become delocalised. This means that instead of being tied to one atom of carbon, each electron is shared by all six in the ring. The resulting molecular orbital has π symmetry (figure 30).

Practically, the porphyrin is grafted to the ZnO through the negatively charged carboxylate anion that contains the group $-COO^-$. Hence, the delocalization of the electron cloud in the porphyrin ring structure will reach the interface with ZnO surface via the $-COO^-$. This will create an induced negatively charged layer at the upper surface of the ZnO nanoparticle.

These two demonstrations could give a clearer view of the physical processes that take place at the interface of a small ZnO nanosphere grafted with H2TCPP dye molecules. The direct consequence of the exciton confinement is the visible bleu-shift in the ZnO exciton emission that is equivalent to the increase in the band gap energy of the small ZnO nanosphere. Additional term should be added to calculate the new enlarged band gap energies. This term is the potential energy created between the negatively charged layer in the ZnO upper-surface and the electron of the ZnO confined exciton. The relationship between the band gap energy and the size of the particles (settled in equation (1-19) of chapter I) will be enlarged by the additional potential term as follows:

$$E_g^* = E_g + \frac{h^2}{8\mu R^2} - \frac{1.8e^2}{4\pi\varepsilon_0\varepsilon_\infty R} + \frac{\langle\beta\rangle e\ e}{4\pi\varepsilon_0\varepsilon_\infty d} \tag{4-3}$$

where d is the relative distance between two electrons; one of which resides in the negatively charged surface layer and the other is the one bounded in the ZnO exciton. $\langle\beta\rangle$ is the mean degree of the charge transfer by the totality of the grafted molecules; $\langle\beta\rangle = \beta(hkl)N$ where

$\beta(hkl)$ is the individual charge transfer of dye molecule as a function of the crystallographic plane where the molecule is grafted.

Indeed, in this approach, we used simplified assumption to calculate electrostatic confinement within semiconducting nanoparticle. More exact developpement can be found from solution of the radial Schrodinger equation [46,47], or from molecular dynamics simulations.

Estimation of this newly added potential is about 0.166 eV when considering the simplified model of two electrons that are separated by a distance of 1 nm. Practically, we assumed that the total surface charge is about $1{,}6.10^{-19}$ Coulomb, which interacts with the confined electron. Here, the separation distance between the surface (portion of induced charges) and the confined electron was taken of about 1 nm. Those values correspond to the ZnO nanoparticle with diameter 5.6 nm and exciton Bohr radius of 2.34 nm. We must point to the fact that this estimated value of the electrostatic confinement (using our simplified model) is in very good agreement with our experimental results. Indeed, experimentally we measured maximal shift of the edge excitonic emission relatively to the pure ZnO of about 3.503-3.384=0.119 eV.

Qualitative picture used in this estimation is shown in figure 31, where we can see the dye molecules grafted on several crystallographic edges of a small ZnO nanoparticle whose upper-layer surfaces are affected by the dye through creation of negatively induced charged layers (*dark gray regions*). We are showing also the exciton that is further confined upon increasing the negatively charged layers.

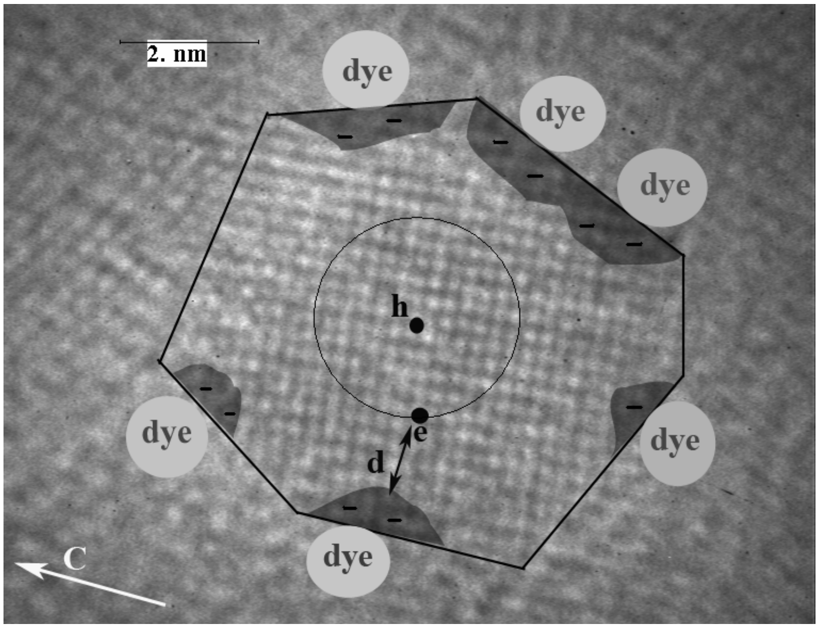

Figure 31. Qualitative picture showing the induced negatively charged layers in a small nanoparticle via the dye grafting, and where the exciton is further confined because of the surface charged layers.

Summing up, we have seen through the photoluminescence data analysis of the H2TCPP/ZnO nanospheres that:

- The ZnO contributes to the enhanced fluorescence of relaticvely isolated dyes up to a specific dye concentration, beyond which the aggregation becomes the main factor causing the dye emission quenching.
- The increase in the ZnO band gap inducing a charge separated layers at the ZnO/H2TCPP interface is enhanced upon adding more dyes.

Hence, we believe that the ZnO contribution to the dye emission is done via two ways:

■ Forster energy transfer input that decreases with increasing the dye densities because of the reduction in the overlap between the H2TCPP absorbance spectrum and the ZnO emission spectrum that is blue-shifted thanks to the dye presence, as shown in figure 32.

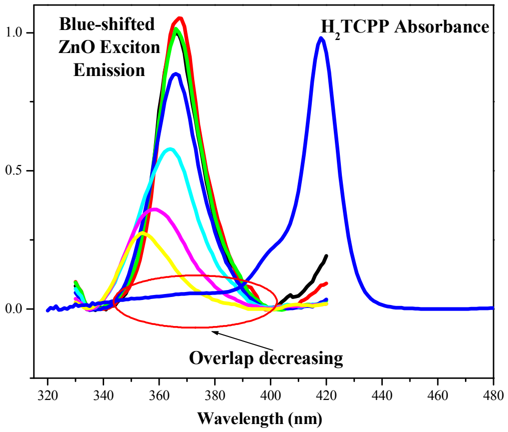

Figure 32. Overlap decreasing between the H2TCPP absorbance and the blue-shifted ZnO emissions upon increasing the dye amount.

■ Electron transfer that is further enhanced because of the increase in the ZnO band gap energy upon adding the dye. Hence, this facilitates transferring the charges from the ZnO to the dye.

## 4.4.2.2. B Fluorescene efficiency of grafted H2TCPP dyes

In order to determine the emission spectrum of a particular fluorophore (dye), the wavelength of maximum absorption (usually the same as the excitation maximum) is determined and the fluorophore is excited at that wavelength which is of 420 nm in our case. The fluorescence emission spectra of dye molecules in centrifuged hybrid samples at 420 nm excitation wavelength are illustrated in figure 33-a where the relative intensity of emission is plotted against the measured wavelength. Intensities of the intense dye emission peak (~652 nm) of pure dyes and hybrids after centrifugation are plotted in figure 33-b for different dye concentrations.

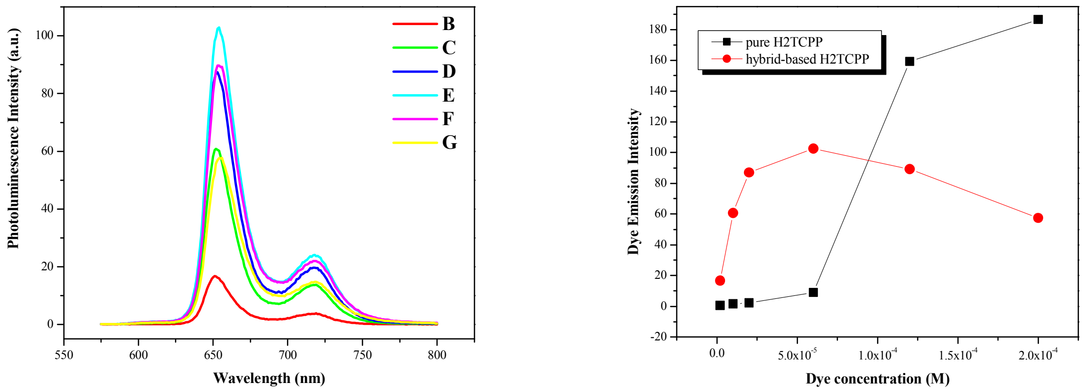

(a) (b)

Figure 33. (a) Fluorescence emission spectra of centrifuged hybrid samples at 420 nm excitation wavelength. (b) Intensities of the intense dye Emission peak (~652 nm) of pure dyes and hybrids after centrifugation for different dye concentrations.

To determine the efficiency of the dye grafting process on the ZnO surface, relative fluorescence quantum yields of grafted H2TCPP molecules at different concentrations were calculated. The efficiency with which absorbed light induces some effect is quantified by the fluorescence quantum yield $\phi$. Theoretically, the fluorescence quantum yield is defined as the ratio of the number of photons emitted to the number of photons absorbed;

$$\phi = \frac{\#\text{photons emitted}}{\#\text{photons absorbed}} \tag{4-4}$$

We estimated the number of emitted photons by integrating the photoluminescence spectra that is the area under the curve of fluorescence intensity versus wavelength, when the excitation wavelength is at the dye Soret band of 420 nm, that is:

$$\#\text{ of photons emitted} = \int PL(\lambda)d\lambda \tag{4-5}$$

The number of absorbed photons should be those absorbed at the Soret band (420nm), and is equal to:

$$\#\text{ of photons absorbed} = n_0\left(1 - e^{-A}\right) \quad \text{(see Equation (3) Appendix III)} \tag{4-6}$$

where $n_0$ is the number of incident photons that is a constant common factor, and A is the absorbance $A = \alpha Lc$ at 420nm.

Thus, the fluorescence quantum yield is set as:

$$\phi = \frac{\beta}{n_0}\frac{\int PL(\lambda)d\lambda}{\left(1 - e^{-A}\right)} \tag{4-7}$$

where $n_0$ is the number of incident photons, and $\beta$ is the detection efficiency factor. This factor is needed because the detector senses only a small part of the emitted photons thus inducing some errors if we are to calculate the accurate value of the quantum yield.

Nevertheless, this rectifying factor $\beta$ and the incident photons $n_0$ are two constant common factors in all our measurements.

Hence our calculation of the relative fluorescence quantum yield of the dyes can be estimated from:

$$\phi = \frac{\int PL(\lambda)d\lambda}{\left(1-e^{-A}\right)} \tag{4-8}$$

Quantum Yields of free and adsorbed dyes onto the ZnO nanospheres are plotted in figure 34, without any explicit scale because here we calculated relative values. Increment in the free dyes quantum yields is expected to some extent with increasing dye concentration following the relative increase in the fluorescence emission as shown earlier. The observed quantum yield improvement in the hybrid matrices, compared to the pure dyes at low concentration is interpreted as a reduction of non-radiative relaxation channels by isolation of the grafted-dye molecules on the surface of ZnO in addition to the ZnO contribution. This strong enhancement of the florescence quantum yield in hybrid systems is destinated to vanish with increasing dye concentration inducing further quenching aggregate centers. Nevertheless, these aggregates are less present in the pure systems with same highly concentrated dye samples implying higher quantum yields with respect to their corresponding hybrids.

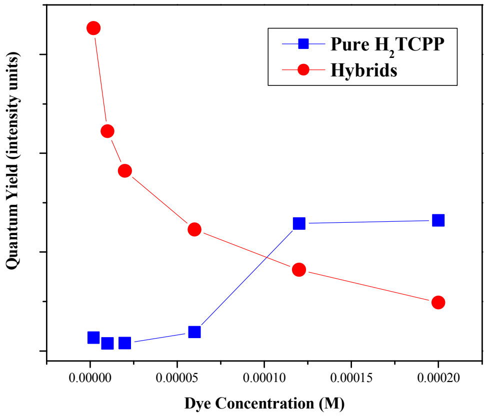

Figure 34. Comparison of Quantum Yield of free (■), and adsorbed (●) dyes onto the ZnO nanospheres.

The continuous decrease of the dye quantum yield in the hybrid systems with concentration (figure 34) can be explained through the schematic representations of the photophysical processes in figure 35.

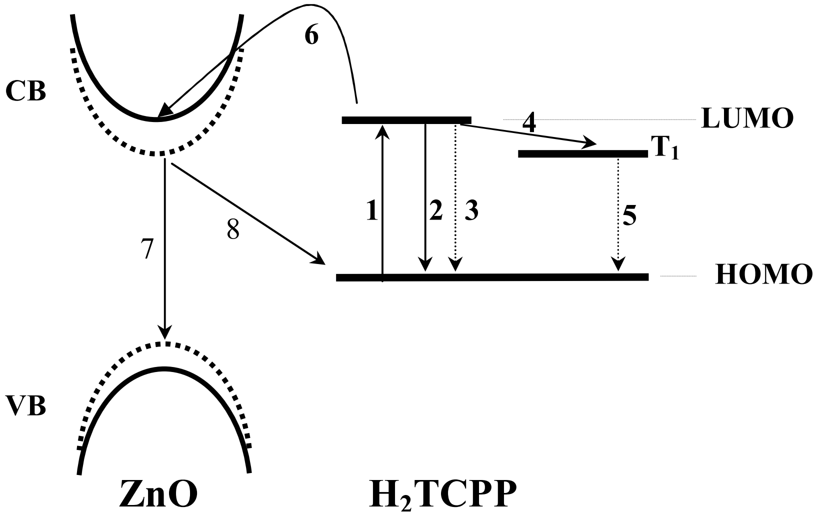

1- Molecular photoexcitation
2- Molecular radiative decay
3- Molecular nonradiative decay
4- Intersystem crossing
5- Radiationless decay
6- Interfacial electron transfer
7- Intrinsic charge recombination
8- Interfacial charge recombination

Figure 35. Schematic representations of the photophysical processes underlying interfacial charge exchange in ZnO/H2TCPP hybrids for excitation wavelength equal to 420nm.

Upon excitation at 420nm, dye photoexcitation (1) occurs followed either by radiative decay (2), interfacial electron transfer (6) or intersystem crossing (to its triplet state) (4). Hence, occurrence of processes (4) and mainly (6) decreases the radiative decay (2). On the other hand, process (6) can be followed either by intrinsic charge recombination (7) or by interfacial charge recombination (8), this latter being the most probable mechanism. Hence, we can assume that continuous decrease of the fluorescence quantum yield originates mainly from aggregation among dyes because the charge transfer (6) to the ZnO decreases with dye concentration due to augmentation in the ZnO band gap, thus the conduction band is placed at higher levels. This can give a proof of the amplified dye aggregation effects on the hybrids optical properties.

### 4.4.2.3 Concluding remarks on H2TCPP/ZnO nanospheres

The important feature materialized via the absorption and fluorescence analysis plots is that the aggregated pure dye molecules suspended in pure solutions at concentrations less than ($< 1.10^{-4}$ M) become isolated to some extent once grafted onto the ZnO surface. At these dye concentrations the dye is excited via the ZnO mainly through the electron transfer mechanism with a modest input of the Forster energy transfer. For higher dye concentrations ($>1.10^{-4}$ M), H-aggregation occurs among grafted dyes and becomes more pronounced with increasing dye amount as manifested by the less absorption and quenched emission than free dyes. This fact leads to the strong enhancement of the florescence quantum yield in hybrid matrices that is destinated to vanish with increasing dye concentration inducing further quenching aggregate centers.

A H2TCPP molecule lying in a flat geometry occupies an area of about 2.3 nm$^2$, while an edgewise oriented H2TCPP occupies an area of 0.6 nm$^2$ [48]. Hence, 42 flat dye molecules are needed to totally cover the surface of one ZnO nanosphere, whereas 164 molecules are needed for the edgewise oriented H2TCPP. However according to our observational optical measurements, aggregation starts to be evident for grafted dye concentrations higher than $1.10^{-4}$ M. Indeed, table 1 stated that 18 dye molecules are available for sample "E" with the concentration $6.10^{-5}$ M, while 36 dyes are available for sample "F" with $1,2.10^{-4}$ M concentration. As we have assumed, aggregation should affect sample "F" having a concentration higher than $1.10^{-4}$ M, certainly with its 36 molecules it approaches the saturation flat coverage with 42, thus the existing probability to initiate aggregation. While for sample "E" with its 18 dye molecules, all dyes were isolately adsorbed and exhibited higher absorption and emission than its corresponding pure dye. Therefore, it seems reasonable to believe that the H2TCPP molecule is lying flat on the ZnO surface. Hence, H2TCPP molecules lying flat on the ZnO nanosphere surface match up a 42% of surface coverage for sample "E" with the $6.10^{-5}$ M concentration.

Nevertheless, the most authentic and essential fact is the grafting consequences on the outer layers of the ZnO surfaces as marked by the decreased blue-shifted ZnO exciton with increasing dye concentration. Upon increasing the dye amount, the ZnO energy gap increases due to confinement features inducing a charge separated layers at the ZnO/H2TCPP interface.

Till now grafting analyses are done on ZnO nanospheres obtained right after the 2 hours and 15 minutes that is just prior to the condensation step (refer to synthesis procedures at the beginning of this chapter). From now, grafting of the same dye molecule H2TCPP on a second ZnO type with rod-like shape achieved after 48 hours will be investigated.

### 4.4.3 Optical studies of H2TCPP-based nanohybrids of ZnO nanorods

The nanohybrids are fabricated in the same way as in the previous case in the tetrahydrofuran solvent (THF) at different dye concentrations. After 48 hours reaction time, ZnO rods with 9 nm as diameter and 38 nm as length are of abundance of $7,4.10^{13}$ particles/ml with an available surface area of 1201 nm$^2$/ZnO particle. Table 2 lists the samples names along with their corresponding dye concentration values and the calculated number of dye molecules per ZnO nanoparticle.

| Sample Name | H2TCPP concentration [M] | # of dyes /one ZnO nanoparticle |
|---|---|---|
| 1 | zero | zero |
| 2 | $2.10^{-6}$ | 16 |
| 3 | $1.10^{-5}$ | 81 |
| 4 | $1,5.10^{-5}$ | 121 |
| 5 | $2.10^{-5}$ | 162 |
| 6 | $6.10^{-5}$ | 486 |
| 7 | $1,2.10^{-4}$ | 972 |
| 8 | $2.10^{-4}$ | 1621 |
| 9 | $3.10^{-4}$ | 2432 |
| 10 | $2.10^{-3}$ | 16216 |

Table 2. Names of nanohybrid samples with their corresponding dye concentrations.

Real visualization of the hybrid mother solution of sample “8” for example is shown in figure 36. Agitated sample shows a thick solution (figure 36-a) that is cleared-up after few minutes upon apparent species precipitation (figure 36-b). Finally at rest total hybrid precipitation demonstrates two phases: (i) clear upper liquid with remaining traces of hybrids and (ii) precipitated hybrids at the bottom (figure 36-c). This quasi-speedy precipitation points toward the certainty of grafting and may insinuate the possibility of aggregates formation among hybrid nanoparticles promoted by the grafted dyes.

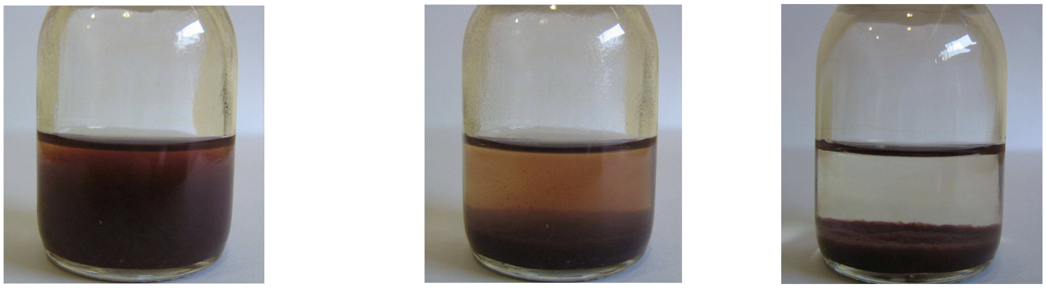

(a) (b) (c)

Figure 36. Real visualization of the hybrid mother solution of sample “8”: (a) agitated (thick solution), (b) rested for few minutes after agitation (precipitation phase), and (c) at rest with total hybrid precipitation.

### 4.4.3.1 Absorbance measurements

Elementary study for each hybrid sample before and after centrifugation along with their parallel pure dye solutions are presented in the ensemble of figure 37, where the data of the centrifuged samples are corrected to the same ZnO peak intensity value of each corresponding non-centrifuged sample. Figure 37-a shows identical absorbance spectra of the pure ZnO (sample “1”) before and after centrifugation. All dye absorption peaks in the grafted systems are red-shifted with respect to those of the pure dye as clearly quantified by position peaks values in figure 37-b. This red shift confirms once again the occurrence of the dye grafting.

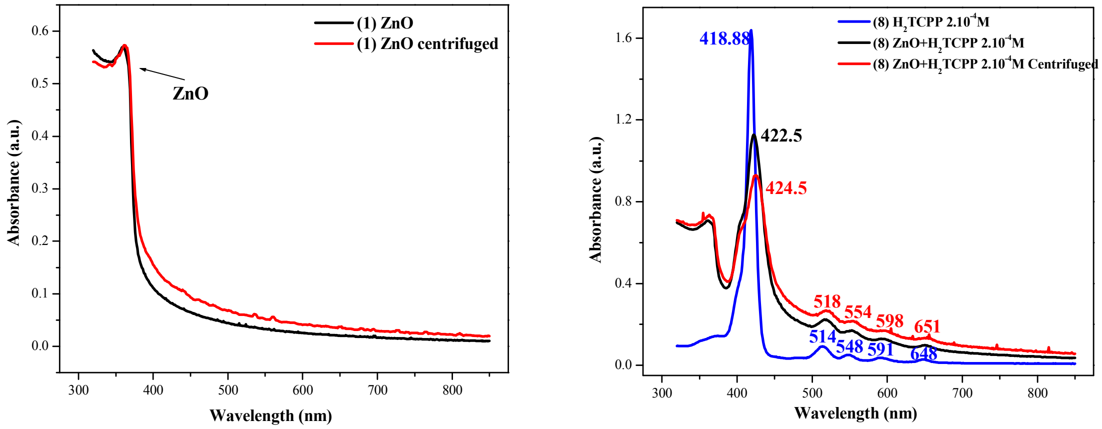

(a) (b)

Figure 37. Absorbance spectra of the “diluted” and their corresponding treated “centrifuged diluted” spectra of dye-grafted ZnO solutions: (a) Sample “1” and (b) Sample “8”.

Absorbance plot investigations of the Soret dye peak are summarized in figure 38. Soret peak positions in the hybrid samples are red-shifted to higher wavelengths from those of pure dye (figure 38-a). The real grafting effect on the Soret band behavior is given through the centrifuged hybrid samples, whose ascendant peak positions are slightly additionally red-shifted from those of non-centrifuged hybrids; insinuating that the excess of non-grafted dye molecules tends to behave as the pure dye solutions especially for higher dye densities. Thus by eliminating this excess, the true effects of aggregate formation becomes detectable. This fact is precisely reflected through the significant broadening of the Soret band [38,39] as seen in figure 38-c, where the Soret absorption bandwidth in the hybrids increases with dye concentration providing a direct proof of the dye aggregation on the surface of the ZnO nanoparticles. This is demonstrated once more in the absorbance intensity plots, in figure 38-b, where the aggregates in the centrifuged samples exhibit Soret band intensities lower than the non-centrifuged ones for high dye concentrations, while the dye Soret intensities coincide in both samples before and after centrifugation for dye concentrations up to $6.10^{-5}$ M (sample “6”).

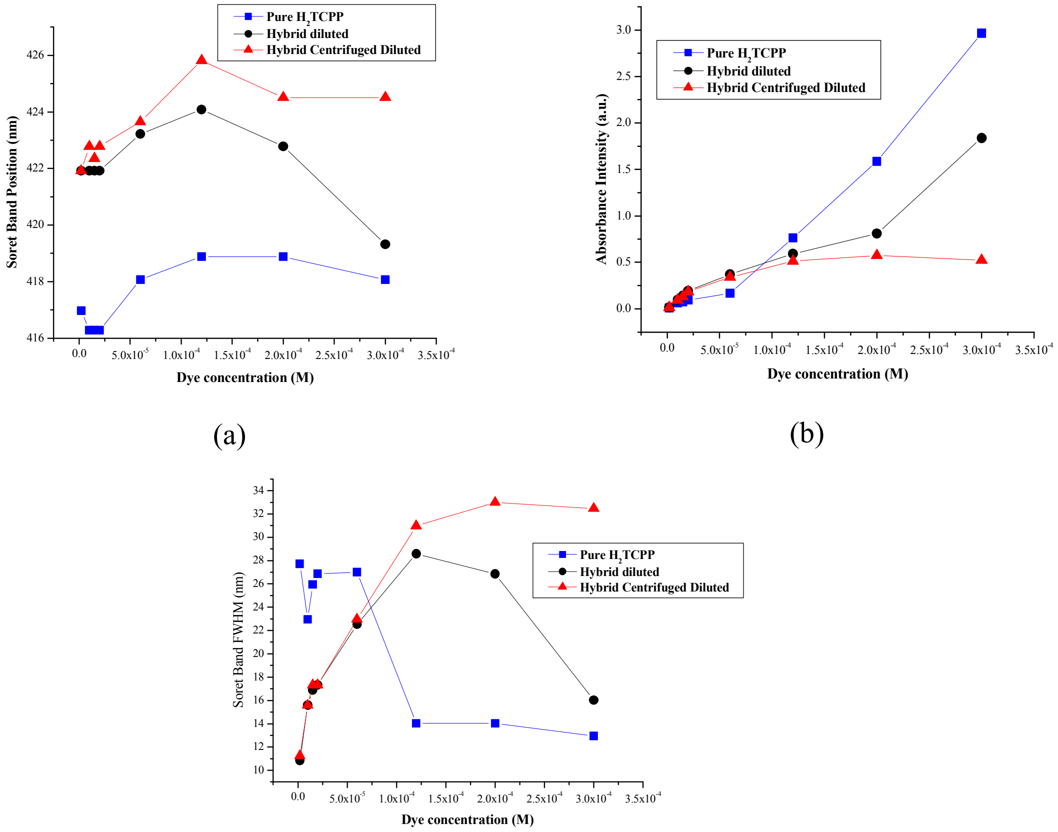

(a)

(b)

(c)

Figure 38. (a) Absorbance maxima positions, (b) intensities and (c) Full Width Half Maximum of the Soret dye peak of pure dyes and hybrids before and after centrifugation at different dye concentrations.

As in the grafting previous case with ZnO nanospheres, the aggregated pure dye molecules at small concentrations become isolated (to some extent) once grafted onto the surface of ZnO nanorods. Hence, grafted dyes absorb more than the agglomerated pure non-grafted dyes, as seen in figure 38-b, for the samples “2”, “3”, “4”, “5” and “6”. For higher dye concentrations aggregation among grafted dyes becomes more pronounced as manifested by the less absorptions and larger bandwidths than those of the pure dyes (figure 38-c).

Examination of the Soret band absorption peak reveals the presence of different types of agglomerates. Samples “5” (low concentration), “8” and “9” (high concentration) will be studied in detail. Figures 39-a and -b demonstrate absorption Soret band of grafted H2TCPP of centrifuged hybrids of samples “5” and “8”, and whose corresponding pure dye Soret band are given previously in figures 9-a and 9-b, respectively.

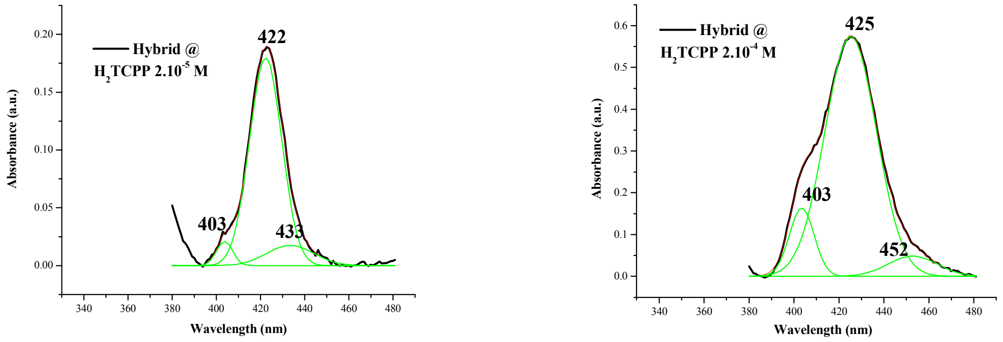

(a) (b)

Figure 39. H2TCPP Absorption spectra of the Soret band of grafted dyes of centrifuged hybrids: (a) sample “5” and (b) sample “8”. Green lines show the individual fitting components; their summation in red solid line is the best fit to the experimental absorption spectra. (Identical x-scale)

Soret band of sample “9” is also presented in pure solution (figure 40-a same as figure 9-c), in non-centrifuged solution (figure 40-b) and centrifuged solution (figure 40-c). Hence through figures 40, we can see the evolution of the bandwidth and the fitting components especially those at around 404 nm whose development insinuates the existence of H-aggregates. The quasi-similar broadening in the centrifuged “8” and “9” Soret band originates from higher dye concentration arising more intermolecular interactions thus higher degree of H-aggregation. While the fitting of the non-centrifuged sample “9” (figure 40-b) is almost described as the same as its corresponding pure dye behavior, indication of the effects of highly non-grafted dye density.

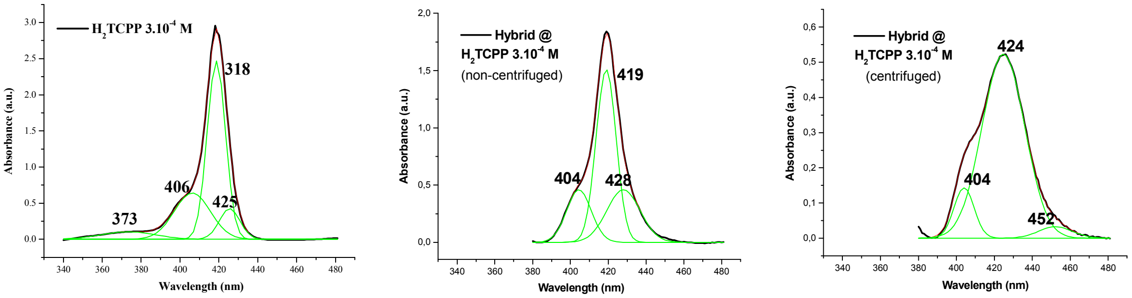

(a) (b) (c)

Figure 40. Absorption spectra of the H2TCPP Soret band of (a) pure dye, and its corresponding treated (b) non-centrifuged and (c) centrifuged spectra of dye-grafted ZnO solution: of Sample “9”. Green lines show the individual components; their summation in red solid line is the best fit to the experimental absorption spectra. (Identical x-scale)

Up to now, absorption analysis plots had revealed that aggregated pure dye molecules in THF at concentrations less than ($<6.10^{-5}$ M) are grafted separately onto the ZnO nanorod surface. At dye densities higher than $6.10^{-5}$ M, H-aggregated dyes become more abundant with increasing dye amount noticeable through the less absorption if compared to those of free dyes.

### 4.4.3.2 Photoluminescence measurements

Excitation spectra of grafted dyes at different concentrations (figure 41) were registered at 652 nm being the maximum λ emission.

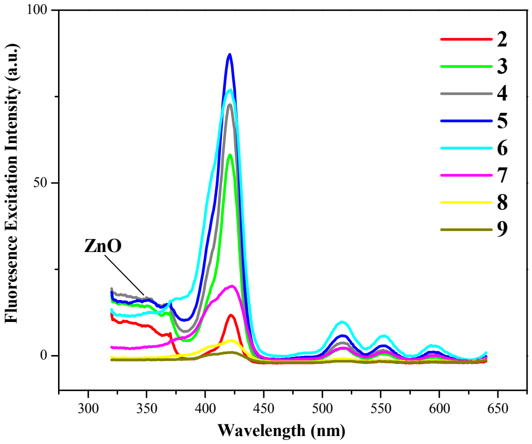

Figure 41. Fluorescence excitation spectra of the hybrids (after centrifugation) at different dye concentrations.

For low dye concentration (< $6.10^{-5}$ M), Soret band intensities in the excitation plots (figures 41) are in agreement with their corresponding Soret band absorption of figure 38-b, which is reported in higher absorption of the grafted dyes in comparison with the non-grafted ones. At these dye concentrations, we can also see that the ZnO contributes to the dye emission. While at higher dye concentrations, broadening and quenching of the Soret band upon increasing the dye concentration is the direct consequence of aggregation of grafted dye molecules. Once again we can see that at dye concentration (>$6.10^{-5}$ M), the contribution to absorption by apparition of the blue-shifted peak in the Soret band becomes more intense when adding dyes, implying that the aggregation is of H-type. And as in the previous case, the ZnO contribute to the dye emission by injecting electrons to the dye's LUMO. This contribution increases up to dye concentrations less than $6.10^{-5}$ M, further than this concentration the ZnO input diminishes due to the induced charged layers that are enlarged by adding further dye, blocking thus any charge exchange between ZnO rods and the dyes, as was proven with the ZnO snanospheres.

Photoluminescence spectra of the hybrids at 325 nm excitation (figure 42-a) show UV exciton and defects emission bands of ZnO as well as the dye emission. Here, the exciton emission of the ZnO nanorods is positioned at 372 nm and exhibits "no" bleu-shift upon dye addition, as before, due to the fact that the confinement effect induced via grafting is not identified in the nanorods because of their huge dimensions if compared to the Bohr radius. However, the space charge layer at the ZnO/H2TCPP interface exists and will grow with dye amount. On the other hand, ZnO exciton and defects intensities are quantified in figure 42-b. The diminution in the exciton intensity is as explained earlier with the ZnO nanospheres, via electron transfer to the dye and the increase of non-radiative recombinations. The intensity drop of the green emission of the band of defects of ZnO with the concentration of dye is accompanied with a slight progressive shift in this defect band position from 560 to 574 nm when going from sample “1” till sample “9”. This means that with rising the dye density, more oxygen vacancies trap centers are passivated by the dye acid group.

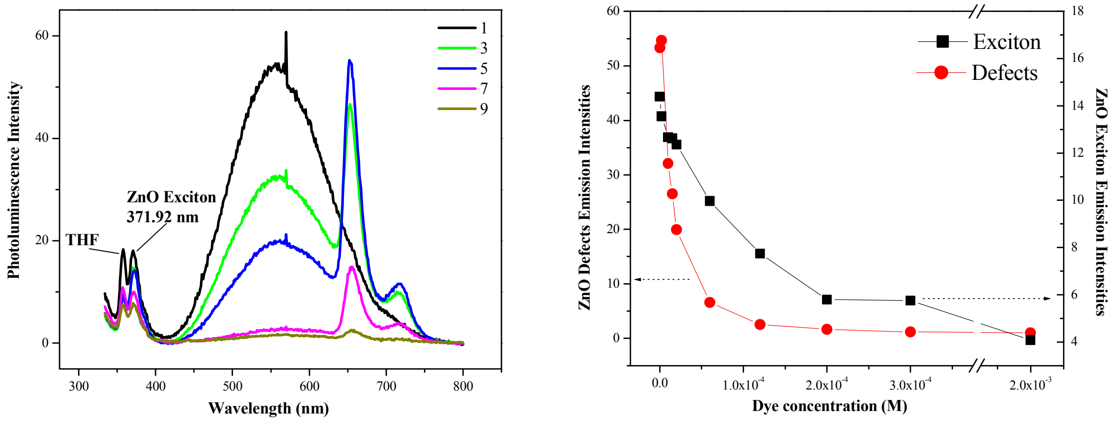

(a) (b)

Figure 42. (a) Global view of Fluorescence emission spectra of some centrifuged hybrids. (b) ZnO exciton and defects emission intensities as a function of dye concentration (excitation wavelength was at 325 nm).

Derived statistics on fluorescence intensities of the intense dye Emission peak (at 652 nm) of pure and grafted-dye in non- and centrifuged samples are depicted in figure 43. Previously absorption data (figure 38) showed that grafting of almost total dye quantity is taking place in the samples with dye concentrations up to $2.10^{-5}$ M (sample “5”) beyond which dye aggregation on the ZnO surface becomes prominent. Fluorescence emissions analysis (see figure 43) reflected this reality through strong increasing intensities of grafted dye emission in the centrifuged samples with increasing dye concentration to be peaked at the sample “5” of $2.10^{-5}$ M dye concentration, whereas the surplus non-grafted dye before centrifugation quenches further the emission intensity. Beyond this concentration the emission is strangled due to aggregation between the grafted molecules of dye in centrifuged samples, while free dyes in the non-centrifuged samples follow the emission rules of pure dye solutions. Hence, at low dye concentration ($<6.10^{-5}$ M), the isolated adsorbed dyes on the ZnO absorb and emit much more than the agglomerated pure free dyes, as clearly seen in figure 43, thanks to some electron and energy transfers from ZnO to the dye as evidenced by the fluorescence excitation data in figure 41. For higher dye concentrations, grafted dye aggregates quench their emission rendering it lesser than free dyes emission.

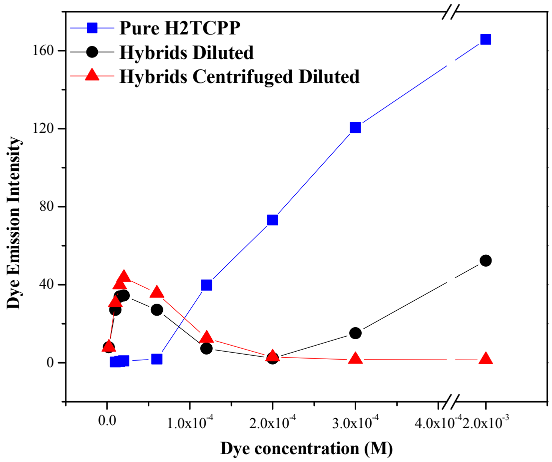

Figure 43. Intensities of dye Emission peak (at 652 nm) of pure dye and grafted dyes in hybrids before and after centrifugation as function of dye concentration at excitation 325 nm.

At 420 nm excitation wavelength, intensities of dye emission peak at 652 nm of pure dyes and hybrids are plotted in figure 44 as function of dye concentrations. Identical conduct of dye emission in hybrid systems is noticed for excitation at either 325 or 420 nm. However, differences emerge in highly concentrated pure dye solutions where the emission starts to be quenched at dye concentrations equal or higher than 1.10$^{-4}$ M (figure 44). This quenching is due to the J-aggregates formation as revealed previously in figure 11-a, which shows that the contribution from absorption at 420 nm decreases severely at high concentrations because of the splitting in the Soret band peak. This provokes reduced emissions due to reduced absorption at 420 nm. Whereas exciting at 325 nm (see figure 43) promotes the contribution of absorption of all the present peaks in figure 11-a even the splitted ones, leading to a gradual increase in the emission intensity (figure 43).

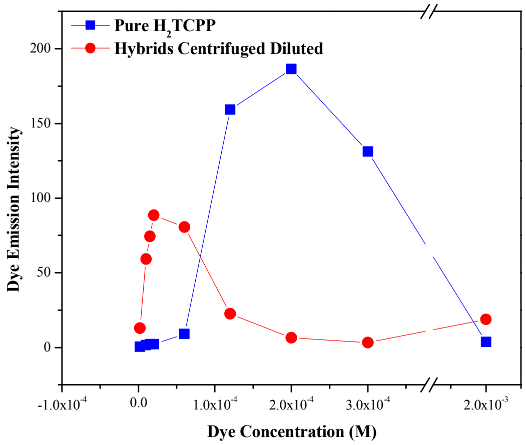

Figure 44. (a) Fluorescence emission spectra of centrifuged hybrid samples at 420 nm excitation wavelength. (b) Intensities of the intense dye Emission peak (~652 nm) of pure dyes and hybrids after centrifugation for different dye concentrations.

Estimated quantum yields of the pure and grafted H2TCPP are illustrated in figure 45. In free dyes case, the quantum yields increase to some extent then decrease due to aggregate formation with increasing dye concentration according to its dye fluorescence emission. However, the decrease of the dye quantum yield in the hybrid systems with increasing concentration corresponds to the conclusion stating that this fall in quantum yield is essentially due to the non-radiative decay of the absorbed energy among the aggregates besides to the electron injection to the ZnO at very low grafted-dye concentration (as already supposed in the previous case of ZnO nanospheres). Isolation of the low grafted-dye molecules densities on the surface of ZnO implies reduction in non-radiative relaxation channels meaning quantum yield improvement once compared to the pure dyes. At higher concentrations, abundance of quenching dye-aggregate centers in the hybrid systems cause the decrease in the quantum yield to values less than their corresponding pure dyes.

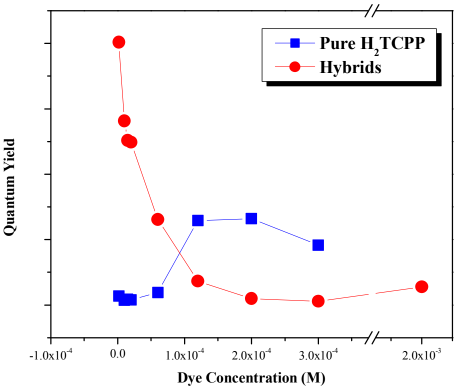

Figure 45. Comparison of Quantum Yield of free (■), and adsorbed (●) dyes onto the ZnO nanorods. (Excitation wavelength at 420 nm).

Summing up, we have observed via the photoluminescence and excitation data analysis of the H2TCPP/ZnO nanorods that:

▪ At dye concentration lower than $6.10^{-5}$ M, the dye fluorescence was enhanced due to the relatively isolated grafted-dyes, that absorb and emit more than their corresponding free dye solutions.

▪ At 325 nm excitation wavelength of samples with dye concentrations lower than $6.10^{-5}$ M, the emission of H2TCPP molecules is promoted because of the ZnO contribution via two possible ways:

(i) Forster energy transfer that is of small input as demonstrated at the introduction of this chapter, but its input here in the case of nanorods hybrids is constant for all samples because we observed no blue-shift of the ZnO nanorods exciton emission as in the previous case of ZnO nanospheres.

(ii) Electron transfer that is probably the dominant charge exchange mechanism, but its contribution decreased when increasing the dye densities because of the formation of charged layers at the ZnO/dye interface, reducing thus the electron transfer from ZnO to the dye molecules.

- At $6.10^{-5}$ M and higher densities, the aggregation among the dyes becomes dominant causing the dye emission quenching.
- The improvement in fluorescence quantum yield in the hybrid matrices, compared to the pure dyes at low concentration, is interpreted as a diminution of non-radiative relaxation channels through isolation of the grafted-dye molecules on the surface of ZnO nanorods. This strong improvement in the quantum yield dies away with amplified dye-aggregates at higher concentrations inducing more quenching centers.

Furthermore, fluorescence time resolved measurements in the next section can contribute to understand certain molecular interaction in the hybrid matrix by measuring the changes in its components' fluorescence lifetime.

#### 4.4.3.3 Time-resolved fluorescence decay of free H2TCPP and H2TCPP/ZnO hybrids

H2TCPP fluorescence lifetime was studied in its free and grafted state (on ZnO nanorods) in THF solution-based at a concentration of $2 \times 10^{-4}$ M, as normalized and depicted in figure 46. Excitation wavelength of 400 nm was used to excite the dye that absorbs significantly at this wavelength. The time-resolved fluorescence was then performed for the emission wavelength at 652 nm, knowing that identical behavior goes for the emission wavelength at 716 nm. Experimental setup along with its operational functioning is given in the Appendix IV.

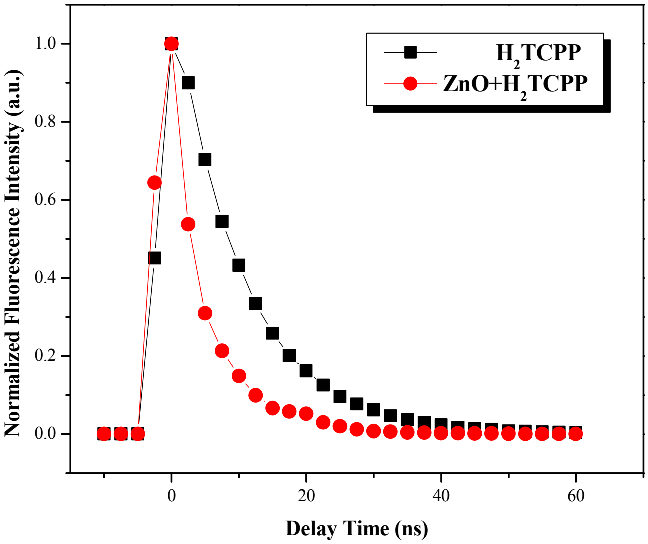

Figure 46. Fluorescence decay time measurements of fluorescence lifetime was studied free-H2TCPP and grafted-H2TCPP on ZnO nanorods in THF solution at a concentration of $2 \times 10^{-4}$ M,

Normally, fluorescence time decay profiles can be fitted through several exponential by:

$$I(t) = \sum_i A_i e^{-\frac{t}{\tau_i}} \tag{4-9}$$

$A_i$ being the individual intensity amplitude.

In pure H2TCPP, the time profile at 652 nm fits a first-order decay with $\tau_1 = 11.27 \pm 0.35$ ns.

While in hybrid systems, the decay profile at 652 nm fits a second-order decay (see figure 46) with a fast time and slower fall time of $\tau_1 = 2.52 \pm 0.19$ ns and $\tau_2 = 8.5 \pm 0.63$ ns.

Analyzing these obtained experimental data seems to be a non-easy task because more precise time-resolved experiments must be performed, but we will try to give some rational assumptions. Fluorescence lifetime $\tau_f = \frac{1}{k_r + k_{nr}}$ (refer to equation (2-9) chapter 2) reflects the behavior of radiative decay $S_1 \rightarrow S_0$ in the H2TCPP dye, where $k_r$ measures the radiative rate and the $k_{nr}$ the non-radiative ones.

Grafting the H2TCPP into the surface of the ZnO nanorods leads to visible changes in its both fluorescence lifetime and intensity that is severely quenched as seen in figure 44 and was ascribed to the dye aggregation at this dye concentration of $2 \times 10^{-4}$ M. The aggregation among the dye molecules greatly enhances the rate of non-radiative transitions ($k_{nr}$) [27], hence decreasing the radiative fluorescence lifetime. We have also seen that hybrid systems exhibit at 652 nm a radiative decay composed of two exponential fits. This means that a part of the excited charges in the grafted-dye's LUMO level is involved in mechanisms other than the simple radiative decaying process, thus inducing rapid decaying of the other remaining part of the excited charges. In addition to the aggregation effect, several nonradiative relaxation processes as the intersystem crossing (to the triplet state $T_1$), the internal conversion (in the dye itself $S_2 \rightarrow S_1$) and the interfacial electron transfer (to the ZnO) could occur. These factors increase the nonradiative rate $k_{nr}$, thus decreasing the radiative time decay.

However, we can believe that fitting the decay profile of the grafted-dye by two-exponentials is attributed to the grafting effects on the ZnO nanorod surface that is delimited by unequivalent facets components implying different facets polarities; that is the ZnO surface is constructed with Zn planes, with Zn and O planes, and with O planes. For that reason, different grafting influences (via different distribution of surface charges) are induced implying the nonhomogeneity in the dye grafting. This fact could be the cause of the existence of two different decaying times due to dissimilar channel charge exchanges among the H2TCPP and the different ZnO surfaces.

### 4.4.3.4 Fourier Transform Infra Red measurements (FTIR)

Upon dye molecular adsorption onto the ZnO oxide material, surface species are generated by reactions at the interface of the present components. Vibrational spectroscopy provides the most definitive means of identifying these surface species. Fourier Transform Infrared (FTIR) spectroscopy is the standard technique for chemical characterization and has proven useful for the study of dye structure and dye adsorption behaviour on the ZnO. It is based on the fact that infrared illumination stimulates molecular vibrations and rotations. Infrared energy will only be absorbed if there is a net change of dipole moments due to the vibrational and rotational motion of the molecule. This energy adsorption is monitored to construct the FTIR spectrum as a function of the wavenumber ($cm^{-1}$), which is inversely related to the wavelength. The FTIR set-up is illustrated in the Appendix V.

Figure 47 shows the IR spectra of the pure ZnO nanorods, the pure H2TCPP and the H2TCPP/ZnO hybrids over the range of 600-3800 $cm^{-1}$. Samples were prepared by drop-casting the colloidal solution onto a germanium wafer to be dried afterwards under ambient temperature. Hence the samples were measured in their solid form. The hybrid used was a centrifuged one with a dye concentration of $3 \times 10^{-4}$ M, along with its analogous pure dye.

In pure ZnO, the broad band at 3500 $cm^{-1}$ is assigned to the O-H stretching mode of hydroxyl group, originating from the hygroscopic nature of ZnO [49]. Peaks between 2830 and 3000 $cm^{-1}$ are attributed to the C-H stretching vibration of alkane groups [49]. The peaks observed at 1454 and 1570 $cm^{-1}$ are probably due to the symmetrical and asymmetrical stretching of the zinc carboxylate, respectively. All of this suggests the presence of impurities near the ZnO surface, from some remaining traces of the ZnO-synthesis reaction components. In solid-state pure H2TCPP, strong C=O bands with a shoulder (1726 $cm^{-1}$) are located at 1690 $cm^{-1}$ [5]. The peak at 1283 $cm^{-1}$ is due to the stretching mode C-O of the carboxylic acid groups [50]. The other prominent bands over the range of 700-1500 $cm^{-1}$ are due to the ring stretching modes of the porphyrin, as C-H, C=C and C=N [51]. In FTIR spectrum of the adsorbed H2TCPP on ZnO, the C=O and C-O stretching modes disappear relatively with the appearance strong and broad of carboxylate symmetric $–COO^{-}_{s}$ (1404 $cm^{-1}$) and asymmetric $–COO^{-}_{as}$ (1605 $cm^{-1}$) bands. Knowing that hybrids at this dye concentration manifest high degrees of aggregation; the presence of carboxylate bands in the IR spectrum of grafted-H2TCPP on ZnO show that majority of the carboxylic acid groups are adsorbed on the ZnO surface while the rest is created by the dimerization among the aggregated dyes.

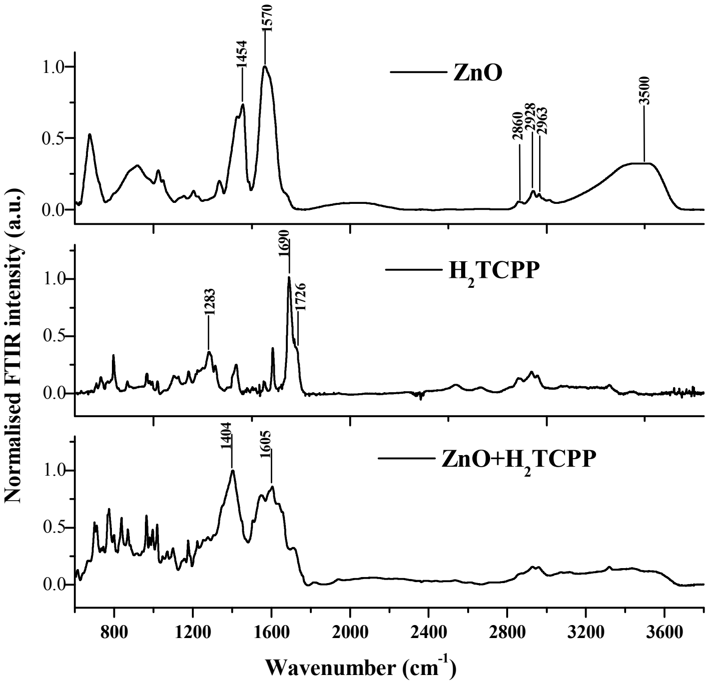

Figure 47. FTIR spectra of pure ZnO, pure H2TCPP and H2TCPP/ZnO hybrids.

The possible binding modes for porphyrins containing carboxylic acid groups on a metal oxide are schematically depicted in figure 48. Carboxylic acids form stable covalent bonds with metal oxide nanoparticles such as TiO2, mainly through bridging bidentate mode (III in figure 48) [5,50]. Lately, carboxylic acid groups binding to ZnO was found to be a bidentate carboxylate binding mode (figure 48, type II and/or type III) [52].

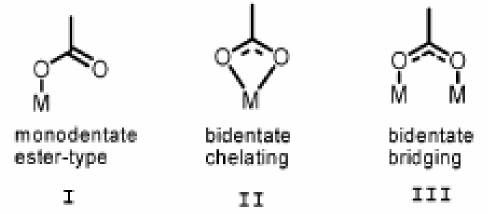

Figure 48. The three main binding modes between a COOH carboxylic acid group and a metal oxide surface.

Briefly, from the changes in the 1350-1700 cm$^{-1}$ carbonyl region in the FTIR plots, we can assume that the COOH groups of the H2TCPP dye bind as bidendate carboxylate (II and III in figure 48).

### 4.4.3.5 Effects of introducing alkyl Chains in the grafting process

In order to get a deeper understanding of the different processes that are related to the dye-induced fluorescence emission quenching of the ZnO defect band, the $C_6H_{11}COOH$ acid with alkyl chain at a concentration $8.10^{-2}$ M was adsorbed on the surface of pure ZnO nanorods under identical conditions as described in the case of $H_2$TCPP-ZnO at $2.10^{-4}$ M dye concentrations. We can clearly assume that at these concentrations, $4{,}8.10^{17}$ carboxyl groups (COOH) are assigned to the dye, while $4{,}8.10^{19}$ carboxyl groups to the alkyl chain, thus an amount of hundred times higher than the dye.

Fluorescence spectra shown in figure 49, demonstrate that severe drop in the ZnO defect band in addition to a drop in the ZnO exciton is taking place when grafting the H2TCPP dye onto the ZnO (*green line*). While acid alkyl chains at very large concentrations leave the intensity of ZnO exciton intact and passivate slightly the ZnO surface oxygen vacancies without inducing severe reduction in the ZnO exciton and defects emission as when grafting the dyes (*red line*).

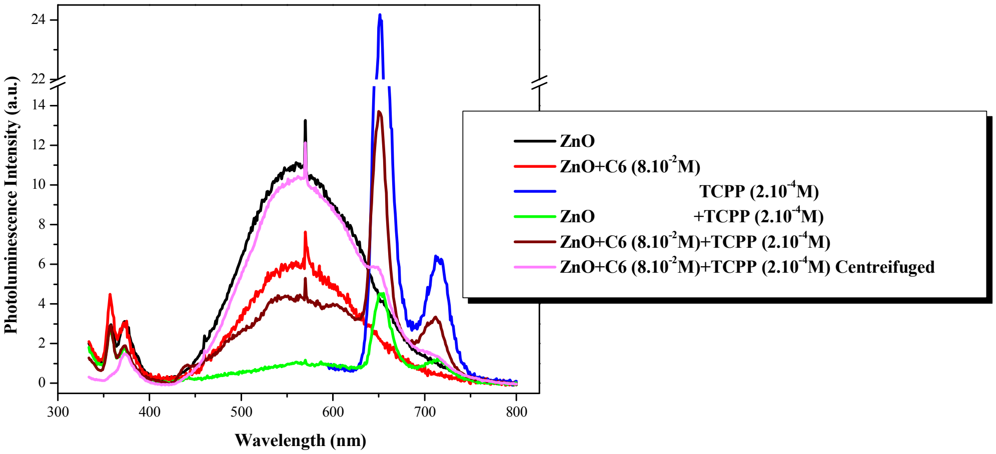

Figure 49. Fluorescence emission of pure ZnO, pure H2TCPP and blends of ZnO/$C_6H_{11}COOH$/$H_2$TCPP at several conditions.

Hence, these facts confirm the existence of more complex photophysical mechanisms to explain the decrease in the ZnO defect band when grafting the porphyrin that do not exist when grafting the alkyl chains. These photophysical processes are explained earlier in much detail as presented in the figure 27. The steep decrease in the defect band reinforces the reality of electron transfer from the ZnO to the dye's LUMO, thus decreasing both the ZnO exciton and defects emission. Another mechanism can also be responsible of the defect quenching; this mechanism is the enhancement of the interfacial non-radiative recombinations from both ZnO conduction band and defect level via the HOMO level of the dye, whose further addition will increase the probability of non-radiative recombinations. All of these facts leave relatively lesser electrons in the ZnO conduction band to be trapped in the defect level and finally to radiatively recombine, hence, the progressive diminution with increasing dye concentration in the radiative recombinations of ZnO defect emission.

On the other hand, blending the dyes with the two hours-aged mixture ZnO/$C_6H_{11}COOH$ leads to an increment in the dye emission with respect to that in the hybrid

$ZnO/H_2TCPP$ (see figure 49). This increment is due to the presence of the acid chains that prevents the grafting of a large amount of the present dye, hence the high quantity of free dyes will tend to imitate to some extent that of pure dye solution. Surprisingly, centrifugation of the same sample, i.e. the blend $ZnO/C_6H_{11}COOH/H_2TCPP$, induces a restoration of the ZnO defect band and a small dye emission. This means that a major part if not all of the $C_6H_{11}COOH$ acid was expelled by the centrifugation due to their weakly bonding via its single carboxylate terminal to the ZnO. The presence of the dye emission insinuates that the dyes are attached firmly to ZnO thanks to their four carboxylate groups.

Briefly, through grafting alkyl chains, we clarified and confirmed the main photophysical processes that imply the decrease in the ZnO exciton and defects emissions upon increasing the grafted dye densities. We proved the fact of electron transfer from the ZnO as well as the enhancement of the non-radiative recombinations processes with mounting the dye concentrations. We also confirmed that the dye molecules are firmly binding to the ZnO surface.

### 4.4.3.6 Concluding annotations on H2TCPP/ZnO nanorods

Following the same reasoning given in the concluding remarks of nanosphere-based hybrids; we can believe that 522 flat dye molecules are needed to totally cover the surface of one ZnO nanorod, whereas 2000 molecules are needed for the edgewise oriented H2TCPP. At $6.10^{-5}$ M dye density, 486 dye molecules are available for each ZnO nanorod, as stated by table 2. This dye number approaching the 522 number of total flat coverage means that aggregation will be appearing for this dye density and higher densities as well. Whereas the 162 dyes available for sample “5” with $2.10^{-5}$ M concentration were isolately adsorbed and displayed higher absorption and emission than its parallel pure dye. Hence, H2TCPP molecules lying flat on the ZnO nanorod surface corresponds to a 29% of surface coverage for sample “5” with the $2.10^{-5}$ M density.

Fairly comparable optical aspects are found in the nanorod-based hybrids as in the previous case of nanosphere-based hybrids.

▪ ZnO nanorods offer less total grafting surface with respect to the small nanosphere, so we expect to reach grafted-dye aggregation at concentrations lower than that with nanospheres. Indeed, we assumed that hybrids with dye concentrations equal or higher than $6.10^{-5}$ M make evident the aggregation among grafted dye molecules, while dye aggregation starts to be evident in the nanospherical hybrids for grafted dye concentrations higher than $1.10^{-4}$ M.

▪ Absorption and fluorescence analysis plots demonstrate that aggregated pure dye molecules suspended in pure solutions at concentrations less than ($< 6.10^{-5}$ M) become isolated to some extent once grafted onto the ZnO nanorod surface. Additionnaly, at these concentrations and at an excitation wavelength of 325 nm, the emission of the H2TCPP dye increases because of the ZnO contribution by transferring small but constant amount of energy via Forster model whereas the electron transfer mechanism is likely to decrease upon increasing the dye due to the charge layer formation at the ZnO (nanorod)/H2TCPP interface. Whereas, energy and electron transfer were different in the case with the nanospherical hybrids where we have demonstrated that the Forster energy transfer input decreases while the electron transfer process increases. This is because of the decreased blue-shifted ZnO exciton hence increasing the band gap energy with increasing dye density in the case of ZnO nanospheres. However, no change in the ZnO energy gap was detected with nanorods hybrids due to its large volume to surface ratio with respect to that of the nanspheres.

▪ For dye concentrations higher than $6.10^{-5}$ M, H-aggregated dyes on the surface of the ZnO nanorods become more abundant with increasing dye amount as manifested by the less absorption and quenched emission than free dyes.

▪ The upper stated details guide to the strong improvement in the florescence quantum yield in hybrid systems that fade away with increasing dye concentration indicating an enhanced non-radiative decay of the excited aggregates. This statement was also equally found in the nanospherical hybrids.

▪ Through time-resolved fluorescence several hypotheses were driven concerning electron transfer and aggregates effects. While, via FTIR spectra we confirmed the grafting by the apparition of carboxylate symmetric and asymmetric binding modes.

Hence, we can tell that through optical data we have found interesting outcomes from the H2TCPP dye grafting on both ZnO nanospheres and nanorods.

Hereafter, we will study the optical properties of the hybrids elaborated by adsorbing the PP9 porphyrin dye molecules onto the surface of ZnO nanoparticles of spherical and rod-like shapes.

## 4.5 PP9-ZnO hybrids

### 4.5.1 Optical properties and organization of pure PP9 in THF solutions

PP9 molecule structure, shown in figure 50-a, is a molecule functionalized by two carboxylic acid groups. Absorbance spectrum of this porphyrin (figure 50-b) reveals an intense near-UV Soret-band absorption peaked at 406 nm and four Q-bands in the visible spectral region of 500-640 nm. We note that this wavelength absorption is slightly shorter than that of the H2TCPP, thus promoting the energy transfer via Forster model as already stated in the introduction part of this Chapter. Two fluorescence emission peaks are situated at 634 and 702 nm in addition to a small emission located in-between for an excitation wavelength of 407 nm (figure 50-b).

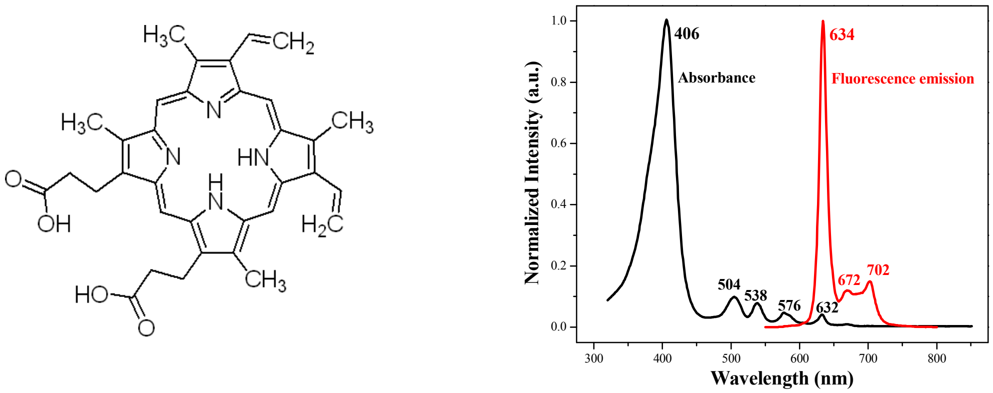

(a)

(b)

Figure 50. (a) PP9 structure along with its (b) absorbance and emission spectra.

Identical dye concentrations are adopted for PP9 as in the previous case. Simple Gaussian deconvolution of the Soret absorption peak give in four individual bands in the two pure dye solutions of $2.10^{-5}$ and $2.10^{-4}$ M, as seen in figure 51. Spectral maxima and bandwidths of these components are written on the plots. The existence of four fitting peaks in the pure dye Soret band indicates the presence of both H- and J-aggregates. The relatively intense blue shifted peak at 389 nm in figure 51-a, if compared to figure 51-b, reveals that the H-aggregates are more abundant than the J-aggregates at low concentration.

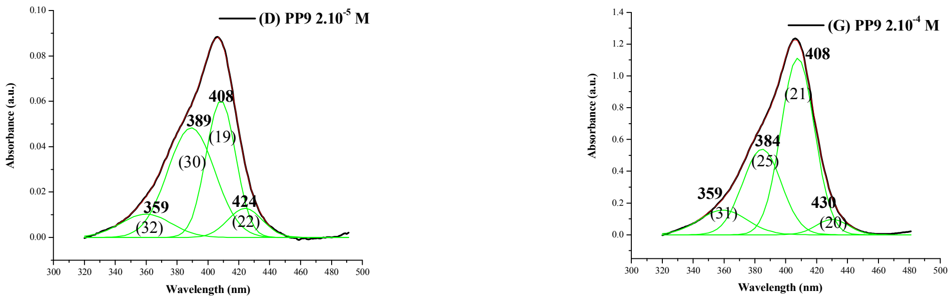

(a)

(b)

Figure 51. PP9 Absorption spectra of the Soret band of pure dye at (a) $2.10^{-5}$ and (b) $2.10^{-4}$ M. Soret Band fitting maxima are written and bandwidths at half height (nm) are given in brackets. Accuracy in the absorption maxima and bandwidths is about ± 1nm.

Emission spectra at 407 nm excitation wavelength of pure dyes are presented at different concentrations in figure 52-a and whose intensities at the three different emission peaks are summarized in figure 52-b. Furthermore, fluorescence excitation measurements of these free dyes are shown in figure 52-c and were registered at the value of λ emission 634 nm. Let us try to correlate between the above mentioned fluorescence plots. The Soret bands in the excitation plots peaked at 406.02 nm match that of the absorbance plots. J-aggregation among free dyes begins to appear for concentration of $2.10^{-4}$ M as demonstrated by the broadening and splitting of the Soret band (figure 52-c) similar to the previous case with H2TCPP [34]. That's why the emission starts to be quenched at this concentration as clearly seen in figures 52-a and -b. On the other hand, excitation spectra of figure 52-c tell that the very intense dye emission at 634 nm (figure 47-b) originates from the total absorption of the free dyes, while the two other emission peaks remain relatively weak.

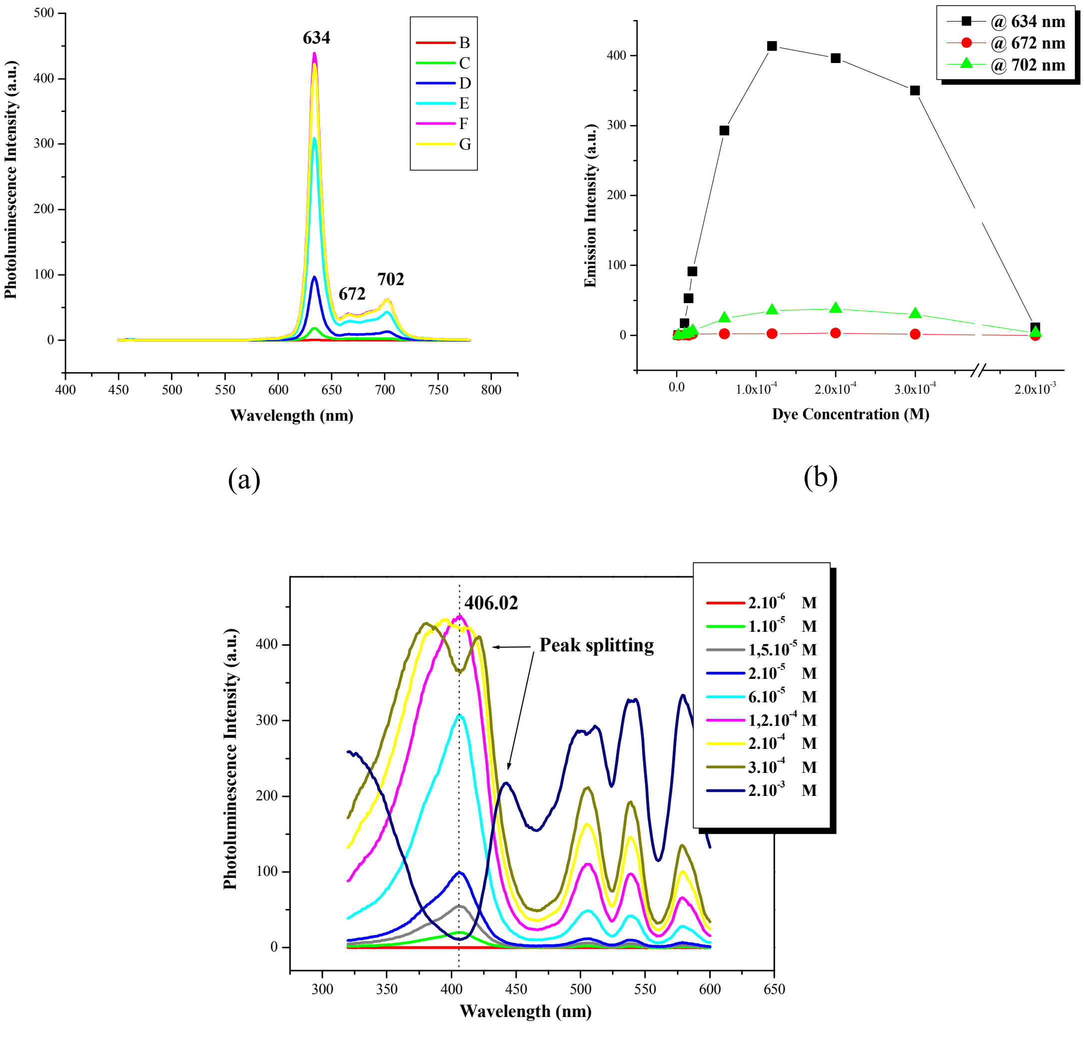

(a) (b)

(c)

Figure 52. Pure dye solutions fluorescence (a) emission spectra at 407 nm excitation wavelength, (b) their corresponding intensities for different emission peaks, and (c) their corresponding excitation spectra at 634 nm emission wavelength.

Through our observational version, we can suggest that pure dyes in THF solutions are generally softly H-aggregated for very small dye concentrations, while the J-aggregates are formed for higher concentrations.

Afterwards, PP9 molecules were grafted onto the two same series of ZnO nanoparticles as in the previous case with H2TCPP. Besides PP9 concentrations that were employed are identical to those of H2TCPP.

### 4.5.2 Optical studies of PP9-based nanohybrids of quazi-nanospherical shaped ZnO

Identical operational handling and dye concentrations are adopted in grafting the PP9 as in the previous case. We can then refer to Table 1 previously listed in the H2TCPP case. Samples emanating from dilution of mother samples along with their corresponding centrifuged mother samples are examined through optical studies to analyze grafting conditions and effects.

#### 4.5.2.1 Absorbance measurements

High material concentration causes a signal saturation in the UV-Vis absorption spectra of the “concentrated’ hybrid PP9-ZnO samples at different dye concentrations in THF, as shown in figure 53-a.

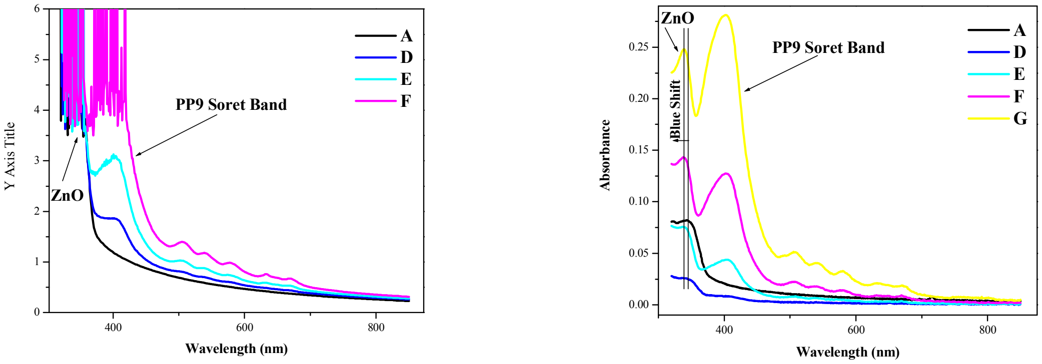

(a) (b)

Figure 53. Absorbance spectra of (a) mother-concentrated PP9-ZnO hybrid solutions at different dye concentrations, and (b) upper colorless liquids of the non-agitated samples.

We noticed that the precipitation of the hybrid species in the case of PP9 is less significant and greatly slower than the precipitation in the case of H2TCPP. That’s why we still find some amount of suspended species in the upper rested liquid (53-b). Accidental small quantity of pure ZnO sample “A” are still floating at rest owing to their slight weight. Over-weighted by the grafted dye molecules, the samples “D” and “E” show less presence of hybrids in the upper liquid. The significant quantity of dye-grafted ZnO floating in the upper liquid means that these hybrids are much more soluble in the case of PP9 than in the case of H2TCPP.

Absorbance spectra of the “diluted” and their corresponding treated “centrifuged diluted” spectra of dye-grafted ZnO “D” and “G” samples along with the pure dye absorption are shown in figure 54-a and -b, respectively. In each hybrid sample, the Q absorption peaks in the grafted systems are red-shifted with respect to those of the pure dye as clearly quantified by position peaks values, confirming the occurrence of dye grafting.

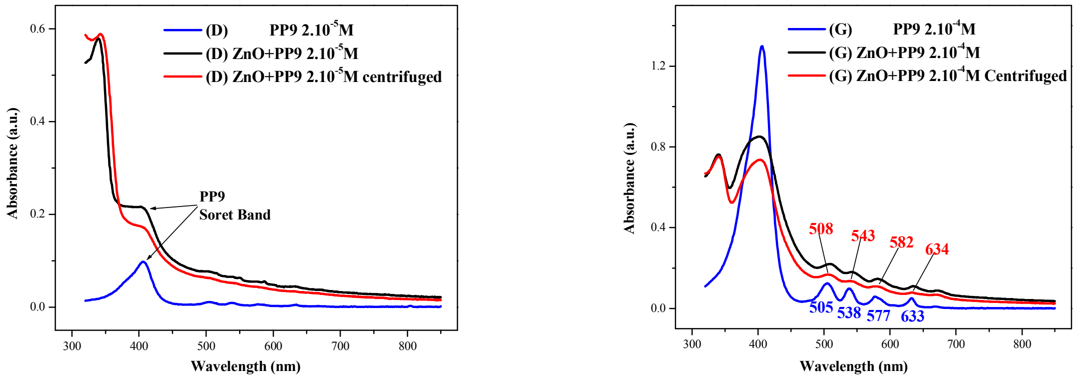

(a) (b)

Figure 54. Absorbance spectra of “diluted” PP9-ZnO hybrid solutions at different dye concentrations. Absorbance spectra of the “diluted” and their corresponding treated “centrifuged diluted” spectra of PP9-grafted ZnO solutions: (a) Sample “D”, and (b) Sample “G”.

Positions, intensities and widths of the Soret dye peak of pure dye solutions and hybrid solutions before and after centrifugation at different dye concentrations are shown in figures 55-a, -b and -c, respectively. Soret peak positions in the hybrid samples before and after centrifugation are approximately similar, while they differ from those of the pure dye having relatively higher peak positions (figure 55-a). This blue shift in peak position upon dye grafting indicates the presence of H-aggregates, whose formation is reinforced by the broadening of the Soret band upon increasing dye concentration (figure 55-c). Surprisingly, only the first two samples with low dye concentration present slightly higher Soret band absorption intensities in pure dye solutions (see figure 55-b). This fact indicates that the degree of aggregation among grafted dye molecules is practically higher than free dye molecules in almost all samples.

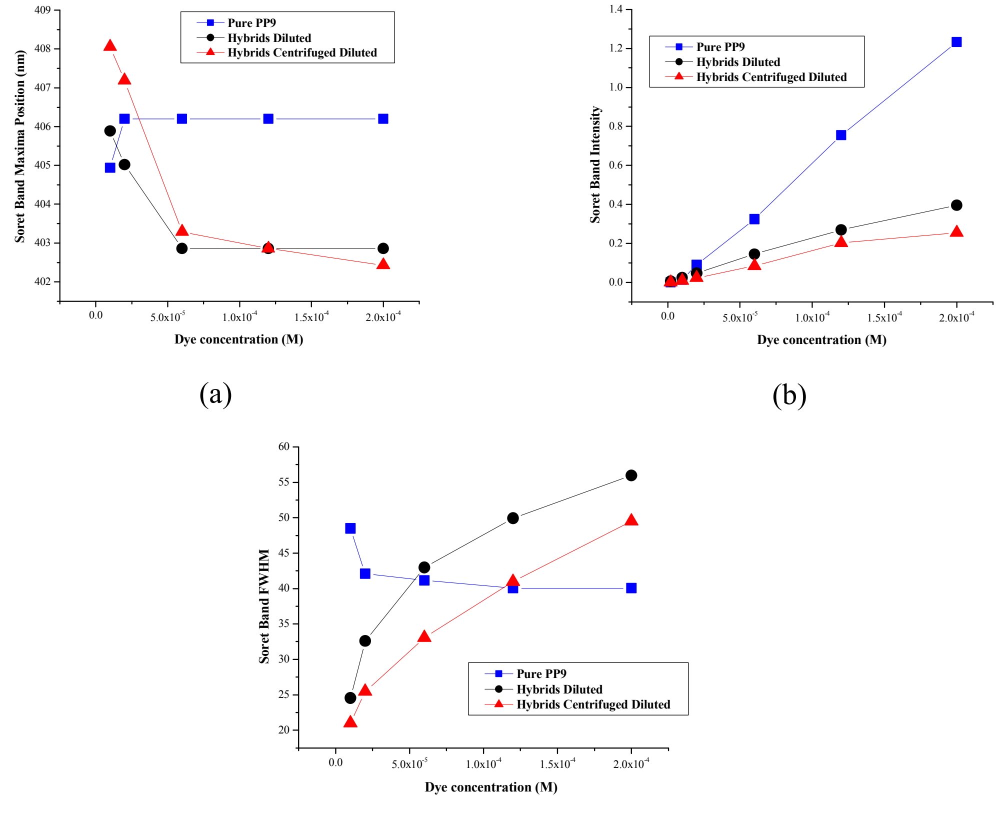

(a) (b)

(c)

Figure 55. Dye concentration dependence of (a) Absorbance positions, (b) intensities and (c) Full Width Half Maximum of the Soret dye peak of pure dyes and hybrids before and after centrifugation.

Detailed studies of the Soret band absorption of two samples illustrate in figures 56 the presence of different fitting components which are characterized by different geometric arrangements of the dyes. Spectral maxima and bandwidths of these components are also illustrated and must be compared to their corresponding pure dye solutions in figures 51-a and -b.

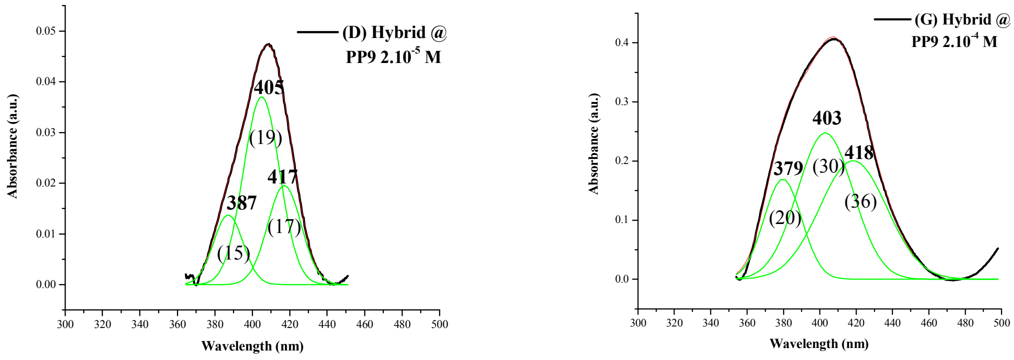

(a) (b)

Figure 56. PP9 Absorption spectra of the Soret band of centrifuged hybrids (a) sample “D” 2.10$^{-5}$ M and (b) sample “G” 2.10$^{-4}$ M. Soret Band components maxima are written and bandwidths at half height (nm) are given in brackets. Accuracy in the absorption maxima and bandwidths is about ± 1nm.

The increase in blue shifted dominant peaks at 380 and 403 nm (figure 56-b) with increasing dye concentration in hybrid samples demonstrates that aggregation of adsorbed dyes occurs in the H-aggregation form.

Up to now, from these absorbance measurements, we can conclude that:

- Barely the first two samples exhibit a Soret band absorption slightly higher than their parallel pure dye solutions. Hence, the aggregation among the grafted-PP9 molecules is likely to be instantly if compared to that with the H2TCPP.

- Aggregation of adsorbed dyes is believed to occur in the H-aggregation form.

### 4.5.2.2 Photoluminescence measurements

Emission and excitation measurements of grafted dye molecules in centrifuged hybrid systems are portrayed in the ensemble of figure 57. Interestingly, the relative dye ratios of the three different emission peaks (figures 57-a and -b) differ radically from those of pure dye emission peaks. This indicates the strong modifications of the electronic structure of the dye due to the grafting and charge transfer to the nanoparticles. To find the absorption origin that implies these altered emission peaks, we must refer to the fluorescence excitation measurements. Excitation spectra registered at the value of λ emission 634 nm are shown in figure 57-c, where the absorption red-shift with respect to free dyes highlights the certainty of grafting. The increase followed by a decrease in the emission at 634 nm (figure 57-b) reflects precisely the behavior of the absorption responsible for these emission intensities (figure 57-c). Emission at 702 nm follows the same trend as the emission at 634nm. Aggregation effect arises for dye densities equal or superior than $2.10^{-5}$ M, when emission at 672 starts increasing at the expense of the decreasing 634 nm as visible in figure 57-b. Excitation plots in figure 52-d registered at the 672 nm detection emission for the two samples “E” ($6.10^{-5}$ M) and “G” ($2.10^{-4}$ M) describe blue-shifted H-aggregate dye absorption contribution to the 672 emission. Additional blue-shift and intensity shrinking in the absorption peak in the sample “G” with the highest dye density (figure 57-d) is attributed to development of bigger H-aggregate centers inducing emission quenching (figure 57-b); thus providing a direct proof of H-aggregate formation among grafted dyes when increasing their concentrations. Hence, we confirmed that the radical increase of the PP9 emission peak at 672 nm, at the expense of the other emission peaks at 634 and 702 nm, is attributed to strong alteration in the electronic structure of the H-aggregated dye molecules. Indeed, this H-type arrangement generally leads to strong interaction among the closest dye molecules through what we call “the π-stacking” or “π-π aromatic interaction”. These π-π interactions are caused by intermolecular overlapping of the p-orbitals of two parallel rings of PP9 dye molecules that overlap in a "face-to-face" orientation. These strong intermolecular interactions have a big influence on molecule based on aromatic compounds.

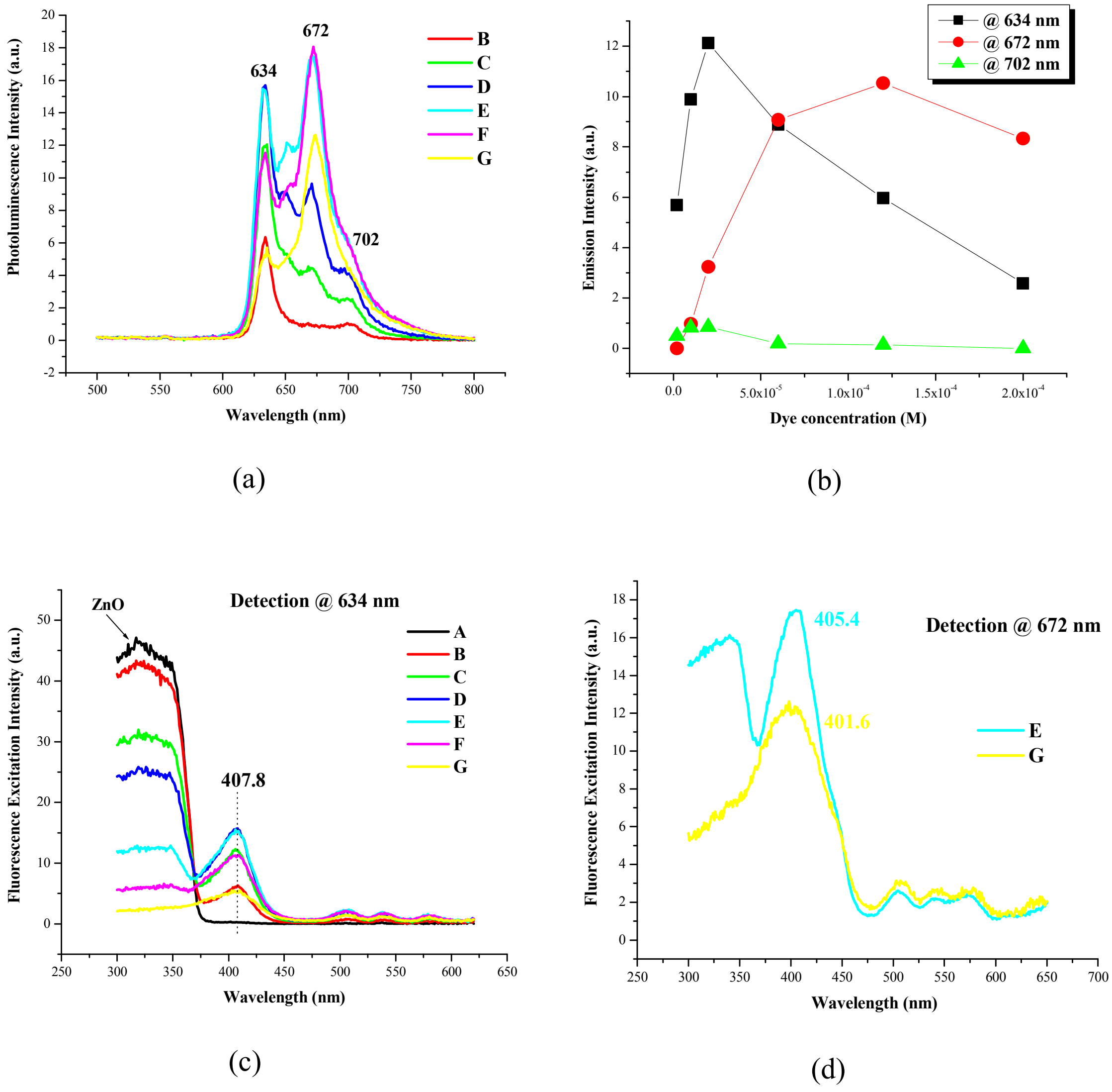

(a) (b)

(c) (d)

Figure 57. Centrifuged hybrids fluorescence (a) emission spectra at 407 nm excitation wavelength, (b) their corresponding intensities for different emission peaks, and their corresponding excitation spectra at emission wavelength of (c) 634 and (d) 672 nm.

The fluorescence excitation spectra pictured in figure 57-c show the ZnO contribution to the emission at 634 nm, as also reflected in figures 58-a by further diminution in the ZnO exciton emission. Drop in the defects green-band emission, in figure 58-b, is caused by an upward diminution of oxygen vacancies upon PP9 dye grafting in addition to other photophysical mechanisms as the interfacial non-radiative recombination.

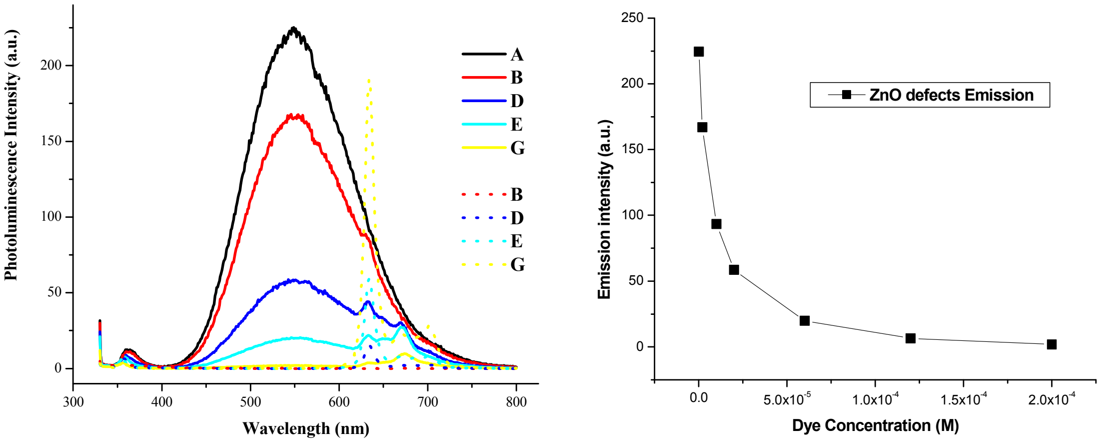

(a) (b)

Figure 58. (a) Treated fluorescence emission spectra for excitation at 325 nm of centrifuged hybrids at different dye concentration. (b) Dependence of ZnO defects emission intensities on dye concentration.

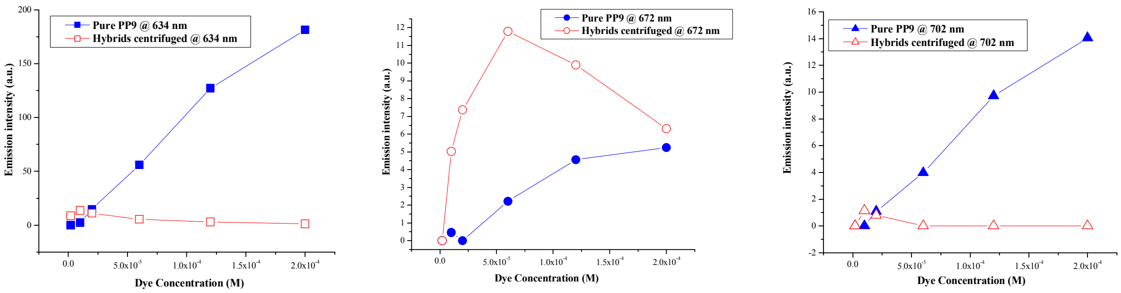

(a) (b) (c)

Figure 59. Fluorescence emission spectra at excitation wavelength 325 nm of free and grafted dyes at (a) 634 nm, (b) 672 nm and (c) 702 nm emission peaks.

Dye emission statistical analyses performed on hybrid emission plots (58-a) and their corresponding pure dye emissions when excited at 325 nm are summed up in figure 59. Identical emission tendencies are registered in the grafted-dye behavior for the two different excitation wavelengths, namely 325 and 407 nm. Emissions at 672 nm of grafted dyes dominate those of pure free dyes as shown in figure 59-b, indicating as previously mentioned the occurrence of strong intermolecular interaction of H-aggregated grafted-dyes. At low dye concentration ($\leq 2.10^{-5}$ M), almost relatively isolated grafted dye molecules emit a little stronger than pure free molecules whose emissions overcome those of grafted dyes at higher concentrations. While in previous case of the H2TCPP porphyrin, we found that for the samples of concentrations up to $1.10^{-4}$ M the grafted-dye molecules are isolated on the ZnO surface, which means that the PP9 even at small amounts tends to aggregate much faster than the H2TCPP.

Similar grafting effects on ZnO nanospheres exciton emission are spotted when using PP9 as in the case of grafting H2TCPP. Figure 60-b summarizes the exciton emission peak intensity and energy dependence of PP9-ZnO nanospheres on dye concentration, derived from the hybrids data for an excitation at 300 nm illustrated in figure 60-a. The adsorption of PP9 molecules leads to decreasing the intensity of ZnO exciton band, which is as well blue-shifted with increasing dye concentration. These very interesting consequences follow the same reasoning as thoroughly explained in the case when grafting the H2TCPP molecules onto the same ZnO nanospheres.

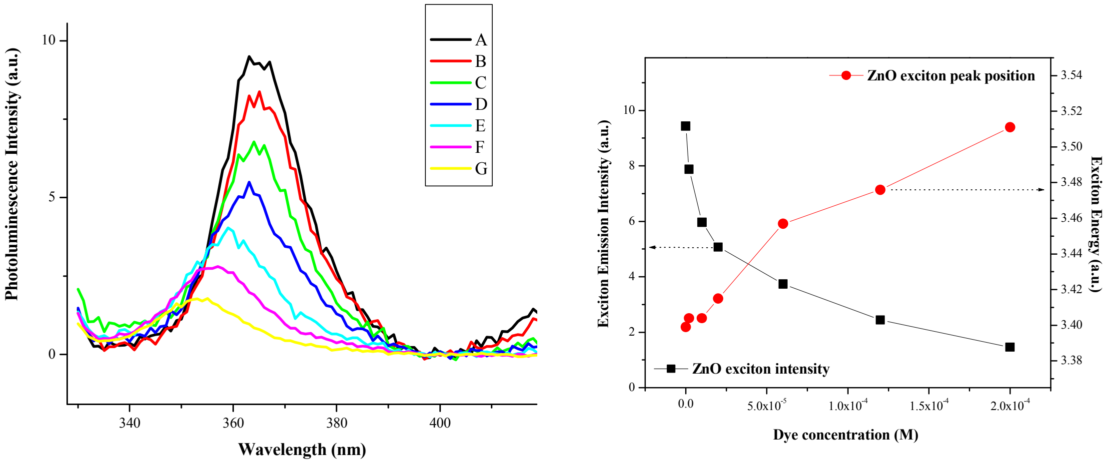

(a) (b)

Figure 60. (a) Fluorescence emission spectra of PP9-based hybrid centrifuged samples at excitation wavelength 300 nm. (b) ZnO exciton peak intensities and positions of the hybrids at excitation 300 nm as a function of dye concentration.

On the other hand, figure 61 provides the comparison between relative Quantum Yields of free and adsorbed PP9 molecules onto the surface of ZnO nanospheres. The observed quantum yield improvement in the hybrid matrices up to $2.10^{-5}$ M dye concentration, compared to the pure dyes is understood as a reduction of non-radiative relaxation channels by the relatively modest isolation of the grafted-dye molecules on the surface of ZnO. For hybrid samples with dye concentrations higher than $2.10^{-5}$ M, the fluorescence quantum yields of the H-aggregated grafted-PP9 diminish with respect to those of pure dye incorporating another type of aggregates (J-type).

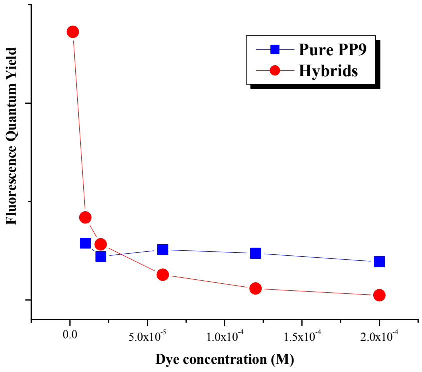

Figure 61. Comparison of Quantum Yield of free (■), and adsorbed (●) dyes onto the ZnO nanospheres. (Excitation wavelength was 407 nm)

Summing up, fluorescence emissions and excitations analyses proved that:

- The grafted-PP9 molecules aggregate strongly and relatively instantly at very low dye concentrations slightly higher than $2.10^{-5}$ M in H-type aggregation.
- At higher dye concentrations ($> 2.10^{-5}$ M), the strong interaction among the "face-to-face" orientated (H-aggregated) dye molecules leads to radical alteration in the ratio of the grafted-PP9 emission peaks.
- The adsorption of PP9 molecules onto the ZnO small nanospheres leads to the important certainty of increasing the energy band gap of the ZnO with increasing dye concentration.
- The decrease of the dye quantum yield in the hybrid systems with increasing concentration is ascribed to the aggregates development. This is in agreement with the observed dye emission quenching as a result of aggregation and other non-radiative mechanisms as previously studied when grafting the first porphyrin molecule (H2TCPP).

## 4.5.3 Optical studies of PP9-based nanohybrids of ZnO nanorods

Identical grafting procedures are applied to graft the PP9 onto the ZnO nanorods of 48 hours. In view of that, we refer to Table 2 in the H2TCPP section, which files the samples names along with their corresponding dye concentration values and the calculated number of dye molecules per ZnO nanoparticle.

### 4.5.3.1 Absorbance measurements

Absorbance spectra of the "diluted" and their corresponding normalized "centrifuged diluted" spectra of PP9-grafted ZnO nanorods "5" and "9" samples along with the pure dye absorption are shown in figures 62-a and -b, respectively. ZnO nanorods and PP9 absorb at very close regions as demonstrated in the absorptions bands overlap in figure 62-b. Dye Soret band absorption in non centrifuged samples acts similarly to pure dyes ascribed to the excess in non-grafted free dyes. Once expelling this excess by centrifugation the Soret band laying in the descendent slope of the ZnO absorption becomes wider and shifts to higher wavelength as seen in figure 63-a.

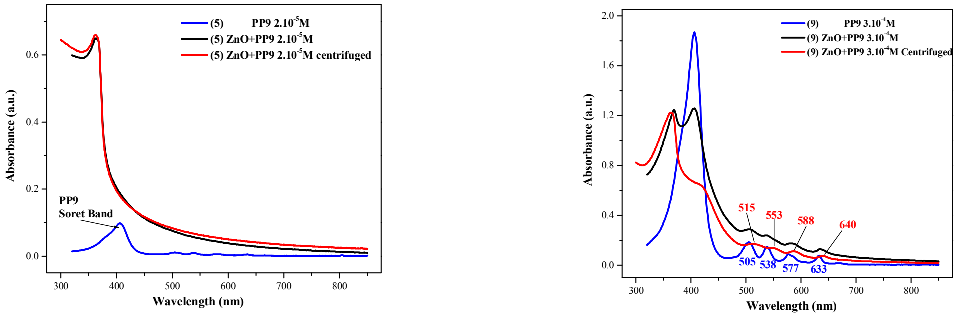

(a) (b)

Figure 62. Absorbance spectra of the "diluted" and their corresponding treated "centrifuged diluted" spectra of PP9-grafted ZnO solutions of samples: (a) "5" and (b) "9".

Absorption peaks in the grafted systems are red-shifted with respect to those of the pure dye validating the dye grafting event as shown in figures 62-b and 63-a. Surprisingly even at low dye concentration, figure 63-b shows higher Soret band absorption intensities in pure dye solutions than those of hybrid solutions. This points toward the fact that the degree of aggregation among grafted dye molecules is nearly instantly and higher than free dye molecules. Hence, we can confirm that the formation of grafted-PP9 aggregates on the surface of ZnO nanorods is practically faster than that of PP9 grafted on the nanospheres. This detail is also supported by the fact that the nanorod offers much less surfaces than the nanosphere, thus inducing faster dye aggregation in the case of nanorods.

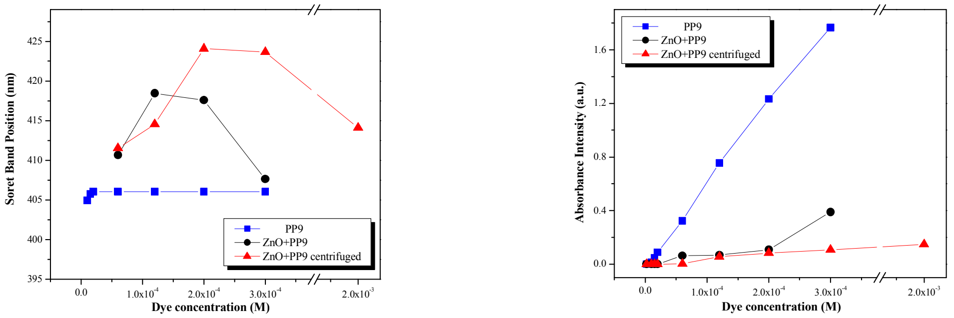

(a) (b)

Figure 63. (a) Absorbance positions and (b) intensities of the Soret peak of pure dyes and hybrids before and after centrifugation at different dye concentrations.

Hence, we can tell that the PP9 molecules adsorbed onto the ZnO nanorods surfaces tend to aggregate straight away, that is clearly seen in the very small Soret band absorption is compared to the bare PP9.

### 4.5.3.2 Photoluminescence measurements

Emission and excitation measurements of grafted dye molecules in centrifuged hybrid systems (figure 64) confirm what was earlier concluded in the case of ZnO nanospheres hybrids. Excitation spectra registered at the value of λ emission 634 nm (figure 64-c) show red-shift absorption with respect to free dyes highlights the certainty of grafting. Emission behavior at 672 nm predicts as previously concluded the formation of H-aggregate among grafted dyes when increasing their concentrations. This is specially implied by the contribution of bleu-shifted absorption peaks demonstrated in the excitation plots of figure 64-d.

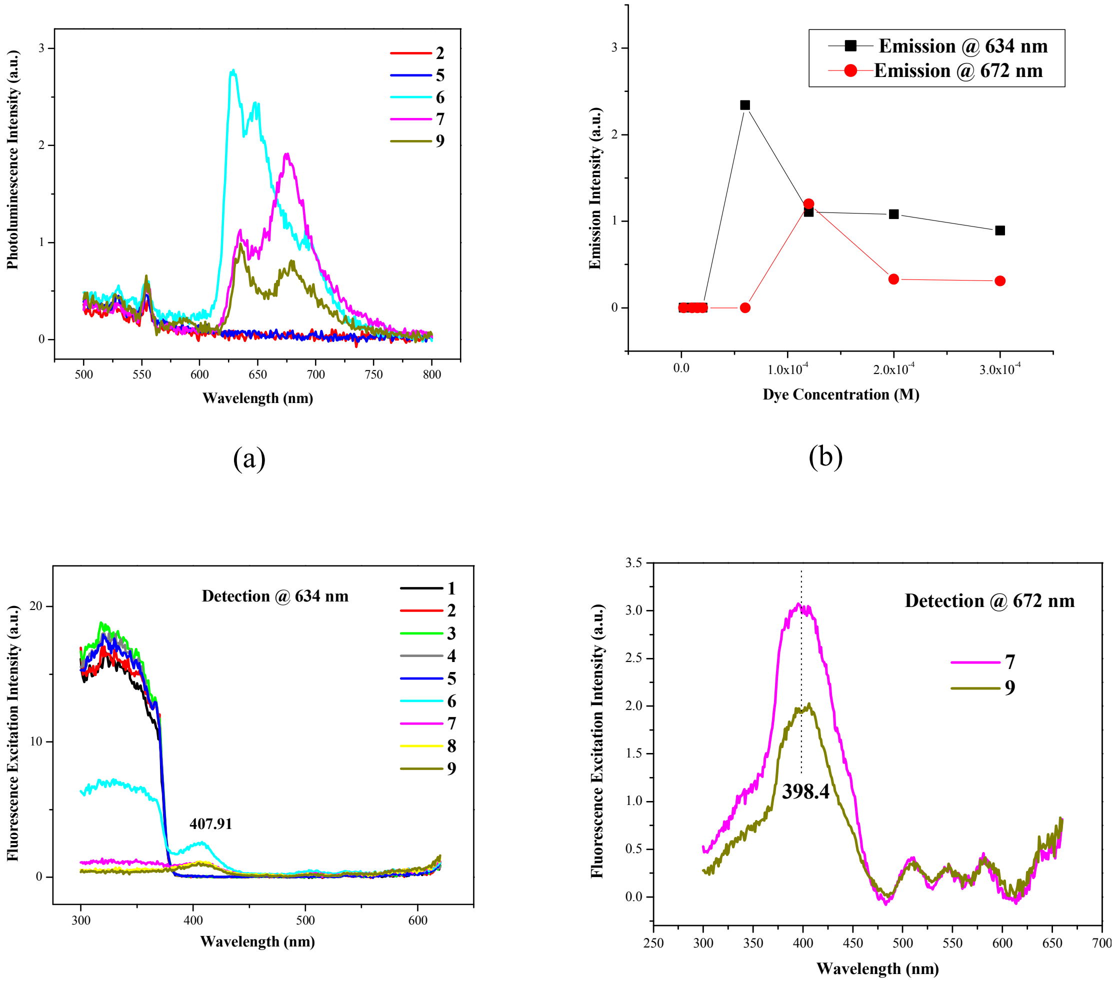

(a) (b)

(c) (d)

Figure 64. Centrifuged hybrids fluorescence (a) emission spectra excited at 407 nm, (b) corresponding intensities for emission peaks at 634 and 672nm, and their excitation spectra at emission wavelength of (c) 634 nm and (d) 672 nm.

Re-oxygenation supplied by the dye molecules to the ZnO surface oxygen-deficiencies reduces the ZnO defects green-band emission as seen in figures 65-a and -b. This drop in the ZnO defects emission is attributed to some other physical processes as the electron transfer and the favored resonant energy transfer (Forster) from the ZnO to the dye, hence reduction of radiative recombinations, which is also observed in fluorescence excitation spectra (at 634 nm detection) pictured in figure 64-c. Reduction in the intensity of ZnO exciton emission that is constantly positioned at 372 nm is presented (figure 65-b); this reduction is due to reduction of the radiative emissions via the Forster energy transfer and via the dye's HOMO level. Pure dye emission dotted plot at $6.10^{-5}$ M is added into the hybrid emission spectra in figure 65-a. Practically, grafted-dye emissions in centrifuged hybrids were barely detected as seen in figure 65-a and quantified in figure 66. More points can be found in the emission statistics in non-centrifuged samples due to freely non-adsorbed PP9 molecules, where we can see that the pure dye emission is higher than that in the hybrids at all of three peaks emissions.

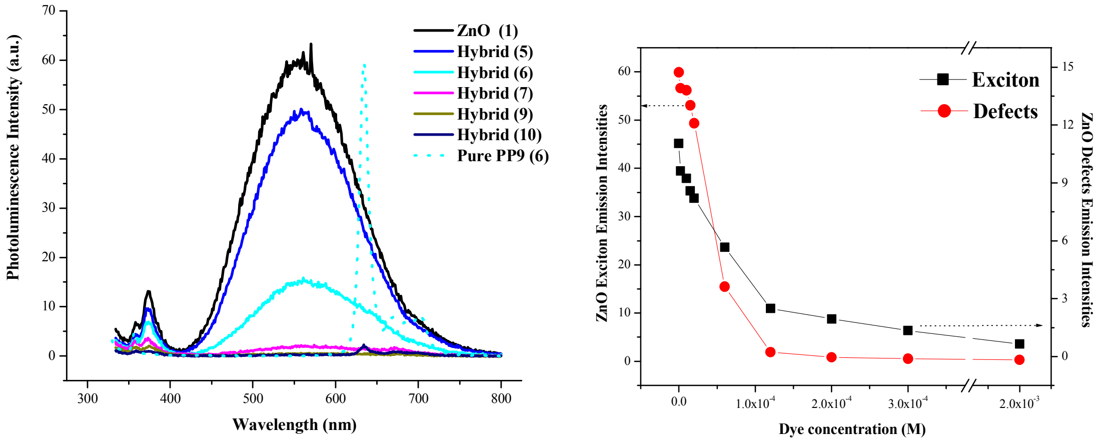

(a) (b)

Figure 65. (a) Global view of fluorescence emission spectra of centrifuged hybrids excited at 325 nm. (b) ZnO exciton and defects emission intensities as a function of dye concentration.

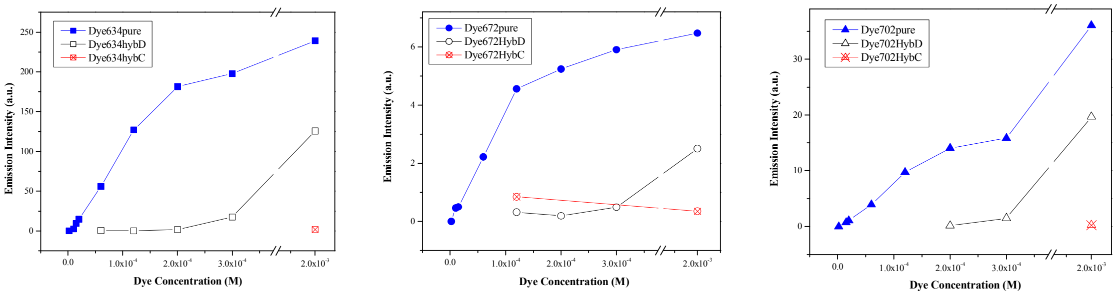

(a) (b) (c)

Figure 66. Fluorescence emission spectra at excitation wavelength 325 nm of free and grafted dyes in samples before and after centrifugation at (a) 634 nm, (b) 672 nm and (c) 702 nm emission peaks.

Alternatively, figure 67 shows the relative Quantum Yields of both free and adsorbed PP9 molecules onto the surface of ZnO nanorods. No Quantum yields are given for hybrids with dye concentration less than $6.10^{-5}$ M because of the absence of absorbance and emission in these samples. Fluorescence quantum yield in the hybrid systems decreases with increasing dye concentration due to aggregates intensification. J-aggregated pure dye molecules present higher fluorescence quantum yields than those of the hybrids.

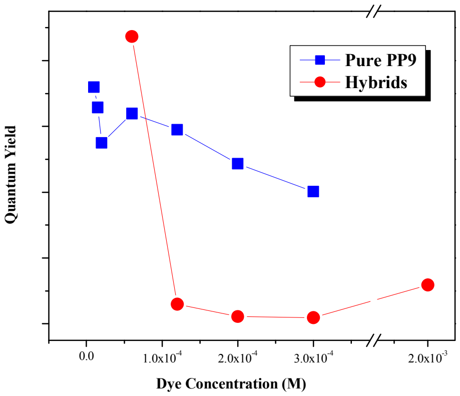

Figure 67. Comparison of Quantum Yield of free (■), and adsorbed (●) PP9 dyes onto the ZnO nanorods.

We can thus conclude that:

▪ The H-type aggregation among the grafted PP9 molecules is quite visible through the fluorescence emissions and excitations analyses.

▪ We can also tell that this aggregation is quite rapid, because of the quenched emission even at very small dye densities.

▪ No absorbance and emission are detected for hybrids with dye concentration less than $6.10^{-5}$ M, thus relative fluorescence Quantum yields are given for samples with higher dye amounts, whose aggregates formation tend to decrease the roughly estimated quantum yields.

## 4.5.4 Concluding comments on grafting the PP9

We proposed throughout our observational description that:

▪ Pure PP9 dyes in THF solutions are generally gently H-aggregated for very small dye concentrations, though they J-aggregated for higher concentrations.

▪ PP9 is positioned edge-wisely thanks to its only two binding acids. In the nanospherical hybrids, and up to $2.10^{-5}$ M PP9 density thus at 4% surface coverage, the sample "D" presents the limit at which aggregation on the surface of ZnO nanospheres starts to be visibly evident, as revealed via our optical data, while the aggregation becomes visible at a surface coverage of 42% in the case of H2TCPP. At low dye amout ($\leq 2.10^{-5}$ M), almost relatively isolated grafted PP9 molecules emit a little stronger than pure free molecules whose emissions surmount those of grafted dyes at higher concentrations. While the aggregation begins at a 29% surface coverage of ZnO nanorods when grafting the H2TCPP, it was found to be relatively instantly when grafting the PP9 onto ZnO nanorods. This confirms the high aggregation tendency of the grafted-PP9 with respect to the H2TCPP.

▪ H-aggregation was concluded for grafted-PP9 dyes either on ZnO nanosphere or nanorod. This H-arrangement presents high interaction among the grafted-PP9 molecules leading thus to alteration in the ratio of the dye's emission peaks.

▪ Grafting PP9 molecules onto the ZnO surface passivates the oxygen vacancies by oxygen provided by the dye carboxyl acid, decreasing thus the ZnO defect band. Besides, decrease in the ZnO exciton and defects emission with dye concentration is accredited to the reduction in radiative decays via electron transfer and mainly Forster (favored due the large overlapping between ZnO exciton emission and PP9 Soret absorbance) and also via the HOMO level of the dye.

▪ Improvement in the hybrid quantum yield up to $2.10^{-5}$ M dye concentration, compared to the pure dyes is seen as a diminution of non-radiative relaxation channels by the relatively modest isolation of the grafted-dye molecules on the surface of ZnO nanospheres. Higher dye concentrations lead the fluorescence quantum yields to diminish with respect to those of pure dye. However, and even at low dye densities, nanorod-based hybrids show no improvement due to the rapid and high degree of aggregation among grafted dye molecules than free dye molecules. These PP9 fluorescence yields are relatively less efficient than those estimated for the H2TCPP, simply because of the higher intermolecular PP9 interaction leading to less charge and energy exchanges with the ZnO nanoparticles.

▪ Similar grafting effects on ZnO nanospheres exciton emission are marked when using PP9 as in the case of grafting H2TCPP. The adsorption of PP9 molecules leads to decreasing the intensity of ZnO exciton band, which is as well blue-shifted with increasing dye concentration. Same reasoning as given in the case of H2TCPP inspires these very fascinating and radical changes.

## 4.7 General conclusion

In this chapter, we reported on a new type of hybrid nanoparticles based on the inorganic semiconducting ZnO nanoparticles grafted with different types of organic dye molecules that are functionalized by carboxylic acid functions. The ZnO templates of two shapes: nanospheres (5,6 nm in diameter) and nanorods (9 nm×38 nm), were synthesized via simple chemical processes. Here, two different porphyrin molecules were selected, namely the H2TCPP and the PP9, and the third dye was the Z907 (a Ruthenium-containing sensitizing dye) that is sited in the Appendix VII, where, FTIR confirmed the grafting by the apparition of carboxylate symmetric and asymmetric binding modes. Through optical detailed studies, we concluded that:

● The ZnO nanospheres and nanorods morphology via HRTEM observations was not affected by adsorbing the above mentioned dyes. Whereas, some favored orientations among the nanorod-hybrids could occur as a consequence of the interaction established between close ZnO particles through grafted-dyes.

● We postulated that pure H2TCPP dyes in THF solutions are H-aggregated for dye concentrations less than $1.10^{-4}$ M, above which they agglomerate in the J-aggregate type. Practically, related optical aspects are found in the nanorod-based hybrids as in the case of nanosphere-based hybrids when grafting H2TCPP. Because the ZnO nanorods offer less total grafting surface than the small nanosphere, we found that the grafted-H2TCPP dye reach H-aggregation at concentrations lower than that with nanospheres. This aggregation is obviously marked when increasing the dye amount by their quenched absorption and emission intensities if compared to those of their analogous free dyes. However, the important feature materialized via the optical analyses plots is that the aggregated pure dye molecules suspended in pure solutions at low dye concentrations become isolated to some extent once grafted onto the ZnO surface, inducing thus an enhancement of absorption and fluorescence. This enhancement in the fluorescence is also promoted through ZnO contribution by: (i) increasing occurrence of electron transfer and decreasing of the small input of Forster energy transfer in the nanoshperical hybrids and (ii) decreasing amount of electron transfer and a small constant contribution of Forster energy transfer in the nanrod-like hybrids. These features are found up to dye surface coverage of 42% and 29% of the ZnO nanosphere and nanorod, respectively, where the hybrid samples exhibit absorption and fluorescence higher than their corresponding pure H2TCPP dyes. These details guide to the strong improvement in the florescence quantum yield in hybrid systems that fade away with increasing dye concentration indicating an enhanced non-radiative decay of the excited aggregates.

● The most authentic and essential fact is the grafting consequences on the outer layers of the ZnO surfaces. This is marked, upon increasing the dye amount, by the increment in the ZnO gap energy due to confinement features inducing charged layers that block gradually the charge exchanges between the ZnO nanospheres and the grafted dye molecules. Yet, this fundamental effect was not detectable in the case of ZnO nanorod due to its large volume to surface ratio with respect to that of the nanospheres, preventing thus any visible confinement effects. However, the effects of induced charged layers must exist with hybrid based on ZnO nanorods.

● Grafting the PP9 onto the ZnO small nanospheres demonstrates as well the important certainty of increasing the energy band gap of the ZnO with increasing dye concentration. However, the grafted-PP9 molecules tend to aggregate quite rapidly if compared to the grafted-H2TCPP. Up to 4% surface coverage, H-aggregation of the grafted-PP9 on the surface of ZnO nanospheres starts to be visibly evident, where almost relatively isolated grafted dye molecules emit a little stronger than pure free molecules whose emissions surmount those of the aggregated grafted-dyes at higher concentrations, as additionally promotes by the favored Forster energy transfer from the ZnO. Nevertheless, aggregation was found to be relatively instantly when grafting the PP9 onto ZnO nanorods. This is not surprising because it is credited to the smaller grafting surface of the nanorods and to the high aggregation tendency of the PP9. Decrease of the dye fluorescence quantum yield in the hybrid systems with increasing concentration is ascribed to the aggregates development. We also succeed to metallate the grafted-PP9 molecules by the Zn atoms as confirmed via the modifications of the absorbance, emission and excitation spectra (see Appendix VI).

● The Z907 was proved to be efficiently grafted to the rod-shaped ZnO, where we have seen that electron may transfer from excited dye to the ZnO particles. But, this mechanism is likely to be pursued by non-radiative interfacial recombinations from the ZnO back to the dye because we have seen no enhancement in the ZnO emissions (see Appendix VII).

We can thus confirm that we succeeded in creating nanohybrids based on the spherical and rod-like ZnO inorganic templates grafted separately with three types of organic dye molecules, namely two porphyrins and a Ruthenium-based dye. The major effect that emanates from this hybridation process is the creation of charge separated layers at the interface ZnO/dye, dictating thus the charge carriers exchange between the ZnO and the grafted-dye.

# Bibliography

[1] A. N. Shipway, E. Katz, and I. Willner, Phys. Chem. Phys, 1 (2000) 18

[2] K.G. Thomas, and P. V. Kamat, Acc. Chem. Res. 36 (2003) 888

[3] K. Kalyanasundaram, and M. Graetzel, Coord. Chem. ReV., 177 (1998) 347

[4] S. Cherian, and C.C. Wamser, J. Phys.Chem.B, 104 (2000) 3624

[5] T. Ma, K. Inoue, K. Yao, H. Noma, T. Shuji, E. Abe, J. Yu, X. Wang, and B. Zhang, Journal of Electroanalytical Chemistry 537 (2002) 31

[6] J. N. Clifford, E. Palomares, Md. K. Nazeeruddin, M. Gra¨tzel, J. Nelson, X. Li, N. J. Long, and J. R. Durrant, J. Am. Chem. Soc., 126 (2004) 5225

[7] J. R. Durrant, S. A. Haque, and E. Palomares, Coord. Chem. ReV., 248 (2004) 1247

[8] W. M. Campbell, A. K. Burrell, D. L. Officer, and K. W. Jolley, Coord. Chem. ReV., 248 (2004) 1363 and references therein.

[9] R. Argazzi, N. Y. Murakami Iha, H. Zabri, F. Odobel, and C. A. Bignozzi, Coord. Chem. ReV., 248 (2004) 1299

[10] M. K. Nazeeruddin, R. Humphry-Baker, D. L. Officer, W. M. Campbell, A. K. Burrell, and M. Graetzel, Langmuir, 20 (2004) 6514

[11] D. F. Watson, A. Marton, A. M. Stux, and G. J. Meyer, J. Phys. Chem. B, 108 (2004) 11680

[12] A. Brune, G. Jeong, P. A. Liddell, T. Sotomura, T. A. Moore, A. L. Moore, and D. Gust, Langmuir, 20 (2004) 8366

[13] J. Jasieniak, M. Johnston, and E. R. Waclawik, J. Phys. Chem. B, 108 (2004) 12962

[14] E. Michaelis, K. Nonomura, D. Schlettwein, T. Yoshida, H. Minoura, D. J. Woehrle, Porphyrins Phthalocyanines, 12 (2004) 1366

[15] L. Schmidt-Mende, W. M. Campbell, Q. Wang, K. W. Jolley, D. L. Officer, M. K. Nazeeruddin, and M. Graetzel, Chem. Phys. Chem., 6 (2005) 1253

[16] T. Hasobe, S. Hattori, P. V. Kamat, Y. Urano, N. Umezawa, T. Nagano, and S. Fukuzumi, Chem. Phys., 319 (2005) 243

[17] Q. Wang, W. M. Campbell, E. E. Bonfantani, K. W. Jolley, D. L. Officer, P. J. Walsh, K. Gordon, R. Humphry-Baker, M. K. Nazeeruddin, and M. Graetzel, J. Phys. Chem. B, 109 (2005) 15397

[18] T. Hasobe, S. Hattori, P. V. Kamat, and S. Fukuzumi, Tetrahedron, 62 (2006) 1937

[19] C.-F. Lo, L. Luo, E. Wei-Guang Diau, I.-J. Chang, and C.-Y. Lin, Chem. Commun. (2006) 1430

[20] L. Luo, C.-F. Lo, C.-Y. Lin, I.-J. Chang, and E. J. Wei-Guang Diau, Phys. Chem. B, 110 (2006) 410

[21] M.K. Nazeeruddin, P. Pechy, T. Renouard, S.M. Zakeeruddin, R. Humphry-Baker, P. Comte, P. Liska, L. Cevey, E. Costa, V. Shklover, L. Spiccia, G.B. Deacon, C.A. Bignozzi, and M. Grätzel, J. Am. Chem. Soc., 123 (2001) 1613

[22] Y. Tachibana, S. Haque, I. Mercer, J. Durrant, and D. Klug, J. Phys.Chem. B, 104 (2000) 1198

[23] M. Law, L. E. Greene, J. C. Johnson, R. Saykally, and P. Yang, Nat. Mater., 4 (2005) 455

[24] E. Galoppini, J. Rochford, H. Chen, G. Saraf, Y. Lu, A. Hagfeldt, and G. Boschloo, J. Phys. Chem. B, 110 (2006) 16159

[25] W. Beek, M. Wienk, M. Kemerink, X. Yang, and R. Janssen, J. Phys. Chem. B, 109 (2005) 9505

[26] P. Ravirajan, A. Peiro, M. Nazeeruddin, M. Graetzel, D. Bradley, J. Durrant, and J. Nelson, J. Phys. Chem. B, 110 (2006) 7635

[27] R. F. Khairutdinov, and N. Serpone, J. Phys.Chem. B, 103 (1999) 761

[28] R. Kasha, H. R. Rawls, and M. Asraf El-Bayoumi, Pure Appl. Chem., 11 (1965) 371

[29] C. A. Hunter, J. M. K. Sanders, and A. J. Ed. Stone, Chem. Phys., 133 (1989) 395

[30] M. Kasha, Radiat. Res. 20 (1963) 55

[31] S.K. Ghosh, A. Pal, S. Nath, S. Kundu, S. Panigrahi, and T. Pal, Chem. Phys. Lett. 412 (2005) 5

[32] D. C. Barber, R. A. Freitag, and D. G. Whitten, J. Phys.Chem. 95 (1991) 4074

[33] K. Kalyanasundaram, and M. Neumann-Spallart, J. Phys. Chem., 86 (1982) 5163

[34] E. Fagadar-Cosma, C. Enache, I. Armeanu, and G. Fagadar-Cosma, Digest Journal of Nanomaterials and Biostructures, Vol. 2, No. 1 (2007) 175

[35] J. S. Hu, Y. G. Guo, H. P. Liang, L. J. Wan, and L. Jiang, J. Am. Chem. Soc., 127 (2005) 17090

[36] C.F. Bohren, and D. Huffman, Absorption and scattering of light by small particles, John Wiley, New York (1983)

[37] R. W. Ditchburn, Light, 2nd ed., London: Blackie & Sons, (1963) pp 582-585

[38] R. Wiglusz, J. Legendziewicz, A. Graczyk, S. Radzki, P. Gawryszewska, and J. Sokolnicki, J. All. Com., 380 (2004) 396

[39] D. M. Chen, Y. H. Zhang, T. J. He, and F. C. Liu, Spectrochimica Acta Part A, 58 (2002) 2291

[40] Y. S. Wang, P. John Thomas, and P. O'Brien, J. Phys. Chem. B, 110 (2006) 4099

[41] I. Ozerov, M. Arab, V. I. Safarov, W. Marine, S. Giorgio, M. Sentis, and L. Nanai, Appl. Surf. Sci. 226 (2004) 242

[42] S. Monticone, R. Tufeu, and A.V. Kanaev, J. Phys. Chem.B, 102 (1998) 2854

[43] T. M. R. Viseu, G. Hungerford, and M. I. C. Ferreira, J. Phys. Chem. B 106 (2002) 1853

[44] R.F. Khairutdinov, and N. Serpone, J. Phys. Chem. 99 (1999) 11952

[45] M. W. de Lange, J. G. van Ommen, and L. Lefferts, Applied Catalysis A: General, 220 (2001) 41

[46] V. A. Harutyunyan, K. S. Aramyan, H. Sh. Petrosyan, and G. H. Demirjian, Physica E, 24 (2004) 173

[47] V. A. Harutyunyan, Physica E 39 (2007) 37

[48] S. Cherian, and C.C. Wamser, J. Phys.Chem. B 104 (2000) 3624

[49] G. Xiong, U. Pal, J. G. Serrano, K. B. Ucer, and R. T. Williams, Phys. Stat. Sol., N. 10 (2006) 3577

[50] M. K. Nazeeruddin, R. Humphry-Baker, D. L. Officer, W. M. Campbell, A. K. Burrell, and M. Gratzel, Langmuir, 20 (2004) 6514

[51] J. Rochford, D. Chu, A.Hagfeldt, and E. Galoppini, J. Am. Chem. Soc. 129 (15) (2007) 4655

[52] O. Taratula, E. Galoppini, D. Wang, D. Chu, Z. Zhang, H. Chen, G. Saraf, and Y. Lu, J. Phys. Chem. B, 110 (13), (2006) 6506

# Chapter 5

# Photovoltaic properties of Dye-ZnO nanorods based solar cells

## 5.1 Introduction

Lots of efforts are devoted to boost the research for new photovoltaic cell fabrication techniques. In order to successfully convert solar energy into electrical energy, all the following four processes should be optimized: (1) light absorption, (2) charge separation, (3) charge carrier migration and (4) charge collection. Evolution of several solar cell concepts can be reviewed through inorganic, organic, photoelectrochemical (dye sensitized) and hybrid (organic/inorganic) cell-based components. Conventional solar cells were built from inorganic materials such as the expansive silicon. An organic solar cell consists of two organic materials; an electron-donor and an electron-acceptor to make a percolating structure within interpenetrating networks. Dye sensitized solar cells are a combination of different materials as for example inorganic semiconductor and organic dye embedded in an electrolyte or polymer. The dye being the component that contributes to the light harvesting. This opens the way widely to the hybrid solar cell perception that consists on blending of organic and inorganic materials thus, combines the unique properties of inorganic semiconductors with organic dyes and polymers. The proof that the operation mechanism in this system is by electron injection from photoexcited dye molecules into the semiconductor conduction band dates back to the 1960s [1]. Conceptual and practical breakthroughs were achieved in the late 1980s by the work of Grätzel and co-workers, who introduced the application of nanostructured semiconductors for dye-sensitized solar cells [2]. In the following years, the Grätzel cell has become the eminent prototype of research in photovoltaics.

In the present work, we are in particular interested in developing the "hybrid" model. So far several studies were carried out on the wide gap TiO2 oxide material while very few studies were done on the Zinc oxide (ZnO) that incarnates our field of interest. Our study is thus based on grafting, in solution, the organic light-harvester dye molecules on the surface of ZnO nanorods in order to significantly enlarge their photoactive interface, being the heart of the carriers' separation, and to improve electronical exchange between the ZnO and the polymer. This hybrid mixture is then blended with an organic conducting polymer which is needed to complete the circuit pattern and to assure uniform active cell layer coating. Since our study deals with the properties of the materials in the novel generation of ZnO-based dye-sensitized solar cells, a more detailed description underlying its working mechanisms is fully displayed. Details of chosen dyes and polymer, fabrication techniques as well as solar-electricity conversion results and discussions are to be revealed in the subsequent chapter parts. But first, outline and operation principles of the various solar devices concepts must be exposed.

## 5.2 Solar cell concepts

### 5.2.1 Inorganic solar cells (ISC)

Historically, Edmund Becquerel discovered the photovoltaic effect in 1839, when he observed a light-dependent voltage between electrodes immersed in an electrolyte [3]. Though, the dawn of compelling photovoltaic solar cells arises in 1954, where solar cells were built by p-n junctions from inorganic single-crystal Si with efficiencies of 6% by D. Chapin, C. Fuller, and G. Pearson at Bell Labs [4]. This innovative Si-based solar cell of were optimized up to 24% efficiency [5] and governs today by 85% the present commercial photovoltaic market. Moreover, solar cells have been made from many other semiconductors (CuInSe2, CuGaSe2, CuInS2, CdTe, CdS [6]) as single-crystal, poly-crystalline, and amorphous thin-film structures and using various device configurations.

Basically all conventional inorganic solar cells integrate a semiconductor that is doped to form a p-n junction across which the photovoltage is generated. The p side contains an excess of the positive charges (holes) with localized empty states of energy slightly above the valence band edge of the p-type semiconductor, and the n side contains an excess of the negative charges (electrons) with localized energy states just below the conduction band edge of the n-type semiconductor. Bringing in contact the two semiconductor types, i.e. n-type and p-type, leads to a transport of electrons and holes across the junction until equilibrium is established through equalization of the Fermi-level in the both materials. This will set up a depletion region near the junction at the interface where there are no free charges, but instead an electric field (potential difference) is thus created across this region. The configuration of the pn-junction is portrayed in figure 1.

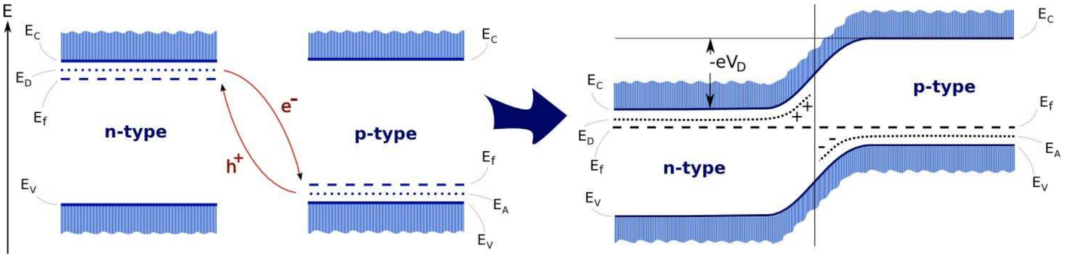

Figure 1. Semiconductor pn-junction. a) Band structure of an n-type and a p-type semiconductor showing conduction $E_C$ and valence band $E_V$ edges, acceptor level $E_A$ in the p-type material and donor level $E_D$ in n-type material, and the Fermi level $E_f$. b) pn-junction in thermal equilibrium presenting the potential difference $V_D$ across the junction.

The built-in electric field in the depletion region is merely the source of photovoltaic activity in the cell. Upon illumination, absorbed photons in the semiconductors create free electron and hole charges. These created minority charge carriers (holes in the n-type) and (electrons in the p-type) diffuse to the depletion interface where they are directed by the local internal electric field to opposite sides of the cell structure: electrons are therefore accumulated in the n-type material and holes in the p-type material, see figure 2. These carriers are then collected through electrodes to produce a current and a voltage; hence generating electrical power.

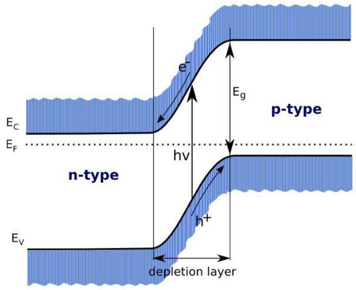

Figure 2. Mechanism of charges circulation in inorganic solar cells under illumination.

Consequently, this type of inorganic solar cells assumes two simultaneous tasks: it harvests the incident sunlight and conducts the thus-produced charge carriers. In order to assure perfect carriers diffusion, the concentration of defects in the solid must be minimized by using ultra-pure highly crystalline materials, rendering solid state solar cell devices production quite expensive. This problem may be resolved trough another solar cell type as the “Organic” solar cell.

## 5.2.2 Organic solar cell (OSC)

Spawned in the mid-1980s, the “Organic” solar cell based on “organic” materials makes unnecessary the use of highly cost solid state components in the system. The discovery that doped organic polymers can display conductivity led to the application of these polymeric materials in the so-called full-organic plastic solar cells, as well as in bulk heterojunctions based on (C60) derivatives [7]. Construction of a typical organic photovoltaic device is shown in figure 3 where the active layer (red) can be constructed by a bilayer of vapor-deposited molecules, or polymer/polymer blend layer (efficiencies up to 6% [8,9]), or a bulk heterojunction layer.

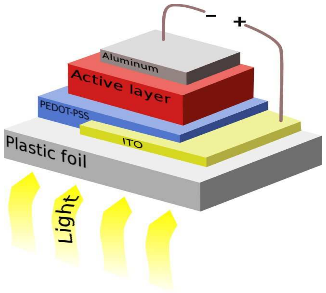

Figure 3. Typical component structure of an Organic solar cell.

For example, bulk heterojunction organic solar cells can be described in figure 4 where the active layer is a blend of a semiconducting conjugated polymer (like p-type polyphenylvinylidene or polythiophene MEH-PPV) and another semiconductor (like n-type fullerene C60) [10,11]. Initially, both organic materials are selected so that their energy bands present a cascade configuration in order to guarantee charge generation after photo-excitation (figure 4-a). Secondly, each material must offer a continuous path for the transport of separated charge to the electrodes (figure 4-b) [12].

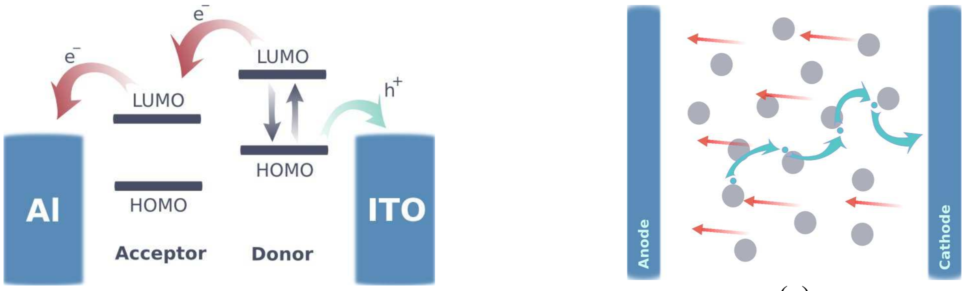

(a) (c)

Figure 4. (a) Energy-level diagram bands of a typical Bulk heterojunction Organic solar cell. (b) Cartoon visualization showing the polymer and the fullerene where red and blue arrows designate respectively the hole and the electron percolations through the solar active layer.

Upon illumination, the polymer harvests the light and causes electrons to leave the HOMO to the LUMO band inducing the creation of bounded electron-hole pairs called excitons whose formation is attributed to the polymer's low dielectric constant (i.e. charges carriers can not move freely inside a polymer). Dissociation of efficiently contributing excitons takes place within 5 to 10 nm thickness at donor/acceptor interface, due to the difference in electron affinities that creates a driving force at the interface between the two materials. In other words, the LUMO band of the acceptor must be lying at lower energies than the LUMO band of the donor. After charge separation, the charges are collected by the electrode contacts. So far highest efficiencies of about 3.5% have been reported and up to 5% [13-15].

In order to work out the problem of low efficiencies in the organic cells and at the same time to gather benefits from the inorganic cells, a novel solar hybrid cell is shaped. This hybrid cell adopts the concept of organic-inorganic combination of unique tailored properties.

### 5.2.3 Hybrid solar cell

New generation of solar cells is hence developed in order to increase the solar cells conversion efficiencies and extend their spectral range of optical absorption with respect to the solar emission spectrum by chemisorption of organic dye molecules on wide band gap inorganic semiconductor. Since the operation of dye-sensitized hybrid solar cell imitates that of photoelectrochemical solar cells based on nanoporous TiO2 electrodes, it would be useful to illustrate first how this latter cell works. After that, different configurations of hybrid cells are thoroughly elucidated.

#### 5.2.3.A The dye-sensitized solar cell (DSSC)

First proof of dye-sensitization of semiconductors dated back to 1887 but remained of low efficiency [16]. These cells adopt the concept of using particles grown on one electrode to provide an enhanced larger surface interface with the sensitizer dye [17]. The principle of operation Dye sensitized solar cell (DSSC) or Grätzel cell with over 10% efficiency [18] are schematically depicted in figure 5.

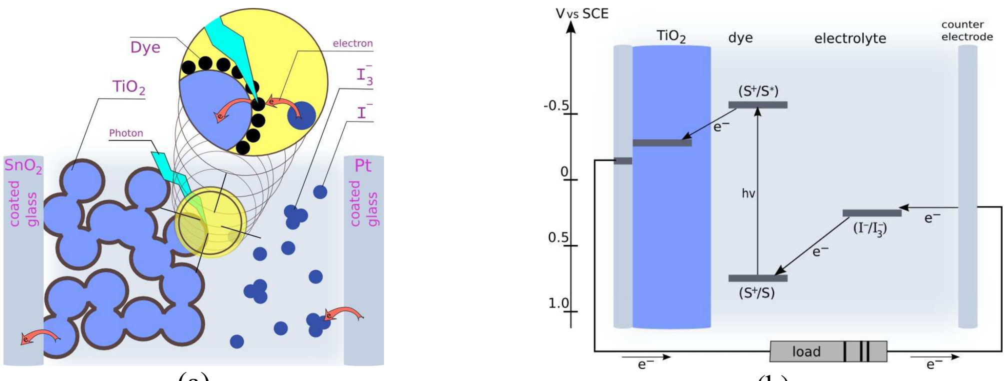

(a) (b)

Figure 5. (a) Schematic sketch illustrating the principle of operation and (b) energy level scheme of the dye-sensitised nanocrystalline solar cell.

The TiO2 being a cheap and largely abundant material constitutes the nanoporous film based on nanoparticles that have been sintered together to establish electric contact between them. The wide band gap TiO2 absorbs mainly in the UV region; rather, the adsorbed dye molecules absorb the sunlight. After photoexcitation of the dye attached to the nanocrystalline surface, an electron is injected into the conduction band of the TiO2 semiconductor creating a positively charged dye molecule. The dye is regenerated by electron donation from the iodide ($\mathrm{I}^-$) in the electrolyte, which is an electrically conducting organic liquid containing the iodide/triiodide redox couple. The iodide electrolyte itself is regenerated at the counter electrode by reduction of the triiodide ($\mathrm{I}_3^-$) when the electrons return to the cell through the external load to complete the circuit. Thus the redox couple accepts holes at one electrode and accepts electrons at the other counter electrode, resulting in charge neutralization in the redox species. Hence redox couple in the electrolyte serves to complete the electrical circuit and to produce the electric field requisite for charge separation.

Despite the very promising earlier predictions on performance of these photoelectrochemical cells, they faced unexpected problems arising from the corrosive and volatile nature of the liquid redox electrolyte contributing to the non-stability of cells. From here comes the idea of replacing the electrolyte by an alternative organic material as a polymer for example, thereby forming a solid-state dye-sensitized organic/inorganic heterojunction solar cell.

### 5.2.3.B The solid-state dye-sensitized solar cell (SSD)

Known since the mid 80's [19], the solid state cell has a structure similar to the dye sensitized photoelectrochemical cells (DSSC) but the electrolyte was being replaced by a p-type semiconductor or an organic hole conducting material, as shown in figure 6. When the organic conductor polymer is used, the cells are then referred to be hybrid cells. The charge transport mechanisms inside this cell are very similar to the DSSC, except in the part substituting the electrolyte. So in the SSD, contrary to the DSSC, there are no ions wandering inside the electrolyte, instead holes are hopping from one hole-conductor molecule to the other, as shown in figure 6-b. Nevertheless, hole transport in the hole conducting material is much slower than in electrolyte liquid. This fact will lead to a hole concentration gradient between the organic and the material bulk interface implying an increment in the probability of interfacial recombination, which decreases the cell conversion efficiency.

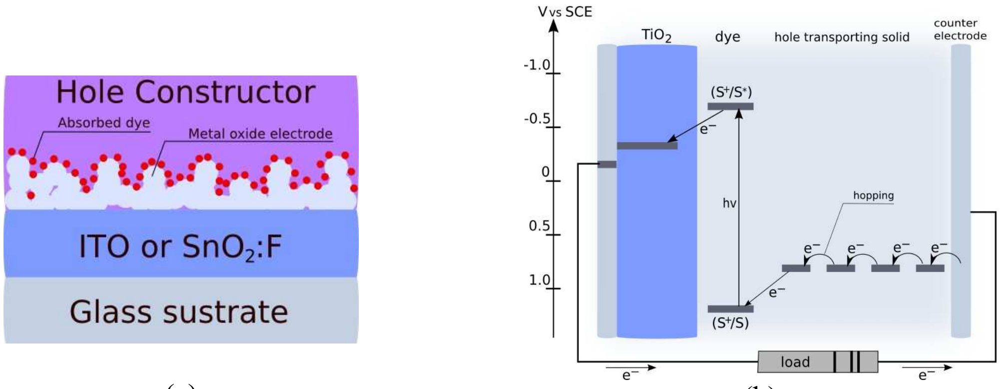

(a) (b)

Figure 6. (a) Schematic description and (b) energy level scheme of a solid state dye sensitized solar cell.

Inorganic p-type semiconductors such as CuI, CuBr or CuSCN were successfully used instead of the liquid electrolyte yet with very small efficiencies [20-22]. This efficiency improved further to attain 6% employing CuI as hole transporter and ruthenium bipyridyl dye complex as a sensitizer [23]. Organic p-type semiconductors hole transport materials were also used in solid state dye-sensitized hybrid solar devices. Accordingly, conducting "polymers" turn out to be potential candidates to be used as hole transporting material. These organic p-type polymers are easily manipulated (like film cast from solution) and of low cost compared to inorganic semiconductors. Solid state devices using poly(3-octylthiophene) as hole conducting materials [24] as well as polythiophene solid state dye sensitized TiO2 solar cells were effectively reported [25].

Though, the conversion efficiencies of most solid state dye-sensitized devices utilizing organic p-type semiconductors are relatively low for the following reasons [26]:

1- Having a large distribution of trap states, a conducting polymer displays generally low hole mobility in comparison to an inorganic material having relatively low conductivity itself.
2- High recombination rate between the electrons in the inorganic semiconductor conduction band and the oxidized hole conductor.
3- Low linkage between the hole transport material and the counter electrode (hole collector).

Development of these solid state devices is actually less than satisfactory although their derivative hybrid branch where the cell devices are based "only" on inorganic and organic components dye-sensitized is of great interest. Hybrid solar cells based on bulk heterojunction concept constitute the inspiration and the heart of our solar cell application model.

### 5.2.3.C Hybrid dye-sensitized Solar Cells Based on Bulk Heterojunction Concept

Here the photovoltaic cell layer is formed by a blend of nanocrystals with semiconductive polymers and where bulk heterojunction model is similar to that used in organic solar cells [27]. In these hybrid solar cells, one of the two organic components is replaced by inorganic semiconductor material. High interfacial area is created thus enhancing the photocurrent generation at the nanocrystal/polymer p-n junctions. Such solar cells have been successfully reported through various blends containing CdSe [28,29], CuInS2 [27], CdS [30] or PbS [31] nanocrystals. Hybrid devices based on blends of TiO2 with MDMO-PPV are achieved with external quantum efficiency up to 11% [32]. Recently, in 2006, W. Beek et al [33] constructed hybrid solar cells of 0.9% efficiency from blends processed from solution of nanocrystalline ZnO and regioregular P3HT polymer. They demonstrated that charge carrier generation depends on the thermal annealing treatment and the amount of ZnO. They showed as well that the device performance was restricted by the morphological roughness of the spin-coated blend films.

Our studies are focused on this type of hybrid solar cells where specific dyes are implanted on the surface of ZnO nanorods and then blended with a polymer. Dye introduction into the above described system increases the light absorption and contributes to the enhancement of the charge transfer from polymer to ZnO, improving thus the efficiency of the light-electricity conversion. Figure 7 pictures a cartoon representation of the photoactive layer of a Hybrid dye-sensitized Solar Cells Based on Bulk Heterojunction Concept, showing the adsorbed dyes onto the ZnO rods blended with the polymer. Upon light irradiation electrons generated in both polymer and dye will be injected into the ZnO network percolation system where electrons are traveling to reach the electrode.

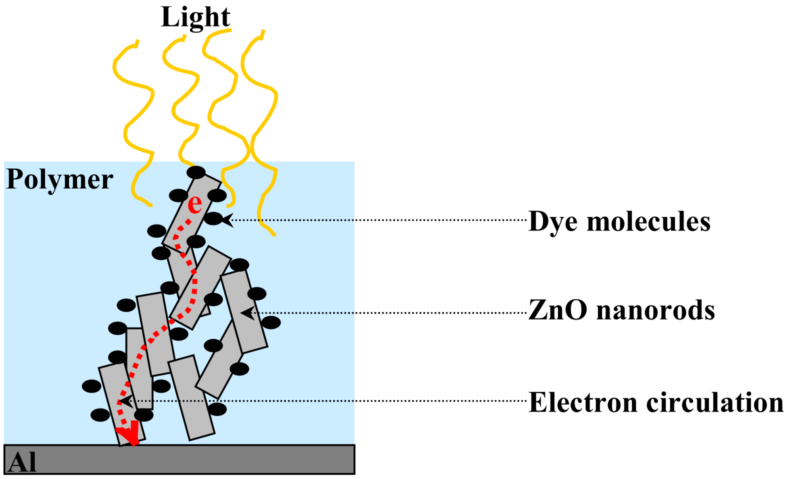

Figure 7. Schematic description of the active layer of a Heterojunction-based Hybrid dye-sensitized Solar Cell.

Architecture of the Hybrid Solar Cell that we constructed will be revealed after presenting details on the present theory and properties of the used materials.

## 5.3 Materials used for Hybrid Dye Sensitized ZnO Solar Cells

### 5.3.1 Inorganic ZnO nanorods

A major advantage of the use of nanocrystalline semiconductors such as ZnO is their ease of fabrication and use in many different morphologies, crystal structures and thicknesses. Chemically elaborated ZnO nanorods obtained after 48 hours of reaction synthesis represent the inorganic element of our hybrid cells. ZnO possesses a bandgap of 3.37 eV implying that photoexcitation of these semiconductors is only possible with UV light. But the ZnO material can be made sensitive to visible light by means of the principle referred to “dye-sensitization”.

### 5.3.2 Organic P-type P3HT polymer

Figure 8 shows the chemical structure of the organic semiconductor polymer poly(3-hexylthiophene) (P3HT) that is used in our photovoltaic systems. P3HT results from the polymerization of thiophenes, a sulfur heterocycle (aromatic ring), which becomes conducting via doping. The P3HT is of p-type when electrons are removed from the conjugated $\pi$-orbitals. A chemically conjugated system is a system of atoms that are covalently bonded with alternating single and double bonds (C=C-C=C-C) in an organic molecule. P3HT is soluble in common organic solvents and has a broad absorption spectra with a maximum peaked at around 550 nm.

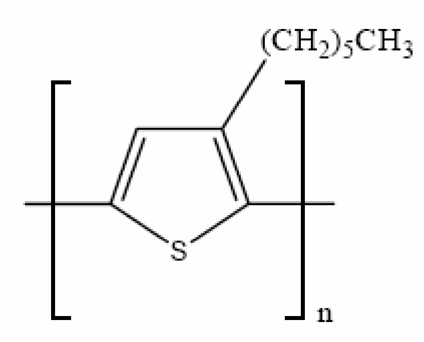

Figure 8. Chemical structure of P3HT polymer.

The most essential aspects for any p-type semiconductor in a dye sensitized solar cell are of twofold, first its ability to transfer holes from the sensitizing dye after the dye has injected electrons into the ZnO, second to generate photocurrent. Both mechanisms can work only if the upper edge of the valence band of p-type polymer is located above the ground state level of the dye.

### 5.3.3 Organic Dye sensitizer

Several demands are imposed on the dyes to be used in dye-sensitized solar cells:

1-Dye's absorption spectrum should show as much overlap as possible with the solar spectrum.
2- The HOMO/LUMO energy difference must be small enough to enable further visible light absorption.
3- The LUMO level should lie high enough above the semiconductor's conduction band to provide sufficient driving force for electron injection.
4- The dye should be cheap, non-toxic and strongly adsorb to the ZnO nanoparticle surface.

Two types of dye molecules were selected; namely, "Porphyrin" (H2TCPP and PP9) and "Ruthenium-containing" (Z907) sensitizing dyes. Properties and band structure of these dyes are depicted and extensively studies in the previous chapter. For example our choice of the porphyrin H2TCPP is further validated through the figure 9-a showing absorption spectra of individual cell components with respect to the solar irradiation spectrum. We can see that the H2TCPP absorbs in the visible light and in the region of very low absorption contribution of both ZnO and P3HT.

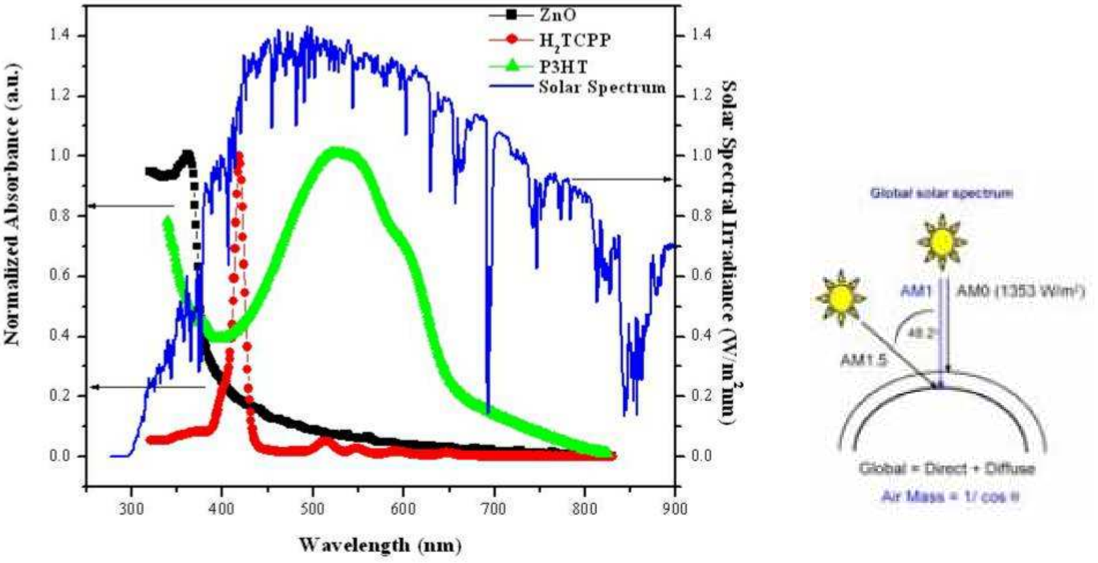

(a) (b)

Figure 9. (a) Normalized absorbance spectra of bare ZnO (■), H2TCPP (●) and P3HT (▲) with the (AM 1.5) solar irradiance [sketched in (b)] spectrum measured at the level sea [34].

*Optical air mass* AM 1.5 is by definition the typical solar spectrum on the Earth's surface in a clear day which, with total irradiance of 1 kW/m$^2$, is used for solar cell calibration. In this case, the sun is at a 48.2° elevation from the horizon, as seen in figure 9-b, and the sunlight path through the atmosphere is 1.5 times that when the sun is at high noon, which corresponds to AM1. This latter path length is the shortest because the sun is directly overhead. Therefore, on a clear summer day at sea level, the sun light flux at zenith corresponds to (AM1) irradiance; at other times, the air mass is approximately equal to 1/cos θ, where θ is the zenith angle.

## 5.4 Hybrid Solar Cell construction

The three dyes that we used are grafted by several concentrations onto the surface of the ZnO nanorods as follows:

i- H2TCPP molecules in THF solution of different concentrations were grafted overnight onto the ZnO nanorods surface following the same grafting procedure adopted and given in the previous chapter. Grafted samples were centrifuged at 40 RPM (round per minute) twice for 5 minutes each to eliminate the surplus in non-grafted dye molecules. These cleaned samples containing each 25 mg of ZnO were thus blended with the P3HT polymer that was previously dissolved in THF in way that the grafted-ZnO nanorods constitute 70% of the total components' weight.

ii- In the case of PP9, a highly concentrated solution of molecules was grafted on ZnO whose surfaces were totally been covered. Same procedure of PP9 sample-cleaning followed by polymer blending was applied.

iii- Cleaning by centrifugation of the hybrid sample when grafting several concentrations of Z907 molecules was not possible due to the high solubility of the Z907. Hence, the Z907-based hybrids were used without centrifugation but in this case less amount of solvent must be employed. Doing so, 25 mg of NaOH-synthesis based ZnO were mixed with the highest dye amount 6 mg of Z907 in 0.5 ml THF. Surprisingly, a solid matter of gel appearance emanating from this combination was formed overnight. Therefore, dealing with this dye must be handled with care; that is Z907/ZnO hybrids must be blended with the polymer right after one hour of the grafting process.

These diverse hybrid blends constitute the photoactive layer of the solar cell after treatment of the cell substrate. As substrates, glass sheets of 2 x 1 $cm^2$ covered with ITO (Indium Tin Oxide) of 80 nm thickness were used. Small part of ITO was removed by etching with a mixture of chloride acid HCL and Water for one hour. The other part of the substrate which forms the contact is covered with a scotch tape preventing the ITO etching. The scotch tape was removed after etching and the substrate was then cleaned by using acetone in an ultrasonic bath. Deposition of the p-type PEDOT-PSS polymer by spin coating over a specific part of the substrate is done and put for 30 minutes in 80°C oven, to assure the uniform repartition of the active layer. This last being the hybrid blend is deposited by spin coating for 20 sec at 1500 RPM and 2000 RPM/mn then for 20 sec at 500 RPM and 100 RPM/mn. Aluminum contacts were deposited then by thermal evaporation in thin rectangular patterns. Final step is the annealing (heating) at 80 °C under $10^{-6}$ mbars high vacuum for 30 minutes. Our solar cell is thus shaped as shown in figure 10.

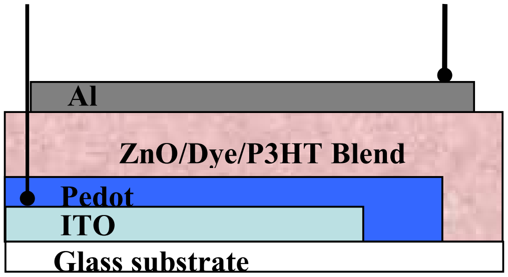

Figure 10. Fabricated cells showing the different layers and components as well as the electrical contacts.

## 5.5 Solar cells electrical characterization

The two usually used techniques for photovoltaic characterizations are the current-voltage (I-V) measurements under simulated sunlight illumination and the monochromatic light generated current measurements (EQE).

Typical inorganic photovoltaic and hybrid cells operate upon the establishment of an electric potential difference between the n- and p-type regions in an inorganic photovoltaic cell or between an n- type semiconductor and p-type polymer in the case of hybrid cells. This potential difference creates an electrical diode structure. Hence, the current-voltage behavior of such junctions follows the diode equations, in which the current flow in one direction across the junction increases exponentially with the applied voltage, whereas the current flow in the other direction across the junction is constant with voltage. The dark current density $J_{dark}$ (amperes/cm$^2$), as a function of the voltage (V) applied to this diode is as follows:

$$J_{dark}(V) = J_0\left(e^{\frac{qV}{kT}} - 1\right) \tag{5-1}$$

where $J_0$ is a constant, q is the electronic charge, k is the Boltzman's constant, and T is the temperature (K).

When the diode is illuminated, absorption of the light will create additional charge carriers inducing an additional current flow across the junction, and that is must be added to the dark current to obtain the total current in the system. For illumination with light at many different wavelengths, the total photo-induced current is calculated by integrating the contributions to the current from excitation at each wavelength. So, the short-circuit photocurrent density ($J_{sc}$) is:

$$J_{sc} = q\int I_s(E)(QY)(E)dE \tag{5-2}$$

where $I_s$ is the solar photon flux, E is the photon energy being inversely proportional to the wavelength, and QY is the quantum yield being the electrons collected per incident photon.
The net current density (J) is given by:

$$J(V) = J_{sc} - J_{dark}(V) = J_{sc} - J_0\left(e^{\frac{qV}{kT}} - 1\right) \tag{5-3}$$

But ideal diode behavior is rarely achieved that is why a non-ideality factor, m, is introducing into Equation (5-3):

$$J(V) = J_{sc} - J_{dark} = J_{sc} - J_0\left(e^{\frac{qV}{mkT}} - 1\right) \tag{5-4}$$

At open circuit no current flows that is J(V) = 0, thus the open-circuit voltage ($V_{oc}$) is equal to:

$$V_{oc} = \left[\frac{mkT}{q}\right]\ln\left[\left(\frac{J_{sc}}{J_0}\right) + 1\right] \tag{5-5}$$

A plot of the net photocurrent density (J) versus voltage showing the current-voltage characteristic of a typical solar cell is depicted in the figure 11-b, whereas figure 11-a represents a circuit of an "ideal diode" solar cell.

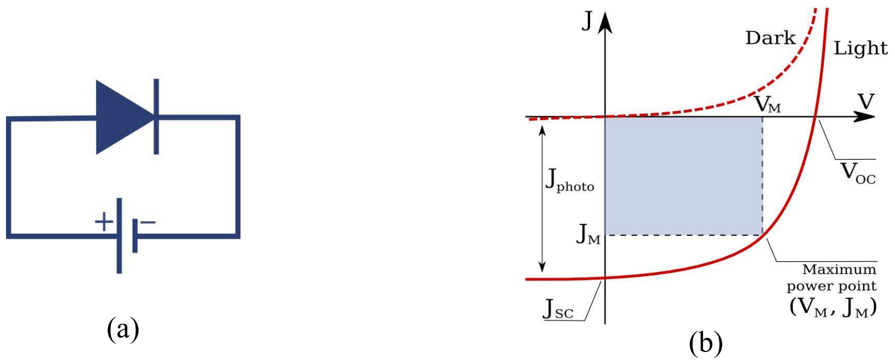

(a)

(b)

Figure 11. (a) Equivalent circuit and (b) I-V characteristics of an "ideal" solar cell.

The maximum power point of the cell is represented by the values of $J_m$ and $V_m$ at which the maximum rectangle in the figure 11-b meets the J-V curve. The “fill factor” (FF) is then defined as:

$$FF = \frac{J_m V_m}{J_{sc} V_{oc}} \tag{5-6}$$

The cell conversion efficiency (η) is the electrical power density ($J_m V_m$) (watts/cm$^2$) divided by the incident solar power density ($P_i$), multiplied by 100 to obtain a percent value. It expresses the ratio of produced power to the incoming power.

$$\eta = \frac{J_m V_m}{P_i} = 100 * \frac{J_{sc} V_{oc} FF}{P_i} \tag{5-7}$$

However, ohmic resistances are quite present related to problems of leaks at the interfaces of p-n materials ($R_{//}$) on one hand, and at semiconductor-metal electrodes interfaces added to the internal resistance of each component in the photovoltaic layer ($R_s$) on the other hand, as shown in figure 12.

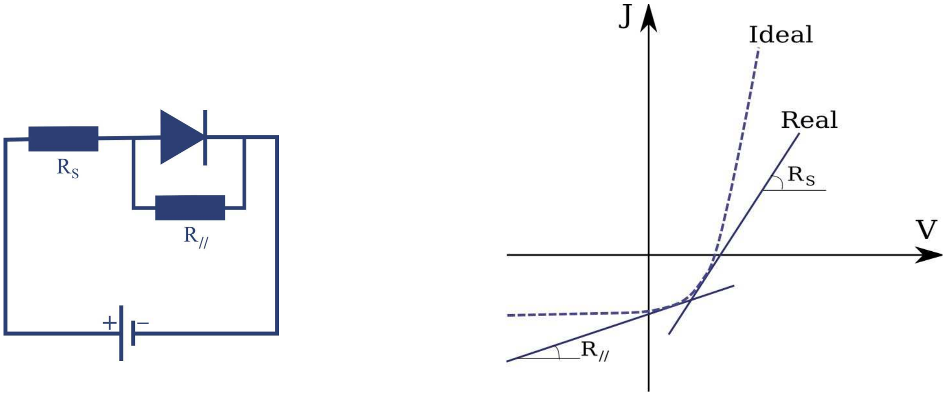

(a) (b)

Figure 12. (a) Equivalent circuit and (b) I-V characteristics of a “real” solar cell showing the presence of resistance in series ($R_s$) and in parallel ($R_{//}$).

Thus the total current (5-4) in a real diode upon illumination in function of the applied tension is defined as:

$$J = J_{sc} - J_0 \left[ \exp\left( \frac{q(V - JR_s)}{mkT} \right) - 1 \right] - \frac{V - IR_s}{R_{//}} \tag{5-8}$$

where the resistances are determined from the slopes as:

$$R_s = \left( \frac{dV}{dJ} \right)_{V=V_{oc}} \quad \text{and} \quad R_{//} = \left( \frac{dV}{dJ} \right)_{J=J_{sc}} \tag{5-9}$$

Another important solar cell characteristic is the External Quantum Efficiency (EQE) which is by definition the photocurrent measured at short-circuit (V=0) per incident light power as a function of wavelength. The EQE measures under monochromatic light the ratio of the number of electrons generated by the solar cell to the number of incident photons on the active surface as determined by the equation:

$$\mathrm{EQE}(\%) = \frac{n_{\text{electrons}}(\lambda)}{n_{\text{Photons}}(\lambda)} \times 100 = \frac{J_{sc}(\lambda)/e}{P_i(\lambda)/h\nu} \times 100 = \frac{J_{sc}(\lambda)}{P_i(\lambda)} \times \frac{1240}{\lambda} \times 100 \qquad (5\text{-}10)$$

where $J_{sc}$ is the short circuit photocurrent density and $P_i$ is the monochromatic incident light power. The EQE provides valuable informations about solar cell internal processes. It is normally used to distinguish the contributions of different components of the solar cell to the total photocurrent. Experimental setup measurements are given in the Appendix VIII.

## 5.6 Results and discussions

### 5.6.1 H2TCPP

To begin with and as mentioned earlier 70:30 weight percentage (wt.-%) of the ZnO:P3HT ratio was found to be the ideal combination to be used in the photoactive cell layer. Using less than 70 wt.% ZnO implied a large decrease in the current density probably due to less connectivity among the ZnO. While using over 70 wt.-% ZnO led to large drop in the $J_{sc}$ and $V_{OC}$ which is attributed to the formation of ZnO aggregates.

Hybrid ZnO-based solar cells were sensitized by the porphyrin H2TCPP at several concentrations to test in the first place the effect of this dye-sensitization and then the consequences of varying its concentration on the cells light-conversion. The few concentrations that we used are some of those that were employed in the previous chapter, namely; (4) $1{,}5.10^{-5}$ M, (6) $6.10^{-5}$ M, (7) $1{,}2.10^{-4}$ M, (8) $2.10^{-4}$ M and (9) $3.10^{-4}$ M. Figure 13 illustrates the energy diagram of each of solar cell components showing theoretical charge transfer pattern for an ideal cell functioning. From this diagram, charge injection from H2TCPP into ZnO as well as from P3HT across H2TCPP should work properly.

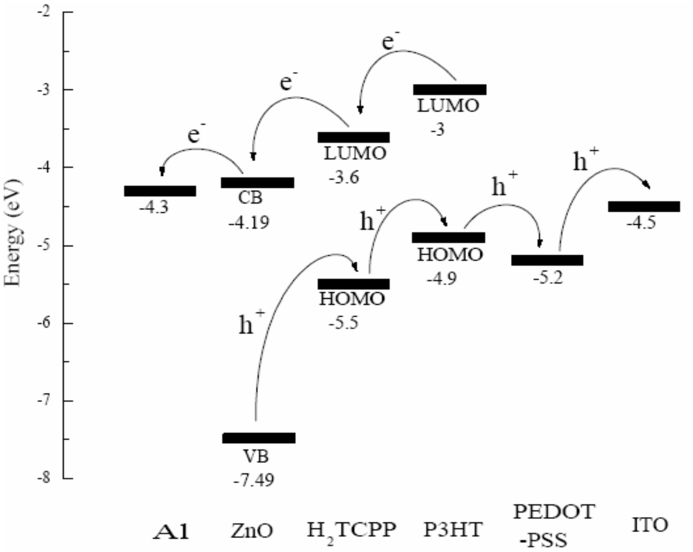

Figure 13. Energy diagram for an efficient charge transfer between solid state dye sensitized solar cell components where the sensitizing dye is the $H_2TCPP$.

Studying the effect of the H2TCPP concentration in the active film on the photovoltaic performance was firstly done by recording the J-V Characteristics under white-light illumination using a halogen lamp in the intensity range of 100 mW/cm$^2$ at a scan rate of 0.5 V/min (see Appendix VIII). Figure 14 shows typical current-voltage characteristics of ZnO+H2TCPP+P3HT solar cells at different amounts of H2TCPP in the dark and under illumination. The cell containing the mixture ZnO/P3HT (black plot) displays the highest photocurrent density but its behavior represented in the figure 14 by a relative steep slope at negative voltages demonstrates high leaks at the interfaces of the p-n Polymer-ZnO. In the dark, this ZnO/P3HT cell reveal excellent diode behavior, this diode behavior in the dark was also found for all other cells (not shown). The resistance effect of leak at the p-n interfaces in the ZnO/P3HT cell is further reduced when adding and increasing the H2TCPP dye concentration. Mounting the dye concentration implies a decreasing in the current density $J_{sc}$, in addition to the change of the plots' slopes at positive voltages which probably indicates the presence of increasing internal resistance with the dye as well as the poor contact at semiconductor-electrode interfaces due to existence of highly concentrated dyes. Furthermore, performance of the blended cells with different dye concentrations is summarized in table 1. Photovoltaic properties are enhanced by blending the smallest dye concentration, whereas general performance loss is induced by further H2TCPP grafting. These facts will be discussed later.

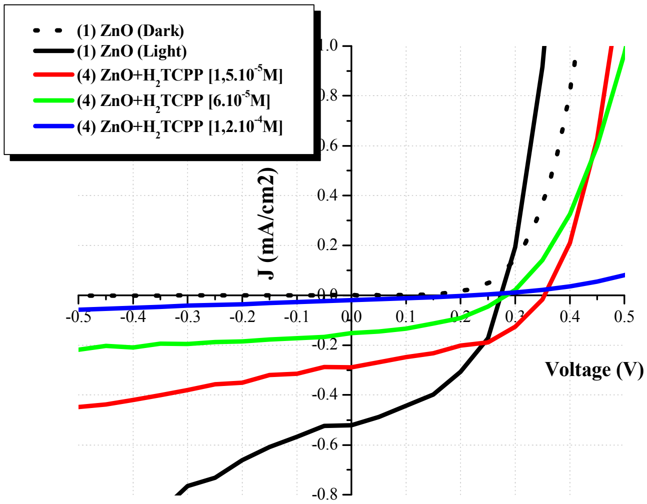

Figure 14. Current-voltage characteristics of ZnO+H2TCPP+P3HT solar cells at different amounts of H2TCPP under illumination (*Solid lines*) and in the dark (*Dotted line*).

| ZnO/ $H_2$TCPP /P3HT samples | $J_{sc}$(mA/cm$^2$) | $V_{oc}$(V) | FF | η (%) |
|---|---|---|---|---|
| ZnO | 0.52 | 0.3 | 0.39 | 0.06 |
| ZnO+$H_2$TCPP [1,5.10$^{-5}$ M] | 0.206 | 0.4 | 0.54 | 0.04 |
| ZnO+$H_2$TCPP [6.10$^{-5}$ M] | 0.151 | 0.3 | 0.38 | 0.02 |
| ZnO+$H_2$TCPP [1,2.10$^{-4}$ M] | 0.0193 | 0.25 | 0.22 | 0.001 |
| ZnO+$H_2$TCPP [2.10$^{-4}$ M] | 0.00845 | 0.43 | 0.08 | 0.0003 |

Table 1. Performance of H2TCPP-sentisized ZnO solar cells under illumination of AM1.5-100mW/cm$^2$. ($J_{sc}$=short-circuit current density, $V_{oc}$=open-circuit voltage, FF=fill factor and η=cell conversion efficiency).

Incident photon-to-current-conversion efficiency denoted as External Quantum Efficiency measurements EQE constitute the second important step to understand the real functioning of our hybrid solar cells. Hence, photocurrents generated by the cells were measured under white-light halogen tungsten illumination, and were monitored in the 300-750 wavelength region (see Appendix VIII). By comparing the spectral response given by the EQE measurements with the optical absorption spectra one can obtain information on the charge carrier generation mechanism. Indeed, the cells' EQE spectra given in figure 16 closely resemble their absorption spectra that are shown in figure 15, indicating that ZnO, H2TCPP dye and P3HT contribute to the charge carrier generation. Absorbance spectra in figure 15 reveal valuable aspects as the increased scattering with increasing dye concentration originating from aggregates formation, and as the increase followed by the decrease of the dye Soret band absorption when increasing its amount.

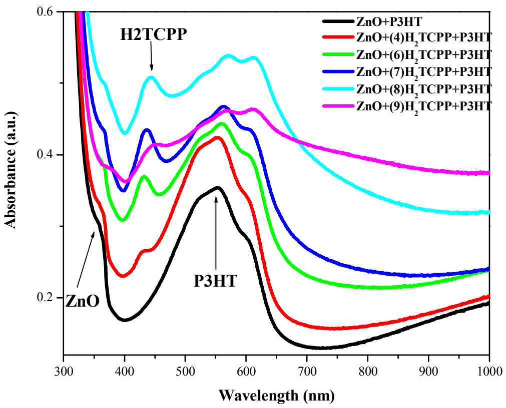

Figure 15. Absorbance spectra of ZnO+H2TCPP+P3HT solar cells at different amounts of H2TCPP (with ITO substrate).

The sensitivity of a solar cell varies with the wavelength of the incoming light. The small overlap of the ZnO, H2TCPP and P3HT individual absorption spectra, as shown in figure 9, allows selective light-absorption which means that photons of specific energies will be almost solely absorbed either in the semiconductor or in the porphyrin or in the polymer, respectively. Hence, selective generation of charge carriers in the ZnO conduction band is produced either directly by bandgap excitation using UV light or indirectly by injecting electrons through dye-sensitization in the visible.

As already mentioned all the cell components contribute to the photocurrent generation as shown in the EQE plots of figure 16. Nevertheless, huge variations of these components contribution are clearly visible when changing the amount of the grafted H2TCPP dye. The ZnO/P3HT cell (*Open squares*) shows two photocurrent peaks recognized as the involvement of electron exchange among both ZnO and P3HT. When grafting small concentration of dye onto the ZnO, we can clearly see the apparition of the dye peak contributing to the photocurrent generation (*Open circles*). Increasing the dye amount (*Open triangles*), leads to a slight increase in the dye peak, which is normally measured (for all samples) by subtracting the baseline. When increasing the dye amount, peaks at ZnO and P3HT decrease continuously with respect to those of the non-containing dye cells. We can clearly see that the decrease in the P3HT band is remarkably strong. However, sharp attenuation in the whole photocurrent intensity and hence the less contribution of all the cell active layer ingredients is taking place at higher grafted-dye amounts (*Open stars*). For cell samples with dye concentrations higher than 1,2.$10^{-4}$ M, the signal was too weak to be treated.

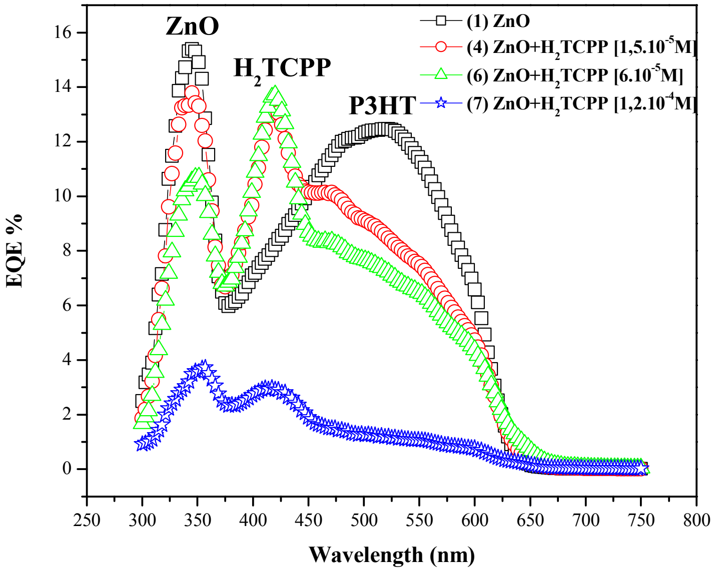

Figure 16. EQE photocurrent spectra of ZnO+H2TCPP+P3HT solar cells at different amounts of H2TCPP under illumination.

The photo-physical processes underlying the working mechanism of the solar cell where the active layer is only constructed by ZnO and P3HT (*Open squares* in figure 16) involve two mechanisms by light absorption of both ZnO and P3HT. The light of wavelength less than 380 nm is totally absorbed by the ZnO nanorods, electron is thus promoted to the conduction band (CB) leaving a hole in the valence band (VB). The hole is thus transferred to the P3HT and transported towards the ITO electrode and the photoexcited electron will leave the ZnO conduction band to reach the other Al electrode. On the other hand the visible light that is mainly harvested by the polymer initiates the formation of excitons which have no net electrical charge and cannot carry current so they must be dissociated in order to produce the free electrons and holes required in the cell to produce electrical power. The subsequent charge-separation of the exciton is produced by the built-in electric field at the interface of the p-n (P3HT-ZnO) junction. The electron will be injected to the ZnO conduction band to be collected afterwards at the Al electrode and the hole is transmitted to the other ITO electrode to complete the circuit. This mechanism is quite feasible due to the cascade formed by the components energy levels (see figure 13).

Adding the dye H2TCPP at lower concentration induces additional photocurrent contribution presented by the Soret band peak appearing around 420 nm in the figure 16. This can be interpreted by the absorption of a visible photon by the grafted H2TCPP molecules adjacent the interface of ZnO followed by interfacial electron injection from the H2TCPP LUMO level into the conduction band (CB) of the ZnO, while the hole is transported through the P3HT polymer. For example, taking into account the very low absorption of the Soret band at the $1,5.10^{-5}$ M dye concentration in the photoactive layer (ZnO/H2TCPP/P3HT) (see figure 15), we can conclude that the charge carrier injection at the ZnO/H2TCPP interface is highly efficient as manifested by the strong dye peak in the photocurrent (see figure 16).

Now, increasing the dye concentration leads to a decrease of the ZnO contribution to the photocurrent generation. This drawback might be interpreted by two different mechanisms as sketched in figure 17. At wavelengths less than 380 nm, the light is absorbed by the ZnO through the direct bandgap photoexcitation process (1), excited electrons in the CB can recombine intrinsically through process (2) or can pass first by electron trapping levels, created by the defects in the ZnO, to recombine afterward through (4), or they can interfacially recombine through (5) and (6). Increasing dye concentration will create surface charged layers at the ZnO/H2TCPP interface, as explained in the previous chapter, inducing a decrease in the interfacial hole transfer from ZnO to dye through the path (7), which presents the exchange at the interface that is greatly modified by dye-grafting. This will probably lead to more intrinsic recombination mechanisms in the ZnO through (2) and (4). Hence, less input of the ZnO to the photocurrent generation is likely to occur.

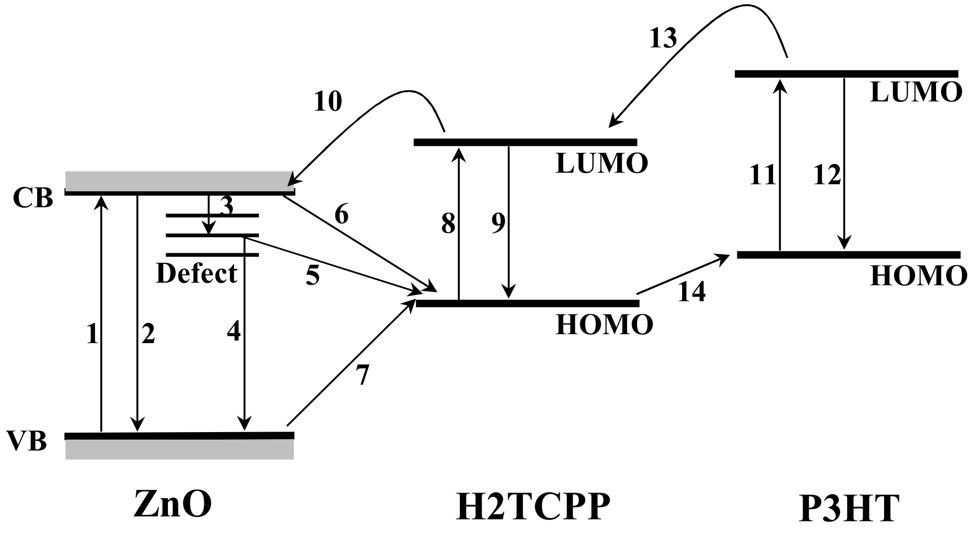

1- Band gap photoexcitation
2- Intrinsic charge recombination
3- Electron trapping
4- Intrinsic charge recombination
5- Interfacial charge recombination
6- Interfacial charge recombination
7- Interfacial hole transfer (H2TCPP/ZnO)

8- Molecular photoexcitation (in H2TCPP)
9- Molecular radiative decay (in H2TCPP)
10- Interfacial electron transfer (H2TCPP/ZnO)
11- Molecular photoexcitation (in P3HT)
12- Molecular decay (in P3HT)
13- Interfacial electron transfer (P3HT/H2TCPP)
14- Interfacial hole transfer (P3HT/H2TCPP)

Figure 17. A schematic diagram of the energy levels of H2TPP and the valence and conduction band positions of ZnO together with the primary and secondary processes that may occur upon optical excitation.

On the other hand, the contribution of the dye to the photocurrent increases to some extent then decreases when mounting the dye quantity (see figure 16). Light harvesting carried out by a small amount of H2TCPP-sensitizer initiates exciton formation (8) leading to charge separation followed by electron transfer (10). The charge-separated state can as well undergo recombination to the ground state (9) or dissociate into free charge carriers by diffusion, thus diminishing their participation in producing the current. Small dye concentrations fairly contribute to the current, but the direct consequence of the higher dye concentrations that is the aggregates formation on the surface of the ZnO nanorods lowers the interfacial transfer from the dye to ZnO (10) at their interface. The other consequence of grafting higher dye concentrations is the surface charged layers formation at the ZnO/H2TCPP interface, as already mentioned, that will prevent any charge transfer blocking thus the channels (7) and (10) at very high dye densities.

P3HT input on the photocurrent decreases steeply with increasing dye concentration, as seen in figure 16. This might be due to the highly packed dyes that form a layer with high thickness between the ZnO and the P3HT, this dye layer is probably constituting recombination centers of the P3HT charges carriers. This growing aggregated-dye layer inhibits any charge transfer between P3HT and ZnO. So the exciton formed in the P3HT upon illumination (11) will undergo two ways; either it will recombine (12) or it will be intrinsically transferred to the dyes (13) that inhibit its passage, thus the electron must be interfacially transferred (12) back to the P3HT HOMO (figure 17).

Morphology of cell surfaces pictured in figure 18 by optical spectroscopy reveals further formation of dye-grafted ZnO networks with dye concentration. The cell containing no dye shows through figure 18-a, well dispersed ZnO layer. Yet, introducing the dye to the active layer demonstrates the agglomeration among the hybrids as clearly visible when increasing the dye amounts in figures 18-b, -c and -d. Figure 18-d shows large isolated islands of aggregated hybrids that are formed at the very high concentration. These aggregates will lower the connectivity between the ZnO nanorods, thus lowering the electron conduction in the ZnO nanorods network and consequently its arrival to the electrode. Hence, aggregation mass that increases with the dye concentration lowers the efficiency of our solar cells.

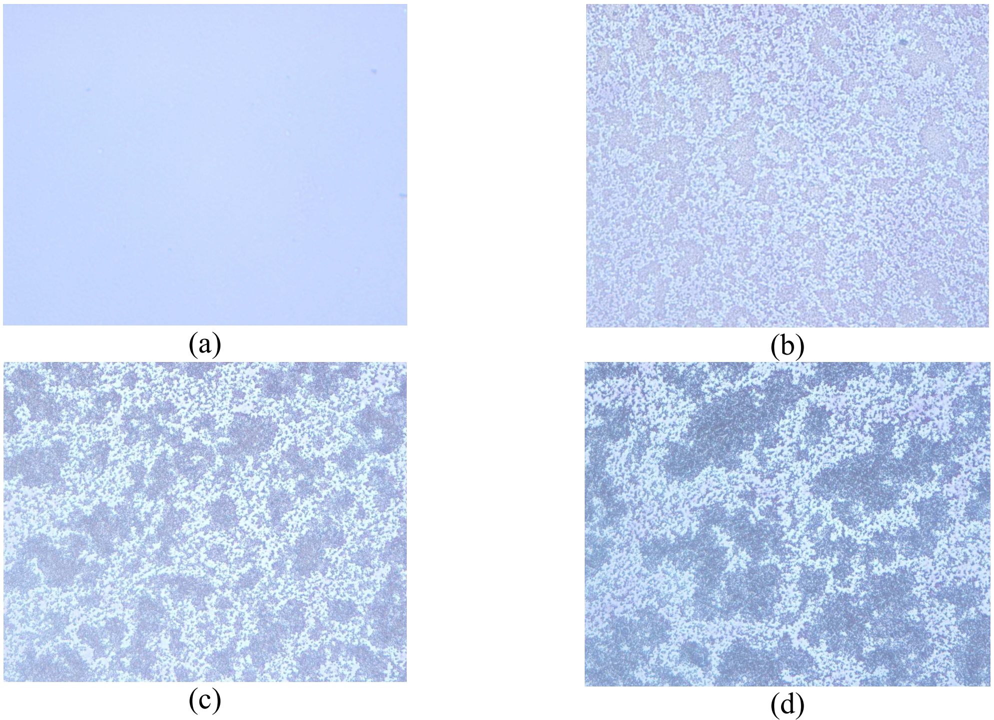

(a) (b) (c) (d)

Figure 18. Morphology images (860×690 μm$^2$) of solar cells with (a) ZnO/P3HT, (b) ZnO/H2TCPP 1,5.10$^{-5}$ M /P3HT, (c) ZnO/H2TCPP 6.10$^{-5}$ M /P3HT (4), and (d) ZnO/H2TCPP 1,2.10$^{-4}$ M /P3HT (done by optical microscopy)

Summing up, we detected photovoltaic response for the H2TCPP-based cells at low grafted-dye concentrations, where the charge carrier injection from the H2TCPP to ZnO interface is highly efficient as manifested by the strong dye peak in the photocurrent if compared to their analogous low absorption of the Soret band. While at higher concentrations our hybrid solar cells performance is weakened. This degradation might be assigned to the formation of induced surface charge at the ZnO/H2TCPP interface preventing charge exchanges at the interface modified by dye-grafting. Simultaneously, P3HT contribution to the photocurrent decreases dramatically with increasing dye concentration. This might be due to the highly packed grafted-dyes that form a layer of recombination centers between the ZnO and the P3HT, thus holding back any charge transfer between P3HT and ZnO. The growing aggregation mass in highly-crowded islands amongst the hybrids lowers the connectivity between the ZnO nanorods and consequently the efficiency of the solar cells.

### 5.6.2 PP9

PP9-based hybrid cells were prepared equally as in the case of H2TCPP, but with a very high dye concentration. It is worth noting that no photovoltaic signals were detected in this sample. Hence, at this high dye concentration, the cells with PP9-sensitizing the ZnO nanorods exhibit identical behavior as cells with highly H2TCPP-based blend.

### 5.6.3 Z907

Hybrid ZnO-based solar cells were as well fabricated by adsorbing the Z907 dye molecules onto the ZnO nanorods at several concentrations, namely $0{,}5.10^{-4}$ M, $1{,}5.10^{-4}$ M and $2{,}5.10^{-4}$ M. Figure 19 presents the energy diagram of each of solar cell components viewing theoretical charge transfer manner for an ideal cell performance.

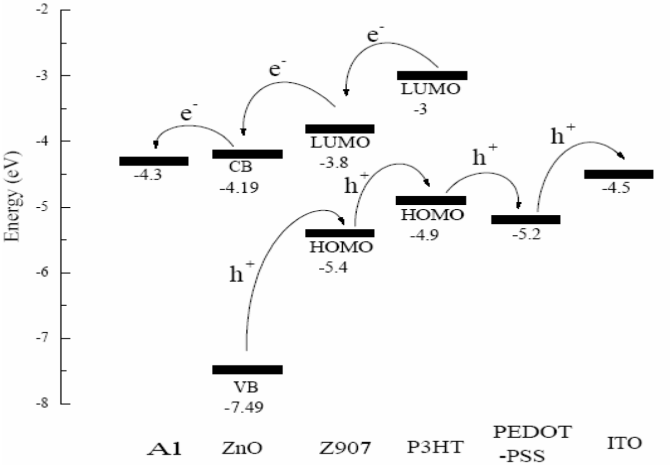

Figure 19. Energy diagram for an efficient charge transfer between solid state dye sensitized solar cell components where the sensitizing dye is the Z907 [35].

The J-V Characteristics of ZnO+Z907+P3HT solar cells that were recorded under illumination are shown in figure 20 and where we varied the amounts of the dye. The cell containing the mixture ZnO/P3HT (*black plot*) exhibits the highest photocurrent density, as well as the cell with the hybrid mixture at the lowest dye concentration ZnO/Z907/P3HT (*red plot*) having higher $V_{oc}$ voltage than the former one. This attests the enhancement of the cell functioning when grafting the Z907 at low concentration. Raising the dye concentration implies a decreasing in both current density $J_{sc}$ and open circuit potential $V_{oc}$, adding up the change of the plots slopes at positive voltages which points to the existence of upward internal resistance with the dye, and the poor contact at semiconductor-electrode interfaces due to the highly concentrated dyes.

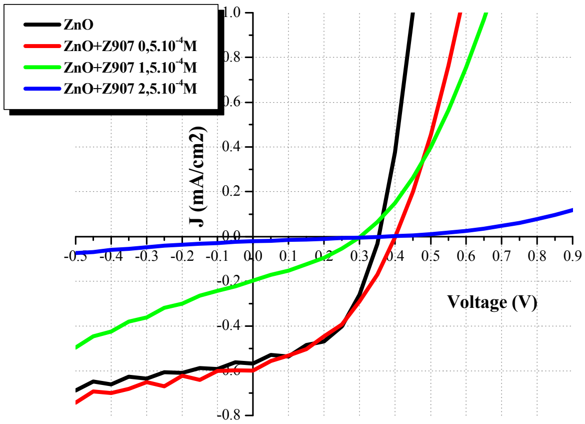

Figure 20. Current-voltage characteristics of ZnO+Z907+P3HT solar cells at different amounts of Z907 under illumination.

Table 2 recapitulates the J-V performance of the cells at different dye concentrations. Photovoltaic properties are improved by introducing small dye concentration, while performance failure is stimulated by additional Z907 grafting.

| ZnO/ Z907 /P3HT samples | $J_{sc}$(mA/cm$^2$) | $V_{oc}$(V) | FF | η (%) |
|---|---|---|---|---|
| ZnO | 0.553 | 0.355 | 0.50 | 0.1 |
| ZnO+ Z907 [0,5.10$^{-4}$ M] (5%) | 0.647 | 0.361 | 0.42 | 0.1 |
| ZnO+ Z907 [1,5.10$^{-4}$ M] (50%) | 0.197 | 0.302 | 0.32 | 0.02 |
| ZnO+ Z907 [2,5.10$^{-4}$ M] (100%) | 0.0275 | 0.37 | 0.20 | 0.002 |

Table 2. Summary of the photovoltaic performance of Z907-sentisized ZnO solar cells under illumination of AM1.5 (100mW/cm$^2$). The % values indicate the estimated surface coverage. ($J_{sc}$=short-circuit current density, $V_{oc}$=open-circuit voltage, FF=fill factor and η=cell conversion efficiency).

External Quantum Efficiency measurements EQE are plotted in figure 21. Colossal variations in the cell components contribution are evident when varying the amount of the grafted Z907 dye. The ZnO/P3HT cell (*Open squares*) shows two photocurrent peaks of both ZnO and P3HT contributions. Grafting small concentration of dye onto the ZnO leads to a relatively small decrease in the ZnO and P3HT peaks (*Open circles*). Surprisingly increasing the Z907 dye amount leads to the total photocurrent vanishing.

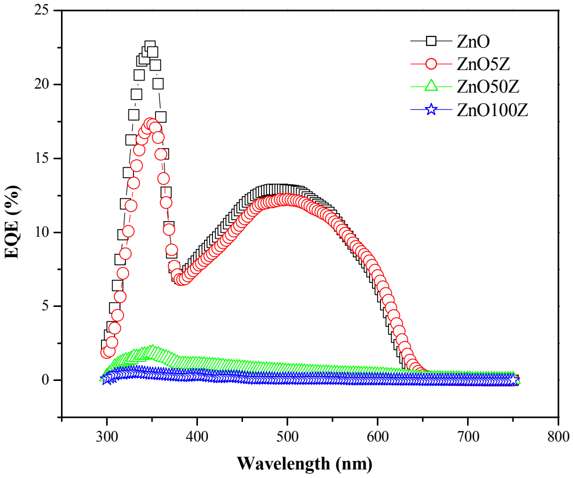

Figure 21. EQE photocurrent spectra of ZnO+Z907+P3HT solar cells at different dye amounts under illumination.

The decrease in the ZnO contribution to the photocurrent creation may be attributed to the bad connection among the ZnO nanorods. This bad connectivity is induced by the small dye concentration presence at that ZnO surface; accordingly reducing somehow the electrons' percolation paths. However, increasing further the dye concentration induces a dramatically choked photocurrent. This fact is almost certainly due to the formation of arranged dye layers on the surface of ZnO. These layers may form crystallized coating preventing any charge exchange with the core ZnO as well as with the surrounding polymer environment. This aspect is actually ascribed to the Z907 tendency of creating arranged networks as we already stated through the formation of a gel-like substance.

Here the morphology of cell surfaces, as imaged in figure 22 by optical spectroscopy, do not resemble to the previous case with the H2TCPP. No mass aggregation among hybrids is noticed even at very high dye densities (see figure 22-c), just little agglomerates spots are visible. This observation strengthens the idea of the crystallized grafted-dye layer created by the self-assembled Z907 molecules.

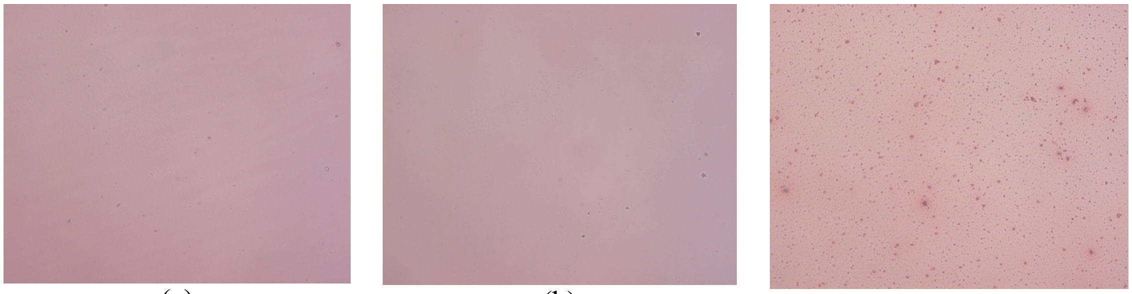
(a) (b) (c)

Figure 22. Morphology images (860×690 μm$^2$) of solar cells with (a) ZnO/P3HT, (b) ZnO/Z907 1,5.10$^{-4}$ M /P3HT and (c) ZnO/Z907 2,5.10$^{-4}$ M/P3HT mixture (done by optical microscopy)

We conclude that the hybrid solar cells fabricated with the Z907 dye display significantly strangled photocurrent at high dye concentrations. Here, the Z907 tendency to form a gel-like could create self-assembled arranged dye molecules that may form a crystallized layer stopping any charge exchange with the core ZnO and with the adjacent polymer.

## 5.7 Conclusion

We succeeded to create solar cells whose photoactive layer is constructed by blending ZnO-based nanohybrids with the P3HT polymer. Actually, three different dyes are used to sensitize the ZnO nanorods. Grafting of these dyes when changing their amounts leads to strong variations in the J-V and the EQE measurements, insinuating thus different behavior of each cell component's contribution to the photocurrent generation. The common features among all of the three hybrid types is that; at low grafted-dye concentrations, we succeeded to detected the cells' photovoltaic response, while at higher concentrations our hybrid solar cells functioning seems to be degraded.

In the case of the H2TCPP, and at low concentrations the charge carrier injection from the H2TCPP to ZnO interface is highly efficient as manifested by the strong dye peak in the photocurrent once compared to their analogous low absorption of the Soret band. At higher dye concentration, the cells' performance degradation could be probably assigned to the formation of surface charged layers at the ZnO/H2TCPP interface preventing charge exchanges at the interface that is greatly modified by dye-grafting. At the same time, P3HT input on the photocurrent decreases dramatically with increasing dye concentration. This might be due to the highly crowded grafted-dyes that form a layer with high resistivity between the ZnO and the P3HT. Hence, this rising aggregated-dye layer slows down any charge transfer between P3HT and ZnO. The growing aggregation mass among the hybrids, observed as highly-packed islands, is also the cause of lowering the efficiency of the solar cells.

Hybrid ZnO-based solar cells fabricated by adsorbing the Z907 dye molecules onto the ZnO nanorods exhibit dramatically choked photocurrent at high dye concentrations. In this case, the interpretation most probably differs from the previous case with H2TCPP. Here, this feature is ascribed to the Z907 tendency of creating arranged networks through the development of a gel-like substance. These arranged network layers may form crystallized coating that prevents any carrier charge exchange with the core ZnO as well as with the surrounding polymer environment.

# Bibliography

[1] H. Gerischer, J. Electrochem. Soc., 113 (1966) 1174

[2] B. O'Regan, and M. Grätzel, Nature, 353 (1991) 737

[3] A. E. Becquerel, Comt. Rend. Acad. Sci, 9 (1839) 561

[4] D. M. Chapin, C.S. Fuller, and G.L. Pearson, J. Appl. Phys., 25 (1954) 676

[5] M. Green, Progress in Photovoltaics, 9 (2001) 123

[6] D. C. Raynolds, G. Leies, L. L. Antes, and R. E. Marburger, Phys. Rev., 96 (1954) 533

[7] G. Yu, J. Gao, J. C. Hummelen, F. Wudl, and A. Heeger, J. Science, 270 (1995) 1789

[8] G. Yu, and A.J. Heeger, J. Appl. Phys., 78 (1995) 4510

[9] J. J. M. Halls, C. A. Walsh, N. C. Greenham, E. A. Marseglia, R. H. Friend, S. C. Moratti, and A. B. Holmes, Nature 376 (1995) 498

[10] G. Yu, K. Pakbaz, and A.J. Heeger, Appl. Phys. Lett. 64 (1994) 3422

[11] A. K. Ohler, H. F. Wittman, R. H. Friend, M. S. Kahn, and J. Lewis, Synth. Met. 77 (1996) 147

[12] C. J. Brabec, Solar Energy Materials & Solar Cells 83 (2004) 273

[13] C.J. Brabec, S.E. Shaheen, C. Winder, N. Sariciftci, and P. Denk, Appl. Phys. Lett. 80 (2002) 1

[14] F. Padinger, R. Rittberger, and S. Sariciftci, Adv. Funct. Mater. 13 (2003) 85

[15] C. Waldauf, P. Schilinsky, J. Hauch, and C.J. Brabec, Thin Solid Films, 451 (2004) 503

[16] J. Moser, Monatsh. Chemie, 8 (1887) 373

[17] D. Duonghong, N. Serpone, and M. Gratzel, Helvetica Chimica Acta, 67 (1984) 1012

[18] M. Gratzel, Nature, 421 (2003) 586

[19] M. Stolka, J. F. Yanus, and D. M. Pai, J. Phys. Chem., 88 (1984) 4707

[20] B.Oreagan and D. T. Schwartz, Chem. Mat., 10 (1998) 1501

[21] G. R. R. A. Kumara, A. Konno, G. K. R. Senadeera, P. V. V. Jayaweera, Dbra De Silva, and K. Tennakone, Sol. En. Mat. Sol. Cells, 69 (2001) 195

[22] K. Tennakone, G. K. R. Senadeera, Dbra De Silva, and I. R. M. Kottegoda, Appl. Phys. Lett., 77 (2000) 2367

[23] K. Tennakone, G. R. R. Kumara, I.R.M. Kottegoda, K. G. U Wijayantha and V. P. S. Perrera, J. Phys. D: Appl. Phys. 31 (1998) 1492

[24] D. Gebeyehu, C. Brabec, N. S. Sariciftci, D. Vangeneugden, R. Kiebooms, D. Vanderzande, F. Kienberger, and H. Schindler, Synth. Met., 125 (2002) 279

[25] G. Smestad, S. Spiekermann, J, Kowalik, C. D. Grant, A. M. Schwartzberg, J. Zhang, L. M. Tolbert, and E. Moons, Sol. En. Mat. and Sol. Cells, 76 (2003) 85

[26] A.F.Nogueira, C. Longo, and M.A. De Paoli, Coord. Chem. Rew., 248 (2004) 1455

[27] E. Arici, D. Meissner, F. Schäffler, and N.S. Sariciftci, Int. Journ. Photoenergy, 5 (2003) 199

[28] A. P. Alivisatos, Science, 271 (1996) 933

[29] W. Huynh, J. Dittmer, and A. P. Alivisatos, Science, 295 (2002) 2425

[30] N. C. Greenham, X. Peng, and A. P. Alivisatos, Phys. Rev. B., 54, (1996) 17628

[31] S. McDonald, G. Konstantatos, S. Zhang, P. W. Cyr, E. J. D. Klem, L. Levina, and H. Sargent, Nature Mat., 4 (2005) 138

[32] P. A. V. Hal, M. M. Wienk, J. M. Kroon, W. J. H. Verhees, L. H. Sloff, W. J. H. V. Gennip, P. Jonkhejm, and R. A. J. Janssen, Adv. Mat., 15 (2003) 118

[33] W. J. E. Beek, M. M. Wienk, and R. A. J. Janssen, Adv. Func. Mat., 16 (2006) 1112

[34] http://www.udel.edu/igert/pvcdrom/APPEND/AM1_5.HTM

[35] P. Ravirajan, A. M. Peiro, M. K.Nazeeruddin, M. Grätzel, D. D. C. Bradley, J. R. Durrant, and J. Nelson, J. Phys. Chem. B, 110 (2006) 7635

# Conclusion

Our project consists of the engineering of functional hybrid (inorganic/organic) systems at the molecular nano-scale that are essential to the development of application fields ranging from materials, physics, chemistry and biomedicine. Herein, we prepared the inorganic ZnO nanoparticles through two different methods; *femtosecond laser ablation in liquid medium* and *chemical processes*. Through femtosecond ablation, we obtained ZnO nanospheres with high quality but with small quantities. Hence, we transit to produce large amount of ZnO nanospheres and nanorods through simple chemical processes to be applied in solar cells.

Femtosecond laser ablation of ZnO in liquid medium is the very cleanest and powerful method to fabricate defectless nanospherical biocompatible ZnO. We produced ZnO particles ablated in deionized water of about 1 to 2 nm as identified via AFM and TEM observations, which also reveal the increase in ablated particle size when raising the fluence. Ablating in dodecanethiol solution implies slow cluster-growth manifested by the development of facetted particles, providing evidence of the adsorption of the thiol molecules onto the ZnO. We grafted ex-situ and in-situ the tetramethylrhodamine B isothiocyante (TRITC) dye molecules onto the ZnO particles ablated in ethanol. We showed through the HRTEM images that ex-situ nanohybrids crystallize in facetted structures with average particle size lesser than the size of pure ZnO. Electron transfer from the ZnO towards the grafted dye molecules occurs via (i) one-photon and (ii) two-photon excitations, respectively. We proved through these results that femtosecond laser ablation is a reliable tool for building-up nanohybrid materials to be potentially applied as bio-sensors.

We reported the detailed investigations on morphological and optical properties of the ZnO nanoparticles synthesized via chemical ways with KOH and NaOH base solutions, at different time stages of the synthesis reaction. We found through the HRTEM that generally the ZnO growth begins with the formation of very small nanospheres to end up with well shaped nanorods. Here, we demonstrated that the growth of nanorods synthesized with KOH is described in its first stage by “Oswald ripening” growth, followed by a directed fusion growth through “oriented attachment", which is assisted by the “Oswald ripening” mechanism at the maturation stage. This clarifies the formation of ZnO nanorods with rough surfaces.

However, nanorods, with smooth surfaces, synthesized with NaOH were basically formed by the "Oswald ripening" growth mechanism, with modest presence of "oriented attachment" at the very first growth stage. Through transmission and photoluminescence measurements of both KOH and NaOH-based ZnO nanoparticles, we found the effect of the quantum confinement at small sized spherical-shaped ZnO particles. All of the NaOH-based ZnO particles showed small degree of oxygen vacancy defects if compared to the KOH-based ZnO.

Through HRTEM observations, we proved that the ZnO nanospheres and nanorods morphology was not affected by adsorbing the two porphyrins (H2TCPP and PP9) and the Ruthenium-containing (Z907) dye molecules. Though, some orientations among the nanorod-hybrids could happen as a result of interaction between close ZnO particles through grafted-dyes. FTIR confirmed the grafting by the apparition of carboxylate symmetric and asymmetric binding modes.

Through absorbance and photoluminescence data in the case of grafting the porphyrin H2TCPP, we showed that because the ZnO nanorods (of dimensions 9 nm×38 nm) offer total surface less than the small nanospheres (5,6 nm in diameter), the flat laying grafted-H2TCPP reach H-aggregation at dye surface coverage percentage lower than that with nanospheres, namely at 29% and 42% of the ZnO nanorod and nanosphere, respectively. This aggregation was marked when increasing the dye amount by their quenched absorption and emission intensities if compared to those of free dyes at identical concentrations in solution. Here, the significant feature that arises at low dye concentrations is that the aggregated pure dye molecules suspended in pure solutions become isolated to some extent once grafted onto the ZnO surface, inducing thus an augmentation of absorption and fluorescence higher than their equivalent pure H2TCPP solutions. We believe that this improvement in the fluorescence emission is also assisted trough ZnO contribution by:

- Decreasing amount of electron transfer (due to the continuous decrease in charge exchange because of the charged layers induced at the interface with the increasing dye) and a small constant contribution of Forster energy transfer ("small" due to little overlap between the ZnO emission and the H2TCPP absorbance spectra) in the "*nanrod-like hybrids*".
- Increasing rate of electron transfer (favored by the continuous increase in ZnO band gap) and decreasing of the small input of Forster energy transfer (due to the deceasing overlap between ZnO emission and the H2TCPP absorbance upon increasing the dye) in the "*nanoshperical hybrids*".

In the case of the porphyrin PP9, we also found the important fact of increasing the energy band gap of the ZnO with increasing dye concentration. However, the grafted-PP9 molecules present higher and faster aggregation tendency than the grafted-H2TCPP. We found that, up to 4% surface coverage, H-aggregation of grafted-PP9 onto ZnO nanospheres starts to be visibly evident, while aggregation was relatively instantly when grafting the PP9 onto ZnO nanorods. With the PP9, we can expect that Forster energy transfer from the ZnO is favored, more than in with the H2TCPP, because of the large overlap between the ZnO emission and the PP9 absorbance spectra.

Fluorescence quantum yields of the PP9 are less efficient than those estimated for the H2TCPP, merely due to higher intermolecular PP9 interactions implying less charge and energy exchanges with the ZnO nanoparticles. At small concentration of both H2TCPP and PP9, we demonstrated the higher quantum yields in the hybrids compared to the pure dyes. While at higher dye concentration, decrease of the dye fluorescence quantum yield in the hybrid systems with increasing concentration is credited to the dye-aggregates development.

We created solar cells with photoactive layer constructed by blending the nanorods ZnO-based hybrids with the P3HT polymer. The common features among all of the three hybrid types (with H2TCPP, PP9, Z907) are that; at low grafted-dye concentrations, we detected the cells' photovoltaic response, while at higher concentrations the hybrid solar cells functioning is degraded mainly due to formation of dye-aggregates acting as recombination centers of the P3HT charge carriers, thus slowing down any charge transfer between P3HT and ZnO. Besides, with H2TCPP, the growing aggregation mass among the hybrids themselves is also the cause of lowering the efficiency of the solar cells.

The main results obtained through this work are as follows:

■ For the first time, in our knowledge, we proved the ability of femtosecond laser in ablating ZnO targets in liquid medium to generate spherical particles of few nanometers revealing thus the effect of quantum confinement due to size reduction.

■ In the hybrid matrices, the electron transfer from the femtosecond ablated inorganic ZnO core towards the grafted organic *Tetramethylrhodamine B isothiocyante* dye molecules was confirmed to occur via two excitation processes; (i) one-photon and (ii) two-photon excitations.

■ We succeeded in creating nanohybrids based on spherical and rod-like ZnO templates, that were synthesized through chemical processes, grafted with dyes via their COOH anchoring groups. These hybrids present very interesting outcomes through optical analyses.

■ We found that the major and most important effect that emanates from the hybridation between the chemically-synthesized small ZnO nanospheres and the porphrin dyes is the alteration of the ZnO electronic structure by the increment of the its band gap energy due to confinement features upon increasing the dye concentration. This grafting process creates as well charge separated layers at the interface ZnO/dye dictating thus the charge carriers exchange. Yet, this fundamental effect of increasing the band gap was not detectable in the case of ZnO nanorod due to its large volume with respect to that of the nanosphere. However, the effects of induced charged layers must exist with hybrid based on ZnO nanorods.

Consequently, we can confirm that we succeeded in creating nanohybrids based on the spherical and rod-like ZnO inorganic templates, produced via two routes, grafted with several types of organic dye molecules. We demonstrated for the first time that upon increasing the porphyrin dye densities we were able to engineer the ZnO band gap via the occurrence of quantum confinement effect in the nanospherical hybrids and thus confirmed the creation of induced charge layers at the interface of spherical and rod-like nanohybrids with the adsorbed porphyrin dyes of COOH anchoring groups.

# Future Outlook

Throughout this thesis, we found very interesting and essential phenomena. Hence, the work that we described contributes to the continuing trend of merging the organic to the inorganic in order to engender multifunctional hybrids at the nano-scale. However, our very essential and important finding is that we proved our ability to engineer the band gap of the small ZnO particles in the nanohybrid matrices via the occurrence of quantum confinement effect. Hence, this provides evidence of peripheral modifications through induced charged layers in the ZnO due to dye grafting mechanism via its COOH anchoring groups.

This genuine result opens the way widely to intensive investigations on the interface ZnO/porphyrin, including much experimental and theoretical work on dye adsorption processes. This might also promote additional researches on the grafting process with other dye types (functionalized by different anchoring groups) and probably with semiconducting materials other than the ZnO, in the intention to probe the limitations or the universality of our discovered stated result.

Following this perspective, we need also to deeply analyse the dynamics of interfacial electron transfer processes down to the femtosecond time domain. Equipments for the femtosecond time-resolved photoluminescence are very recently available in our lab, enabling us now to perform the required measurements. Hence, deep understanding of the grafted systems helps to surpass limitations and greatly expands the freedom of designing well-designed hybrid materials.

Finally, improving hybrid systems designed in the laboratory and incorporating them into realworld applications is the ultimate challenge. We projected (i) applying the nanohybrids based on the ablated ZnO grafted by organic dyes and functional molecules as biosensors, and (ii) enhancing the hybrid solar cell efficiencies via molecular design and synthesis of new sensitizers having enhanced near-infrared light response.

# Contenu de la thèse

L'élaboration des matériaux nanohybrides avec de nouvelles propriétés physiques est un domaine de recherche motivant. Ces nanohybrides composés de matrices inorganiques, fixent les molécules organiques de colorants. L'association des propriétés des composés organiques et inorganiques dans une nanoparticle conduit à des matériaux innovants. De telles nanoparticules hybrides seront exploitées par exemple dans la réalisation des cellules photovoltaïques à colorant, ou dans l'imagerie bi-photonique en biologie concernant la compréhension des structures neuronales et la dynamique d'une cellule vivante. La maîtrise de l'ensemble du développement de fabrication de ces matériaux « sur mesure », ainsi que leur caractérisation demeure essentielle à la valorisation de leurs propriétés distinctes.

Possédant des propriétés optiques particulières, l'oxyde de Zinc (ZnO), qui est un semiconducteur à large bande interdite de 3.3 eV, est un candidat inorganique bien adapté à ce type de matériaux. Nous avons proposé l'utilisation du ZnO sous forme de nanoparticules préparées par deux méthodes différentes, notamment par *ablation laser femtoseconde* ou par *des processus chimiques*. Par ablation laser femtoseconde, nous avons obtenu des nanosphères de ZnO de haute qualité mais en petites quantités. Nous avons alors abordé la fabrication de plus grandes quantités de nanosphères et nanobâtonnets de ZnO par des simples processus chimiques capables d'être appliqués ultérieurement dans la création des cellules solaires.

Les cellules photovoltaïques à colorant sont une alternative peu coûteuse aux dispositifs classiques à jonction p-n qui nécessitent des matériaux extrêmement purs et des processus de fabrication sophistiqués. Généralement, ce type de cellules repose sur un semi-conducteur inorganique à large bande interdite sensibilisée par un colorant. Les nanoparticles de ZnO ont une photoactivité limitée sous irradiation dans le visible. Le fait d'y attacher de chromophores photoactifs accorde à l'hybride inorganique-organique, des propriétés optoélectroniques modulables. Une des propriétés principales est le pouvoir de récolter plus de lumière sur une large gamme du spectre solaire pour amplifier les efficacités de conversion photon-électricité.

Ainsi, les objectifs principaux de nos recherches sont:

i- La synthèse d'une nouvelle famille de nanohybrides par greffage de molécules organiques appropriées sur la surface des nanoparticules inorganiques pour l'imagerie bi-photonique et les cellules photovoltaïques à colorant.

ii- L'étude approfondie des propriétés optiques et électroniques de ces matériaux ainsi que l'étude du transfert d'énergie entre les deux parties (inorganique et organique).

Cette thèse est alors formulée selon deux grands titres :

● La 1ère partie montre les principes de synthèse des nano-agrégats de ZnO par ablation laser femtoseconde (ultrarapide) ainsi que les résultats expérimentaux émanant de cette ablation dans différents milieux liquides. L'impact de ces divers liquides sur la croissance du ZnO ablatés est evalué. Le greffage sur le ZnO est realisé par un chromophore dont le niveau du 1$^{er}$ état excité est d'une énergie plus basse que celle de la bande de conduction de ZnO, favorisant ainsi les transferts d'excitations du ZnO vers le colorant. Ces transferts seront illustrés par les excitations à un et deux photons.

● La 2ème partie concerne le greffage des chromophores sur du ZnO (nanosphères et nanobâtonnets) synthétisés chimiquement. Dans ce cas, notre choix du chromophore est basé sur plusieurs critères, en particulier sur les énergies des niveaux électroniques par rapport aux bandes de valence et de conduction du ZnO. Nous décrivons, en premier lieu, les modes de croissance de ZnO en fonction des réactifs et du temps de synthèse. Puis, nous présentons les propriétés optiques innovantes et prometteuses des hybrides en solution colloïdale par des mesures de photoluminescence (statique et en temps résolu) et d'absorbance.

Ces deux domaines de fabrication utilisent les mêmes outils pour mesurer et contrôler les nano- structures : les microscopes champ proches avec la résolution nanométrique telles que la Microscopie à Force Atomique (AFM) et la Microscopie Electronique de Transmission Haute Résolution (HRTEM).

Cette thèse contient cinq chapitres, une introduction au sujet, puis les détails expérimentaux, les résultats, les discussions et les conclusions.

Le premier chapitre donne un aperçu général des propriétés fondamentales connues de ZnO, où je montre les différents plans et orientations cristallographiques du ZnO, ainsi que l'effet du confinement quantique illustré par modification des propriétés de la bande interdite due à la réduction de la taille des nanoparticules.

Le deuxième chapitre est dédié à la synthèse de nanohybrides basée sur des nanosphères de ZnO synthétisées par ablation laser femtoseconde, où nous récapitulons les principes d'ablation laser dont l'irradiation conduit à la formation d'un plasma dense contenant des atomes, des ions et des petits clusters directement éjectés de la tablette. Nous avons utilisé un laser femtoseconde infrarouge (longueur d'onde 800 nm et durée d'impulsion 90 fs), pour ablater la tablette de ZnO en phase liquide: eau ($H_2O$), éthanol ($C_2H_5OH$), et solution de dodécanethiol ($C_{12}H_{26}S$). La taille de ces nanoclusters et leur concentration sont contrôlées par les paramètres d'ablation et la nature du solvant. En faisant varier la fluence et le nombre de tirs du laser, on a pu contrôler la taille des nano-agrégats. On obtient des tailles de l'ordre de 1 à 2 nanomètres pour des faibles fluences. L'augmentation de la fluence entraîne l'accroissement en taille des nano-agrégats, identifiés via les observations d'AFM et de TEM. Les mesures optiques de photoluminescence présentées dans la figure 1-a montrent l'existence des particules de ZnO (ablatées dans l'eau à une fluence de 3 J/cm$^2$) de taille inférieure ou comparable au Rayon de Bohr.  Ces mesures mettent en évidence l'effet du confinement quantique par l'augmentation du gap optique des particules (vue par le déplacement de l'émission de l'exciton vers le bleu). La figure 1-b montre l'émission exitonique des nanoparticules de ZnO (ablatées dans l'eau à une fluence de 11 J/cm$^2$), de taille bien supérieure à celle de Rayon de bohr.

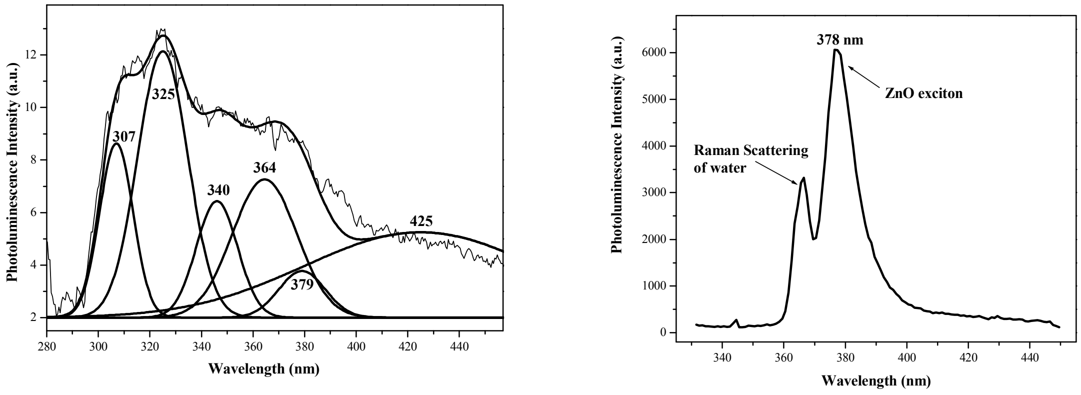

(a)

(b)

Figure 1. Spectres de photoluminescence des colloïdes de ZnO ablatés (a) à une fluence de 3 J/cm$^2$ (excitation à 254 nm), et (b) à une fluence de 11 J/cm$^2$ (excitation à 325 nm).

Nous démontrons aussi que l'ablation dans le dodecanethiol, implique une croissance lente caractérisée par le développement des facettes, du à l'adsorption des molécules de thiol sur le ZnO. Par ailleurs, nous avons greffé ex-situ et in-situ les molécules du colorant isothiocyanate de B de tetraméthylrhodamine (TRITC) sur les nanosphères de ZnO ablatées dans l'éthanol. Nous avons prouvé par les images de HRTEM (figure 2) que les nanohybrides ex-situ cristallisent en formant des facettes et que leur taille est légèrement inférieure à celle du ZnO pur. Au contraire, les hybrides in-situ ont une taille nettement inférieure a celle du ZnO non-greffé. Le transfert d'électrons du ZnO vers les molécules de colorant greffées se produit selon les deux procédés d'excitations à (i) un et (ii) deux-photons. Nous avons ainsi prouvé que l'ablation laser femtoseconde est un outil fiable pour élaborer des nanohybrides capables d'être potentiellement exploités comme bio-détecteurs.

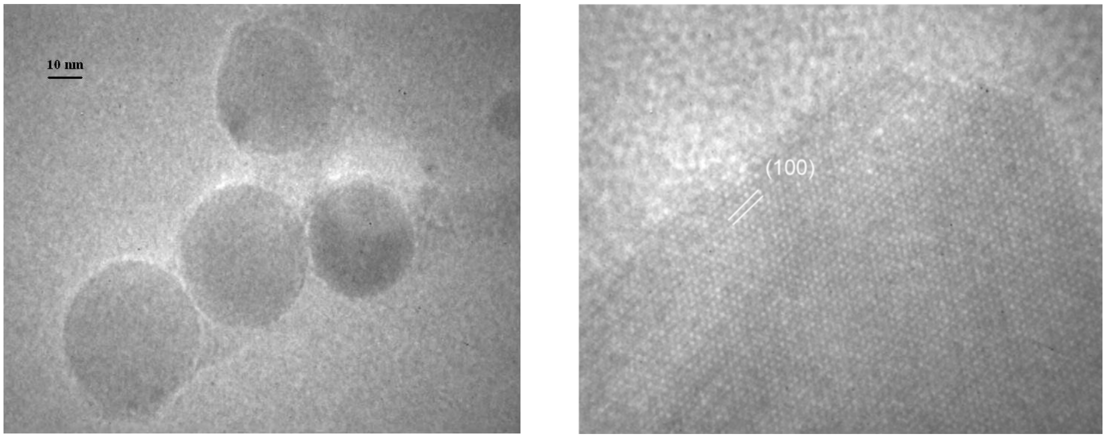

(a) (b)

Figure 2. (a) Image TEM des nanosphères de ZnO pur et (b) Image HRTEM de ZnO facetté après greffage.

Le troisième Chapitre explore l'élaboration de nanobâtonnets de ZnO par les procédés chimiques et la croissance morphologique est étudiée par HRTEM. Nous avons décrit les investigations détaillées sur les propriétés morphologiques et optiques des nanoparticles de ZnO synthétisées avec KOH et avec NaOH, à différentes étapes de la réaction de synthèse. Nous avons montré par HRTEM, que la croissance de ZnO commence en général par la formation de très petites nanosphères puis donne des nanobâtonnets bien formés. Ce procédé est simple, on mélange la base (KOH ou NaOH) avec l'acétate de zinc dans du méthanol et de l’eau. Des nanospheres de ZnO de 5,6 nm de diamètre sont obtenues après 2 h 15 minutes. Pour fabriquer des nanobâtonnets, le mélange a été concentré et chauffé à 60$^{o}$C pendant quelques heures.

Nous avons démontré que la croissance de nanobâtonnets synthétisés avec KOH est décrite dans sa première étape par le «murissement d’Oswald», suivie par une croissance par «attachement orienté», et par le mécanisme de «murissement d’Oswald», à l'étape finale. Ceci clarifie la formation des nanobâtonnets de ZnO avec des surfaces rugueuses. Par ailleurs, les nanobâtonnets, avec des surfaces lisses, synthétisés avec NaOH, ont été formés par le mécanisme de «murissement d’Oswald», avec peu d’«attachement orienté» à la première étape de croissance, d’où la formation uniforme et homogène des nanobâtonnets. Par les mesures optiques de transmission et de photoluminescence, de ZnO élaboré avec KOH et NaOH, nous avons détecté l'effet du confinement quantique pour les petites particules sphériques de ZnO formées pendant les toutes premières étapes de croissance. Les figures 3-a et 3-b montrent respectivement les nanosphères de ZnO (présentant l’effet de confinement dû à leur taille miniature) et les nanobâtonnets bien formés de ZnO.

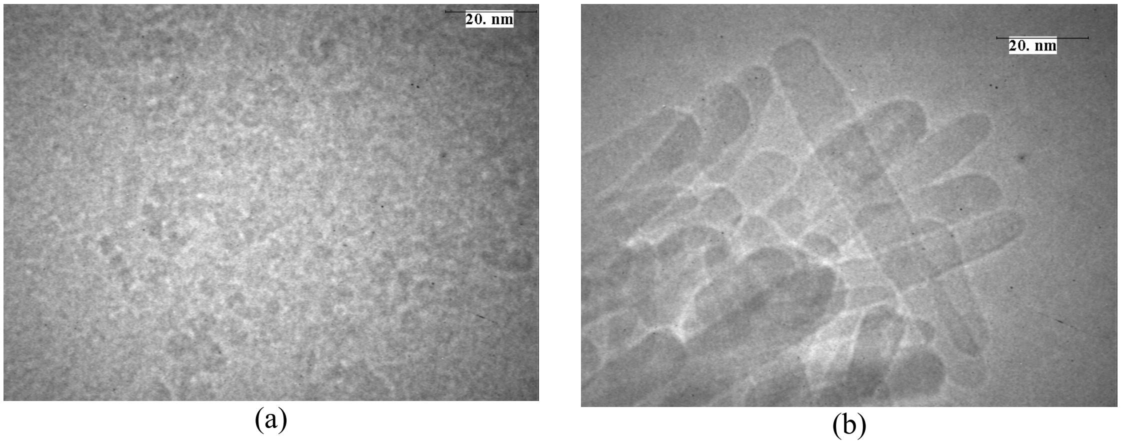

Figure 3. Image TEM des (a) petites nanosphères de ZnO après 2h 15m juste avant la condensation, et (b) nanobâtonnets synthétisés à 48h de temps de réaction (avec KOH).

Le Chapitre 4 constitue la section la plus importante de ma thèse avec des résultats innovants. Ce chapitre contient les études morphologiques et optiques détaillées des hybrides colloïdaux basés sur le greffage des molécules de deux types de porphyrines (H2TCPP et PP9) et d'un colorant à base de Ruthénium (Z907) sur du ZnO (nanosphères et nanobâtonnets) fabriqués chimiquement. Le greffage de ces molécules est réalisé en solution de THF et à différentes concentrations.

Par observations en HRTEM, nous avons prouvé que la morphologie des nanosphères et des nanobâtonnets de ZnO n'a pas été affectée par l'adsorption des trois types de colorants (déjà mentionnés). Cependant, quelques orientations parmi les nanobâtonnets-hybrides pourraient être dues à l'interaction entre particules de ZnO par l'intermédiaire des molécules greffées.

Dans le cas du greffage de la porphyrine H2TCPP, à partir des données d'absorbance et de photoluminescence, nous avons montré que : les molécules de H2TCPP greffées à plat sur les bâtonnets atteignent l'agrégation de type « H » pour des pourcentages de couverture de surface bien inférieurs à celles des nanosphères, notamment à 29% et 42% du ZnO nanobâtonnet et nanosphère, respectivement. En effet, les bâtonnets de ZnO (de dimensions 9nm×38nm) ont une surface spécifique bien inférieure à celle des nanosphères (de diamètre 5,6nm). Cette agrégation a été marquée, en augmentant la quantité du colorant, par leurs faibles intensités d'absorption et d'émission par rapport à celles des chromophores libres pour des concentrations identiques. Néanmoins, l'effet le plus significatif se présente pour les basses concentrations de colorant où les molécules de colorant pur préalablement agrégées dans les solutions deviennent isolées une fois greffées sur la surface de ZnO. Cela est manifesté par des intensités d'absorption et de fluorescence supérieures à celles des solutions équivalentes de H2TCPP pur, comme l'illustre la figure 4 pour le greffage sur des nanosphères de ZnO.

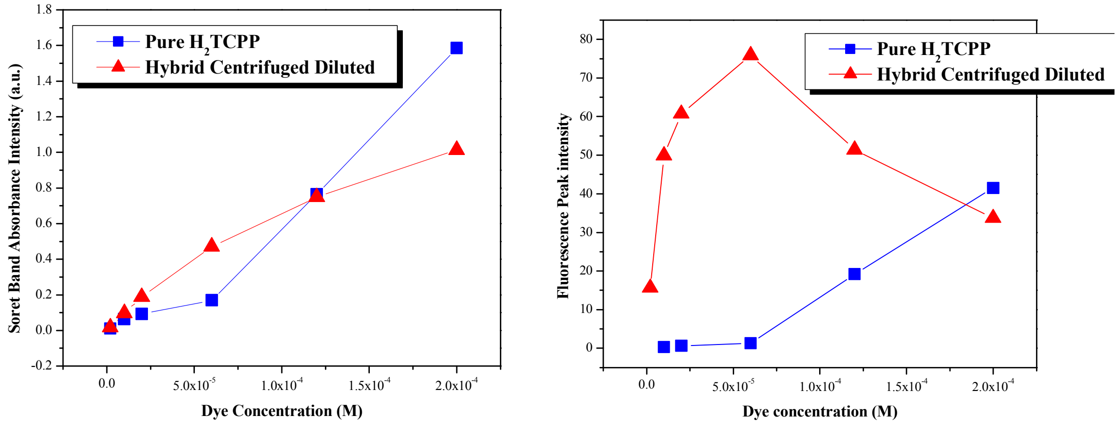

(a) (b)

Figure 4. (a) Intensités d'absorption de la bande de Soret et (b) intensités d'émission du H2TCPP pures et greffées sur les Zno nanosphères en fonction de la concentration du H2TCPP.

Cependant, à travers le greffage de la porphyrine sur les petites nanosphères de ZnO, nous avons aperçu l'effet majeur et le plus marquant qui émane de nos études sur l'hybridation. Nous avons découvert et pour la première fois, le changement de la structure électronique du ZnO par l'augmentation de sa bande interdite à fur et à mesure que l'on augmente le nombre des molécules de colorant. Ce résultat est mis en évidence par les mesures d'absorbance et de photoluminescence présentées dans les figures 5-a et -b, respectivement, où on peut voir qu'en augmentant la concentration du colorant l'intensité de l'exciton diminue, et les pics d'absorbance et d'exciton de ZnO se décalent vers le bleu pour des énergies supérieures. Ces observations mettent en évidence le confinement quantique. Ce procédé de greffage génère des couches négativement chargées à l'interface du ZnO/H2TCPP qui confinent davantage les excitons de ZnO et imposent ainsi les transports de charge entre les deux éléments de l'hybride. Pourtant, cet effet fondamental d'augmentation de bande de ZnO n'était pas discernable dans le cas des nanobâtonnets de ZnO en raison de leur grand volume par rapport à celui des nanosphères. Toutefois, les effets de couches chargées doivent exister dans les hybrides basés sur des nanobâtonnets de ZnO.

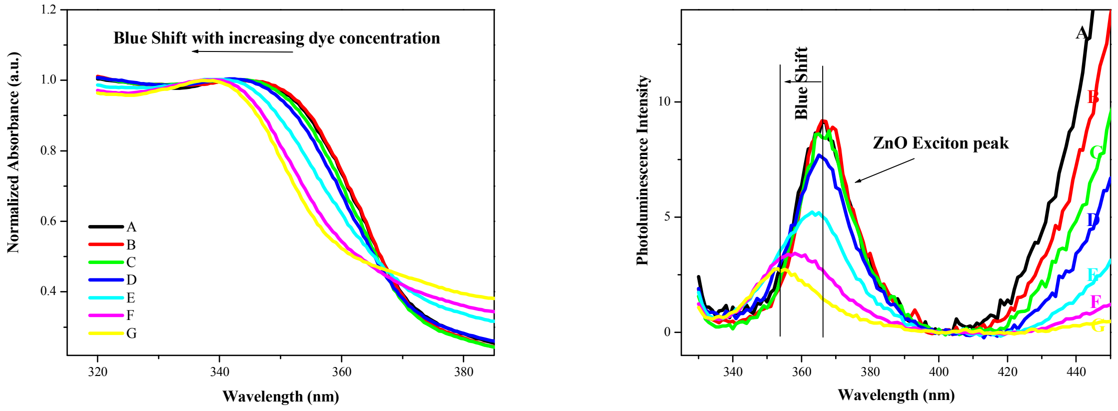

(a)

(b)

Figure 5. (a) Pis d'absorption et (b) d'émission de l'exciton des nanosphères de ZnO greffées par la porphyrine H2TCPP montrant le décalage des bandes vers le bleu (énergies supérieures) en augmentant la concentration du colorant.

Ainsi, nous croyons que l'amélioration dans l'émission de la porphyrine qu'on a observée auparavant (figure 4-b) est assistée par la contribution de ZnO via:

- le transfert d'électrons avec un impact qui diminue (en raison de la diminution continue dans l'échange de charge à cause des couches chargées à l'interface avec l'augmentation du colorant) et le transfert d'énergie de Forster qui contribue avec un effet petit mais constant («petit» en raison du petit recouvrement entre l'émission de ZnO et l'absorbance du H2TCPP) dans le cas des « *hybrides basés sur les nanobâtonnets de ZnO* ».
- le transfert d'électron avec un taux qui augmente (favorisé par l'augmentation continue de l'énergie de la bande interdite de ZnO) et le transfert d'énergie de Forster qui diminue (en raison de la réduction du recouvrement entre l'émission de ZnO et l'absorbance du H2TCPP avec l'augmentation du colorant) dans le cas des « *hybrides basés sur les nanosphères de ZnO* ».

Dans le cas de la porphyrine PP9, nous avons également montré l'augmentation de l'énergie de la bande interdite des nanosphères de ZnO avec la concentration croissante du colorant. Cependant, les molécules de PP9 greffées présentent une tendance d'agrégation plus grande et plus rapide que celle du H2TCPP greffée. Nous avons trouvé que l'agrégation « H » des molécules de PP9 greffées sur les nanosphères de ZnO commence à être évidente à 4% couverture de surface, tandis que l'agrégation était relativement instantanée pour les PP9 greffées sur des nanobâtonnets. Avec le PP9, on peut prédire que le transfert d'énergie de Forster du ZnO est favorisé, plus qu'avec la H2TCPP, à cause du grand recouvrement entre l'émission d'exciton de ZnO et l'absorbance du PP9.

On a également montré que les rendements quantiques de la fluorescence du PP9 greffée sont inférieurs que ceux estimés pour la H2TCPP, simplement en raison de fortes interactions intermoléculaires des PP9 impliquant moins d'échanges de charge et d'énergie avec les nanoparticules de ZnO. A faible concentration de H2TCPP et PP9 greffés, nous avons démontré que les rendements quantiques dans l'hybride sont beaucoup plus élevés que les rendements quantiques des solutions de ces colorants purs. Cependant les fortes concentrations de colorant entraînent la diminution du rendement quantique de la fluorescence des porphyrines dans les systèmes hybrides; cette diminution correspond au développement des agrégats des porphyrines greffées.

En ce qui concerne les applications, notamment les photopiles, nous avons montré dans le cinquième Chapitre la création des cellules solaires. La couche photoactive de ces cellules est construite en mélangeant les hybrides basés sur des nanobâtonnets de ZnO, avec le polymère P3HT qui est utilisé dans les cellules à colorant dans le but de régénérer le colorant photo-oxydé et transférer les charges à travers la cellule. Les caractéristiques communes pour les trois types d'hybrides (avec H2TCPP, PP9, Z907) se résument comme suit : à faible concentration du colorant on a pu détecter une réponse photovoltaïque, tandis que les fortes concentrations du colorant provoquent la dégradation du fonctionnement des cellules. Cette dégradation est due à la formation des agrégats des molécules de colorant qui vont jouer le rôle des centres de recombinaison des transporteurs de charge du P3HT, ralentissant ainsi tout transfert de charge entre P3HT et ZnO.

Nous avons donc réussi à greffer des molécules de colorant sur des nanosphères et des nanobâtonnets de ZnO fabriqués par des procédés chimiques. Les molécules de colorant utilisées appartiennent aux familles de Porphyrine et de Rhodamine. Nous avons de même pu montrer le transfert d'excitation entre le colorant organique et le ZnO inorganique, et confirmer notre aptitude à manœuvrer et modifier l'énergie de la bande interdite du ZnO par une simple variation de concentration du colorant greffé.

## Conclusion

On peut confirmer pour la première fois, à notre connaissance, la capacité du laser femtoseconde à ablater des cibles de ZnO dans un milieu liquide pour façonner des particules sphériques de quelques nanomètres révélant ainsi l'effet du confinement quantique dû à la réduction de taille des particules de ZnO. On a de même prouvé que dans les matrices hybrides, le transfert d'électron du ZnO ablaté par le laser femtoseconde vers les molécules de chromophores greffées s'opère via deux modes d'excitation : (i) un-photon et (ii) deux-photons.

Nous sommes arrivés avec succès à générer des nanohybrides basés sur du ZnO (sphériques et en forme de bâtonnets) synthétisé chimiquement et greffé avec des colorants via leurs groupes d'attachement « COOH ». Les propriétés optiques des suspensions colloïdales de ces ZnO greffées qui ont été étudiées par des mesures de photoluminescence et de transmission révèlent des informations intéressantes.

Nous avons montré que l'augmentation de la densité de colorant change radicalement le comportement d'absorption et de fluorescence. Le décalage typique vers le rouge des pics d’absorption du colorant greffé sur ZnO par rapport aux pics du colorant pur indique le greffage du colorant. En outre, la diminution de l'intensité de bande d'émission UV de ZnO avec l’augmentation de la concentration de colorant indique l'existence d'un processus de transfert d'énergie du ZnO vers le colorant, qui est confirmé par la spectroscopie d'excitation. La réduction de l'émission de la bande de défauts de ZnO avec la concentration de colorant est attribuée à la passivation des défauts de ZnO par attachement des groupes acides du colorant à la surface du ZnO. De plus la diminution de cette bande pourrait être attribuée à des échanges de charges avec les molécules de colorant greffées. L'intensité de fluorescence du colorant dépend fortement de la concentration de ce dernier, en effet une très forte intensité d'émission est enregistrée à de faibles couvertures de surface de ZnO par le colorant. Cependant à de plus fortes concentrations, cette émission est étouffée par l'agrégation entre les molécules de colorant greffées. On a ainsi prouvé qu’à de faibles concentrations, le colorant s’attache au ZnO d’une façon dispersée impliquant des absorbances et des émissions supérieures à celles des colorants purs.

Nous avons démontré et pour la première fois qu’en faisant varier la concentration de la porphyrine greffée, on peut remodeler l’énergie de la bande interdite des nanosphères de ZnO via le confinement quantique induit sur l’exciton de ZnO par la présence du chromophore à la surface. D’après ce résultat majeur, on a ainsi confirmé la création de couches de charges à l'interface des (sphères et bâtonnets) de ZnO avec la porphyrine adsorbée à la surface du ZnO via ses groupes d’attachement « COOH ».

Par conséquent, nous pouvons confirmer que nous sommes arrivés à créer des nanohybrides à base de nanosphères et nanobâtonnets de ZnO, produits par deux techniques « *ablation laser femtoseconde* » et « *procédés chimiques* », greffés avec divers types de molécules de chromophore organiques.

# Appendix I: Atomic Force Microscopy AFM

We used a MultiMode SPM (NanoScopeIII) to perform the Atomic Force Microscopy (AFM) analyses in the Contact Mode. Basically, the Atomic Force Microscope is used to image, in real space, the surface topography of materials at the atomic scale. It consists of a sharp tip that is attached at the end of a spring cantilever, and records the small force between the tip and the surface, as the tip scans over the sample's surface, as seen in figure I.1-a.

In the Contact Operational Mode, the tip is made to gently touch and slide over the sample surface, while continually recording the deflections of the cantilever that are due to the interatomic repulsive forces between the tip and the sample.

The detection system of the deflection of the laser beam that is reflected off the back side of the cantilever-tip system is as shown in figure I.1-b. The reflected beam falls on a split photodiode detector whose output voltage depends on the difference between the voltages generated by each segment of the photodiode. The output voltage is then fed back into the piezoelectric PZT scanner so that the sample is moved back, in the Z-direction, in such a way that the laser spot goes back to its original position. This ensures that the distance (as subsequently the force) between tip and sample is constant.

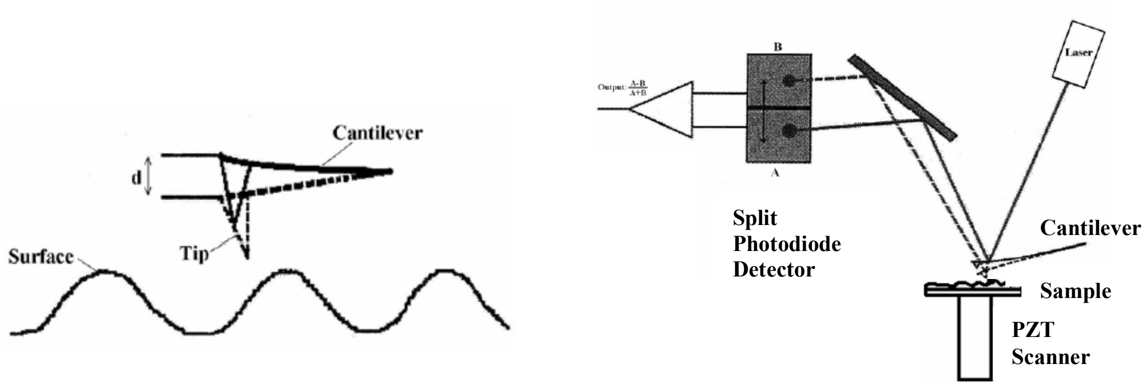

(a) (b)

Figure I.1. (a) Sketch of the tip mounted at the end of a spring cantilever scanning a sample's surface. (b) The beam-bounce detection scheme.

# Appendix II: Techniques of electronic microscopy: Transmission Electron Microscopy (TEM)

## II.1- Historical recall

The idea to build an electron microscope occurred little of time after the statement of the duality wave-matter by Louis of Broglie (1924). If the electrons can be associated to a wave, why not use them as electromagnetic source in a microscope at the place that photons have in the visible light. In their giving sufficient energy, the electrons can reach very small wavelengths, which then make it possible to obtain a higher resolution. It is Leo Szilard and Denis Gabor which had, the first, this idea while being also based on the appearance of the "electromagnetic" lenses established by Hans Busch.

Nowadays, transmission electronic microscopy is the most widespread apparatus for the characterization of crystallographic structures, because it reaches, for the most powerful microscopes, a resolution about the Angström and makes it possible to reach the structure at atomic scale.

## II.2- Operation of the electron microscope

A transmission electron microscope is composed of a source of electrons, electromagnetic lenses, a sample holder and a fluorescent screen. The source of electrons generally a single-crystal filament of LaB6, is heated until emission of electrons at the top of a vacuum column (10-7 torr). The electrons are accelerated by a potential difference on the level of the gun. A first device including 2 lenses and a diaphragm (condensing system) make it possible to direct the electron beam in order to obtain a nearly parallel beam. The electron beam crosses then the sample introduced into the column by a sample holder and placed in the interior of the objective lens. It is this objective lens that makes it possible to obtain either the image of the object in its image plan or the diagram of diffraction in its focal plan by the intermediary of a diaphragm. Finally, a last device of lenses makes it possible to enlarge and project the image or the diagram of diffraction on a removable fluorescent screen. Photosensitive films, placed under the screen, allow making photographs of the enlarged sample. A camera (photo detector) can also be placed under the screen for the numerical images grabbing.

To be able to be crossed by the electron beam without absorption, the sample must be sufficiently thin.

The morphological study and the composition of our particles were carried out at the CRMCN lab with a Jeol 3010 whose principal components and functioning mechanisms are shown below.

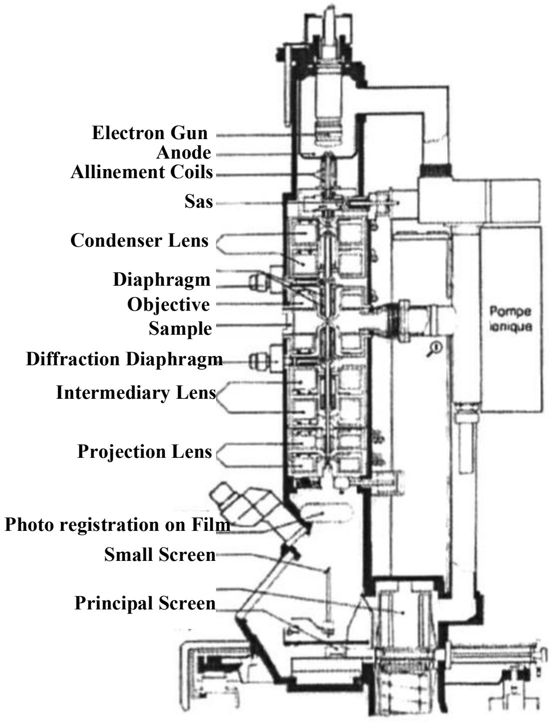

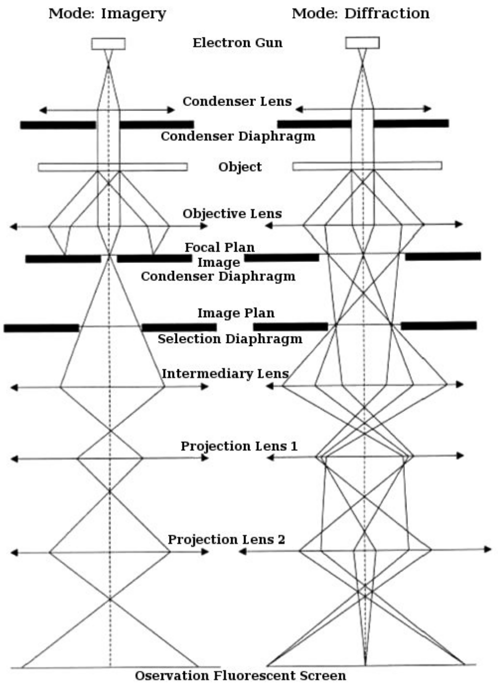

## II.3- Formation of the image

The formation of an image results from the generation of a contrast i.e. a variation of light intensity between the points of the image. In optical microscopy, contrast comes primarily from the absorption of a part of the light by the sample. In conventional electronic microscopy the phenomenon of absorption is neglected because the little thickness of the sample. In other words, in the interactions between the electrons and the matter one holds account only the elastic interactions. The electrons which interact with the matter are deviated of their trajectory while keeping their energy. Once sample crossed, the beam is composed of a transmitted wave (not of electron-matter interactions) and of a diffused or diffracted wave (elastic interaction). At the exit of the objective, a diaphragm is placed whose aperture is very weak ($\alpha$=5.10-3 rad). Only rays diffused with an angle lower than $\alpha$ will contribute to the formation of the image. Contrast is thus produced by the subtraction of the diffused or diffracted rays. The diagram below describes the formation of an image in the case of a crystalline object. If the diaphragm of the objective is centered on the direct beam, the crystalline parts appear dark on white background zone (image in clear field -a). If the diaphragm is centered on one of the diffracted beams, the crystalline parts appear clear on dark background zone (image in dark field -b).

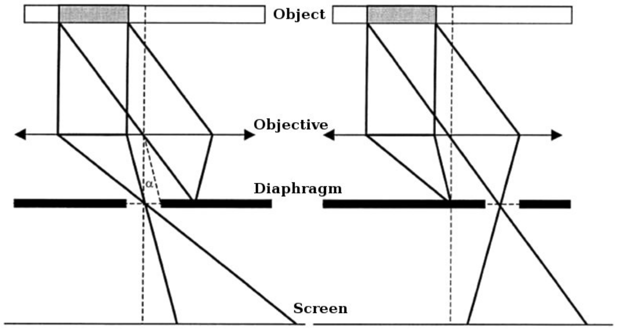

## II.4- Formation of the image of high resolution

The high resolution transmission electron microcopy (HRTEM) is one of the most powerful techniques for the characterization on an atomic scale. HR Microscopes have a high voltage of acceleration (300 KV) which gives to the electrons a very great kinetic energy and consequently a very small wavelength. It is this small wavelength, about interatomic distances, which makes it possible to obtain a structural resolution.

## II.4-1. Formation of the image of high resolution: phase contrast

In TEM the formation of the image is generated by a contrast of diffraction. When the resolution distance becomes lower or equal to the parameters of the crystal lattice, a contrast related to the structure is superimposed on the contrast of diffraction. The effect of structure is directly related to the variations of the internal potential of the crystal V(x, y, z). For better understanding the formation of the image of high resolution, let us follow the path of the electromagnetic wave resulting from the object f(r) taking into consideration the objective lens as a filter (see the following diagram).

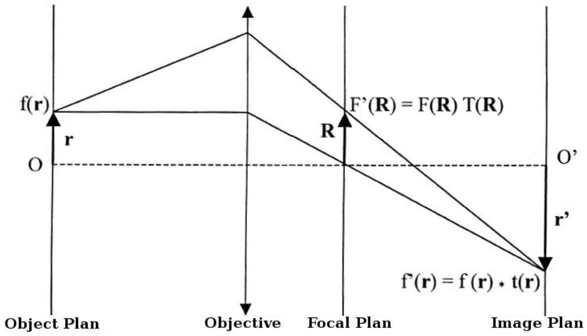

The function f(r) represents the distribution of the wave in amplitude and in phase at any point r(xy) of the exit face of the object. It corresponds to the projection of the structure "seen" by the electrons.

$$f(r) = \left[1 - s(r)\right] e^{i\varphi(r)} \qquad (1)$$

s(r) being the absorption component

Approximation for an object slightly diffusing: $s$ and $\varphi \prec\prec 1$

$$f(r) = 1 - s(r) + i\varphi(r) \tag{2}$$

In TEM the focal plan can be seen as the sphere of Ewald containing all points R(XY) (reciprocal network) corresponding to a diffraction direction. In the case of an ideal objectif, one can consider, in any point R(XY) of the focal plan, ideal function F(R) like the Fourrier transform of the object function f(r):

$$F(R) = TF\{f(r)\} = \Delta(R) - S(R) + i\Phi(R) \tag{3}$$

In fact the non-perfect objective plays the role of a filter represented by a transfer function T(R) whose amplitude A(R) will depend on the aperture angle of the objective and the phase $\gamma(R)$ of the spherical aberration and the defocusing.

$A(R) = 1 \quad \text{if} \quad R \prec R_0$ ($R_0$ being the diameter of the objective diaphragm)
$A(R) = 0 \quad \text{if} \quad R \succ R_0$

And:

$$\gamma(R) = \frac{2\pi}{\lambda}\left[\Delta f \lambda^2 \frac{R^2}{2} + C_S \lambda^4 \frac{R^4}{4}\right] = \gamma_D(R) + \gamma_s(R) \tag{4}$$

where $\gamma_s(R) = \frac{\pi}{2} C_s \lambda^3 R^4$ is the dephasing due to the aberration $C_s$
$\gamma_D(R) = \pi\,\lambda\,\Delta f\,R^2$ is the dephasing due to the defocusing $\Delta f$

The transfer function is written as follows:

$$T(R) = A(R)\,e^{[-i\gamma(R)]} \tag{5}$$

The function of real wave F' (R) resulting from the objectif lens is then the product of ideal function F(R) by the transfer function T(R):

$$F'(R) = F(R)T(R) = (\Delta' - S\,A\cos\gamma + \Phi\,A\sin\gamma) + i(S\,A\sin\gamma + \Phi\,A\cos\gamma) \tag{6}$$

where $\Delta' = 0 \quad \text{for} \quad R \neq 0$

For the objects slightly diffusing, the amplitude of the transmitted wave represented by $\Delta'$ is large compared to that of the diffused wave. Consequently, in observation in clear field, the imaginary part of the transfer function can be neglected as compared to the real part containing $\Delta'$:

$$F'(R) = \Delta' - S\,A\cos\gamma + \Phi\,A\sin\gamma \tag{7}$$

After crossing the optical system of enlarging and projection, the wave on the plan image is defined by the function image f' (r) in any point of the image r(xy) of the plan image. This function is the Fourier transform of F' (R):

$$f'(r) = TF\{F'(R)\} = TF\{F(R)T(R)\} = f(r) * t(r) \tag{8}$$

where t(r) is the confusion function that is the TF of the transfer function

Always in the approximation of the object slightly diffusing:

$$f'(r) = 1 - TF\{S\,A\cos\gamma\} + TF\{\Phi\,A\sin\gamma\} \qquad (9)$$

On the other hand, the contrast in amplitude c(r), due to the diffracted rays, is obtained by cutting off the amplitude transmitted without diffusion:

$$c(r) = f'(r) - 1 = TF\{S\,A\cos\gamma\} + TF\{\Phi\,A\sin\gamma\} \qquad (10)$$

Two types of contrasts are then possible:

a- If $\sin\gamma \cong 0 \Rightarrow \cos\gamma = 1$

So $c(r) \cong TF\{S(R)\} = s(r)$ (11)

It is then the contrast of absorption (or contrast of amplitude) which dominates but it does not offer the structural resolution.

b- If $\sin\gamma \cong \pm 1 \Rightarrow \cos\gamma \cong 0$

So $c(r) \cong TF\{\Phi(R)\} = \varphi(r)$ (12)

Here, in the case of a weak phase object (thin object), it is the contrast of phase that dominates. However dephasing $\varphi(r)$ in any point r(xy) of the exit face is directly proportional to the projection of the crystalline potential V(r):

$$\varphi(r) = \frac{(\pi\,V(r))}{\lambda\,E_0} \qquad (13)$$

$$\text{So } c(r) \cong \frac{(\pi\,V(r))}{\lambda\,E_0} \qquad (14)$$

In these conditions of focus, the contrast can thus be directly interpreted as being the projection of the structure potential. One obtains then an image on the atomic scale.

## II.5- Simulation method of high resolution electronic microscopy images

In the case of thick objects, the interpretation of the images obtained is often very difficult and it is strongly dependent on the adjustment of the microscope, which can introduce artifacts into the image. This is why; generally the microscopists have recourse to the techniques of image simulation. One of most widespread is the "multislice" method, stated by Cowley and Moodie (1957). The method is primarily based on an approach of "physical optics" of electronic microscopy. It consists in cutting out a crystal of thickness z into n fine sections of small thickness dz (see Schema).

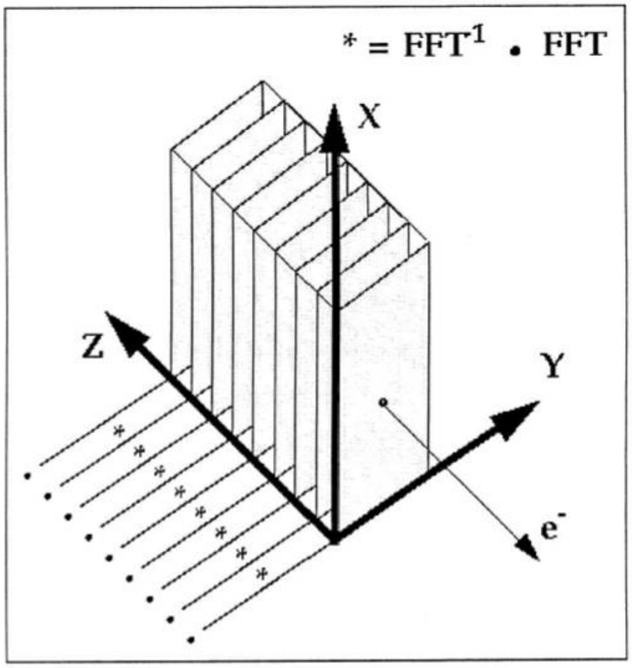

For each section, the crystalline potential is projected on a plan (usually the plan of entry of the section). For instance, for a section labeled n, the diffraction of the incident wave $\Psi_n$ at exit of the section, depends on the function of transmission of the section:

$$q(x,y) = e^{-i\,\sigma\,V(x,y)\,\Delta z} \text{ where } \sigma = \frac{\pi}{\lambda E} \tag{15}$$

If one considers then the following section labeled n+1, the incident wave $\Psi_{n+1}$ will depend on the function of wave at exit of section n, and the function of propagation p(x,y) between the 2 sections:

$$p(x,y) = \left(\frac{i}{\lambda\,\Delta z}\right) e^{-\frac{i\,k\,(x^2+y^2)}{\Delta z}} \tag{16}$$

From these two functions one can establish the following relation:

$$\Psi_{n+1} = \left[\Psi_n \cdot q_n\right] * p_{n\to n+1} \tag{17}$$

This relation then makes it possible to calculate the wavefunction $\Psi$ at the exit of the object. Then, the intensity of the image is $I = \Psi * \Psi^*$.

P. Stadelmann developed a simulation program of images (E.M.S) using the method multislice [1,2]. In the case of the crystals thickness (e), the image simulation program of Stadelmann makes it possible theoretically to calculate the image of the crystal by taking into account of the experimental conditions of formation of the image in the microscope. The intensity of the calculated image in the image plan take into consideration of:

-the focusing at the object level
-the spherical aberration of the objectif lens
-the diaphragm aperture of the objectif lens

The simulated images obtained by the EMS program is very much used in the various studies of structures, of the shapes of nano-objects, of crystalline defects, deformations of networks, interfaces, edge effects.

[1] Stadelmann P. A., EMS. *A Software package for for electron diffraction analysis and HREM simulation in materials science*, Ultramicroscopy, 21 (1987) 131-146

[2] Stadelmann P. A., EMS Guide, (1993)

# Appendix III: Techniques of optical Spectroscopy: Steady state Absorbance and Photoluminescence

Optical mechanisms of Absorption and Fluorescence (or photoluminescence for the semiconductor materials) are shown in the Jablonski band diagram in figure 1.

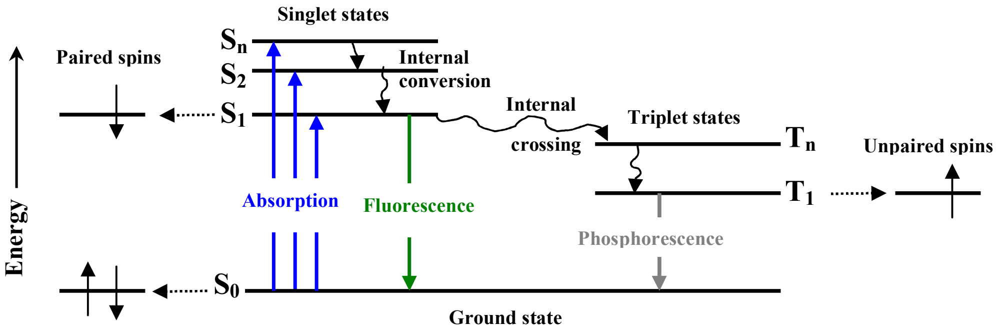

Figure 1. Jablonski band diagram showing different optical mechanisms.

## III.1- UV-Vis spectroscopy via Cary VARIAN 50 spectrophotometer

*It is worth noting that absorbance refers to the mathematical numerical quantity unlike the term absorption being the physical process of absorbing light.*

After absorption of the electromagnetic energy, atoms and molecules are excited to higher energy states. Absorption of radiation occurs only when the energy of an exciting photon matches the energy difference between the ground state and one of the excited states. These energy differences are the finger-prints for each compound and a plot of absorption spectrum as a function of wavelengths therefore provides a characterization of a compound.

Absorption takes place when a beam of parallel radiation passes through a solution of a compound, (see Figure 2). The radiant Intensities before and after the beam passage through our colloidal hybrid solution are $I_0$ and I, respectively, the thickness of the solution is L=1cm and the species concentration is c.

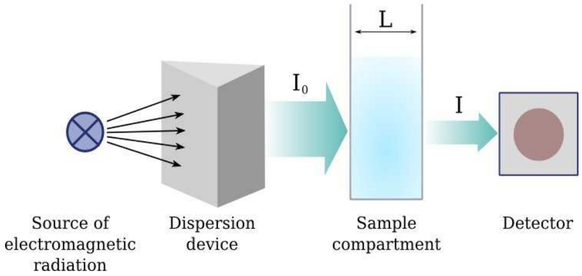

Figure 2. Main parts of a spectrophotometer (Cary VARIAN 50 with Xenon lamp) used for measuring absorbance or transmittance, with an attenuated radiation beam by an absorbing solution.

The Beer-Lambert law is defined through the transmittance (T) in an exponential form by:

$$T = \frac{I_T}{I_0} = e^{-\alpha Lc} \qquad (1)$$

The logarithm of the transmittance T is called the absorbance, A, and is given by

$$A = -\ln \frac{I_T}{I_0} = \alpha Lc \qquad (2)$$

where $\alpha$ is the absorption cross-section coefficient.

A limitation of the Beer-Lambert law, $A = \alpha Lc$, is that it is only linear for solutions having an absorbance of about < 3 AU (Absorbance Units). Therefore, with too high concentration, no longer linear relationship exists between the absorption and the concentration.

▪ We can estimate the number of photons absorbed via the following relations to be used in the calculation of the dye's Fluorescence Quantum Yield:

$$\begin{aligned} & I_0 = I_{Trans} + I_{Abs} \Leftrightarrow I_{Abs} = I_0 - I_{Trans} = I_0\left(1 - e^{-A}\right) \\ & \Rightarrow n_{Abs} = \#\text{ of photons absorbed} = n_0\left(1 - e^{-A}\right) \end{aligned} \qquad (3)$$

## III.2- Photoluminescence Spectroscopy

When a molecule is excited, the excited electrons fill molecular orbitals in pairs and their spins are in opposite directions. So, the two electrons are said to be *paired* (see figure 1) and the electronic state is known as a *singlet excited state*. The re-emission of light from this singlet-excited state is called fluorescence emission. Throughout this thesis, we studies the photoluminescence for samples excited either by Xenon or mercury lamps or by He-Cd laser.

● Figure 3 shows the basic components of the Cary VARIAN with Xenon lamp spectrophotometer that we used. A scanning fluorescence spectrophotometer can measure in two different scan modes: *excitation* and *emission*. In excitation scan the emission wavelength is fixed while the excitation wavelength is changed, thereby recording an *excitation spectrum*. Emission scan measures the emission at different wavelengths (via the monochromator that allows narrow bands of light wavelengths to pass) with the excitation wavelength fixed, which results in an *emission spectrum*.

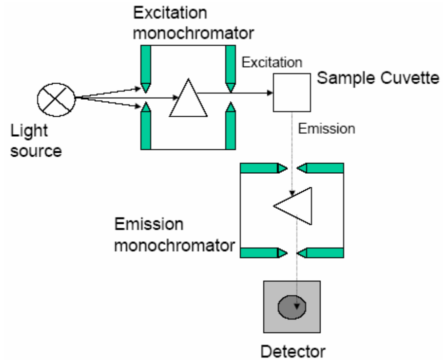

Figure 3. Main functioning parts of a spectrophotometer (Cary VARIAN with Xenon lamp) used for emission and excitation measurements.

- Figure 4 shows the basic set-up, that we used, of the photoluminescence PL measurements via the one-photon excitation light being either a mercury lamp or a He-Cd laser.

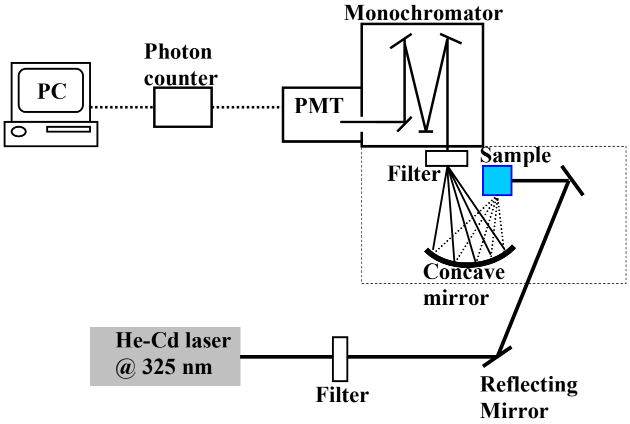

Figure 4. Schematic representation of photoluminescence set-up for the He-Cd excitation source.

The He-Cd laser beam of 325 nm as excitation wavelength was filtered, and whose energy was measured, and then focused onto the vessel (1cm length) containing the hybrids colloidal sample, which absorbed the light. Emission from the sample was collected at approximately 90° from the laser beam, sent through a grating monochromator, and then detected by a Peltier cooled photomultiplier tube (PMT). The signal from the photomultiplier tube was processed through the photon counter and stored digitally in a computer. It is worth noting that the first filter, which is on the way of the laser beam, is required to select the main laser emission line and cut off undesirable lines, while the other filter on the way of PL is needed to cut off some wavelengths of the emitted light and to attenuate the laser light intensity.

# Appendix IV: Time-Resolved Photoluminescence

By measuring the photoluminescence PL intensity at chosen emission wavelength as a function of time delay after an excitation pulse, information can be obtained about the recombination mechanisms. A full emission spectrum can hence be measured at successive points of time.

Figure 1, shows the time-resolved photoluminescence experiment. By frequency doubling the output of the pump source Ti:Sapphire laser (800 nm, 1KHz), we obtain UV (400 nm) fs pulses. We frequency double the femtosecond pulses by focusing the laser pulses on a non-linear BBO crystal. The remaining non frequency-doubled red beam is then separated from the frequency-doubled blue beam using a polarizer and some filters. The resulting photoluminescence is imaged through the spectrometer [a monochromator (Acton, Princeton)] to the gated CCD camera, with gate time fixed at 3 or 5 ns, that is triggered synchronously with the repetition rate of the laser pulses. In addition, a delay generator is used to temporally position the triggering of the camera monitor at sequential time slice of the emitted photoluminescence.

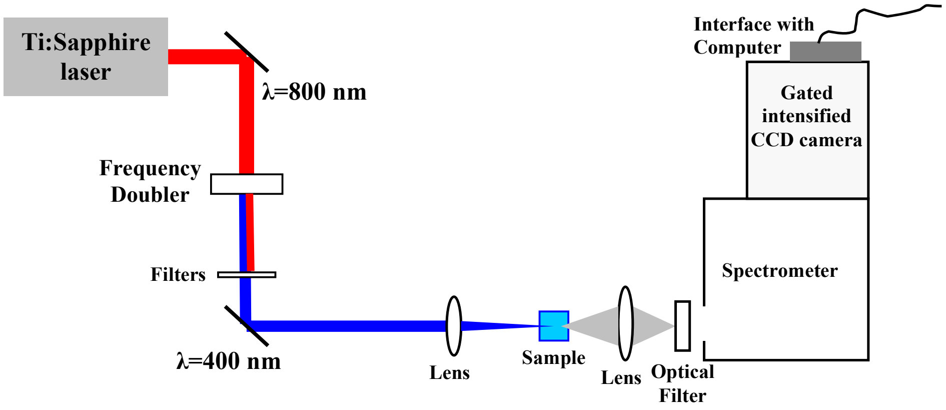

Figure 1. Time-resolved photoluminescence set-up.

# Appendix V: Fourier Transform Infrared spectroscopy

In contrast to classical spectrometers, where the spectral absorption of a sample is being scanned, Fourier-Transform Infrared (FTIR) spectroscopy is an interferometric method. Figure 1 shows the main component of a Fourier Transform Infrared Spectrometer which is a Michelson interferometer containing an IR source, a fixed mirror, a movable mirror, a beamsplitter and a detector. As the light beam enters this interferometer, the beamsplitter transmits half of it to the moving mirror and the other half to the fixed mirror. Then these two secondary beams recombine back into one beam carrying an interference pattern which is recorded as a function of the optical path difference between these two beams $I(x)$. This is called the interferogram that is modified due to infrared absorption in the sample. At the detector, the computer allows the digitization of this interferogram followed by Fourier transformation of the data into the actual infrared spectrum, which is the absorbance or transmittance intensity as a function of wavenumber $I(\lambda)$.

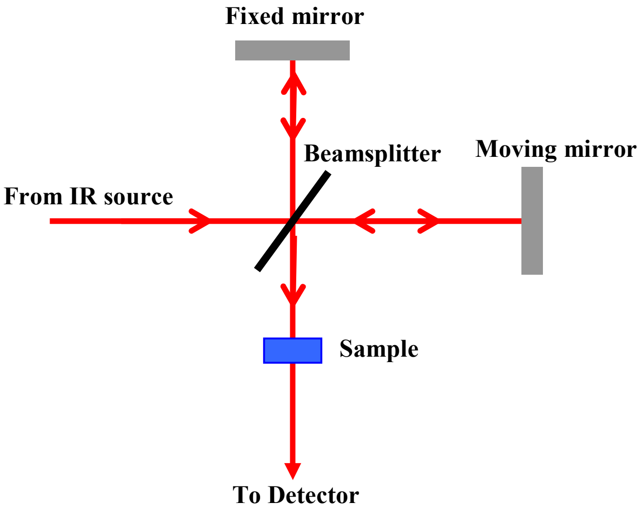

Figure 1. Main components of a Fourier Transform Infrared Spectrometer.

# Appendix VI: Metallation of PP9-based hybrids

In this section, we tried and succeeded to metallate by the zinc (Zn) the PP9 porphyrin after being grafted to the ZnO nanorods. This initiative is adopted because of the role of metalloporphyrins as chemically interactive materials in chemical sensors that has interested researchers for long time. The rich organization chemistry of the porphyrin structure is responsible for their use in chemical sensor applications using the changes induced in their physicochemical properties by the addition of lateral groups and central metal whose nature defines the sensor's properties. The aromatic system of the porphyrin is responsible for the high molar absorbance. This method provides means to produce derivatives of free-base porphrins, thus altering their functionality photosensitive compounds to be applied in a wide range of applications. Hence, with only a little variation in synthesis, sensors with different responses can be obtained [1]. Absorbance and fluorescence emission constitute the mode of detection. Spectral changes occur due to the co-ordination of detected molecules (as toxic gases) to the central metal ion in the immobilized metalloporphyrins.

Experimental wise, the PP9/ZnO hybrid sample at $2.10^{-4}$ M PP9 concentration was blended with a solution of Zinc acetate ($2.10^{-4}$ M $Zn(Ac)_2$) containing a number of Zn ions that equals the number of PP9 molecules in the solution. Absorbance spectra in figure 1 reveals the augmentation of the two absorption peaks at 546 and 584 nm and the disappearance of the two other Q-bands at 513 and 640 nm, in addition to the Soret band red-shift of about 12 nm from that of free dye based hybrid.

Fluorescence emission spectra at 325 nm excitation wavelength depicted in figure 2-a, show the apparition of two emission peaks in the metallated sample: (i) intense peak at 588 nm and (ii) less intense peak at 642 nm that is red-shifted and more intense with respect to the emission peak at 635 nm of the free PP9-based hybrid. Excitation spectrum at 589 nm detection wavelength of the metallated sample (figure 2-b) demonstrates a strong absorption contribution at the newly established Soret band absorption (at 418 nm).

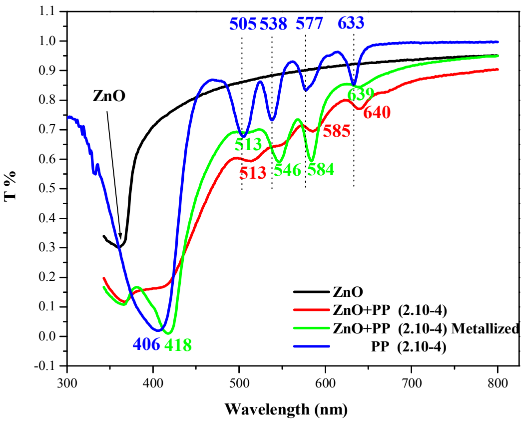

Figure 1. Absorbance spectra of pure PP9 at $2.10^{-4}$ M (bleu plot), PP9-ZnO hybrid solution (red plot), PP9-ZnO hybrid METALIZED solution (green plot).

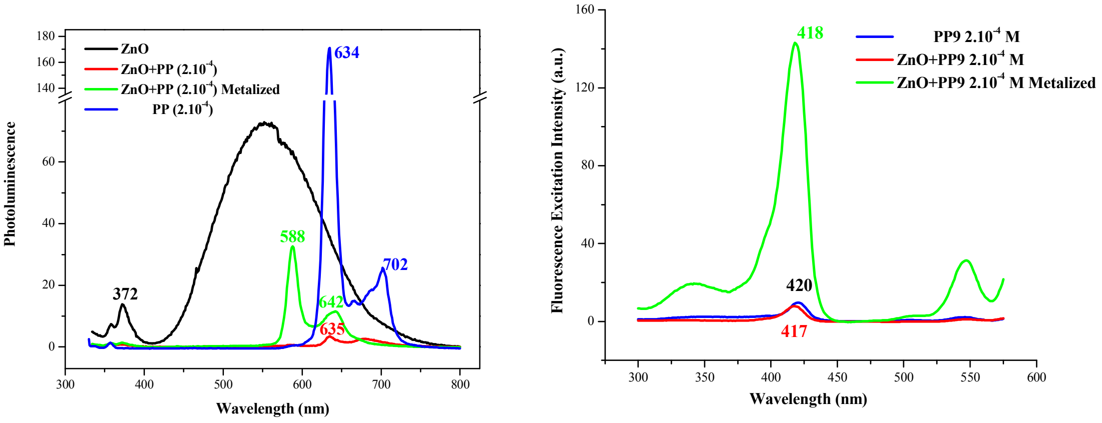

(a) (b)

Figure 2. Fluorescence (a) emission at 325 excitation wavelength and (b) excitation spectra at 589 nm detection wavelength of pure PP9 at $2.10^{-4}$ M (bleu plot), PP9-ZnO hybrid solution (red plot), PP9-ZnO hybrid METALIZED solution (green plot).

Altered features of absorbance (figure 1) and fluorescence (figure 2) spectra of the derived metallated sample with respect to the free dye based hybrid prove the occurrence of metallation, where the Zn is placed in the center of the aromatic ring as shown in figure 3.

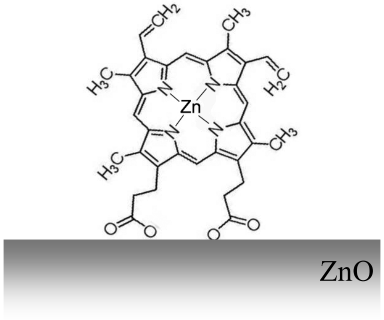

Figure 3. Metallation of the grafted- PP9 onto the surface of a ZnO nanorod.

Briefly, we succeeded to metallate the grafted-PP9 molecules by introducing the Zn atoms at the middle of the porphyrin ring. We proved this metallation process by the alteration of the absorbance, emission and excitation spectra via the vanishing and apparition of some peaks.

[1] Natale, C. et al., ‘The exploitation of metalloporphyrins as chemically interactive material in chemical sensors’, Materials Science And Engineering, Vol. C5 (1998) 209

# Appendix VII: Z907-ZnO hybrids

The Z907 with molecular formula $C_{42}H_{54}O_6N_6S_2Ru$ is structured in figure 1. Z907 images showing top and side view of the Z907 molecule are illustrated in figures 2-a and -b. Z907 molecule has:

1- two bipyridyl ligands bonded to ruthenium to create the photosensitivity;
2- two thiocyanide ligands to vary the spectral response;
3- two carboxyl groups to chemisorb to the semiconductor oxide surface;
4- two hydrocarbon chains.

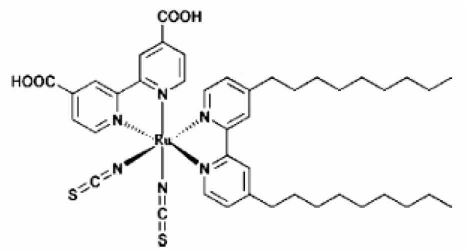

Figure 1. Structure of the Z907 amphiphilic dye.

(a) (b)

Figure 2. Z907 images showing (a) top view and (b) side view. The atoms of H, C, N, O, and S, are shown by light gray, gray, blue, red, and yellow, respectively

The nanohybrids are experimentally handled identically to those with the porphyrins. The grafting is done in the tetrahydrofuran solvent (THF) on NaOH-based ZnO nanorods (of 48 hours synthesis time) at different Z907 concentrations. ZnO rods with 10.2 nm as diameter and 55.7 nm as length are of abundance of $3{,}9.10^{13}$ particles/ml with an available surface area of 1948 $nm^2$/ZnO particle. Table 1 lists the samples names and their corresponding dye concentrations and the calculated number of Z907 molecules per ZnO nanorod.

| Sample Name | Z907 concentration [M] | # of dyes /one ZnO nanorod |
|---|---|---|
| 1 | zero | zero |
| 2 | $0{,}5.10^{-4}$ | 769 |
| 3 | $1{,}5.10^{-4}$ | 2307 |
| 4 | $2{,}5.10^{-4}$ | 3846 |

Table 1. Names of nanohybrid samples with their corresponding Z907-dye concentrations.

## • Optical studies of nanohybrid-based on rod-like ZnO

In figure 3, we can see the transmittance spectra originating from pure dye solutions (*dotted lines*) and their corresponding hybrid systems (*solid lines*). All samples are diluted 10 times without centrifugation that was not possible due to the high solubility of the grafted Z907. Z907 molecules absorb simultaneously in the UV and the visible range as shown. Peaks of pure dyes are denoted first by "d" then by the peak's value as written in figure 3, peaks of grafted dyes are also given in colors matching each appropriate curve. Pure Z907 absorption in the visible changes from 520 to 529 nm when increasing the dye concentration, meaning that interaction among dye molecules slightly alters their absorption. On the other hand, the red-shifted dye peaks in the hybrids confirm the grafting.

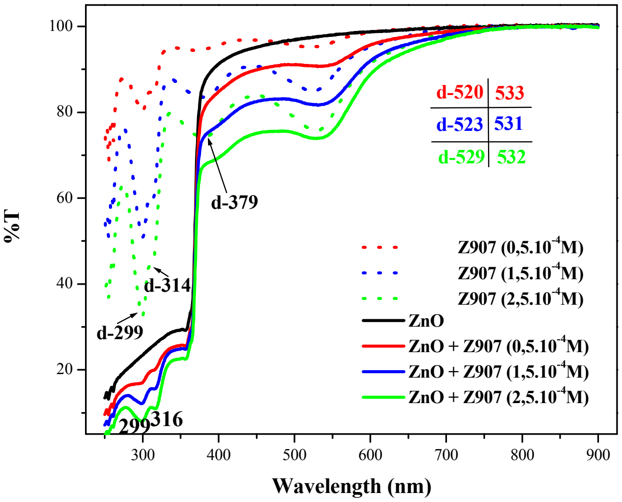

Figure 3. Absorbance spectra of the diluted Z907-ZnO nanorods hybrid solutions at different dye concentrations. Pure dye solutions are the dotted lines whose colors match those of their corresponding hybrids.

Overall view of fluorescence emission spectra of diluted hybrids excited at 325 nm is described in figure 4-a. We can notice a reduction in the ZnO exciton peak intensity when adding further dye molecules, beside a severe drop of the visible defects band. Generally, the reduction of the green defects emission of ZnO with dye concentration is attributed to the passivation of the oxygen vacancies upon ZnO surface functionalization by the dye acid group [1]. To verify this assumption let us graft alkyl chains, namely $C_{11}H_{23}COOH$ at $1.10^{-3}$M as shown in figure 4-b, where a small reduction in the ZnO defects band occurs while the ZnO exciton intensity remains constant. Knowing that the alkyl chain at $1.10^{-3}$ M concentration corresponds to $6.10^{17}$ carboxyl groups (COOH), which are higher than the $30.10^{16}$ carboxyl groups number of the highest Z907 concentration [$2,5.10^{-4}$ M]. Thus even at very large concentrations, alkyl chains can passivate ZnO surface oxygen vacancies to some extent but it can not induce severe reduction in the ZnO exciton and defects emission when grafting the dyes. Hence other mechanisms must exist to elucidate and explain these facts as briefed afterwards in figure 6.

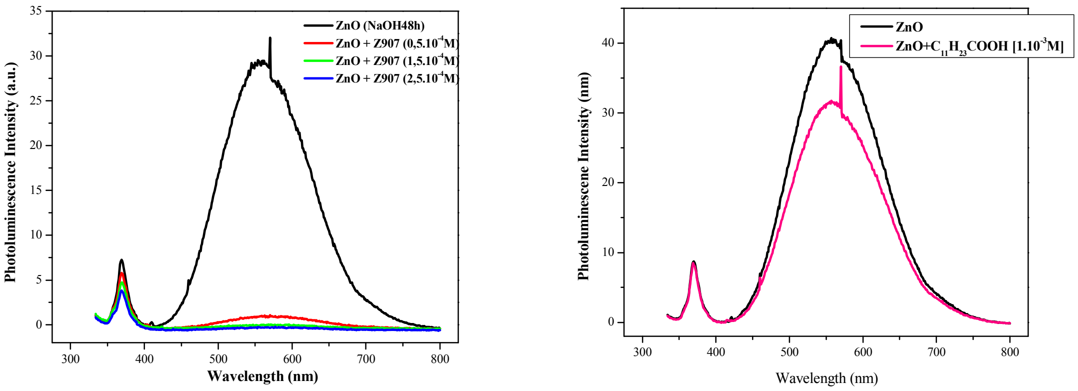

(a) (b)

Figure 4. Global view of fluorescence emission spectra of (a) hybrid based Z907 and (b) ZnO+alkyl chain $C_{11}H_{23}COOH$ excited at 325 nm.

Fluorescence emission spectra of pure Z907 and Z907-based hybrids at 2,5.10$^{-4}$ M excited at 325 and 530 nm are given in figure 4. When exciting at 325 nm, pure dye solution exhibits relatively small emission at ~736 nm (*cyan line*) while this emission diminishes totally in the hybrids (*bleu line*). Excitation at 530 leads to similar emission in pure dye solution (*light gray line*) while the grafted dyes display less red-shifted emission at ~760 nm (*dark gray line*). The decrease of the grafted-Z907 fluorescence might occur by two possible quenching pathways on the surface of ZnO: (i) concentration self-quenching amongst the adsorbed dye molecules most likely aggregated, or (ii) electron transfer from excited dye to the ZnO particles.

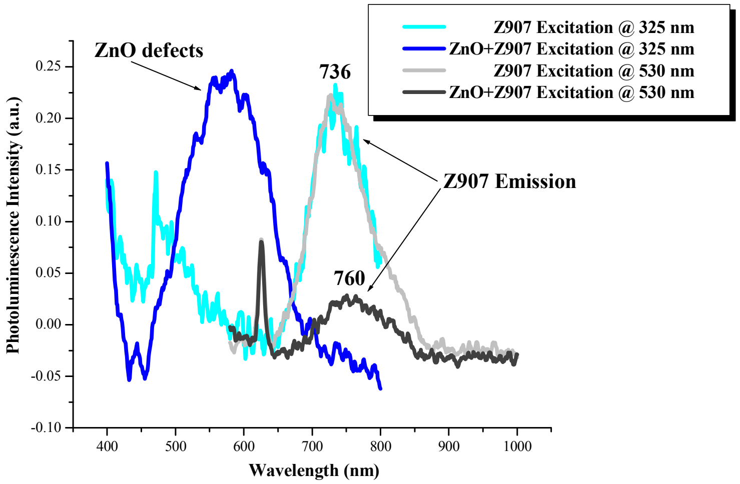

Figure 5. Fluorescence emission spectra of pure Z907 and Z907-based hybrids at 2,5.10$^{-4}$ M excited at 325 nm (cyan and bleu lines) and 530 nm (light gray and dark gray lines).

In attempt to enlighten the stated optical outcomes, a schematic diagram of the ZnO and Z907 energy levels along with the photophysical processes that might occur upon optical excitation are presented in figure 6.

Excitation at the wavelength 325 nm excites mainly the ZnO as well as the Z907 that absorbs at this UV region (figure 3). Therefore, various photophysical processes can happen. In pure ZnO, all the emitted light goes on through the three processes (3) and (5). Adding dye molecules opens the way to processes: (6) when the electron is transferred to the dye's LUMO, (7,8) when the electrons recombine from the ZnO conduction band (CB) and defect level to the holes left in the HOMO level of the dye being himself excited along (9). Hence, boosting processes (6), (7) and (8) leads to the decrease in radiative recombinations (3) and (5), this fact explains the diminution the ZnO exciton and defects. Nevertheless, interfacial hole transfer (12) leads to less hole recombination centers in the ZnO valence band (VB), thus less ZnO radiative emissions. In the dye himself, dye photoexcitation process (9) is followed by three other processes (10), (11) and (13). According to figure 5, no dye emission was detected after dye grafting, thus molecular radiative decay (10) does not exist. This opens the way to the remaining two processes (11) and (13). If the intersystem crossing (3) from the singlet $S_1$ to the triplet $T_1$ is the operating one, then no dye emission would be detected. But when the operating channel is along (11), ZnO is affected through this interfacial electron transfer (11). And since no enhancement in the ZnO emission upon grafting, one can assume that the interfacial charge recombinations (7) and (8) are the mainly acting channels that follow the process (11).

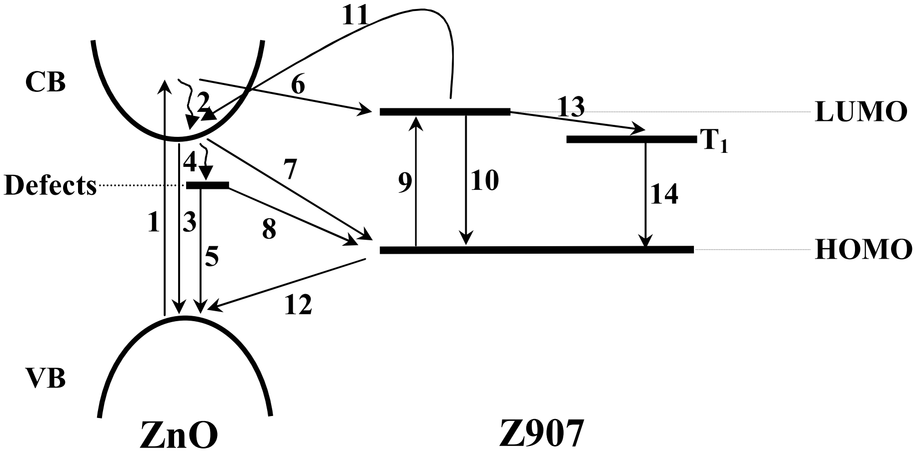

1- Band gap photoexcitation
2- Non-radiative relaxation
3- Intrinsic charge recombination
4- Non-radiative relaxation trap
5- Defect radiative recombination
6- Electron transfer
7- Interfacial charge recombination (from CB)
8- Interfacial charge recombination (from defects)
9- Molecular photoexcitation
10- Molecular radiative decay
11- Interfacial electron transfer (from dye's LUMO)
12- Interfacial electron recombination (to VB)
13- Intersystem crossing (to $T_1$)
14- Radiationless decay

Figure 6. A schematic diagram of the energy levels of ZnO and Z907 together with the processes that may occur upon optical excitation.

On the other hand, the wavelength at 530 nm excites the Z907 along (9). No ZnO defects emission is detected (see figure 5), thus (11) is pursued by (7) and (8) inducing less

ZnO emission. Figure 5 reveals remaining grafted-dye emission implying that process (10) of molecular radiative decay is now acting.

## ● Concluding observations on Z907 grafting

In this subsection, we used another type of dyes that are Ruthenium-based. The Z907 was proved to be efficiently grafted thanks to its red-shifted absorption peaks in the hybrids, where the ZnO are rod-shaped and were synthesized after 48 hours reaction with NaOH. Photoluminescence data at 325 nm excitation showed that when grafting the Z907 molecules, severe reduction in the ZnO exciton and defects emission intensities occur due to some physical assumptions as the dye-aggregation and the increase in the non-radiative recombination centers. Excitation at 530 demonstrates quenches and red-shifted emission of the dye at ~760 nm. This can be the consequence of the concentration self-quenching amongst the aggregated adsorbed dye and the electron transfer from excited dye to the ZnO particles. Yet, this later mechanism is likely to be pursued by non-radiative interfacial recombinations from the ZnO back to the dye.

[1] M. W. de Lange, J. G. van Ommen and L. Lefferts, Applied Catalysis A: General 220 (2001) 41

# Appendix VIII: Experimental setup of Solar cells characterization

The External Quantum Efficiency (EQE) is by definition the photocurrent measured under monochromatic light at short-circuit (V=0) per incident light power as a function of wavelength. The optical system, shown in figure 1, consists of a single concave mirror which creates an image of the 100 watts halogen lamp source magnified 1.8 times at the entrance slit of the motorized monochromator (Cornerstone 130TM model 74000). At 4 to 5 cm from the monochromator exit, the light impinge into the placed solar cell, and whose emanating photocurrent is measured by a Keithley 238 current measure unit.

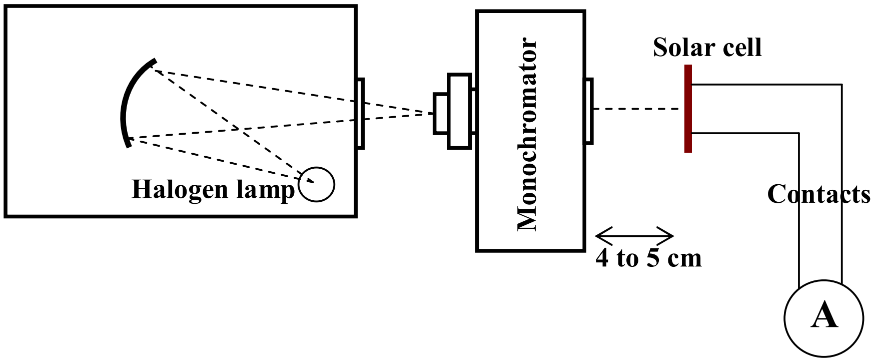

Figure 1. Experimental set-up for the EQE measurements.

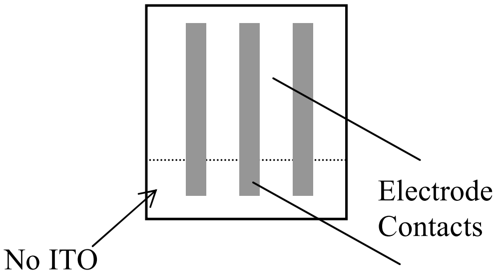

Figure 2. Electrode Contacts for measuring the EQE and the J-V.

Figure 2 shows the exact placement of the electrical contacts in order to measure both the EQE and the J-V. The current to voltage J-V characteristics were recorded under white-light illumination using a halogen lamp in the intensity range of 100 mW/cm$^2$, here the cells were directly exposed to the halogen lamp with no monochromator.

# Liste des publications

## Publications dans des Revues Internationales

[1] A. Said, L. Sajti, S. Giorgio, W. Marine, *Synthesis of nanohybrid materials by femtosecond laser ablation in liquid medium*, Journal of Physics: Conf. Ser. 59, (2007) 259-265.

[2] L. Sajti, A. Said, S. Giorgio, W. Marine, *Towards new biocompatible and nanostructured biomarkers by femtosecond laser ablation in liquid environment*, Proc. SPIE 61910Y (2006), 242-248.

## Participations à des Conférences Internationales

[1] Guillaume Poize, Aurore Said, Cyril Martini, Julien Hocq, James Durrant, Johann Boucle, Jenny Nelson, Wladimir Marine, Suzanne Giorgio, Frederic Fages and Jorg Ackermann. *Photovoltaic Properties of Hybrid Bulk Heterojunction Solar Cells from P3HT and Dye Sensitized ZnO Nanorods*. MRS Boston, MA, USA. 2007 Fall Meeting. Oral

[2] Cyril Martini, Aurore Said, Wladimir Marine, Suzanne Giorgio, Frederic Fages and Jorg Ackermann. *New Insights in how to Control Size Dispersion and Surface Roughness of Solution-phase Grown ZnO Nanorods*. MRS Boston, MA, USA. 2007 Fall Meeting. Oral

[3] G. Poize, A. Said, C. Martini, J. Hocq, J. Durrant, J. Ackermann and F. Fages. *Cellules solaires hybrides à jonctions p-n interpénétrées à base de P3HT et de nanobâtonnets de ZnO*. Matériaux et Nanostructures Pi Conjugués, MNPC, Montpellier, France, 2007. Poster

[4] J. Ackermann, G. Poize, A. Said, C. Martini, W. Marine and F. Fages. *Hybrid heterojunction solar cells from P3HT and ZnO nanorods*. ECHOS'05 European Conference on Hybrid and Organic Solar Cells, Paris, France, 2006. Poster

[5] J. Ackermann, A. Said, C. Martini, L. Sajti, G. Poize, W. Marine and F. Fages. *Hybrid nanoparticles based on porphyrin and oligothiophene functionalized ZnO*. The Seventh International Symposium on Functional π- Electron Systems, Osaka, Japon, 2006. Poster

[6] A. Said, C. Martini, G. Poize, L. Sajti, F. Fages, W. Marine and J. Ackermann. *Hybrid materials based on porphyrin and oligothiophene functionalized ZnO*. E-MRS 2006 Spring Meeting, Functional Materials for Micro and Nanosystems, Nice, France, 2006. Oral

[7] L. Sajti, A. Said, S. Giorgio, V. Khodorkovsky and W. Marine. *Femtosecond laser synthesized nanohybrid materials for bioapplications*. E-MRS 2006 Spring Meeting, Photon-Assisted Synthesis and Processing of Functionnal Materials, Nice, France, 2006. Oral

[8] L. Sajti, A. Said, S. Giorgio and W. Marine. *Towards new biocompatible and nanostructured biomarkers by femtosecond laser ablation in liquid environment.* Photonics Europe, Strasbourg, France, 2006. Oral

[9] A. Said, C. Martini, F. Fages, W. Marine and J. Ackermann. *Hybrid Nanoparticles Based on Porphyrin and Oligothiophene Functionalized ZnO*. 3rd International Conference on Photoresponsive Organics and Polymers, Val Thorens, France, 2006. Poster

[10] L. Sajti, A. Said and W. Marine. *Synthesis of Nanohybrid Materials by Femtosecond Laser Ablation in Liquid Medium*. Conférence Internationale COLA 05, the 8th International Conference on Laser Ablation, Banff, Canada, 2005. Oral

[11] A. Said, L. Sajti and W. Marine. *Synthèse par ablation laser femtoseconde de matériaux nanohybrides à base de ZnO en milieu liquide*. Congrès Général de la Société Française de Physique et de la Société Belge de Physique 2005 « Matière condensée», Lille, France, 2005. Poster

[12] A. Said, L. Sajti, S. Giorgio and W. Marine. *Synthèse des Nanohybrides à la base de ZnO par ablation laser femtoseconde en phase liquide: Analyse par AFM et HRTEM*. Colloque Méditerranéen « Analyses, Synthèse, Modification et Manipulation des Nanomatériaux par et pour des photons », Marseille, France, 2005. Oral

## Séminaires et Communications

[1] A. Said, C. Martini, L. Sajti, S. Giorgio , W. Marine, F. Fages and J. Ackermann. *Materiaux nano-hybrides à base de ZnO: études de la synthèse, des propriétés et des applications*. Journées de l'Ecole Doctorale, Marseille, France, 2007. Oral

[2] A. Said, C. Martini, L. Sajti, S. Giorgio , W. Marine, F. Fages and J. Ackermann. *Synthesis of nanohybrid based on chromophore-functionalized ZnO*. Journées de l'Ecole Doctorale, Marseille, France, 2006. Poster

[3] A. Said. *Synthèse des Nanohybrides à la base de ZnO par ablation laser femtoseconde en phase liquide: Analyse par AFM et TEM*. Journées de l'Ecole Doctorale « Physique et Sciences de la Matière », Marseille, France, 2005. Poster

**Résumé:** Ma thèse consiste en l'étude du greffage des molécules de colorant sur des nanoparticules de ZnO, de leurs propriétés optiques et morphologiques, ainsi que les interactions électroniques entre le ZnO inorganique et le colorant organique. Nous avons créé des nanohybrides à base de nanosphères et nanobâtonnets de ZnO par deux voies: Ablation laser femtoseconde en phase liquide et Procédés chimiques. Des particules sphériques de quelques nanomètres sont générées par ablation laser révélant par la photoluminescence l'effet de confinement quantique due à la réduction de taille. Transfert d'excitation des ZnO synthétisées par ablation laser vers les molécules de colorant greffées est détecté par les excitations à un- et deux-photons. La croissance des bâtonnets de ZnO synthétisés chimiquement s'effectue par mûrissement d'Oswald et par attachement orienté. Ces modes de croissance sont étudiées en fonction du temps de synthèse et de la nature des réactants par le Microscope Electronique de Transmission à Haute Résolution. Les propriétés optiques des hybrides dépendent fortement de la forme de ZnO ainsi que du type et concentration du colorant greffé. Nous avons parvenu à remodeler l'énergie de la bande interdite des nanosphères de ZnO dans le système hybride par simple variation de la concentration du colorant. Nous avons ainsi montré l'effet de confinement quantique dû à la création de couches de charges dans le ZnO induites par la porphyrine adsorbée via ses groupes d'attachement COOH.

**Title: Large Band gap Nanohybrid Materials: Study of their Syntheses, Properties and Applications.**

**Abstract:** My thesis consists on the design of dye-functionalized ZnO nanoparticles and the investigation of their optical and morphological properties, and electronical interactions between the inorganic ZnO and the organic dye molecules. We produced Nanohybrids based on spherical and rod-like ZnO templates via two routes: Femtosecond laser ablation in liquid medium and Solution-based chemical procedures. Spherical particles of few nanometers were generated by laser ablation revealing by photoluminescence the effect of quantum confinement due to size reduction. Excitation exchange from the ablated ZnO core towards the grafted dye molecules is detected via one- and two-photon excitations. The chemically-synthesized ZnO rod-growth occurs through Oswald repining and oriented attachment. These growth modes were monitored depending on synthesis time reaction and reactant nature by the High Resolution Transmission Electron Microscope (HRTEM). Optical properties of the hybrid samples strongly depend on the ZnO shapes as well as on the adsorbed dye type and concentration. We were able to engineer the band gap of the small ZnO particles in the nanohybrid matrices simply upon varying the dye concentration. We showed thus the quantum confinement effect through induced charged layers in the ZnO due to the adsorbed porphyrin dyes of COOH anchoring groups.

**Discipline:** Sciences des Matériaux, Physique, Chimie et Nanosciences

**Mots-clés :** Hybride (Organique-Inorganique) / Nanoparticules de ZnO (Sphères et bâtonnets)/ Ablation laser femtoseconde / Confinement Quantique / mûrissement d'Oswald / Attachement orienté / HRTEM (High Resolution Transmission Electron Microscopy) / Fluorescence conventionnelle et résolue en temps / Transfert d'excitation / agrégation / Porphyrine (H2TCPP et PP9) / Cellule solaire Hybride

*Centre de Recherche en Matière Condensée et Nanosciences,*
*CRMC-N CNRS UPR 7251,*
*Centre conventionné aux Universités Aix-Marseille II & III*
*Faculté des Sciences de Luminy, Case 901, 13288 Marseille Cedex 09, France*